Novel probes to map biology at the nanoscale

By:

Zhen Zhao

A thesis submitted for the degree of Doctor of Philosophy
November 2017

Department of Chemistry,
University of Sheffield

Abstract

Biology is apparent across the length scale from the atomic to whole populations and ecosystems. At the cellular and subcellular levels processes occur at a scale often too small to be deciphered with conventional microscopy. The advent of super resolution microscopy has the potential to revolutionize our understanding of biological mechanisms, providing a hitherto impossible level of detail, which relies on the ability to interpret the images, in-turn requiring appropriate probes.

The bacterial cell wall is essential for viability and shape determination. The major structure polymer in the cell wall is peptidoglycan (PG). PG synthesis is the target of crucial antibiotics such as penicillin. In this study, a variety of fluorescent probes were used to label bacterial PG to reveal its dynamic nanoscale architecture and role in cell growth and division. Initially, three kinds of fluorescent probes based on D-amino acids were incorporated into the side chain of newly synthesised PG, using a natural biosynthetic mechanism. Then, fluorescent derivatives of vancomycin were specifically applied for binding to nascent PG, due to the highly specific vancomycin-binding mechanism. Having achieved successful side chain labelling, the reducing terminus of PG was investigated based on oxime formation between hydroxylamine functionalised fluorophores and aldehyde groups. All of these proved successfully as highly sensitive molecular probes to image PG and to decipher the complex system of growth and assembly of the cell wall.

Inspired by this work, multifunctional probes were designed and synthesised with bioorthogonal-chemistry moieties, including hydroxylamine, alkyne and/or azide, for imaging the cell wall by super resolution microscopy. Although super-resolution imaging makes it possible to observe biomolecules at the nano level, there is still a lack of even higher resolution that is a prerequisite to provide the truly molecular details of cell dynamics. As a result, such probes were specifically designed that could be used with multi-imaging modalities such as gold nanoparticles and metallocenes. Combining this with electron microscopy highlights their potential to provide further details of cell wall dynamics.

Acknowledgements

Firstly, I would like to express my sincerest gratitude to Prof. Simon Jones and Prof. Simon Foster for giving me the opportunity to carry out my PhD. Special thanks go to Prof. Simon Jones for his continued support and guidance through all these years. Without his patience and encouragement, this work would never have been completed. Many thanks also to Prof. Simon Foster, who has not only academically and emotionally supported my study, but also kindly provided amazing biscuits and coffee.

I am also greatly appreciative of the University of Sheffield 2022 Futures Studentship for funding my study and life in Sheffield.

I would like to extend thanks to the many people of the two Simon's groups, who generously provide tremendous suggestions and guidance. Particularly I thank Dr Andrew Reeder and Dr Dan Cox for much advice in organic synthesis and vivid elaboration of English proverbs that make the PhD life more enjoyable. I'm also incredibly grateful to Dr Victoria Lund and Dr Robert Turner for making significant contributions to the STORM and EM experiments. Thanks to Christa Walther and Darren Robinson for the use of the super-resolution microscopes at the Light Microscopy Facility.

Finally, but by no means least, I am grateful to my parents for unreservedly supporting my study. Thanks to all my friends. Also to the fantastic food and football in the UK.

Abbreviations

3D	Three dimensional
^{o}C	Degree Celsius
ADA	3-Azido-D-alanine
AFM	Atomic force microscopy
ala	Alanine
Alkyne488	Alexa Fluor 488 Alkyne, triethylammonium salt
Alkyne647	Alexa Fluor 647 Alkyne, triethylammonium salt
AuNP	Gold nanoparticle
BHI	Brain heart infusion
BODIPY	Boron-dipyrromethene difluoride
Cbz	Benzyloxycarbonyl
CLSM	Confocal laser scanning microscopy image
CP	Cyclopentadienyl
CT	Computed tomography
CTCED	Corrected total cell electronic density
CTCF	Corrected total cell fluorescence
CuAAC	Copper-catalyzed azide-alkyne cycloaddition
Cy	Cyanine
D-Ala	D-alanine
DAP	Diaminopimelic acid
DCDHF	2-dicyanomethylene-3-cyano-2,5-dihydrofuran
D-Glu	D-glutamic acid
dH_2O	Distilled water
DIAD	Diisopropyl azodicarboxylate
DMAP	4-dimethylaminopyridine
DMSO	Dimethyl sulphoxide
EM	Electron microscopy
EI	Electron Ionization
Ery	Erythromycin
Fc	Ferrocene
FDAA	Fluorescent D-amino acid
FM	Fluorescence microscopy
FP	Fluorescent protein
FRAP	Fluorescence Recovery After Photobleaching
GFP	Green fluorescent protein
Glc*N*Ac	*N*-acetyl glucosamine
GLOX	Glucose oxidase
glu	Glutamic acid
Gly	Glycine
GSH	Glutathione

GT	Transglycosylase
HADA	7-hydroxycoumarin-3-carboxylic acid-3-amino-D-alanine
HAF488	Alexa Fluor 488 hydroxylamine
HMM	High-molecular-mass
IR	Infrared
Kan	Kanamycin
LAA	L-Ala amidase
L-Ala	L-alanine
Lin	Lincomycin
L-Lys	L-lysine
LMM	Low-molecular-mass
LPS	Lipopolysaccharide
m-DAP	meso-diaminopimelic acid
MEA	Mercaptoethylamine
MIC	Minimum inhibitory concentration
mM	Millimolar
Mn-QD	Mn-doped ZnSe quantum dot
MRI	Magnetic resonance imaging
MRSA	Methicillin-resistant *Staphylococcus aureus*
MS	Mass spectrum
Mur*N*Ac	*N*-Acetyl muramic acid
NaAc	Sodium acetate
NADA	7-nitrobenzofurazan-3-amino-D-alanine
NB	Nutrient broth
Neo	Neomycin
NLSs	Nuclear localization signals
nm	Nanometre
NMR	Nuclear magnetic resonance
NSOM	Near field scanning optical microscopy
OD	Optical density
PA-FP	Photoactivatable fluorescent protein
PALM	Photo-activated localization microscopy
PBP	Penicillin-binding protein
PBS	Phosphate buffered saline
PC-PALM	Pair correlation photoactivated localization microscopy
PEG	Polyethylene Glycol
PG	Peptidoglycan
PET	Positron emission tomography
PFA	Paraformaldehyde
PSF	Point spread function
PS-FP	Photoshiftable fluorescent protein
QD	Quantum dot
Rc	Ruthenocene
rpm	Revolutions per min

RT	Room temperature
SADA	7-nitro-2,1,3-benzothiadiazole-3-amino-D-alanine
S. aureus	*Staphylococcus aureus*
SD	Standard deviation
SDS	Sodium dodecyl sulfate
SIM	Structured illumination microscopy
SPAAC	Strain-promoted azide-alkyne cycloaddition
SPECT	Single photon emission computed tomography
SSIM	Saturated structured illumination microscopy
STED	Stimulated emission depletion microscopy
STORM	Stochastic optical reconstruction microscopy
TADA	Tetramethylrhodamine 3-amino-ᴅ-alanine
TBAB	Tetrabutylammonium bromide
TEM	Transmission electron microscopy
TEG	Triethylene glycol
TLC	Thin layer chromatography
TSB	Tryptone soy broth
UDP	Uridindiphosphate
Van	Vancomycin
WGA	Wheat germ agglutinin

Appendix: Names and structures of dyes used

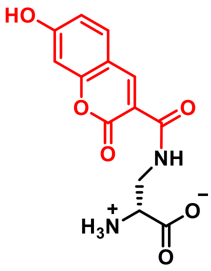

HADA

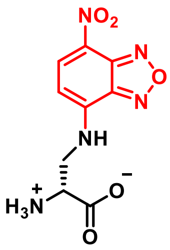

NADA

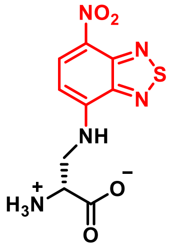

SADA

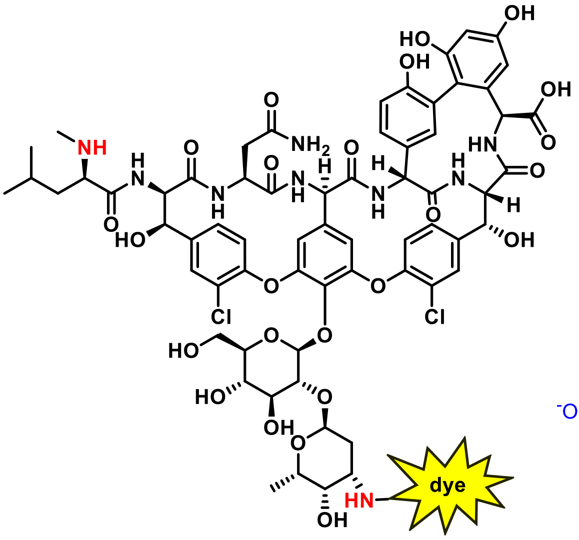

Fluorescent derivatives of vancomycin

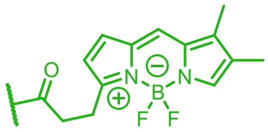

BODIPY

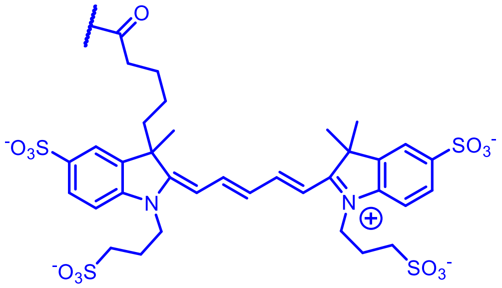

AlexaFluor 647

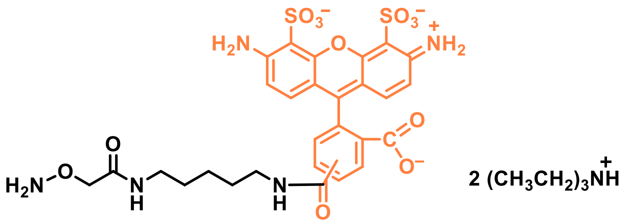

Alexa Fluor 488 hydroxylamine
(HAF488)

Contents

Chapter 1 Introduction

As a complex collection of basic inorganic and organic elements, the natural world is continually conducting a variety of chemical reactions and physical changes. Living organisms contain a multitude of cells, which, in turn, contain an enormous variety of biomolecules. These biomolecules perform a vast array of functions based on chemical reactions such as acid/base chemistry, ligand substitution, as well as isomerisation and catalytic transformations. Also, the concentrations, locations, modifications, and interactions of these molecules are generally controlled in a precise spatial and temporal fashion. Deciphering this complex system and learning more about the mechanism and dynamics of these processes presents not only critical challenges, but also a unique opportunity for biologists to explore new viewpoints on the research of living organisms.

1.1 Methods in bioimaging

As a key step towards the ultimate goal of deciphering complex biological systems, bioimaging has greatly advanced over recent years. Ever since the first microscope was built four hundred years ago, morphological observations have pushed the course of biology. Bioimaging, an exciting and growing field, resides at the interfaces of chemistry, physics, biology, and engineering, as well as mathematics and computer sciences. Compared with other approaches, it can not only track molecular changes, but also interrogate intact living samples with spatial resolution under physiologically relevant conditions in real time, which is more perceptually vivid and directly demonstrated in a visual field. Bioimaging can be considered as a non-invasive process that provides comprehensive views of a living organism in progressively greater depth and detail in real time. Moreover, bioimaging has the potential to interfere as little as possible with life processes and generally collects information on the three-dimensional structure of the fixed sample from the outside, i.e. without physical interference.

Therefore, bioimaging is a powerful tool for viewing the structure, function, mechanism and internal workings of organisms, which range from bacteria and viruses to higher organisms.

In recent years biological discovery has been pushed forward at an accelerated pace, and most of the focus has been on the transition from *in vitro* to *in vivo* models. As such, imaging methods for non-invasive assays of biochemical processes are highly desired and thus considerable efforts have been directed in this area. As a result, numerous bioimaging technologies have been developed, which are generally divided into several categories: magnetic resonance imaging (MRI), ultrasound, computed tomography (CT), positron emission tomography (PET), single photon emission computed tomography (SPECT), optical imaging, electron microscopy (EM) imaging and atomic force microscopy (AFM) imaging.[1-7]

1.2 Bacterial cell wall

Among countless research avenues in biological science, one of the major concerns is the cell wall of bacteria. The existence of the cell wall was discovered after the development of the microscope. The cell wall, an essential element in bacteria, not only plays the principal stress-bearing and shape-maintaining structural role, but also demonstrates critical importance to a variety of cellular processes such as cell viability, morphogenesis, chromosome segregation, pathogenesis and interaction between the bacterium and its environment. Although cell wall composition varies widely amongst bacteria, all cells fall into two major classifications, Gram-positive and Gram-negative, which are defined by their reaction towards the Gram stain. The differences of cell wall structure in Gram-positive and Gram-negative bacteria are given below (Figure 1.1).[8]

Most bacterial have a rigid cell wall offering protection from mechanical damage, osmotic rupture, or lysis, which mainly utilises the rigid structure of peptidoglycan. Peptidoglycan, a huge polymer of cross-linked chains composed of basic units, is found only in bacterial cell walls, whose backbone is composed of two derivatives of glucose: *N*-acetyl glucosamine and *N*-acetyl muramic acid.[9]

In Gram-positive bacteria, the cell wall consists of several layers of peptidoglycan which make up as much as 90% of the thickness.[10] Apart from peptidoglycan, there are other components in the cell wall, such as teichoic and lipoteichoic acids and complex polysaccharides. Teichoic acids, running perpendicular to the peptidoglycan, are water-soluble polymers of polyol phosphates, usually with sugars and/or the amino acid as substituents, and are unique to the Gram-positive cell wall. As a major constituent of the cell wall, lipoteichoic acids are anchored in the cytoplasmic membrane via diacylglycerols, which vary between the different species of Gram-positive bacteria.

Gram-negative bacteria, on the other hand, have a much thinner cell wall, which is low in peptidoglycan but high in lipid content.[11] Also, Gram negative cell walls have two separate areas with an additional membrane besides the cellular membrane and thus are more complicated than Gram-positive cell walls. In the Gram-negative bacteria, the outer membrane surrounds a single layer of peptidoglycan in cell walls, which is unique to Gram-negative bacteria. The outer membrane functions as an effective barrier and is composed of a high concentration of polysaccharides, lipids and proteins. Among them lipopolysaccharide (LPS) is a unique component and constitutes the outer leaflet of the outer membrane, which typically elicits strong immune responses in human and animals. The space between the cytoplasmic and outer membranes is an open area called the periplasm which is filled with water and proteins.[10]

In short, the cell wall of bacteria protects the cell from osmostic shock and physical damage, and its composition varies widely amongst bacteria, which can be helpful in bacterial species analysis and differentiation.

a Gram-negative bacteria

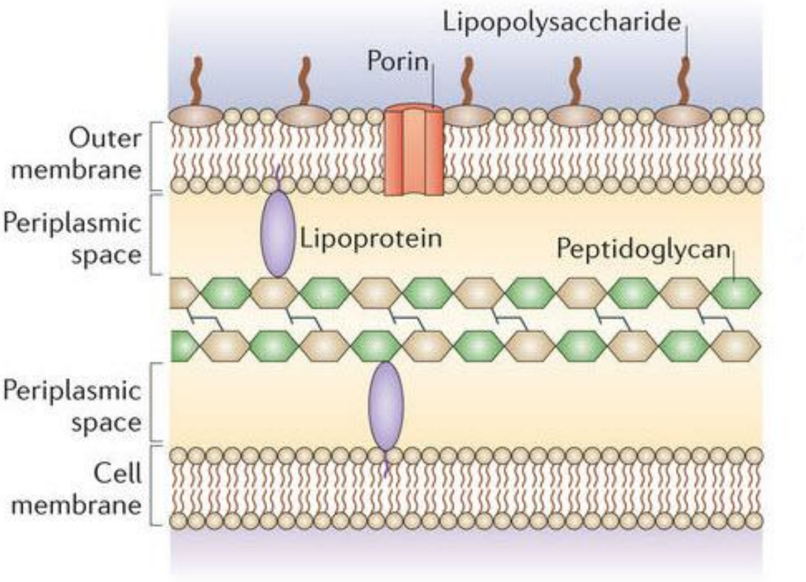

b Gram-positive bacteria

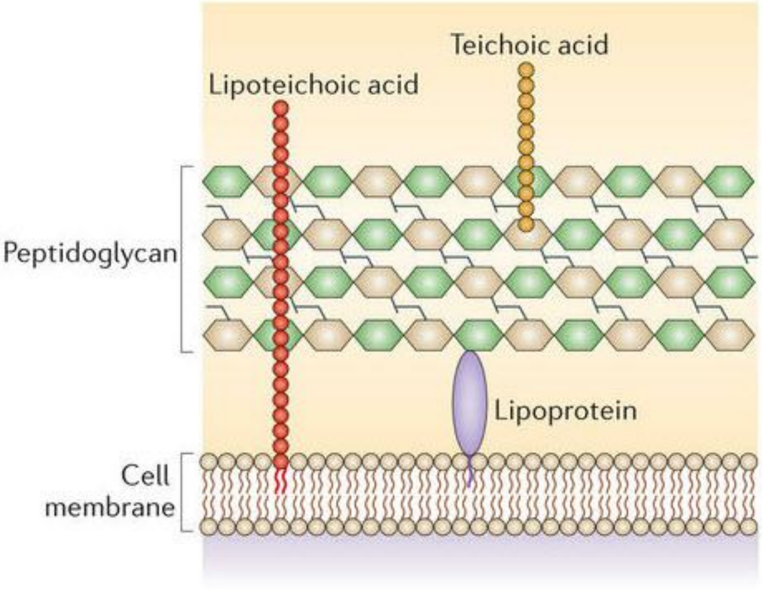

Figure 1.1 Structure and composite of bacteria cell envelopes. **(A)** In the Gram negative cell wall, there are three primary layers. Peptidoglycan is thin and positioned between the outer membrane and the cytoplasmic membrane. **(B)** In the Gram-positive bacteria the outer membrane is absent, but they have much thicker peptidoglycan layers surrounding the plasma membrane. Ref 8 with permission from *Nature Reviews Microbiology*.[8]

1.2.1 Peptidoglycan

As mentioned previously, both Gram-positive and Gram-negative bacteria do share one thing in common that is unique to bacteria - peptidoglycan (PG). PG is of critical importance for cells for maintenance of viability, shapes and termination. Importantly, PG synthesis is not only a well-known target for antibiotics due to its uniqueness to bacteria, but also can be recognized by the host, inducing variety of biological effects such as inflammation, toxicity, accumulation of pus, arthritis, fever, sleepiness, decreased appetite, hypotension, and thrombocytopenia.[12]

1.2.1.1 Chemical structure of Peptidoglycan

PG, also called murein, was derived from terms of peptide and glycan, and is a rigid, but flexible polymer consisting of cross-linked chains of identical simple subunits, forming a mesh-like layer outside the plasma membrane of bacteria.

Each subunit consists of two connected amino sugars, *N*-acetyl glucosamine (Glc*N*Ac) and *N*-acetyl muramic acid (Mur*N*Ac), and these alternating molecules make up the long glycan backbone by the connection of beta 1,4-glycosidic bonds (Figure 1.2).[9] A short peptide consisting of L- and D-amino acids is attached to the Mur*N*Ac, the precise composition of which may vary between bacteria. In most Gram-negative bacteria (ie *Escherichia coli*) and Gram-positive bacilli (ie, *Bacillus subtilis*), the stem peptides possess meso-diaminopimelic acid (m-DAP) at the third position whereas the third amino acid is L-lysine in most other Gram-positive bacteria (ie, *Staphylococcus aureus*). These peptide chains can be cross-linked to the peptide chain of another strand, either directly or through an interpeptide bridge between m-DAP/L-Lys on one chain and D-Ala on the other (Figure 1.2).[13] PG may be distinguished by different amino acids in the side-chains and different ways to be cross-linked.[14] The assembly of PG is mediated by a group of enzymes, including transglycosylases, transpeptidases and carboxypeptidases.

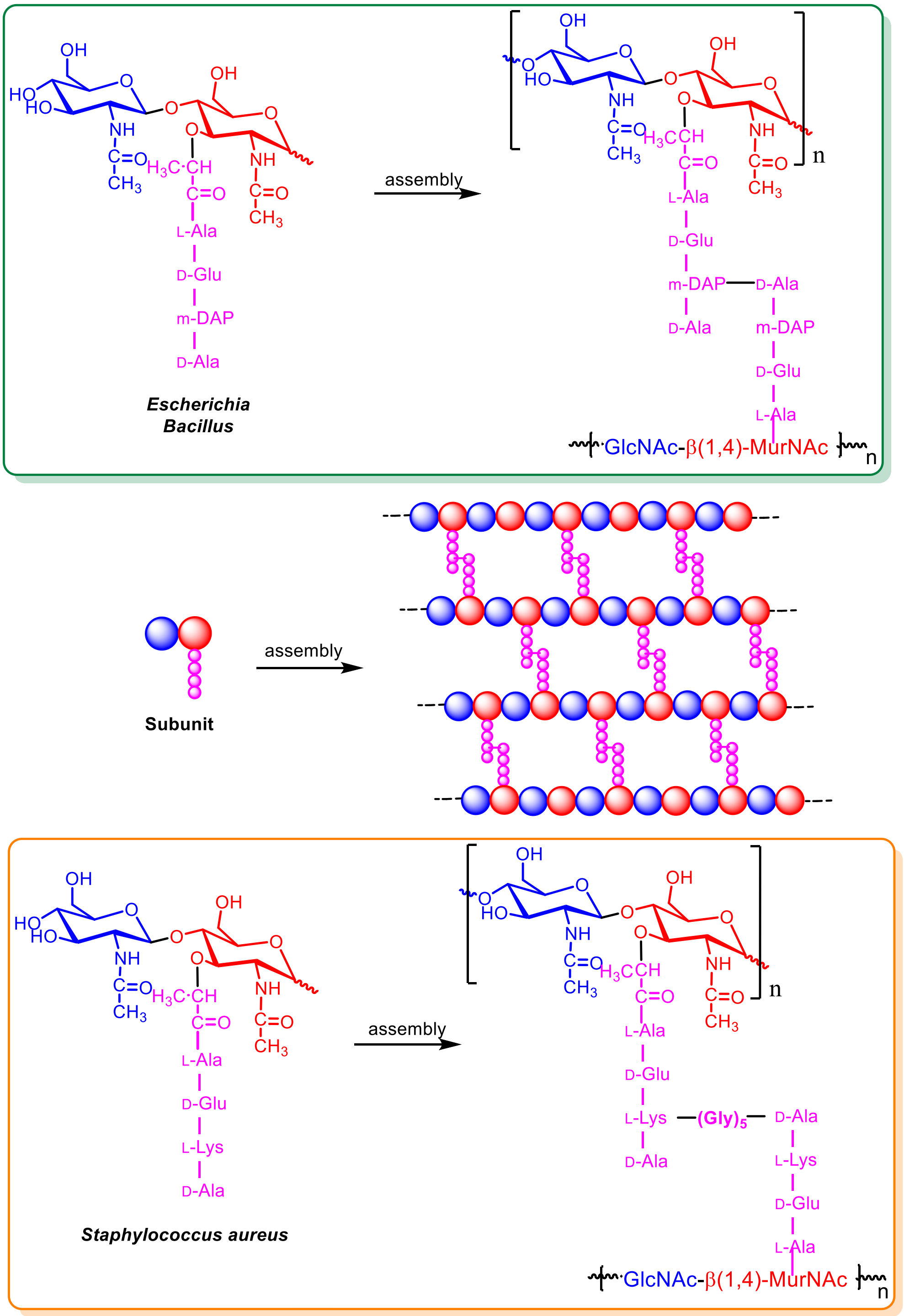

Figure 1.2 Chemical structure and assembly of peptidoglycan. The glycan backbone is a polymer of two connected amino sugars (subunit), *N*-acetyl glucosamine (blue) and *N*-acetyl muramic acid (red). Cross-linking generally occurs at nearby peptide side chains (pink) directly between m-DAP and D-Ala (top), or through an interpeptide bridge (bottom), forming peptidoglycan. Abbreviations: D-Ala, D-alanine; L-Lys, L-lysine; D-Glu, D-glutamic acid; L-Ala, L-alanine; Gly, Glycine.

1.2.1.2 Peptidoglycan biosynthesis

The biosynthesis of PG, a complex process involving approximately 20 enzyme reactions, takes place both in the cytoplasm and cytoplasmic membrane, which can be divided into several key stages (Figure 1.3).[15]

The first stage occurs in the cytoplasm and results in the synthesis of the nucleotide activated precursors uridindiphosphate-*N*-acetylmuramyl-pentapeptide (UDP-Mur*N*Ac-pentapeptide) and uridindiphosphate-*N*-acetylglucosamine (UDP-Glc*N*Ac), which are synthesised from fructose 6-phosphate. In the second stage, with the help of integral membrane proteins (MraY, MurG and flippase), precursor lipid I and II are synthesized and then flipped, which take place at the cytoplasmic membrane. In detail, a C_{55}-polyisoprenoid carrier (usually referred to as bactoprenol) attaches to the phospho-Mur*N*Ac-pentapeptide moiety from UDP-Mur*N*Ac-pentapeptide to form lipid I, the undecaprenyl pyrophosphoryl-Mur*N*Ac-pentapeptide by MraY. Then, in the presence of MurG, Glc*N*Ac from UDP-Glc*N*Ac is added to lipid I to give precursor lipid II, Glc*N*Ac-β-(1,4)-Mur*N*Ac-(pentapeptide)-pyrophosphoryl-undecaprenol, which is the substrate for next polymerization reactions. Then, flippase transports lipid II from the cytoplasmic side to the periplasmic leaflet of the cytoplasmic membrane. In the third stage, the newly synthesized disaccharide-peptide units are polymerised and inserted into the autolysin-induced breaks in the existing PG cell through penicillin-binding proteins (PBPs), which takes place at the outer side of the cytoplasmic membrane.

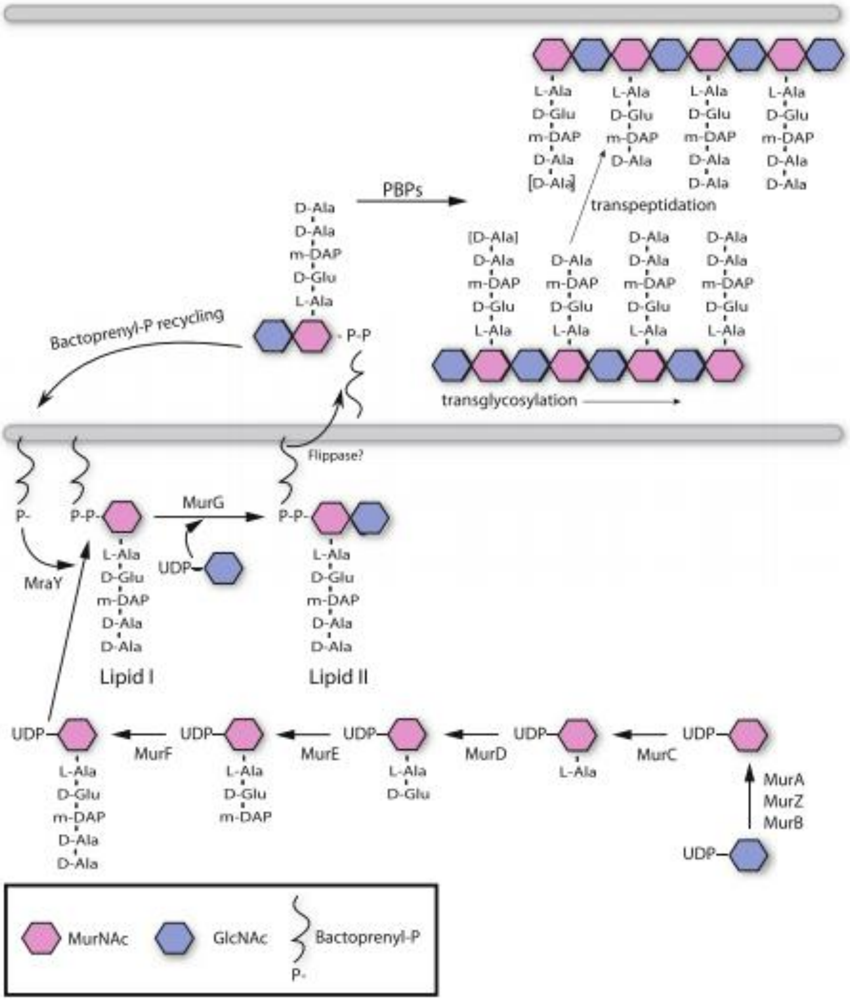

Figure 1.3 Biosynthesis of peptidoglycan (PG). UDP-Glc*N*Ac is synthesized and assembled to form a variety of PG precursors in the cytoplasm. Precursors are then translocated across the cytoplasmic membrane and incorporated into the PG polymer through transglycosylation and transpeptidation guided by the penicillin-binding proteins (PBPs). Copyright Open Access Subset of PubMed Central.

1.2.1.3 Peptidoglycan hydrolysis

Apart from the above mentioned numerous synthetases involved in the PG biosynthesis pathway, hydrolases also play a crucial role in plentiful aspects of cells growth and division, which cleave covalent bonds in PG and/or their multi precursors.[16] PG hydrolases are an enzyme family of highly diverse species that are specifically classified by the cleavage sites they recognize and are found in both prokaryotes and eukaryotes.

In bacteria, they have vast of activities in PG dynamics and cell physiology, including new material insertion, PG turnover, splitting of the cell wall, cell autolysis, spore formation and germination, and biofilm formation. For instance, to maintain the thickness of the cell wall, PG synthesis needs the insertion of new chains, and hydrolases cleave the pre-existing PG and/or the cross-linking formed between side chains to facilitate the insertion process. Moreover, during cell growth, a septal feature is required to be synthesized and split, before daughter cells are completely formed. This feature is later split by PG hydrolases to complete cell separation.

Chemically, there are routinely two kinds of covalent bonds within the PG network; glyosidic bonds in the glycan chain, and amide bonds occurring between the glycan chain and the peptide side chain and within the side chain (peptide bonds). Correspondingly, there are broad classes of bacterial PG hydrolases characterized by cleavage sites, including glycosidases, peptidases and amidases responsive for glyosidic and amide bonds within the PG network (Figure 1.4). Glycosidases are classified as enzymes that catalyse the hydrolysis of the glyosidic bond of PG glycan backbone and possess three main categories; glucosaminidases, muramidases and lytic transglycosylases.[17] Glucosaminidases hydrolyze the β-1,4-glycosidic bond between Glc*N*Ac and Mur*N*Ac, giving a reducing terminal Glc*N*Ac. In *Staphylococcus aureus*, earlier work identified four enzymes with glucosaminidase activity, including Atl, SagA, ScaH, and SagB, which are collectively required for cellular enlargement and characteristic short glycan strands present in PG.[18] On the contrary, the β-1,4-glycosidic bond between Mur*N*Ac and Glc*N*Ac is recognized by muramidases or lytic transglycosylases. While muramidases (also called lysozymes) and lytic transglycosylases cleave the same glycosidic bond, the cleavage mechanisms between two enzymes are different. Distinct to the hydrolytic enzyme of muramidases, lytic transglycosylases function as non-hydrolytic enzymes to cleave the glycosidic bond and also catalyse an intramolecular transglycosylation reaction that forms 1,6-anhydro-Mur*N*Ac-peptide.[19] S*taphylococcus aureus* has two likely lytic transglycosylases, IsaA and SceD, which subtly modify the PG structure and are essential for normal growth, nasal colonization and successful host-pathogen interactions.[20] Muramidases act in most bacterial species, resulting in a reducing terminal Mur*N*Ac residue. However, S*taphylococcus aureus* is resistant, which is attributed to the *O*-acetylation of the PG.[21]

Amidases are enzymes that specifically catalyse the cleavage of the amide bond between the lactyl group of Mur*N*Ac and the α-amino group of the N-terminal L-alanine within the stem peptide, and thus are referred as *N*-acetylmuramyl-L-Ala amidases (Mur*N*Ac-LAAs).[19,22] In most bacteria, Mur*N*Ac-LAAs possess a signal peptide at their N-terminal for the transportation across the cytoplasmic membrane. They play their crucial role in cell metabolism as autolysins. An autolysins is an enzyme able to cause lysis of the organism that produces it. There are six Mur*N*Ac-LAAs in *Escherichia coli*, which contain AmiA, AmiB, AmiC, AmpD, AmiD and one 39-kDa amidase that has not well characterized.[23] Although all are zinc-ion-dependent amidases, AmiA, AmiB, AmiC and AmiD are periplasmic while AmpD is cytoplasmic.[17] According to the Pfam database, AmiA, AmiB, and AmiC are classified as the amidase 3 family while AmiD and AmpD belong to the amidase 2 family.

Classified on the basis of cleavage specificity, peptidases fall into two main categories, including carboxypeptidases and endopeptidases. The former catalyse the elimination of a C-terminal amino acid and the later cleave the various peptide bonds within the stem peptides. Depending on the structural specificity of the amino acids referred to the processing, peptidases are categorized as DD-, DL- or LD-peptidases, which cleave bonds between two D-amino acids, or between a D- and an L-amino acid, respectively.[16] Due to the complex existence of amino acids type and stereo-chemical structure, there have been reported at least 20 peptidases present in *Escherichia coli*.[23]

Finally, it is worth noting that although there are a number of examples of hydrolases for covalent bonds within PG, including glycosidic and amide bonds, that have been found and investigated, not every specificity is found in every species, and not all functionalized mechanisms are certain.

1.2.2 Penicillin-binding proteins

As stated above, in order to stimulate and complete the crosslinking of the peptides and polymerise the glycan strand of PG, transpeptidases and glycosyltransferases are required, which are also called penicillin-binding proteins (PBPs). PBPs are named by the original study that they covalently bind to penicillin (Figure 1.5).[24] Although there are a variable number of PBPs in different bacteria, PBPs mainly fall into two categories, as high-molecular-mass (HMM) PBPs and low-molecular-mass (LMM) PBPs. The HMM PBPs are multimodular enzymes and consist of several functionalized modules. Two linked domains as the main module are localized on the outer surface of the cytoplasmic membrane where PG biosynthesis is occurring, while the N-terminal module is a non-cleavable signal peptide anchored to the cytoplasmic membrane, and the C-terminal one is determined as penicillin-binding domain serving to the cross-linking of the PG peptides.[25] Based on their chemical structure and biological activity of their N-terminal domain, HMM PBPs are further divided into two main classes, A and B. Class A PBPs are bifunctional enzymes and possess both transpeptidase (cross-linking the PG peptides) and glycosyltransferase (polymerizing the glycan strand) activities. Class B PBPs are determined as monofunctional enzymes and possess only transpeptidase activity.[26] The LMM PBPs, occasionally referred as Class C PBPs, are primarily soluble enzymes and work as monofunctional DD-peptidases, mainly acting as DD-carboxypeptidases.[25]

Different bacteria types possess a variable number of PBPs, although they may share the typical sequence modules of PBPs (Figure1.5).[27] For example, *Bacillus subtilis*, a well-investigated Gram-positive bacterium, possesses 16 PBPs while there are 12 recognized PBPs in the Gram-negative *Escherichia coli*.[28,29] By comparison, a Gram-positive, round-shaped bacterium, like *Staphylococcus aureus* has merely four or five PBPs and is therefore scrutinized as a minimalist research paradigm model for cell wall synthesis. PBP1, PBP2, PBP3 and PBP4 are present as four native PBPs, whereas an additional PBP2A is only present in methicillin-resistant *Staphylococcus aureus* (MRSA) strains, which is genetically encoded for β-lactam resistance.[30] Distinct from native PBPs, the penicillin-binding domain of Class B PBP2A has greatly reduced affinity for β-lactam antibiotics and this PBP catalyses the cross-linking of the PG in the case of inhibition of other PBPs occurring, which results strain survival at therapeutic levels of methicillin. In *Staphylococcus aureus*, PBP2 belongs to HMM PBPs Class A and is a bifunctional enzyme with both transpeptidase and glycosyltransferase activities. PBP1 and PBP3 are classified as HMM class B and PBP4 belongs to the LMM PBPs, all merely possessing transpeptidase activity.

1.2.3 PG models and cell wall dynamics

While the basic chemical structure of PG is well studied, the three-dimensional structure and dynamics of PG are still elusive. To address these questions, multiple imaging technologies are strategized and involved, including nuclear magnetic resonance (NMR), fluorescence microscopy, atomic force microscopy (AFM) and electron microscopy.[31] All these efforts have contributed to the proposal of many architectural models.

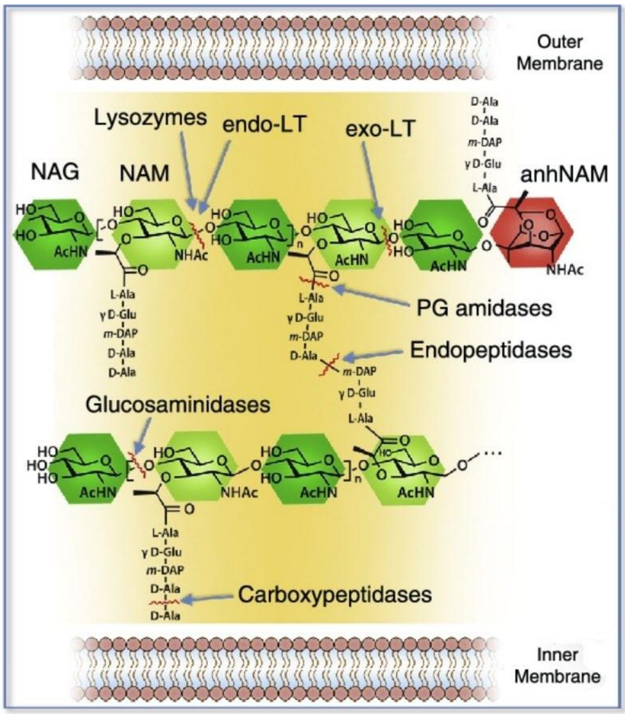

Figure 1.4 Summary scheme of peptidoglycan hydrolases. Blue arrows indicate locations of action of PG hydrolases involved in the cell wall dynamics. Ref 17 with permission from *Elsevier*.[17]

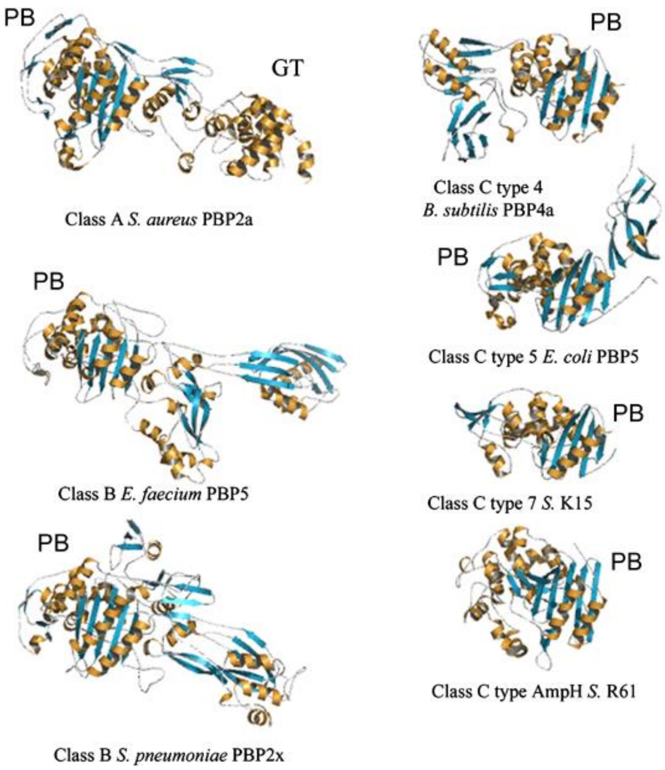

Class A *S. aureus* PBP2a

Class C type 4 *B. subtilis* PBP4a

Class C type 5 *E. coli* PBP5

Class B *E. faecium* PBP5

Class C type 7 *S.* K15

Class C type AmpH *S.* R61

Class B *S. pneumoniae* PBP2x

Figure 1.5 PBPs Structural features. PB: penicillin-binding domain; GT: transglycosylase domain. Ref 27 with permission from *FEMS Microbiol Rev*.[27]

1.2.3.1 Planar vs. scaffold model for orientation of the glycan strands

Historically, there are two opposing models of glycan strand orientation proposed for PG organization, including the classical planar model and the vertical scaffold model (Figure 1.6).[32] The planar model assumes that the glycan chains are orientated parallel to the cytoplasmic membrane. Compared with a single stress bearing layer occurring in Gram-positive bacteria, there would be multiple planar layers needed to construct the thick cell wall of Gram-positive bacteria.[33] Moreover, considering the anisotropy in elasticity that a cylindrical sacculi was observed to have with strong lateral forces and less elasticity in the circumferential direction, the glycan backbones are supposed to be predominantly perpendicular to the cell longitudinal axis.[32]

An alternative vertical or scaffold model for orientation of the glycan strands was proposed later by Dmitriev *et al.*, in which the glycan chains extended perpendicularly to the surface of the sacculus and the cross-linking peptides were parallel to the surface of the membrane.[34] This scaffold model has also extended to Gram-positive *Staphylococcus aureus*, as this bacteria possesses short glycan chains.[35] However, several experimental findings suggested the scaffold model was unsuitable for *Escherichia coli*. For example, an average glycan chain length was experimentally determined as 25-30 disaccharides and this number is much higher than the 2.5 saccharides, the theoretical calculating value from the scaffold model.[32]

1.2.3.2 Peptidoglycan architecture

While the knowledge of PG chemistry and glycan strand length has been achieved in some organisms, PG architecture modelling remains challenging. In previous work, visualization of subcellular architectural features using EM or AFM has provided a direct approach for understanding of PG architecture.[36] PG architecture of representative Gram-positive and negative bacteria with different shapes is summarized in Figure 1.7.

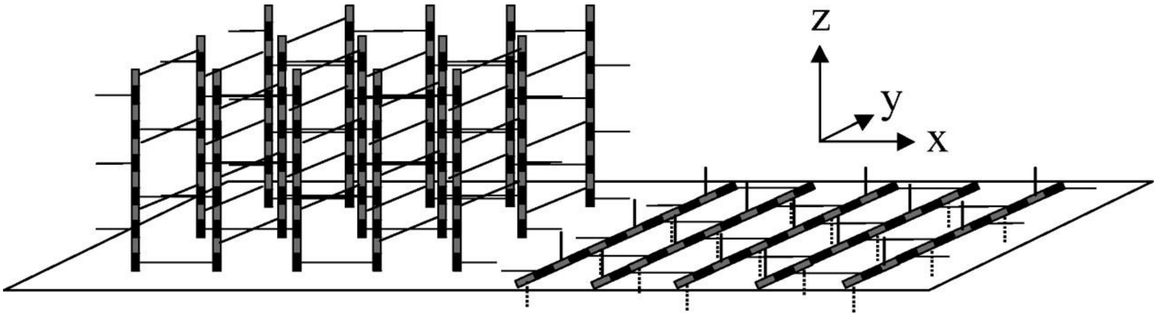

Figure 1.6 Two possible orientation models of the PG glycan strands with respect to the cytoplasmic membrane. In the classical planar model (right side), the glycans are oriented parallel to the cytoplasmic membrane (xy plane). In the scaffold model (left side), the arrangement of glycans is opposed that perpendicular to the cytoplasmic membrane. Bars represent disaccharide units; solid lines represent peptides. Ref 32 with permission from *Journal of Bacteriology*.[32]

Bacillus subtilis was revealed to possess approximately 25% of long glycans that were over 500 disaccharides in length. Strands up to 5 μm corresponding to 5,000 disaccharides in length were also confirmed. AFM imaging showed the inner surface of the cell wall had cable peptidoglycan features running basically across the short axis of the cell while the outside of the cell wall appeared rough, due to hydrolysis (Figure 1.7).[36] The cabling architecture was also maintained at the septum.

In *Staphylococcus aureus*, two PG architectures were observed. The nascent septum is bounded by a thick piecrust feature surrounding a smooth septal plate made up of a ring morphology. Mature PG has a more "knobbly" architecture. After septal scission, the ring architecture changes to knobbles via the activity of hydrolysis.[37]

Compared with *Bacillus subtilis* and *Staphylococcus aureus*, *Escherichia coli* has a thin peptidoglycan layer and the organization is heterogeneous. As shown in Figure 1.7, features appeared in many directions in relation to the axis of the cell and bands of porosity distributed roughly circumferentially around the sacculi were also confirmed. As a result, it was concluded that thickness varies across the sacculus.[36]

1.2.3.3 Models of cell wall dynamics in cocci shaped bacteria

Rod- or ovococci- shaped bacterial cells routinely grow and divide by elongating the lateral cell wall or ellipsoid, and constructing the septum, a new cell wall disc for separating the mother cell into two identical daughter cells. This is needed for synthesis and insertion of new peptidoglycan. As a result, there are two synthesis machines or systems responsible, whether independently and/or cooperatively for elongation and septation. Cocci, especially *Staphylococcus aureus*, have a spherical shape and grow by cell division. They exhibit peripheral cell wall synthesis but without an apparent elongation machinery.

PBP1and PBP2 are recruited to start synthesis of PG and initialize the formation of the septum (Figure 1.8 A).[28] At a subsequent stage of synthesis of the septum, PBP4, is localized at the septum by teichoic acids through a temporally and spatially regulated mechanism, and in responsible for producing highly crosslinked PG, even though it is not essential for bacterial viability.[38] This expandable cross wall has two outer wall layers of high-electron density separated by an inner wall zone of low-electron density.[39] Once septum formation in complete, it is cleaved along the middle zone and allow expansion of the cross-wall, becoming one-half of the new cell wall in daughter cells. During the processes of cell growth and division, multiple autolysins are encoded, although solely Atl has been identified to be involved in the splitting.[28]

In spite of a lack of a "true" nucleus like eukaryotic cells, bacteria still need a number of temporally and spatially regulated molecules and pathways to guarantee that the bacterial chromosome is replicated and segregated in a correct and controllable fashion. It has been confirmed that *Staphylococcus aureus* divide sequentially in orthogonal planes with fidelity in three dimensional space during consecutive division cycles.[40] However, the lack of key morphogenetic components including MinCDE and MreB, raises the question of what the regulation and control mechanisms are, how the division machinery are re-orientated and how information is collected from previous planes of division to ensure the fidelity.[41,42] Given the key role in cell morphology, PG presumably possesses epigenetic architectural features in the form of piecrust, quarter, half and whole ribs to decipher localization of sequential perpendicular planes in *Staphylococcus aureus*.[37] On basis of all these results, a model for cell division in three perpendicular planes in *Staphylococcus aureus* has been proposed (Figure 1.8 C). The rib features demark variety of generation of division planes. To maintain the three-plane sequence, ribs are bounded by T junctions and the quarter rib feature is subsequently recognized to provide enough biological information for determination of the location of the next plane of division.

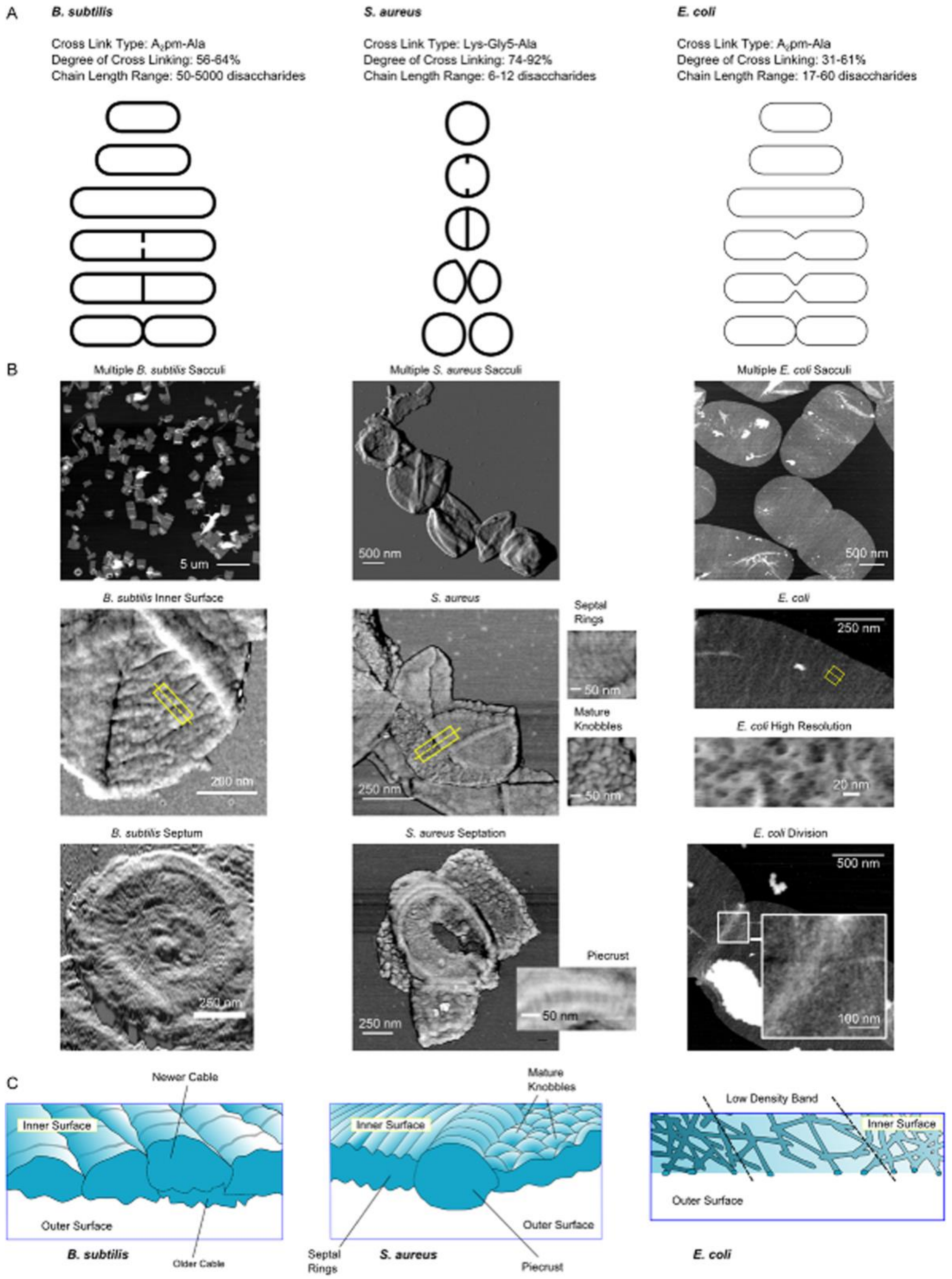

Figure 1.7 Overall architecture of peptidoglycan. (A) Comparison of the cell envelope of *Bacillus subtilis*, *Staphylococcus aureus* and *Escherichia coli*. **(B)** AFM images of purified sacculi with architectural features. **(C)** Schematic of architectural features. Ref 36 with permission from *Molecular Microbiology*.[36]

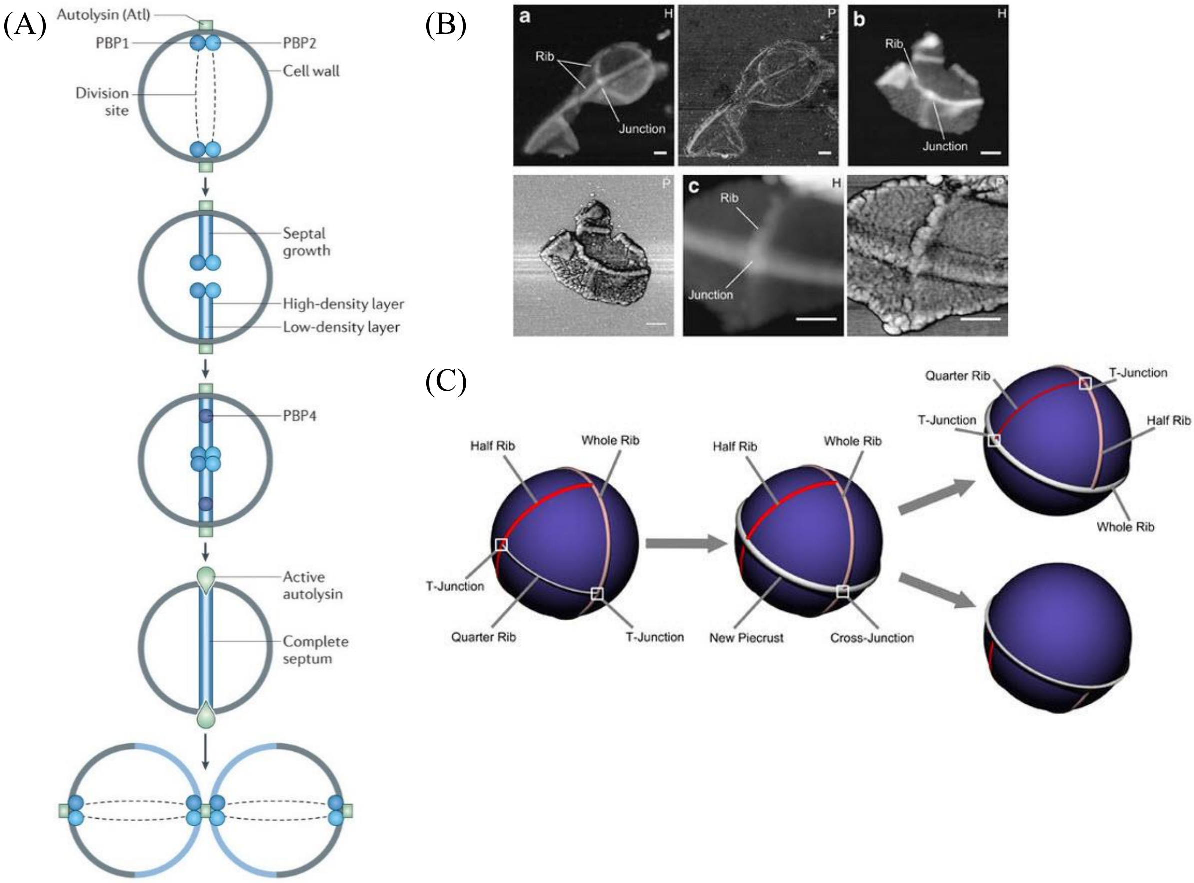

Figure 1.8 Schematic model for the cell growth and division in *Staphylococcus aureus*. (A) Synthesis and split of the septum. PBP1 and PBP2 are recruited, and in order to increase peptidoglycan crosslinking at a later stage, PBP4 is also needed. When synthesis is complete, the septum is cleaved by autolysins. **(B)** AFM images of characteristic features of PG. Height (H) and phase (P) images clearly showed the appearance of rib features. **(C)** Sectoring of PG as a result of three perpendicular division planes. The rib features denote the location of the division plane for two further generations, which bound to form cross and T junctions. The whole one is from the most recent and the half from the second most recent, whilst the quarter as the third most recent determines the next active division. Ref 28 and 37 with permission from *Nat Rev Microbiol* and *Nat Commun*.[28,37]

1.3 Fluorescence-based bioimaging

As mentioned above, bioimaging is a key step towards the ultimate goal of deciphering complex biological systems. Of those bioimaging techniques, fluorescence-based imaging has become an essential and critical method for the study of many of biological processes now, which provides an efficient system for quantitating and characterizing target issues.

1.3.1 Basic Fluorescence mechanism

Fluorescence, a form of photoluminescence, is the physical property of emitting light by absorption of photons coming from other light or electromagnetic radiation. This phenomenon was first observed and recorded by a Spanish physician, Nicolás Monardes, which was known as *lignum nephriticum* (Latin for "kidney wood").[43] Although it was not understood at the time, further application of this phenomenon was investigated. In 1852 George Gabriel Stokes, a physicist and professor of mathematics at University of Cambridge, published the paper entitled 'On the change of refrangibility of light' on the change of wavelength of light, in which the phenomenon was first named as fluorescence.[44] His research clearly showed that the wavelength of the original light was always shorter than the wavelength of the dispersed light and this phenomenon was named after him, which is an important trait of fluorescence. This change of wavelength depends on different energy levels.

The possible mechanism and processes involved in the optical absorption and subsequent emission of fluorescence can be illustrated by a Jablonski diagram (Figure 1.9). In general, there are different quantum states for a certain molecule or atom, which are dedicated to different energy levels. The quantum state when the molecule shows lowest energy is called the ground state, a very stable state for an electron. Under natural environment the majority of molecules normally stay at their lowest energy level in their ground state. Once exposed for an external stimulus, especially light with specific wavelengths, the molecules can absorb energy and, as a consequence, electrons can be elevated to a higher energy level, an excited state which is unstable compared with the ground state.[45] This unstable state only exists for a very short time (typically 1-10 nanoseconds). Having stayed at a high energy level, the molecules or atoms will then release the excess energy by molecular collision and, thus, return to the lowest energy state. This released energy can be performed in form of emitted photons (microcosmic point) and in the form of fluorescence (macroscopical view). However, in this process, not all the energy initially absorbed can be released and only partial energy of excited state is dissipated, due to the occurrence of vibrational energy relaxation. The relaxation creates an excited state (S_1) with lower energy prior to fluorescence emission (Figure 1.9). Due to the loss of energy, photons with lower energy are emitted, and thus the wavelength of emitted fluorescence is increased compared to the absorbed light. This change of wavelength is also called the Stokes shift.

1.3.2 Instrumentation used for fluorescence imaging

1.3.2.1 Common microscopy

The first microscopes made were composed of a single, high-quality lens of very short focal length, which had the ability to magnify up to 500 times. Although these microscopes had been regarded as relatively simple devices, the research was of remarkably high quality and revealed an entire world of microscopic life to scientists. Generally, the principal use of fluorescence microscopy is to observe biological samples that have been treated with fluorescent probes or reagents. In contrast to other imaging techniques, such as electron microscopy, fluorescence microscopy presents the decided superiority in its compatibility with living cells, which allows dynamic and minimally invasive imaging experiments.

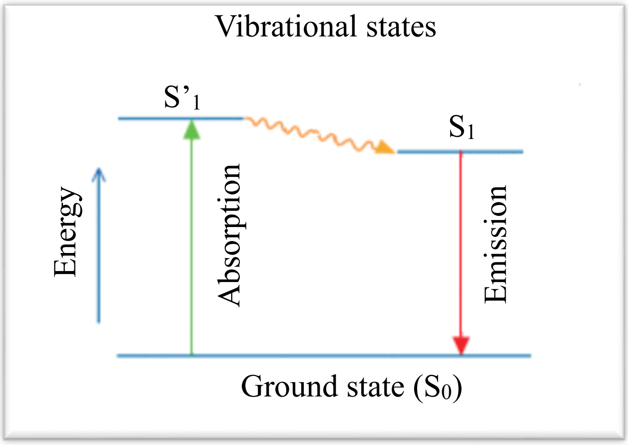

Figure 1.9 A simplified Jablonski diagram showing the formation of fluorescence. Energy transitions between different states (S_0, S'_1 and S_1) occur from the exposure of a molecule to a particular wavelength of light. The state S_1 is of lower energy than S'_1 and return to S_0 with emission of fluorescence.

Despite their success, conventional microscopy methods demonstrate several obvious limitations for their application in biological research. For example, because of the diffraction limit of light, light microscopy cannot resolve distances that are below l/2 NA based on the Abbe equation in which l is the wavelength of light in nanometres and NA means the numerical aperture. This minimum distance is typically about 200 nm. Unfortunately, as shown in Figure 1.10, most intracellular components are smaller than 200 nm and thus cannot be resolved using these techniques.[46] This means conventional microscopy has limitations and thus new innovations, termed super-resolution imaging, are used to break the diffraction resolution limit.

1.3.2.2 Super-resolution microscopy development

The recent emergence of new fluorescence imaging techniques, super-resolution microscopy, has attracted much interest because of theoretically enabling no limit to their spatial resolution. Super-resolution microscopy can be considered as a novel microscopy on the basis of improvement of common light microscopy, including near-field and far-field super-resolution imaging.

1.3.2.2.1 Near-field super-resolution imaging

Near-field scanning optical microscopy (NSOM) is a powerful tool for offering ultra-high spatial resolution beyond the conventional limit imposed by diffraction via the employment of a sub-wavelength light source that is localized in close proximity to the sample (Figure 1.11).[45]

In 1928, the near-field concept was originally described by E.H. Synge [47] and then similar theory was developed by O'Keefe in 1956. [48] This technique was first developed at microwave frequencies (wavelength, A= 3 cm), breaking Abbe's diffraction limit, by Ash and Nicholls in 1972.[49] The extension of the technique to optical imaging appeared, in 1986 with several reports of resolutions below 50 nm in size was achieved.[50,51]

Although there have been many applications of NSOM in the nano-scale biomolecule or organization, e.g., membrane proteins, there are limitations of NSOM.[52,53] The aperture probe is difficult to construct and it needs extremely long scan times for high resolution images or large specimen areas. Moreover, evanescent fields used by NSOM exist only near the surfaces of the medium, therefore the detector must be designed and set very close to the sample in the near field zone. As a result, only surface features can be imaged and studied. NSOM remains primarily a technique for surface study and tends to have difficulty in intracellular imaging.[53]

1.3.2.2.2 Far-field super-resolution imaging.

Compared with NSOM, super-oscillatory lenses and hyperlenses are used in far-field imaging, which are set with a certain distance from the sample. Novel far-field fluorescence imaging techniques allow this limit to be bypassed and offer unlimited spatial resolution in theory, which include structured illumination microscopy (SIM), stimulated emission depletion (STED) microscopy, photo-activated localization microscopy (PALM) and stochastic optical reconstruction microscopy (STORM).[54]

1.3.2.2.2.1 Structured illumination microscopy (SIM)

Structured illumination microscopy (SIM), is a generic term for a series of similar microscopy techniques in concept based on the use of patterned illumination, which illuminates a sample with a patterned light and release fluorescence (Figure 1.12 A).[55,56] Typically, when a sinusoidal interference pattern resulting from light passing through an optical grating is applied to excite the fluorescent sample, overlapping moiré fringes are obtained. As a result, normally unobservable high frequency information is captured at lower spatial frequencies. By measuring a series of these moiré patterns in different spacing and rotation angles for the same sample, an image with resolution enhancement by a factor of two is achieved after computational post-processing and reconstruction. To further improve the resolution, saturated structured-illumination microscopy (SSIM) is developed on the basis of nonlinear structured illumination. When using a high power excitation, the fluorescence emission would be saturated in a nonlinear response and therefore produce a series of higher-order harmonics. As a result, the sub-diffraction-limit spatial features are "carried" into the detection range of the microscopy, provide an image with the enhanced resolution. Gustafsson has demonstrated fluorescent beads imaging with a lateral resolution of 50 nm by SSIM.[57]

Compared with other imaging technologies, SIM has features that make it widely applicative for imaging range of biological samples.[58-60] Apart from fast imaging, there are also other advantages of SIM, including a relatively low complex imaging solution and no need of point-scanning to achieve the required intensity. Considering the key role of probes in super-resolution techniques, SIM requires no probes with special properties or designs, and is the closest to traditional fluorescence microscopy, and can easily be expanded to multicolour super-resolution imaging. Another attractive feature of SIM is that 3D-SIM imaging has been developed with an approximately eightfold enhanced resolution in comparison to conventional microscopy.[61] These characteristics make SIM the most broadly accepted super-resolution microscopy technique among biologists.

1.3.2.2.2.2 Stimulated emission depletion (STED) microscopy

STED microscopy is essentially based on switching off the fluorescence of excited molecules in the outer regions of the diffraction limited excitation spot by stimulated emission using two synchronized ultrafast laser sources (Figure 1.13).[54] One is the conventional laser beam to excite fluorescent molecules and the other is a red-shifted donut-shaped depletion laser beam to quench the peripheral fluorescence within picoseconds through stimulated emission. Only fluorescence emission from the sub-diffraction-limited centre is thus detected to form the high resolution images. As the fluorescence is ideally unaffected at all at the doughnut hole, the fluorescent spot can be effectively narrowed down by increasing the intensity of the doughnut-shaped STED, which even theoretically reaches to the size of a molecule. The narrow point spread function (PSF) of the microscope improves the resolution and permits the achievement of super resolution e.g. 20 nanometer (or better) lateral resolution and 40 to 65 nanometer axial resolution.[62]

In contrast with other kinds of super-resolution microscopy, STED microscopy is a purely optical method and there is no need for any mathematical manipulation or image processing. Moreover, in theory STED resolution is unlimited by indefinitely increasing the depletion laser power.[63] Up to now, resolutions down to nano scale, such as 15-20 nm, have been achieved and significant applications in various biological samples have been reported.[64,65]

1.3.2.2.2.3 Photo-activated localization microscopy (PALM)

As a far-field fluorescence microscopy technique, photo-activated localization microscopy (PALM) demonstrates extreme improvement on the spatial resolution of the optical microscope by at least an order of magnitude (15 to 25 nm of resolution), and this offers the ability to investigate biophysical activity and physiological mechanism at close to the molecular scale.

The key idea of PALM imaging is to precisely localize each individual molecule in a sample. In PALM, abundant fluorescent probe molecules are fixed spatially within the diffraction-limited spot and only a sparse subset of molecules can be switched on through a light-induced environment at a time (Figure 1.14). A large fraction of the whole probe ensemble, in principle, can be localized over time and the sequential acquisition of images of the labelled structure is achieved by repeated bleaching or deactivating the active molecules in concert with activating other inactive probe molecules. The accumulation of localized particles from the sequential images is then plotted. As a result, a PALM image with super resolution is created and reconstructed, exploring the sequential steps, the final resolution of which relies only on the localization precision for each fluorescent molecule. In turn, the observable signal-to-noise ratio of molecules determines the localization precision. Effectively, several hundred to thousands of molecules can be detected with enough photons to be precisely localized and sufficient images can be collected to accurately generate a super-resolution imaging process that highly resolves the cell or intracellular ultra-structure. In general, PALM presents a solution for breaking the limit by the integration of the stochastic switching-on and -off of fluorescent probes with the sequential acquisition of images.

Compared to other techniques with high spatial resolution, including electron microscopy (EM) and NSOM, PALM provides new capabilities to investigate diverse types of proteins associated with various structures and environments inside cells and tissues, which are expressed with a fluorescent marker.[66] This fluorescent marker is a photoactivatable fluorescent molecule that generates a high level of contrast by switching to a new fluorescent state as the result of activation and maximally obviates invasive sample handling.[67,68] Moreover, PALM has more versatile applications, including remodeling of cell surface protein distributions with nanometer precision across the whole plasma membrane instead of just in a very small area. Furthermore, pair correlation photoactivated localization microscopy (PC-PALM) utilizes a pair-correlation algorithm to decipher quantitative features of protein organization within subcellular compartments, which enables quantification of changes in protein density at the normal physiological state of the cell.[69]

1.3.2.2.2.4 Stochastic optical reconstruction microscopy (STORM)

Stochastic optical reconstruction microscopy (STORM), is conceptually analogous to single-molecule localization microscopy depending on single-molecule detection. The fundamental principle behind STORM and its related methodology is high-accuracy localization of individual fluorescent molecules that are activated and deactivated using light. The fluorescence emission of such molecules needs to be temporally controlled, which means only a single one, or a sparse subset, of the molecule is activated as switchon state, at any point in time, in a given region of the sample. The individual molecules are thus imaged without overlapping and localized with high precision. Then a new subset is activated to the switched-on state and can also be localized while former fluorescent molecules are deactivated to the switched-off or dark state. Additionally, before activated molecules enter a dark state or become deactivated, it must emit sufficient photons for precise localization, and also must be controlled at a distance exceeding the Abbe diffraction limit for the parallel recording of many individual emitters. The positions of a stochastically different subset of molecules are measured after repeating this process of activation, localization, and deactivation. Once sufficient information has been recorded, a super resolution image can thus be reconstructed (Figure 1.14).

As the only limit is the number of photons detected, using efficient reversibly photo-switchable probes makes localization with nanometre accuracy (as high as 1.5 nm) achievable in lateral dimensions under ambient conditions.[70] Moreover, the axial position of the particle can also be demonstrated with detail based on the centroid and shape of the image. Furthermore, by introducing defocusing or astigmatism into the image, the z dimension can reach nanoscale localization accuracy and there is no need for substantially compromising the lateral positioning capability.[71]

Although STORM is quite similar with PALM, and even considered to be the same technique by some researchers because of the use of the same basic principles used to form super-resolution images, there is an obvious difference: the nature of fluorescent molecules used for imaging. PALM uses genetically encoded fluorescent proteins such as Green Fluorescent Protein whilst STORM uses proteins and photoswitchable fluorescent dyes including Alexa Fluor and cyanine dye.[72-74]

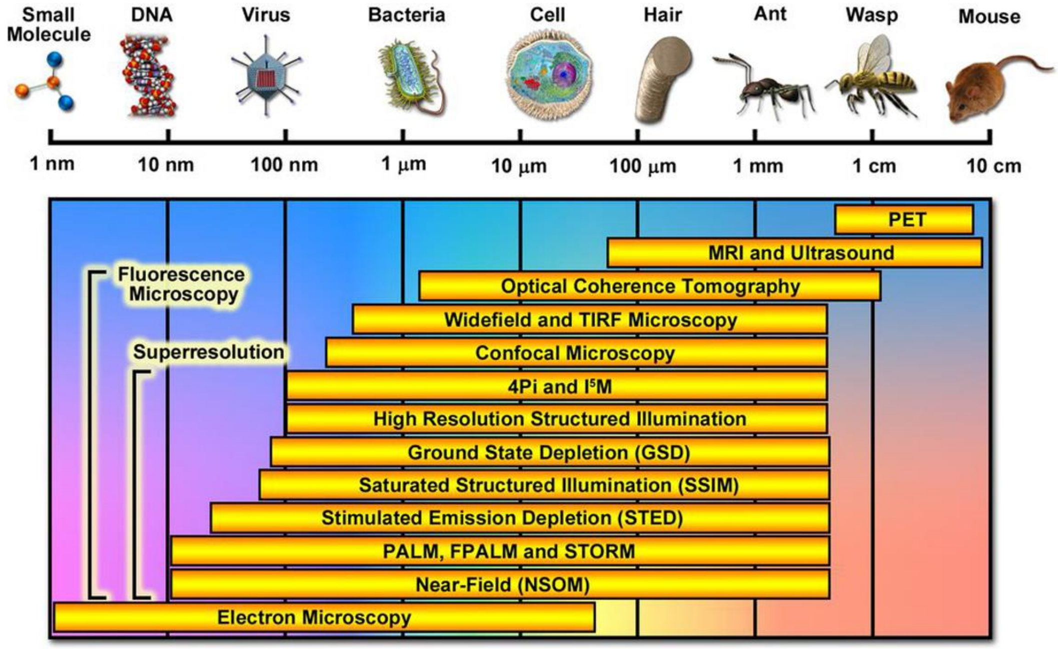

Figure 1.10 Scales of biological issues of interests and comparison of the spatial resolutions of variety of imaging techniques. Ref 46 with permission from *J Optics*.[46]

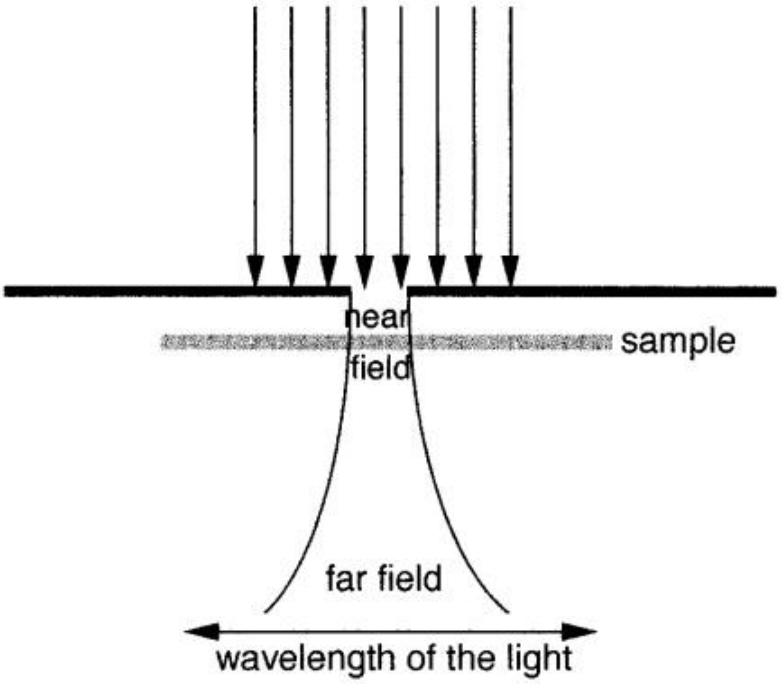

Figure 1.11 Basic theory of near-field optics. A sub-wavelength hole or an optical fiber is positioned near the sample. When a light passes through it, an evanescent field is created as local excitation source to interact with the sample. As a result, high frequency spatial information is detected. Ref 45 with permission from Wiley & Sons.[45]

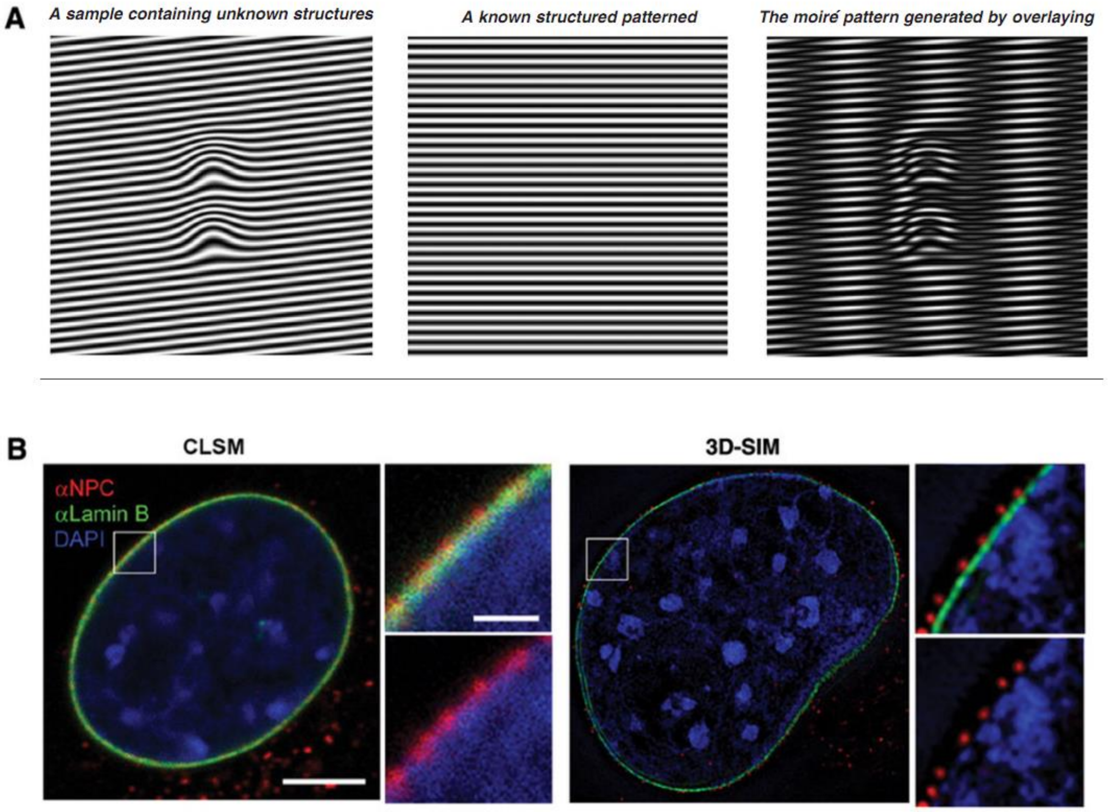

Figure 1.12 SIM super resolution imaging. (A) Schematic of basic principles. When two features with different angles or mesh sizes are overlaid, the moiré pattern will be created. As a result, higher resolution images of the sample (the unknown feature) are provided after deconvolution on the basis of the known pattern. **(B)** Comparison of a confocal laser scanning microscopy image (CLSM, left) and a 3D-SIM image (right) of a similarly stained nucleus. Ref. 55 with permission from *Applied Spectroscopy*.[55]

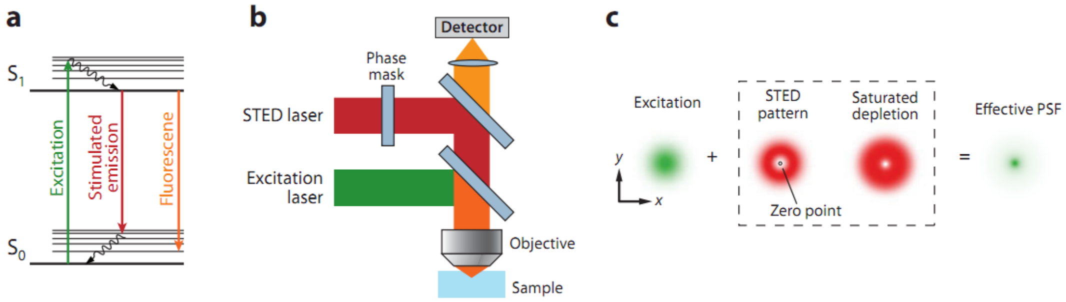

Figure 1.13 The principle of stimulated emission depletion (STED) microscopy. (a) The process of stimulated emission; **(b)** scheme of a STED microscope; **(c)** decrease of the effective PSF in the *xy* mode using a donut-shaped STED laser. Ref. 54 with permission from *Annual Reviews*.[54]

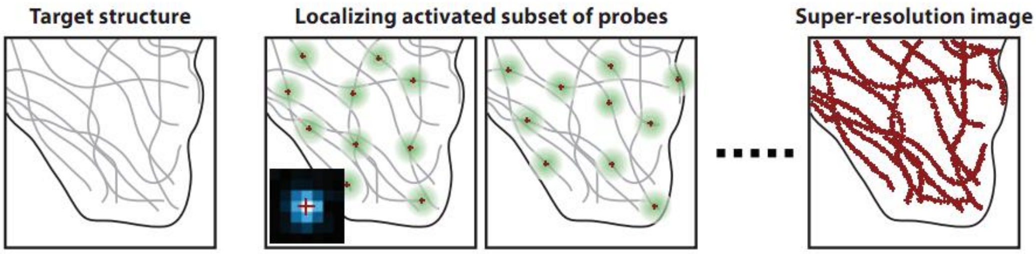

Figure 1.14 Basic imaging principle of PALM/STORM. Fluorescent probes are stimulated and captured individually, allowing subsets of probes to be imaged without spatial overlap and to be localized to high precision. After repeating the process of stimulation and capture many times, each probe in its precise location is determined and a super-resolution image is reconstructed. The insert indicates an experimental image of a single fluorescent probe (blue). Ref. 54 with permission from *Annual Reviews*.[54]

1.3.3 Probes used for fluorescence imaging

The ability of super-resolution microscopy to map individual molecules and the suitability for studying cells strongly depends on the characteristics of fluorescent probes used, labelling techniques, and data interpretation strategies. Generally, fluorophores used for super-resolution imaging can be broadly ranged into two types, either genetically-encoded reporters including fluorescent proteins or synthetic fluorescent compounds, such as organic dyes and quantum dots.

1.3.3.1 Genetically-encoded reporters

As their name suggests, genetically-encoded reporters have the ability to transfer the analysis of a specific biological event or process into an observable fluorescent signal. A genetically encoded process means that the introduction of fluorescent reporters is engineered into living systems at the DNA level which is followed by de novo synthesis and subcellular targeting by the endogenous cellular machinery. As a result, genetically encoded reporters are proving to be an extremely powerful tool for accurately and rapidly dissecting protein interactions and signalling pathways. Routinely used reporters to study biological processes are based on fluorescent proteins (FPs).[75]

Green fluorescent protein (GFP) was the first member of families of fluorescent protein, which was first isolated from *Aequorea victoria* by Osamu Shimomura about forty years ago.[76] Native GFP produces its fluorescence by backbone cyclization, dehydration of tyrosine, and the activation from oxygen, which is called maturation and mainly refers to tripeptides of serine, tyrosine, and glycine (Figure 1.15).[77] In principle, the fluorescence of proteins comes from an imidazolidone ring with conjugated double bonds and a planar structure which is formed via posttranslational modification. Mutations in the ring structure may result in shift of the fluorescence excitation or emission. GFP derivatives are then developed with enhanced properties, including reduced temperature sensitivity and increased expression, for extensive application *in* *vivo* imaging experiments.[78] Modification or mutation of the GFP encoding gene, can be used to produce fluorescent protein derivatives (e.g. blue fluorescent protein, yellow fluorescent protein and cyan fluorescent protein) with varied absorption or emission properties which makes it possible for researchers to employ a variety of fluorescent protein probes within the same cell at the same time for multicolour imaging.

Up to now, over twenty different varieties of FPs have so far been created and studied.[79] Among them, FPs that are used for super-resolution imaging can fall into three broad classes based on their response of light activating: irreversible photoactivatable FPs (PA-FPs), reversible PA-FPs (also termed reversibly switchable FPs) and photoshiftable FPs (PS-FPs) (Figure 1.16).

Irreversible PA-FPs only emit fluorescence with light irradiation at a specific wavelength and intensity. This photoactivation process involves a permanent photochemical modification of the FP and thus it is irreversible. As a result, there is an obvious and permanent change of state of FPs, from a non-fluorescent (dark) state to a fluorescent (bright) state.[80] Reversibly photoactivatable FPs (also termed reversibly switchable FPs) can be activated repeatedly by light irradiation and toggled between a non-fluorescent (dark) state and a fluorescent (bright) state. Most often, the mechanism of this photoswitchable process depends on the state change of isomerization and protonation of molecules. Dronpa, originally discovered in a cDNA screen of the stony coral *Echinophyllia sp.*, is a well-studied reversibly photoactivatable FP and has wide applications in cell research such as protein tracking and multicolour super-resolution imaging, due to its higher brightness, greater stability and monomeric nature (Figure 1.16 c). Following light irradiation at a specific wavelength, photoshiftable FPs (PS-FPs), will change their fluorescence excitation and emission spectra. This process is always accompanied by conformational rearrangements.

There is another class of FPs that features both reversible and irreversible photoactivation. FPs routinely permit essentially noninvasive super resolution imaging by utilizing two different photoactivation modes, either irreversible photoconversion from a non-fluorescent (dark) state to a fluorescent (bright) state, or from fluorescent states to other fluorescent states with different emission wavelengths; or repeated reversible photoactivation between a fluorescent ‘on’ state and a non fluorescent ‘off’ state. The advent of new FPs, such as irisfP, provides more opportunities for cell imaging. IrisFP1, a kind of FP, can be irreversibly photoconverted from a green- to a red-emitting form and reversibly photoswitched between an on and an off state in both forms. Reversible and irreversible photoactivation in combination enables entirely new types of strategies, such as pulse-chase imaging integrated with super resolution localization microscopy (PALM).[81]

1.3.3.2 Synthetic fluorescent compounds

Synthetic fluorescent compounds that have been used in super-resolution imaging can be divided into two main classes, including variety of fluorescent nanoparticles with different size and shape (quantum dots, noble-metal nanoclusters etc.), and organic compounds (Alexa Fluor, Cy 3, Cy 5 and so on).

1.3.3.2.1 Organic compounds

Organic fluorescent dyes have been one sort of the most commonly used optical labels for imaging, including cyanines, fluoresceins, rhodamines, BODIPYs, porphyrines and their derivatives (Figure 1.17). For instance, carbocyanine fluorophores such as Alexa 647 and Cy 5 have been used in STORM for super-resolution imaging based on single-molecule localization.[72] A wide range of organic fluorophores such as Chromeo 488, Atto 565, and rhodamine derivatives, have performed well in STED and improve multicolour capabilities of this technique.[82] Apart from utilizing long-established, commercially available fluorophores, there has been growing interest in exploiting new fluorophores or modifying fluorophore variants for one or more super-resolution technologies, such as DCDHF(2-dicyanomethylene-3-cyano-2,5-dihydrofuran)-based fluorophores and caged rhodamine or fluorescein derivatives.[83,84]

In contrast to FPs, organic dyes possess several superior properties, such as smaller size, a wider available spectral range, much higher emissivity, more resistance to bleaching, and more sensitivity to certain stimuli and the surrounding environment. For example, in STED, the organic dye Abberior STAR 635P can provide an approximately two times better resolution than the best resolution provided by FPs.[85] However, organic fluorophores are not without their drawbacks, and in many cases labelling processes involve many coupling chemical reactions and modification. Meanwhile, as some organic dyes contain aromatic structures, they are sometimes poorly soluble in an aqueous environment, resulting in poorly bioavailability for *in vivo* imaging.

1.3.3.2.2 Quantum dots

In recent years, quantum dots (QDs), robust and bright light emitters, have been used as a new class of probes for *in vitro* and *in vivo* imaging at the cellular level.[86] QDs or nanocrystals, are nearly spherical semiconductor particles in the 2-10 nm size range and include roughly 200-10,000 atoms, which are typically composed of periodic groups of II-VI (e.g., CdSe) or III-V (e.g., InP and InAs) materials. Their unique size-dependent properties and dimensional similarities with biological molecules (e.g. nucleic acids and proteins) are of interest to biologists. Meanwhile, QDs are especially attractive fluorescent labels for super resolution imaging due to their high quantum yield, high molar extinction coefficients, broad excitation spectra, and narrow symmetric and tuneable emission spectra in the visible and infrared regions (Figure 1.18).[87-89] For example, Lidke *et al*. analysed the intermittent fluorescence or ‘blinking’ of quantum dots by an Independent Component Analysis which preceded STORM/PALM type localization-based microscopy.[87] The simulation based on 655 nm emission QDs deposited on coverslips helped a high resolution image consisting of individually localized points to be reconstructed. There have been efforts to apply quantum dots in STORM and dSTORM although they have not found as many as those exploited fluorescent proteins or organic fluorophores.[88] Fluorescence blueing of quantum dots facilitated separation of blinking markers residing closer than the diffraction barrier, which enabled nanoscopy with resolution down to about the size of a single dot. Also, Irvine and co-workers recently reported the direct light-driven modulation of QD fluorescence, which relied only on internal electronic transitions within Mn-doped ZnSe quantum dots (Mn-QDs).[89] The fluorescence of this new QD can be reversibly depleted with efficiencies of over 90% by using continuous-wave optical intensities of approximately 1.9 MW cm^{-2}. Consequently, this type of QD can be used in super-resolution imaging and leads to an increase in the resolution by a factor of 4.4 over that of confocal microscopy.

1.3.3.2.3 Noble-metal nanoclusters

Noble-metal nanoclusters such as Ag and Au nanoclusters are an emerging class of fluorescent probes as promising substitutes for conventional fluorophores. Typically nanoclusters contain less than 150 metal atoms and thus their size is on the molecular scale, less than 2 nm.[90] Owing to their well-defined geometries and strong quantum confinement of free electrons, nanoclusters also exhibit molecule-like properties, including strong luminescence, size-dependent fluorescence emission, discrete size-dependent electronic states and quantized charging, which have been well characterized up to now. Meanwhile, the ultrasmall size of nanoclusters makes them highly tenable in protecting ligands that result in distinctive differences in physicochemical properties among nanoclusters. With proper protection groups, quantum yields of nanoclusters can go beyond 10%, and they also have very high single-molecule emission rates, and essentially no blinking on experimentally relevant time scales (0.1 to >1,000 ms) which are comparable to or sometimes even higher than organic dyes.[91] This new class of fluorophore may well be developed as promising substitutes for conventional fluorophores in live-cell super resolution imaging in the near future due to their small size, unique environmental sensitivities, excellent photostability, and good biocompatibility, although currently rarely reported.

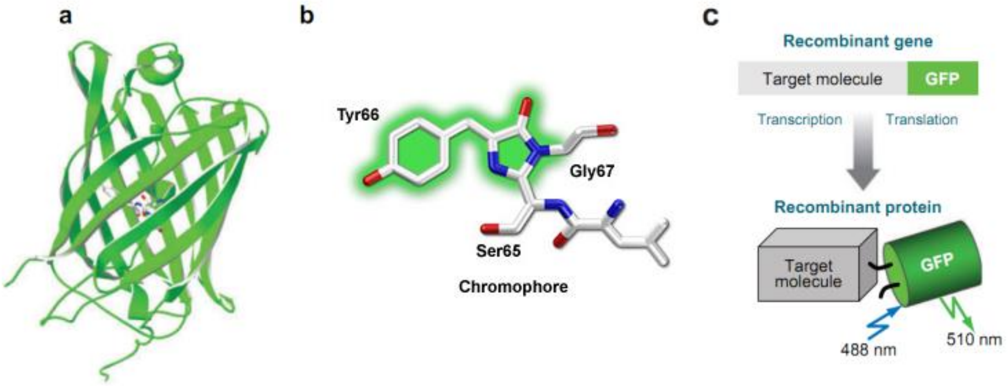

Figure 1.15 The principle of GFP. **(a)** The basic structure of GFP. **(b)** The formation of chromophore by GFP. **(c)** GFP labelling. The gene encoding the protein of interest is fused and the recombinant molecule is thus observable after excitation. Ref. 75 with permission from *Annual Reviews*.[75]

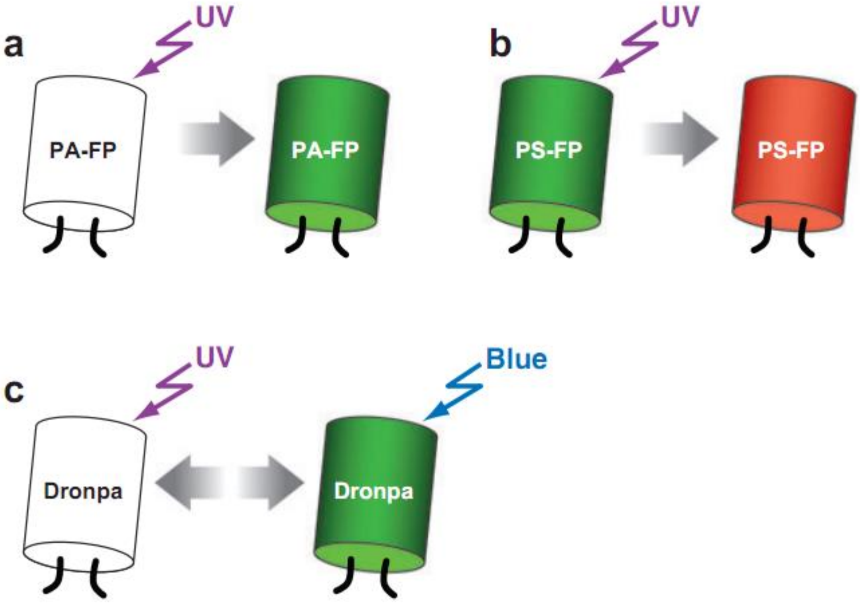

Figure 1.16 Different varieties of FPs. (a) Upon UV excitation, an irreversible PA-FP displays a markedly enhanced fluorescence. (b) UV illumination changes the fluorescence colour of a PS-FP from green to red. (c) UV or blue light illumination reversibly enhances or quenches the fluorescence of Dronpa, respectively. Ref. 75 with permission from *Annual Reviews*.[75]

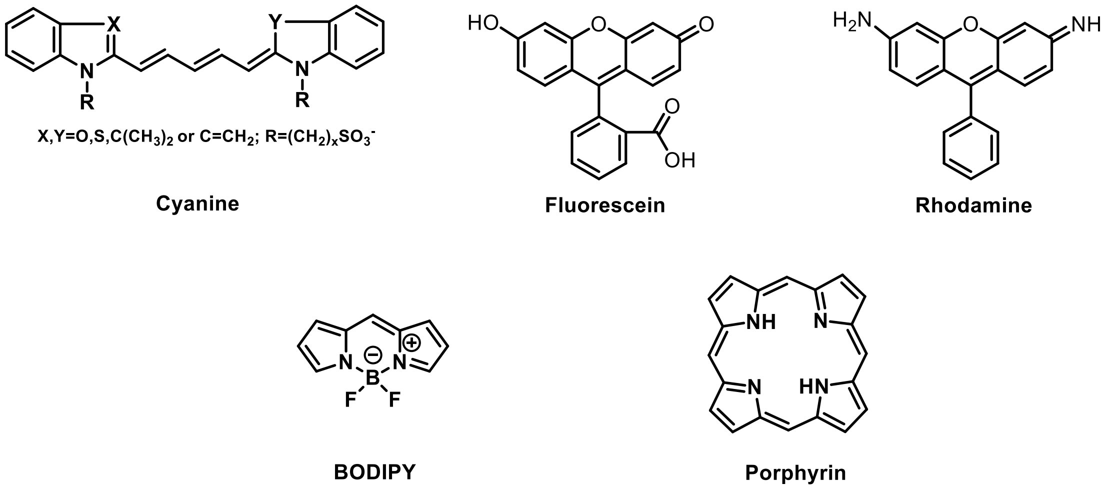

Figure 1.17 Core chemical structures of organic dyes.

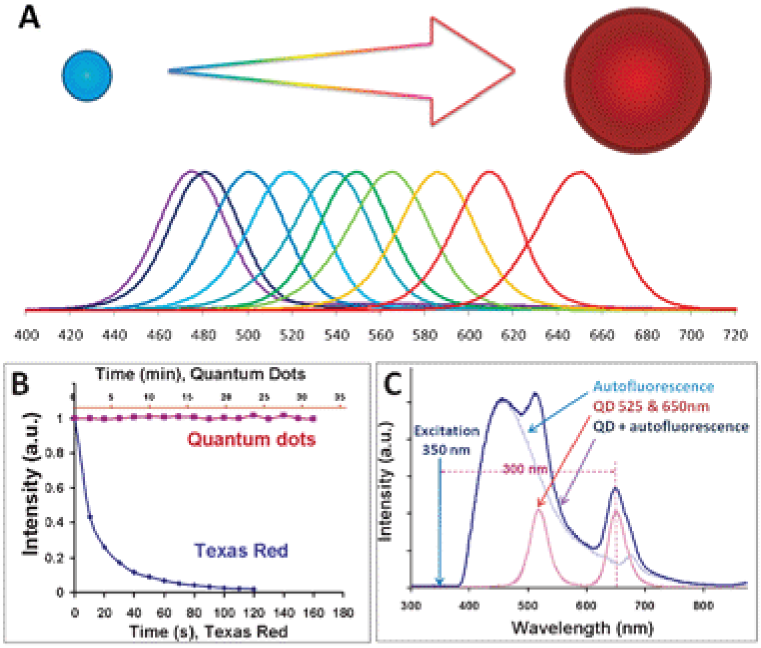

Figure 1.18 Quantum dots properties. (A) Narrow size-tunable light emission related to different sizes of QDs; (B) Outstanding photostability of QDs; (C) Separation of the QD signal over the fluorescent background. Ref. 86 with permission of *Chem Soc Rev*.[86]

1.4 Project aims

PG, the main structural element of the cell wall, plays key role in bacterial growth and provides a high-value target for antibiotics. Previous studies have identified that glycosylation, a key step in biosynthesis of PG, plays a role in many key biological processes including pathogen recognition, immune responses, cell-cell adhesion, the development of autoimmune diseases and other various life activities.[92] Despite the incredible importance of PG, the three-dimensional model of PG and its dynamics during cell growth and division remain largely elusive. One of most import reasons is the lack of a global probes for PG labelling in live cells, a must for super resolution imaging. The aims of this project therefore are to design and synthesize multifunctional probes suitable for super resolution imaging for PG study at nanoscale.

Initially, the first task of the probe is to attach PG with fluorophores for super resolution fluorescence visualization. As mentioned above, there are aldehyde groups formed in the reducing end of polysaccharide in PG, which are suitable for PG labelling. Therefore, the idea presented herein is to take advantage of the oxime ligation of aminooxy functionality with the aldehyde moiety (Figure 1.19). Due to its low cost of synthesis of library-building blocks, the oxime ligation may facilitate key advances in development of *in situ* labelling with high biocompatibility for imaging.

Apart from super resolution fluorescence imaging of the cell wall using above synthetic probes, other complementary technologies were to be applied to provide more biological information for the better understanding of PG dynamics, including electron microscopy (EM) and atomic force microscopy (AFM). A series of new suitable probes were to be designed, synthesized and used to label cells, which allow selective tracking of cellular processes, and also are capable of assembling specific tags such as gold nanoparticles and fullerenes that produce high signal-to-background contrast for EM or AFM observation and later cell morphology analysis.

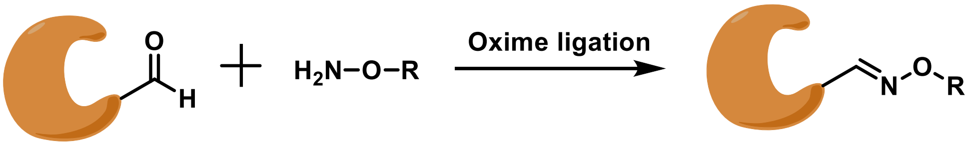

Figure 1.19 Biological targets labelling on basis of oxime ligation. Hydroxylamine functionalized probes are specially recognized the aldehyde moiety of targets via oxime ligation to generate desired labels. R: dyes, nanoparticles or other probes.

Chapter 2 Materials, Methods and Synthesis

2.1 Chemicals

All common chemicals used in this study were purchased from Fisher Scientific, Sigma-Aldrich or TCI unless otherwise stated. Probes for cell labelling were prepared and characterised using mass spectrometry (MS), nuclear magnetic resonance (NMR) spectroscopy, and infrared (IR) spectroscopy.

2.2 Growth media

All media and supplies were purchased from Fisher Scientific. Unless otherwise stated, all media was prepared using distilled water and autoclaved for 20 min at 121 ºC, 15 pounds per square inch, in detergent washed and rinsed glassware. Gel was made by addition of 1.0 % (w/v) agar in liquid media recipes before autoclaving it with the agar. Fresh media was prepared every 2 weeks.

2.2.1 Brain Heart Infusion (BHI)

Brain Heart Infusion (Oxoid/Fluka)	37.00 g/L

For BHI Agar, 1% (w/v) of bacteriological agar (VWR) was added.

2.2.2 Tryptone soy broth (TSB)

Tryptone soy broth (Oxoid)	30.00 g/L

For TSB Agar, 1% (w/v) of bacteriological agar (VWR) was added.

2.2.3 Nutrient broth (NB)

Nutrient broth (Oxoid)	13.00 g/L

For NB Agar, 1% (w/v) of bacteriological agar (VWR) was added.

2.3 Antibiotics

For stock solutions, antibiotics were dissolved at the appropriate concentrations, filter-sterilized by 0.2 µm pore size and stored at -20 ºC. For use in liquid media, antibiotic stock solutions were defrosted and added just before use. For use in agar plates, melted media was cooled to approximately 50 °C in a water bath followed by the addition of antibiotic stock solutions. Concentrations of stock and working solutions were shown in Table 2.1, unless otherwise stated.

2.4 Labelling buffers and stock solution

Unless otherwise stated buffers were prepared using dH_2O, sterilised by autoclaving and storing at room temperature. Stock solutions used for labelling work were as shown in Table 2.2.

Phosphate buffered saline (PBS)

Sodium chloride ($NaCl$)	8.00 g/L
Disodium hydrogen phosphate (Na_2HPO_4)	1.42 g/L
Potassium chloride (KCl)	0.20 g/L
Potassium dihydrogen phosphate (KH_2PO_4)	0.24 g/L

The pH was adjusted to 7.4, using NaOH.

0.1 M sodium phosphate buffer (pH 7.0)

Na_2HPO_4 (1M)	57.70 mL
NaH_2PO_4 (1M)	42.30 mL

The final volume was adjusted to 1 L.

50 mM sodium acetate solution (pH 4.5)

Sodium acetate (NaAc)	4.10 g/L

The pH was adjusted to 4.5, using glacial acetic acid.

16% (w/v) paraformaldehyde

100 mM sodium phosphate buffer (pH 7.0)	50 mL
Paraformaldehyde	8.00 g

The solution was heated to 60 ºC in a water bath and mixed vigorously. NaOH (≥ 5 M) solution was added drop wise, with heating and vigorous mixing, until the solution cleared. The solution was stored at 4 °C for no longer than 8 weeks.

Formaldehyde fixative

Paraformaldehyde, 16% (w/v)	0.5 mL
100 mM sodium phosphate buffer (pH 7)	2 mL

0.1 M sodium carbonate (pH 8.3) buffer

Sodium carbonate (Na_2CO_3)	10.60 g/L

The pH was adjusted to 8.3, using HCl (1 M).

4 or 5% (w/v) Sodium dodecyl sulfate (SDS)

SDS	4 or 5 g/L

Click-iT® reaction buffer mixture

All components were purchased from Molecular Probes or self-made.

Click-iT® cell reaction buffer	220 µL
Click-iT® cell buffer additive	25 µL
100 mM copper (II) sulphate ($CuSO_4$)	15 µL

1 M Potassium hydroxide (KOH) solution

KOH	56.11 g/L

50 mM Tris buffer with 10 mM NaCl (pH 8.0)

Tris base	6.06 g/L

NaCl	0.58 g/L

The pH was adjusted to 8.0.

Mercaptoethylamine (MEA) solution

MEA	77.15 g/L

1M MEA stock was prepared by dissolving MEA in 50 mM Tris buffer with 10 mM NaCl. 10 times dilution of the stock using the above Tris buffer gave 100 mM MEA as the working solution. Storing at -20°C guaranteed the stock for up to 1 month and defrosted working solution was used on ice for up to 6 hours.

GLOX buffer (Oxygen Scavenger)

Glucose oxidase stock	5 mg/mL
Catalase stock	4 mg/mL

100 μL of glucose oxidase stock (0.5 mg/mL) and 10 μL catalase stock (40 μg/mL) were added to 100 mg of glucose in 890 μL of 50 mM Tris buffer with 10 mM NaCl (pH 8.0), which should be freshly prepared and used in less than 2 hours before needed.

GLOX MEA buffer

MEA was added to the above GLOX, giving a final concentration of 10 or 100 mM which was freshly prepared and used within 2 hours.

2.5 Bacterial strains and growth conditions used

2.5.1 *Staphylococcus aureus* strains

The strains were taken from glycerol stocks in Microbank storage beads (Pro-lab diagnostics) and streaked for single colonies onto BHI or TSB agar plates with or without antibiotics (Table 2.3). Plates were incubated at 37 °C overnight and subsequently stored at 4 °C for up to two weeks. Long term storage of strains was achieved by adding 1mL of liquid overnight culture to a Microbank tube containing glycerol beads, shaking to mix and removing most of the liquid before storing at -80 °C. Liquid cultures were generally inoculated with a single colony into a culture and grown overnight at 37 °C with shaking at 250 rpm unless otherwise stated.

2.5.2 *Bacillus subtilis* strains

Bacillus subtilis WT was the strain used in this research, which was marked as HR 168 from Howard Rogers. The strain was taken from Microbank storage beads and incubated on Nutrient broth (NB) plates for solid media, or NB for liquid culture at 37 °C as shown above.

2.6 Determining bacterial cell density

2.6.1 Measurement by optical density

For quantification of the bacterial yield of a liquid culture, spectrophotomeric measurements at 600 nm wavelength (OD_{600}) were conducted. While sterile culture media was used as the blank, necessary culture samples were diluted in the appropriate same media to provide readings within the optimum accuracy range (below 0.6). These measurements were taken using a Biochrom WPA Biowave DNA Life Science spectrophotometer.

2.6.2 Measurement by direct cell counting (cfu/mL)

Direct cell counting was performed to quantify viable cell number of a certain media. Bacterial samples were diluted 1:10 or 1:100 in successive in triplicate. 10 µL of samples from each dilution were spotted onto the appropriate agar plate with antibiotics if necessary. The plates were incubated at 37 ºC until individual colonies were visualised by eye or microscopy (normally 12-24 h). The numbers of colonies were counted to determine the number of colony forming units (cfu).

Name	Stock concentration (mg/mL)	Working Concentration (µg/mL)	Solvent
Kanamycin (Kan)	50	50	dH_2O
Neomycin (Neo)	50	50	dH_2O
Erythromycin (Ery)	5	5	100% (v/v) Ethanol
Lincomycin (Lin)	25	25	50% (v/v) Ethanol
Vancomycin (Van)	0.1	1	dH_2O
Mutanolysin	2.5	10	PBS
Moenomycin	1	5	dH_2O

Table 2.1 Antibiotics stock and working concentrations.

Stock solution	Solvent	Concentration	Storage
HADA	DMSO	1 mg/mL	-20 °C in dark
NADA	DMSO	1 mg/mL	-20 °C in dark
SADA	DMSO	1 mg/mL	-20 °C in dark
Alexa Fluor® 488 hydroxylamine (HAF488)	dH_2O	1 mg/mL	-20 °C in dark
Alexa Fluor® 488 alkyne	dH_2O	0.5 mg/mL	-20 °C in dark
Vancomycin 647	DMSO	1 mg/mL	-20 °C in dark
Vancomycin BODIPY®Fl conjugate	dH_2O	1 mg/mL	-20 °C in dark
Alexa Fluor® 647 NHS Ester	DMSO	4 mM	-20 °C in dark
Alexa Fluor® 647 Alkyne	DMSO	0.5 mg/mL	-20 °C in dark
Azide-TEG hydroxylamine	dH_2O	10 mM	-20 °C in dark
Azide-fullerene	DMSO	10 mM	-20 °C in dark
Alkyne-gold nanoparticles, 5 nm	/	0.05% Au	4 °C in dark
Alkyne-gold nanoparticles, 30 nm	/	0.05% Au	4 °C in dark
Ferrocene-TEG hydroxylamine	dH_2O	10 mM	-20 °C in dark
Ruthenocene-TEG hydroxylamine	dH_2O	10 mM	-20 °C in dark

Table 2.2 Stock solutions and concentrations for cell labelling. Alkyne-gold nanoparticles of different diameters were purchased from Nanocs and the dissolving solutions were unreported.

2.7 Preparation of cell samples for microscopy

Cells were treated differently depending on what was the subject of study.

2.7.1 Cell growth

Generally, cells needed to grow to the exponential stage for live cell studies. The desired strain was streaked to single colonies on agar plates and incubated overnight at 37 °C. A single fresh colony was inoculated into 10 mL of liquid culture and incubated overnight at 37 °C with aeration at 250 rpm. The calculated cultures were inoculated into 200 mL of liquid culture to give a starting OD_{600} as approximately 0.05. Cells were grown to OD_{600} of 0.3-0.4, then harvested by centrifugation (13,000 rpm for 5 min), followed by washing with PBS once.

2.7.2 Purification of cell walls and sacculi

2.7.2.1 Purifying cell walls

A single colony was inoculated to a 10 mL of appropriate media and incubated overnight at 37 °C, which was used to prepare growing media at OD_{600} of 0.05 in a conical flask. When the OD_{600} reached to 0.5 ~ 0.6, the media was boiled for 10 min using a water bath to kill the cells and pellets were harvested by centrifugation (5,000 rpm for 10 min). To remove complexes that non-covalently attached to the cell wall, these pellets were treated with 5% (w/v) SDS at 55 °C for 30 min and with 4% (w/v) SDS for 15 min. Washing with dH_2O at least six times was required to get rid of excess SDS before cells were re-suspended in 50 mM Tris-HCl (pH 7.5) with 2 mg/mL pronase and incubated at 60 °C for 90 min for additional removal of covalently bound proteins. If necessary, 48% (w/v) hydrofluoric acid (HF) was added to remove cell wall polymers by incubation at 4 °C for 48 h. The pellets were repeatedly washed with dH_2O and checked with the pH until the pH was above 5.0, followed by storing at -20 °C.

2.7.2.2 Breakage of cell sacculi

Due to requirements of imaging technology, breaking cell sacculi was occasionally needed, which was achieved by a FastPrep machine (MP Biomedicals Fastprep 24 Homogeniser). As shown in Chapter 2.7.2.1, boiled cells were added to FastPrep tubes containing lysing matrix B (MP Biomedicals) and mechanically sheared at speed of 6.0 m/s for 30 s, six times at 4 °C to prevent overheating. Supernatant visualisation by miscopy was applied to check the breakage state before being centrifuged at 1000 rpm for 30 s to transfer the supernatant to a clean Eppendorf tube for further applications.

2.7.3 Fixation

Cell pellets were resuspended in fixative (0.5 mL of PBS and 0.5 mL of fresh fixation solution) or ethanol, respectively. Then the mixture was incubated on a rotary wheel for 30 min at RT. The fixed cells were washed at least twice in sterile dH_2O followed by centrifugation at 13,000 rpm for 3 min at room temperature and either viewed immediately or kept as pellets at -20 °C.

2.8 Fluorescent amino acid labelling

2.8.1 HADA, NADA and SADA labelling

1 mL of exponential phase culture was added with 5 or 10 µL of dye (HADA, NADA or SADA), and incubated for 5 min at 37 ºC on a rotary mixer. Aliquots were washed at least twice with 10% DMSO in dH_2O by centrifugation (13,000 rpm for 2 min) and resuspension, then fixed with fixative (0.5 mL of PBS and 0.5 mL of fresh fixation solution) as described previously. Cells were washed at least twice with PBS before attaching on the surface of slides.

2.8.2 ADA labelling

5 μL of ADA was added to exponential phase culture (1 mL) and incubated for 5 min at 37 ºC on a rotary mixer. Aliquots were washed twice with 10% DMSO in dH_2O and resuspended with 220 μL of click buffer (Invitrogen), 15 μL of Alexafluor alkyne 647, 15 μL of $CuSO_4$ and 25 μL of additive at RT. After 0.5 h, cells were washed with 10% DMSO in dH_2O and fixed with fixative (0.5 mL of PBS and 0.5 mL of fresh fixation solution) or ethanol as described previously before attaching to the surface of slides.

2.9 Vancomycin labelling in different fixation fashion

2.9.1 Synthesis of fluorophore-modified vancomycin (VanF)

5 μL of triethylamine was added to the mixture of 100 μL of 2 mM vancomycin solution and 100 μL of a 2 mM solution of NHS ester fluorescent dye such as BODIPY and Alexafluor 647 in an Eppendorf tube. The resulting solution was put on a rotary shaker at room temperature for 24 hours, and left in the open air for an hour to allow any excess triethylamine to evaporate. Any remaining NHS groups of fluorescent dyes were eliminated during the addition of 800 μL of 1M Tris-HCl (pH 7.0) and the mixture was stored at -20 ºC.

2.9.2 Post-fixation

A 1 mL aliquot of exponential phase culture was centrifuged. The pellets were resuspended in TSB, BHI, PSB or 0.1 M sodium carbonate (pH 8.3) buffer with a 1:1 mix of vancomycin:VanF (BODIPY or Alexafluor 647) at 0.5 or 1 μg/mL and incubated for 5 min at 37 ºC on a rotary mixer. Aliquots were washed at least twice with sterile dH_2O by centrifugation (14,000 rpm for 3 min) and resuspension, then fixed with fixative (0.5 mL of PBS and 0.5 mL of fresh fixation solution) or ethanol as described previously. Cells were washed at least twice with sterile dH_2O before attaching to the surface of slides.

2.9.3 Pre-fixation

A 1 mL aliquot of exponential phase culture was centrifuged and fixed with fixative (0.5 mL of PBS and 0.5 mL of fresh fixation solution) or ethanol as described previously. Aliquots were washed twice with sterile dH_2O by centrifugation (14,000 rpm for 3 min) and resuspension, then resuspended in TSB, BHI, PBS or 0.1 M sodium carbonate (pH 8.3) buffer with a 1:1 mix of vancomycin:VanF at 0.5 or 1 μg/mL and incubated for 5 min at 37 °C on a rotary mixer. Cells were washed at least twice with sterile dH_2O before attaching to the surface of slides.

2.9.4 No-fixation

A 1 mL aliquot of exponential phase culture was centrifuged. Pellets were resuspended in TSB, BHI, PBS or 0.1 M sodium carbonate (pH 8.3) buffer with a 1:1 mix of vancomycin:VanF (Invitrogen) at 0.5 or 1 μg/mL and incubated for 5 min at 37 °C on a rotary mixer. Aliquots were washed at least twice with sterile dH_2O by centrifugation (14,000 rpm for 3 min) before attaching to the surface of slides.

2.10 HAF488 labelling

Peptidoglycan reducing termini was labelled by HAF488 with different fixation methods as described below.

2.10.1 Post-fixation

Exponential phase cultures were used for labelling. The sample was washed once in PBS and resuspended in 0.1 M sodium carbonate (pH 8.3) buffer, PBS, TSB or BHI. HAF488 was added to a final concentration of 100 μg/mL. The suspension was incubated in the dark on a rotary mixer at room temperature for 1 h or at 37 °C for 5 min. Samples were washed by centrifugation (14,000 rpm for 3 min) at least twice in dH_2O and fixed with fixative (0.5 mL of PBS and 0.5 mL of fresh fixation solution) or ethanol as described previously.

2.10.2 Pre-fixation

Exponential phase cells were resuspended in fixative (0.5 mL of PBS and 0.5 mL of fresh fixation solution) or ethanol for fixation as described previously. Samples were washed by centrifugation (14,000 rpm for 3 min) at least twice in dH_2O and resuspended in 0.1 M sodium carbonate (pH 8.3) buffer, PBS, TSB or BHI with a final concentration of 100 μg/mL of HAF488. The suspension was incubated in the dark on a rotary mixer at room temperature for 1 h or at 37 ºC for 5 min. Samples were washed by centrifugation (14,000 rpm for 3 min) at least twice in dH_2O before attaching to the surface of slides.

2.10.3 Optimization of HAF488 labelling time

Exponential phase cells were incubated with HAF488 in PBS, TSB or BHI in the dark on a rotary mixer at 37 ºC for specified time (0, 2, 4, 8, 15 or 30 min). After washing at least twice in dH_2O by centrifugation (14,000 rpm for 3 min), the pellets were fixed with ethanol, washed again and dried over nitrogen gas before attaching to the surface of slides.

2.10.4 Optimization of HAF488 labelling concentration

HAF488 was dissolved in PBS at a specified concentration and exponential phase cells were incubated with these solutions in the dark on a rotary mixer at 37 ºC for 5 min. After washing twice in dH_2O by centrifugation (14,000 rpm for 3 min), the pellets were labelled with VanF at 37 ºC for 5 min and washed again. These labelled pellets were fixed with ethanol, washed with dH_2O and dried with nitrogen gas before attaching to the surface of slides.

2.11 Azide-TEG hydroxylamine labelling

2.11.1 Post-click labelling

Exponential phase cells pellets were incubated with a specified concentration of azide-TEG hydroxylamine probe in 0.1 M sodium carbonate (pH 8.3) buffer, PBS, TSB or BHI. The suspension was incubated in the dark on a rotary mixer at room temperature for 1 h or at 37 ºC for 5 min. Samples were washed by centrifugation (14,000 rpm for 3 min) twice in 10% DMSO in dH_2O and resuspended in 220 µL of click buffer, 15 µL of Alexafluor alkyne dye (488 or 647), 15 µL of $CuSO_4$ and 25 µL of additive at RT. After 0.5 h, cells were washed with 10% DMSO in dH2O and fixed with fixative (0.5 mL of PBS and 0.5 mL of fresh fixation solution) or ethanol as described previously before attaching to the surface of slides.

2.11.2 Pre-click labelling

15 µL of Alexafluor alkyne dye (488 or 647) was added to variety of concentrations of azide-TEG hydroxylamine probe in 220 µL of click buffer, followed by addition of 15 µL of $CuSO_4$ and 25 µL of additive at RT. After 0.5 h, pellets harvested from 1 mL of culture grown to exponential phase were incubated with the above resulting mixture at 37 ºC for 5 min. Labelled cells were washed with 10% DMSO in dH2O and fixed with fixative (0.5 mL of PBS and 0.5 mL of fresh fixation solution) or ethanol as described previously before attaching to the surface of slides.

2.12 Cell wall reducing with $NaBH_4$

2.12.1 Fluorescent labelling of entire cells or sacculi after $NaBH_4$ treatment

Exponential phase cells pellets or sacculi (Chapter 2.7.2) were resuspended in freshly prepared $NaBH_4$ (0.1 g) in 1 mL of PBS on a rotary mixer at room temperature for 10 min and washed once with PBS. This progress was repeated three times. Before being used for further labelling, pellets or sacculi were washed three times with PBS. These treated pellets or sacculi were incubated with HAF488 in PBS at 37 ºC for 5 min. Meanwhile, pellets or sacculi without $NaBH_4$ treatment were labelled with HAF488 or VanF as controls. After washed once with 10% DMSO in dH_2O, they were treated with VanF at 37 ºC for 5 min. Labelled cell pellets or sacculi were washed with 10% DMSO in dH_2O and fixed with ethanol as described previously before attaching to the surface of slides.

2.12.2 Effects of $NaBH_4$ treatment on WT cells growing

Exponential phase cells pellets were resuspended in PBS or freshly prepared $NaBH_4$ PBS solution (0.1 g/mL) on a rotary mixer at room temperature for 10 min and washed three times with PBS. Another group of pellets harvested from the same culture were treated with $NaBH_4$ PBS solution (0.1 g/mL) three times followed by washing three times with PBS. In all cases pellets were resuspended in TSB liquid and OD_{600} measured and recorded as time 0. These pellets continued to grow at 37 ºC and the OD_{600} was monitored over 60 min to produce a growth curve.

2.13 Cell wall blocking by hydroxylamine solution (NH_2OH) pre-treating

2.13.1 Fluorescent labelling of cells after NH_2OH treatment

Exponential phase cells pellets from 1 mL of culture were treated with 10 µL of hydroxylamine (NH_2OH) solution (50 % w/v in H_2O, Sigma) in 190 µL of PBS at 37 ºC for 5 min. After being washed twice with PBS, cell pellets were labelled with HAF488 or VanF as previously described. Pellets without NH_2OH treatment were labelled with HAF488 or VanF as controls.

2.13.2 Optimization of concentration of NH_2OH used

Exponential phase cells pellets from 1 mL of culture were treated with 200 μL of NH_2OH PBS solution containing 0.01, 0.1, 1, 5, 10, 15 or 20 μL of NH_2OH stock (50 w/v in H_2O, Sigma), respectively, at 37 ºC for 5 min. After washed twice with PBS, cell pellets were labelled with HAF488 and VanF as previously described.

2.13.3 Effects of NH_2OH treatment on WT cells growing

Exponential-phase of *S. aureus* WT strains were treated with NH_2OH in PBS or PBS alone (unblocked) at 37 °C for 5 min with shaking. After washing with PBS, cells were inoculated into TSB followed by incubation at 37 °C. Bacterial growth was monitored by measuring OD_{600} and recorded at 1 hour-intervals to prepare a growth curve. NH_2OH treated cells were labelled with HADA as previously described to verify the cell state.

2.14 Cell regrown for nascent peptidoglycan labelling

2.14.1 Dual labelling NH_2OH blocked cells with HAF488 and vancomycin

To study dynamics of new synthesised PG, WT and mutants were grown to the exponential phase and surfaces of cells were blocked with NH_2OH solution as above described in Chapter 2.13, which were then resuspended in liquid TSB at 37 ºC for 0, 0.5, 1, 2, 5, 10, 15, 30 min. After being immediately centrifuged (14,000 rpm for 2 min), the pellets were labelled with HAF488 for 5 min at 37 ºC as described previously and instantly fixed with fixative (0.5 mL of PBS and 0.5 mL of fresh fixation solution) or ethanol for 30 min at room temperature. After washing twice with 10% DMSO in dH_2O by centrifugation (14,000 rpm for 3 min) and resuspension, cells were fixed with) were incubated with PBS in a 1:1 mix of vancomycin: VanF (BODIPY or Alexafluor 647) at 0.5 or 1 μg/mL for 5 min at 37 ºC on a rotary mixer. Cells were washed at least twice with sterile dH_2O before attaching to the surface of slides.

2.14.2 HAF488-labelled cells regrown and labelled with HADA

Cultures were grown to exponential phase. Cells were incubated with HAF488 in PBS for 5 min at 37 ºC, washed twice with PBS and resuspended in liquid TSB at 37 ºC for 0, 0.5, 1, 2, 5, 10, 15, 30 min. At a specified time, 1 mL of this growing culture was added to 5 µL of HADA stock at 37 ºC for 5 min. After immediately being centrifuged (14,000 rpm for 3 min), the pellets were fixed with fixative (0.5 mL of PBS and 0.5 mL of fresh fixation solution) or ethanol for 30 min at room temperature and washed at least twice with sterile dH_2O before attaching to the surface of slides.

2.15 Antibiotic effects on cell dynamics

2.15.1 The growth curve of *S. aureus* WT cells with or without mutanolysin

Exponential phase live WT cells were resuspended in PBS, 10 µg/mL of mutanolysin in PBS with or without 100 mM $MgCl_2$, or 20 µg/mL of mutanolysin in PBS with or without 100 mM $MgCl_2$, respectively and OD_{600} was measured. After incubation at 37 ºC for 0.5 hour, the cells were spun, washed with PBS, resuspended in pre-warmed TSB liquid and the OD_{600} immediately measured and recorded as time 0 followed by 10 or 20 min-intervals monitoring. Based on these data, the growth curve was drawn and compared with each other.

2.15.2 Fluorescent analysis of mutanolysin activity towards *S. aureus* WT

Live WT cells at exponential phase were treated with 0, 10 or 20 µg/mL of mutanolysin in PBS with or without 100 mM $MgCl_2$ at 37 ºC for 0.5 hour as above mentioned. After washing with PBS, pellets were resuspended in 1 mL of TSB with 5 µL of HADA and the mixture shook at 37 ºC for 5 min. After centrifugation at 14,000 rpm for 3 min, pellets were harvested, washed and labelled with HAF488 at 37 ºC for 5 min. After washing at least twice with sterile dH_2O, those pellets were fixed with ethanol for 30 min at room temperature and washed with dH_2O again and dried with nitrogen gas before being attaching to the surface of slides.

2.15.3 Moenomycin effects on the growth of NH_2OH blocked cells

Cells from variety of strains at the exponential phase were blocked with NH_2OH, and regrown in TSB with or without 5 µg/mL of moenomycin at 37 ºC with shaking over time (5, 10, 15, 30, 45 and 60 min). Cells were later labelled with HAF488, VanF staining and fixed as previously described.

2.15.4 Moenomycin effects on HADA labelling of WT cells

Live WT cells at the exponential phase were labelled with HAF488 in PBS at 37 ºC for 5 min followed by washing twice with PBS. The pellets were resuspended in pre-warmed TSB liquid with or without 5 µg/mL of moenomycin in a 50 mL of conical flask and continued to grow at 37 ºC over time (0, 5, 10, 15, 30, 45 or 60 min). 1 mL of the culture was then added to 5 µL of HADA and incubated at 37 ºC for 5 min. After washing at least twice with sterile dH_2O, pellets were fixed with ethanol for 30 min at room temperature and washed again and dried with nitrogen gas before attaching to the surface of slides.

2.16 Fluorescence microscopy

Fluorescence imaging was carried out using diffraction limited microscopy (Olympus DeltaVision deconvolution microscope, formerly Applied Precision) and super-resolution microscopy (Structured illumination microscopy, SIM or Stochastic optical reconstruction microscopy, STORM) to visualize cells with diverse types of fluorophore labels. All images achieved were processed using ImageJ. More specifically, contrast or background for all the images were uniformly adjusted to facilitate visualization and comparison. Quantification of fluorescence intensity was carried out by measurement of modified corrected total cell fluorescence (CTCF). CTCF was calculated using ImageJ measurement tool on z-projections in a single channel, which was based on the equation that CTCF = Integrated density - (area of selected cell × mean fluorescence of background readings). Also ImageJ measurement tool enabled calibration of the pixel/µm ratio within an image, providing a scale bar to determine the size of cells.

2.16.1 DeltaVision deconvolution microscope

Cells were attached to commercially available poly-prep slides (Sigma-Aldrich) before visualization by microscopy. Cell pellets were resuspended in dH_2O to an appropriate concentration which was judged by eye. A 5 µL of drop spread gently onto the slide, was allowed to dry in air or nitrogen. Slides were then washed by water and dried by nitrogen aspiration. A cover slip was mounted in 5µl of Slow Fade Gold (Invitrogen), gentle pressure applied and sealed with DPX mountant (BDH). The visualization was achieved using an Olympus DeltaVision deconvolution microscope equipped with appropriate filters for imaging labelled fluorophore labels with diverse types of excitation and emission (Table 2.2). An UPLANSAPO 100x oil (NA 1.4) was applied as the objective and images were detected using a Photometrics CoolsnapHQ CCD camera. If required, images were deconvolved using SoftWoRx suite v.3.5.1. Deconvolved fluorescence images were processed, and cell measurements carried out, using ImageJ version 1.50v.

2.16.2 STORM imaging

2.16.2.1 Preparation of coverslips

High-precision coverslips (No. 1.5H, 22 x 22mm, 170±5 µm, Marienfeld) were immersed into 1M KOH solution accompanied by sonicating for 20 min. After the KOH was discarded and rinsed off with dH_2O, 2 mL of poly-L-lysine (0.01% w/v in H_2O, Sigma) was added and incubated for 30 min at room temperature to cover the coverslips. The covered coverslips were then washed with dH_2O and dried with nitrogen before being loaded with a cell sample.

2.16.2.2 Preparation of the calibration slide for N-STORM

Approximately 100 μL of TetraSpeckTM (0.1 μm, blue/green/orange/dark red, Molecular Probes) diluted 1:1000 in 1 × PBS (1 × PBS pH 7.4, Life Technologies), was added to a depression slide (76 × 26 × 1.35 mm, 90° ground edges, 1 cavity, 15-18 mm, depth 0.6-0.8 mm, Marienfeld) before being covered with High-Precision coverslip (No. 1.5H, 22 × 22 mm, 170 ± 5 μm, Marienfeld). The slide was then sealed with a clear nail polish and used for imaging.

2.16.2.3 Preparation of the sample slide for N-STORM

Fixed cell pellets with compatible fluorescent labels were resuspended in a specified amount of HPLC grade water (LC-MS CHROMASOLVE®, Fluka) giving an appropriate sample dilution and 5 μL was dropped onto a prepared coverslip (Chapter 2.15.2.1). The sample coverslip was dried using nitrogen gas, washed with dH_2O and dried again under nitrogen, followed by mounted on a depression slide (76 × 26 × 1.35 mm, 90° ground edges, 1 cavity, 15 -18 mm, depth 0.6 - 0.8 mm, Marienfeld) with approximately 100 μL of GLOX MEA buffer (Chapter 2.3). The slide was then sealed with clear nail polish and used for imaging.

2.16.2.4 Setup of N-STORM

N-STORM imaging was performed under a platform with an objective of SR Apo TIRF 100× and a Nikon Ti-NS N-STORM version 1 with 3D capability. Images were collected using EM-CCD (Andor DU-897) camera and microscope control was achieved using the NIS elements software with the N-STORM module.

2.16.2.5 Calibration of N-STORM

Prepared fluorescent bead samples (Chapter 2.16.2.2) were visualized using the 3D calibration tool in the software over an 800 nm shift in *Z* and the imaged shapes of the beads were employed as the quantitative criteria to calibrate the localisation of fluorescent labels in the Z plane.

2.16.2.6 Data acquisition and processing from N-STORM

Once imaging, ~80,000 frames were collected and focus was achieved using the Nikon perfect focussing system. The imaging laser was used at 647 nm due to dye compatibility and the N-STORM filter-cube was used to collect light above 675 nm, which was capable of Alexa Fluor 647 imaging at 100%. The activation was performed using a 405 nm laser, which was adjusted either manually or using the AutoLP function based on the number of events per frame. The N-STORM module of the Nikon NIS elements software version 4.20.02 retained the default settings of screening minimum and maximum height to collect details of evens localisation. Image processing was conducted following the procedure for 3D STORM imaging.[94] Data processing was carried out by using Matlab to fit Gaussian functions to fluorescence of individual molecule. A fiducial particle was tracked throughout the acquisition sequence and offsetting localizations against its position for the retrospective correction of drift in the focal plane. In order to render images, ThunderSTORM, a modular plug-in for ImageJ was used as previously described.[95] A created image was set as a 256 × 256 pixel area histogram with 100 nm z steps from -500 nm to 500 nm for plotting data points.

Strain	Genotype	Growth conditions (µg/mL)	Source
SH1000	Functional *rsbU*$^+$ derivative of 8325-4	BHI or TSB	Horsbourgh *et al.*, 2003[93]
S4167 (*sagB*)	SH1000 (*sagB::kan*)	Kan 50	Wheeler *et al.*, 2015[18]
S4644 (*sgtA mgt*)	SH1000 (*sgt::tet mgt::Tn*)	Tet 0.5 and Ery 5	Mina Mohaghegh
S4657 (*tarO*)	SH1000 (*tarO::ery*)	Ery 5	Andreas Peschel

Table 2.3 *S. aureus* strains used in this research.

Filter	**Compatible fluorophore**	**Excitation /bandpass (nm)**	**Excitation /bandpass (nm)**
DAPI	HADA	360/40	457/50
FITC/YFP	Alexafluor 488, VancFL488, NADA, SADA, HAF488	492/20	528/38
RD-TR-PE	Rhodamine, Cy3	555/28	617/73
Cy5	Alexafluor 647 VanF647	640/20	685/40

Table 2.4 DeltaVision filter sets.

2.16.3 SIM imaging

Fixed cell pellets with compatible fluorescent labels were resuspended in a specified amount of HPLC grade water (LC-MS CHROMASOLVE®, Fluka) giving an appropriate sample dilution and 5 µL was dropped onto a prepared coverslip (Chapter 2.15.2.1). The sample coverslip was dried using nitrogen gas, washed with dH_2O and dried again under nitrogen, followed by mounted on a depression slide (76 × 26 × 1.35 mm, 90° ground edges, 1 cavity, 15 -18 mm, depth 0.6 - 0.8 mm, Marienfeld) with 5µl of Slow Fade Gold (Invitrogen). The slide was then sealed with clear nail polish and used for imaging.

SIM samples were illuminated using laser illumination with 6 colour widefield illumination module and Ring TIRF (Table 2.4). Objective and filters were the same as for widefield microscopy. Focus was carried out using a UltimateFocus hardware Autofocus 75 Module. Z-stacks taken using a fast piezo -z-axis system on the nanomotion sample stage. Microscope was controlled and images were reconstructed using SoftWoRx version 6.1.3.

2.17 Electron microscopy

Biological samples used in this study were purified cell sacculi from *S. aureus* WT or Taro mutant cells following the procedure in Chapter 2.7.2. These sacculi were labelled with variety of probes, including gold nanoparticles (5 or 30 nm), ferrocene and ruthenocene bared probes, followed by multi sample processing required for visualization by electron microscopy.

For transmission electron microscopy (TEM), 200 mesh copper grids were cut on a Leica UC 6 ultramicrotome, giving ultrathin sections, approximately 85 nm thick, and coated with carbon or polymer by Chris Hill. Sections were examined using a FEI

Tecnai TEM at an accelerating voltage of 80Kv at the Electron Microscopy Unit, University of Sheffield. Electron micrographs were recorded using a Gatan Orius 1000 digital camera and Digital Micrograph software, which were adjusted using ImageJ if required.

2.17.1 Labelling sacculi with gold nanoparticles for TEM imaging

20 µL of azide-TEG hydroxylamine stock (10 mM) was added to 180 µL of PBS with an appropriate amount of purified cell sacculi from *S. aureus* WT or *taro* mutant cells, and incubated at 37 ºC over time. After washing with PBS by centrifugation, the azide-carrying sacculi was mixed with 30 µL of alkyne-gold nanoparticles (5 or 30 nm, 0.05% Au, purchased from Nanocs) in 220 µL of click buffer, followed by the addition of 15 µL of $CuSO_4$ and 15 µL of click additive. The resulting mixture was shaken at room temperature for 30 min. The labelled sacculi were harvested and washed again with dH_2O before undergoing sample post-processing for TEM imaging. Meanwhile, sacculi from the same stock were incubated with freshly prepared $NaBH_4$ PBS solution (0.1 g/mL) at room temperature for 10 min and washed once with PBS. This treatment was repeated three times. These $NaBH_4$ treated sacculi were labelled with azide-TEG hydroxylamine and alkyne-gold nanoparticles using the same method as above mentioned, which were used as controls.

2.17.2 Labelling sacculi with metallocene probes

An appropriate amount of purified cell sacculi from *S. aureus* WT or Taro mutant cells were resuspended in 180 µL of PBS and added with 20 µL of ferrocene- or ruthenocene-TEG hydroxylamine stock (10 mM), and the resulting mixture was incubated with shaking at 37 ºC over time. After centrifugation, the labelled sacculi were harvested and washed again with dH_2O before undergoing sample post-processing for TEM imaging. In control experiments, sacculi from the same stock were treated with freshly prepared $NaBH_4$ PBS solution (0.1 g/mL) at room temperature for 10 min and washed once with PBS, which was repeated three times. $NaBH_4$ treated sacculi were labelled with metallocene-TEG hydroxylamine respectively using the same method as abovementioned and compared with labelling state of sacculi without $NaBH_4$ treatment.

2.17.3 Post-processing of labelled sacculi for TEM imaging

Negative staining to enhance the contrast before visualization by electron microscopy was applied using uranyl formate. Sacculi labelled with nanoparticles or metallocene were dissolved in dH_2O to an appropriate concentration, and 5 μL of the solution was dropped onto a prepared copper grid. After 30 seconds, the grid was dried by blotting with filter paper and placed on a drop of uranyl acetate solution for 15 seconds. The grid was then rinsed in dH_2O for 15 seconds and dried by blotting with filter paper, which was repeated twice. Finally a vacuum line was used to completely dry the grid before it was transferred to electron microscopy observation.

Some labels such as the ferrocene and ruthenocene were extremely small (sub nanoscale) and the high contrast from metal staining probably shielded the metallocene labelling. Therefore, unstained experiments were also performed. 5 μL of the labelled sacculi solution was dropped onto the prepared copper grid. After 30 seconds, the grid was dried by blotting with filter paper and rinsed in dH_2O for 15 seconds, dried by blotting with filter paper and a vacuum before it was transferred to electron microscopy observation.

2.18 Experimental data for synthesized compounds

Unless stated otherwise, dry solvents used were obtained from the departmental Grubbs dry solvent system and stored under a positive pressure of nitrogen before being used. Thin layer chromatography (TLC) was performed on aluminium backed silica plates

(Merck 60 F_{254}) and subsequently visualised using 254 nm UV lamps or by staining within KMnO4 or molybdophosphoric acid solution. Flash column chromatography was carried out by employing different sized columns packed with silica gel (40-63 µ 60Å, Fluorochem Limited). Melting points were measured on a Gallenkamp apparatus and are uncorrected. Infrared spectra were recorded on a Perkin-Elmer 1600 FT-IR machine. ^{1}H and ^{13}C NMR were carried out on a Bruker spectrometer (400 or 250 MHz). Chemical shifts for hydrogen and carbon were given, on the δ scale. Coupling constants were reported as a *J* value in Hz. Mass spectra (m/z) were recorded on a "VG"-Autospec for Electron Ionization (EI) and on a "Water"-LCT for Electrospray (ES).

2.18.1 Synthesis of the azide probe

Benzophenone oxime[96]

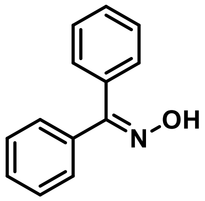

Benzophenone (9.11g, 50 mmol) and hydroxylamine hydrochloride (5.21 g, 75 mmol) were completely dissolved in ethanol (90 mL) and water (10 mL) before addition of NaOH (3.00 g, 75 mmol). The mixture was stirred at RT for 24 hours and heated at 80 °C for another 24 hours. After cooling to RT, the solution was added to a water-ice mixture (approximate 50 g) and the precipitate was filtered, washed with cold water (30 mL), and dried under *vacuum* to afford the desired product as a white solid (9.40 g, 95%).

Mpt 140-145 °C (lit.[96] 143-145 °C); ^{1}H NMR (250 MHz, $CDCl_3$): δ_H 9.10 (1H, brs, O*H*), 7.54-7.43 (7H, m, ArC*H*), 7.41-7.31 (3H, m, ArC*H*); ^{13}C NMR (101 MHz, $CDCl_3$): δ_C 158.0 (*C*=N), 136.2 (Ar*C*), 132.7 (Ar*C*), 129.5 (Ar*C*H), 129.2 (2 × Ar*C*H), 129.1 (Ar*C*H), 128.3 (2 × Ar*C*H), 128.2 (2 × Ar*C*H), 127.9 (2 × Ar*C*H).

1,2-*bis*(2-Bromoethoxy)ethane[97]

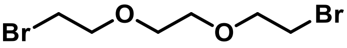

The mixture of triethylene glycol (1.50 g, 10 mmol) and carbon tetrabromide (7.30 g, 22 mmol) in dry THF (50 mL) was cooled to 0 °C, and triphenylphosphine (5.25 g, 20 mmol) in dry THF (20 mL) was added dropwise. After 1 h, the mixture was warmed to room temperature and stirred overnight. The solvent was evaporated and the residue was purified by flash column chromatography on silica gel (gradually eluting with petroleum ether [40-60]/EtOAc, 6:1 to 3:1), giving the desired product as canary yellow oil (2.18 g, 80%).

ν_{max}(ATR)/cm^{-1} 2867 (w), 1422 (w); ^{1}H NMR (400 MHz, CDCl$_3$): δ_H 3.85 (4H, t, *J* 6.2, 2 × BrCH$_2$C*H*$_2$), 3.71 (4H, s, 2 × OC*H*$_2$), 3.50 (4H, t, *J* 6.2, 2 × BrC*H*$_2$); ^{13}C NMR (101 MHz): δ_C 71.3 (2 × *C*H$_2$O), 70.6 (2 × *C*H$_2$O), 30.3 (2 × Br*C*H$_2$); *m/z* (ES$^+$) 315 (5%, M$^+$K$^+$), 299 (100, M$^+$Na$^+$. C$_6$H$_{12}$^{79}Br^{81}Br O$_2$Na requires 298.9), 277 (41, MH$^+$).

2-[2-(2-Hydroxyethoxy)ethoxy]ethyl 4-methylbenzenesulfonate[98]

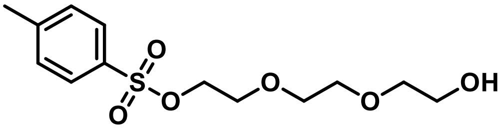

Ag$_2$O (0.348 g, 1.5 mmol), TsCl (0.210 mg, 1.1 mmol), and KI (0.033 g, 0.2 mmol) were added to a stirred solution of commercial triethylene glycol (0.150 g, 1 mmol) in anhydrous CH$_2$Cl$_2$ (15 mL). The reaction mixture was stirred at 0 °C for 5 h and then filtered and washed with water (2 × 15 mL) and brine (15 mL). The organic phase was dried over MgSO$_4$, filtered, and the solvent evaporated to give the desired product (0.248 g, 82%), that was used without further purification in the next step.

^{1}H NMR (400 MHz, CDCl$_3$): δ_H 7.81 (2H, d, *J* 8.2, ArC*H*), 7.35 (2H, d, *J* 8.2 Hz, ArC*H*), 4.17-4.19 (2H, m, C*H*$_2$OS), 3.71-3.74 (4H, m, 2 × C*H*$_2$O), 3.63 (4H, s, 2 × C*H*$_2$O), 3.58-3.60 (2H, m, C*H*$_2$O), 2.46 (3H, s, C*H*$_3$); ^{13}C NMR (101 MHz, CDCl$_3$): δ_C 145.0 (Ar*C*), 133.2 (Ar*C*), 130.8 (2 × Ar*C*H), 128.1 (2 × Ar*C*H), 72.6 (*C*H$_2$), 70.9 (*C*H$_2$), 70.5 (*C*H$_2$), 69.3 (*C*H$_2$), 68.9 (*C*H$_2$), 61.9 (*C*H$_2$), 21.8 (*C*H$_3$); *m/z* (TOF MS ES$^+$) 366 (55%), 322 (51), 305.1053 (100, MH$^+$. $C_{13}H_{21}SO_6$ requires 305.1053), 199 (3).

2-[2-(2-Azidoethoxy)ethoxy]ethanol[99]

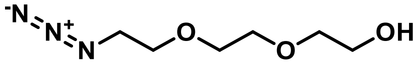

A mixture of 2-[2-(2-chloroethoxy)ethoxy]ethanol (0.843 g, 5 mmol), sodium azide (0.813g, 12.5 mmol) and potassium iodide (0.166 g, 1 mmol) in water (20 mL) were stirred at 80 °C for 18 h. The cooled reaction mixture was extracted with DCM (3 × 15 mL), and the combined organic extracts were dried over $MgSO_4$. After filtration, the solvent was evaporated to give a colorless oil that was used without further purification (0.663 g, 76%).

^{1}H NMR (250 MHz, $CDCl_3$): δ_H 3.76-3.60 (10H, m, 5 × CH$_2$), 3.41 (2H, t, *J* 5.0, C*H*$_2$N$_3$); ^{13}C NMR (63 MHz, $CDCl_3$): δ_C 50.7 (*C*H$_2$N$_3$), 61.8 (*C*H$_2$OH), 70.0 (*C*H$_2$), 70.4 (*C*H$_2$), 70.7 (*C*H$_2$), 72.5 (*C*H$_2$); *m/z* (TOF MS ES$^+$) 237 (13), 221 (58), 214 (9), 198 (17), 193(100), 176 (78%, MH$^+$. $C_6H_{14}N_3O_3$ requires 176), 148 (27).

2-{2-[2-(2-Azidoethoxy)ethoxy]ethoxy}isoindoline-1,3-dione[100]

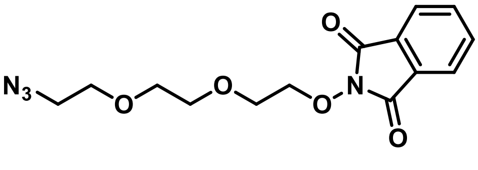

2-[2-(2-Azidoethoxy)ethoxy]ethanol (0.350 g, 2 mmol), triphenylphosphine (0.788 g, 3 mmol) and *N*-hydroxyphthalimide (0.489 g, 3 mmol) were added to anhydrous THF (10 mL) and cooled to 0 °C. Diisopropylazodicarboxylate (0.606 g, 3 mmol) in anhydrous THF (5 mL) was added dropwise to this solution. The reaction mixture was allowed to warm to room temperature and stirred overnight. Removal of the solvent and purification by column chromatography on silica gel (eluting with petroleum ether [40-60]/EtOAc, 3:1) yielded the desired product as a colorless oil which solidified upon standing (0.430 g, 66%).

^{1}H NMR (400 MHz, CDCl$_3$): δ_H 7.87-7.84 (m, 2 H, ArC*H*), 7.80-7.76 (m, 2 H, ArC*H*), 4.42-4.39 (m, 2H, OC*H$_2$*CH$_2$N$_3$), 3.90-3.89 (m, 2H, C*H$_2$*O), 3.72-3.68 (m, 2H, C*H$_2$*O), 3.65-3.57 (m, 4H, C*H$_2$*C*H$_2$*), 3.37-3.35 (t, *J* = 5.1 Hz, 2H, C*H$_2$*CH$_2$N$_3$); ^{13}C NMR (101 MHz): δ_C 163.5 (2 × *C*=O), 134.5 (2 × Ar*C*H), 129.0 (2 × Ar*C*), 123.5 (2 × Ar*C*H), 77.3 (*C*H$_2$O), 70.9 (*C*H$_2$O), 70.6 (*C*H$_2$O), 70.0 (*C*H$_2$O), 69.4 (*C*H$_2$O), 50.7 (*C*H$_2$N$_3$); *m/z* (TOF MS ES$^+$) 359 (MK$^+$), 343.1022 (100%, MNa$^+$. $C_{14}H_{16}N_4O_5Na$ requires 343.1018), 336 (5), 315 (21), 293 (4), 190 (45).

O-{2-[2-(2-azidoethoxy)ethoxy]ethyl}hydroxylamine

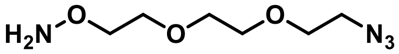

Ethanolamine (0.025 mL, 0.42 mmol) in DCM (5 mL) was added to a solution of 2-{2-[2-(2-azidoethoxy)ethoxy]ethoxy}isoindoline-1,3-dione (0.064 g, 0.20 mmol) in DCM (5 mL) and the mixture was stirred at RT overnight. The mixture was evaporated, dissolved in H$_2$O (5 mL) and filtered. The filtrate was extracted with DCM (4 × 5 mL), and the combined organic layers washed with cold brine (5 mL), dried over MgSO$_4$, and filtered. Removal the solvent in vacuum yielded the product that did not require further purification (0.035 g, 92%).

^{1}H NMR (400 MHz, CDCl$_3$): δ_H 5.52 (s, 2H, N*H$_2$*O), 3.86-3.83 (m, 2H, OC*H$_2$*CH$_2$N$_3$), 3.70-3.68 (m, 8H, C*H$_2$*C*H$_2$*O), 3.41-3.38 (t, *J* = 4.9 Hz, 2H, C*H$_2$*N$_3$); ^{13}C NMR (101 MHz): δ_C 73.4 (*C*H$_2$ONH$_2$), 69.3 (*C*H$_2$O), 69.2 (*C*H$_2$O), 68.7 (CH$_2$*C*H$_2$O), 68.3 (*C*H$_2$CH$_2$ONH$_2$), 49.4(*C*H$_2$N$_3$); *m/z* (TOF MS ES$^+$) 191.1145 (MH$^+$, 100%. $C_6H_{15}N_4O_3$ requires 191.1144).

2.18.2 Synthesis of metallocene probes

2-[2-(2-Iodoethoxy)ethoxy]ethan-1-ol[101]

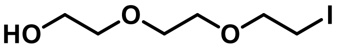

NaI (2.248 g, 15 mmol) was added to a solution of 2-[2-(2-chloroethoxy)ethoxy]ethanol (1.686 g, 10 mmol) in dry acetone (15 mL) and the mixture heated at reflux for 2 days. The precipitate was filtered off, the filtrate evaporated, and the residue dissolved in DCM (30 mL). This was washed with brine (10 mL), water (10 mL), dried over magnesium sulfate, filtered, and concentrated *in vaccuo* to afford the title compound (2.486 g, 96%) as a brownish oil, which was used without further purification.

^{1}H NMR (400 MHz, CDCl$_3$): δ_H 3.79-3.74 (4H, m, C*H$_2$*), 3.71-3.67 (4H, m, C*H$_2$*), 3.64-3.62 (2H, m, C*H$_2$*), 3.28 (2H, t, *J* 6.8 Hz, IC*H$_2$*), 2.44 (1H, s, O*H*); ^{13}C NMR (101 MHz): δ_C 72.6 (*C*H$_2$), 72.0 (*C*H$_2$), 70.5 (*C*H$_2$), 70.3 (*C*H$_2$), 61.9 (*C*H$_2$), 2.8 (I*C*H$_2$); *m/z* (TOF MS ES$^+$) 302.0 (76), 278.0 (50), 260.9989 (100%, MH$^+$. $C_6H_{14}O_3I$ requires 260.9988), 196.0 (12).

2-{2-[2-(2-Hydroxyethoxy)ethoxy]ethoxy}isoindoline-1,3-dione

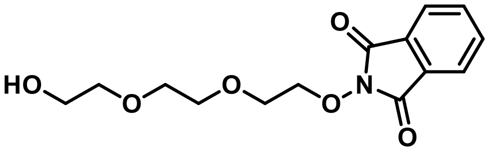

Triethylene glycol (9.010 g, 60 mmol), *N*-hydroxyphthalimide (3.262 g, 20 mmol) and triphenylphosphine (6.304 g, 24 mmol) were dissolved in dry THF (80 mL), cooled to 0 °C, and diisopropylazodicarboxylate (4.853 g, 24 mmol) in dry THF (30 mL) was added dropwise. After 1 h, the mixture was warmed to room temperature and stirred overnight. The solvent was evaporated and the residue was purified by flash column chromatography on silica gel (eluting with petroleum ether [40-60]/EtOAc, 1:2), giving the desired product as oil (5.300 g, 90 %).

v_{max}/cm^{-1} 3425, 2871, 1788, 1723, 1610, 1467; ^{1}H NMR (400 MHz, CDCl$_3$): δ_H 7.88-7.85 (2H, m, ArC*H*), 7.78-7.76 (2H, m, ArC*H*), 4.42-4.40 (2H, m, OC*H$_2$*CH$_2$OH), 3.91-3.88 (2H, m, C*H$_2$*O), 3.72-3.70 (4H, m, 2 × C*H$_2$*), 3.64-3.62 (2H, m, C*H*$_2$), 3.59-3.56

(2H, app t, *J* 4.4, C*H*₂), 2.25 (1H, br s, O*H*); ^{13}C NMR (101 MHz): δ_C 163.5 (2 × *C*=O), 134.5 (2 × Ar*C*H), 129.0 (2 × Ar*C*), 123.5 (2 × Ar*C*H), 77.4 (*C*H$_2$), 70.9 (*C*H$_2$), 70.6 (*C*H$_2$), 70.0 (*C*H$_2$), 69.4 (*C*H$_2$), 50.7 (*C*H$_2$OH); *m/z* (ESI$^+$) 331 (47%), 296.1124 (100, MH$^+$. $C_{14}H_{18}NO_6$ requires 296.1129).

2-{2-[2-(2-Chloroethoxy)ethoxy]ethoxy}isoindoline-1,3-dione[100]

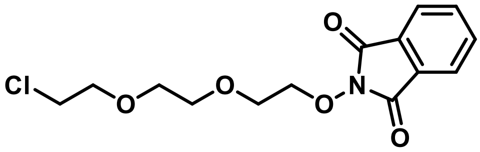

2-[2-(2-Chloroethoxy)ethoxy]ethanol (2.023 g, 12 mmol), triphenylphosphine (4.728 g, 18 mmol) and *N*-hydroxyphthalimide (2.936 g, 18 mmol) were added to anhydrous THF (25 mL) and cooled to 0 °C. Diisopropylazodicarboxylate (3.640 g, 18 mmol) in anhydrous THF (15 mL) was added dropwise to this solution. The reaction mixture was allowed to warm to room temperature and stirred overnight. Removal of the solvent and purification by column chromatography on silica gel (petroleum ether [40-60]/EtOAc, 3:1) yielded the desired product (2.844 g, 76%).

Mpt 55-59 °C; ^{1}H NMR (400 MHz, CDCl$_3$): δ_H 7.87-7.85 (m, 2 H, Ar*CH*), 7.78-7.76 (m, 2 H, Ar*CH*), 4.42-4.39 (m, 2H, OCH_2CH$_2$Cl), 3.91-3.89 (m, 2H, CH_2O), 3.71-3.68 (m, 4H, 2 × CH_2), 3.64-3.62 (m, 2H, CH_2), 3.60-3.57 (t, *J* = 5.6 Hz, 2H, CH_2); ^{13}C NMR (101 MHz): δ_C 163.5 (2 × *C*=O), 134.5 (2 × Ar*C*H), 129.0 (2 × Ar*C*), 123.5 (2 × Ar*C*H), 77.4 (*C*H$_2$O), 71.3 (*C*H$_2$O), 70.8 (*C*H$_2$O), 70.6 (*C*H$_2$O), 69.4 (*C*H$_2$O), 42.7 (*C*H$_2$Cl); *m/z* (ESI$^+$) 314.0787 (MH$^+$, 84%, $C_{14}H_{17}ClNO_5$ requires 314.0790), 331.1053 (100), 190.0497 (10).

Ferrocene carboxaldehyde[102,103]

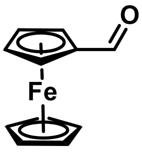

A solution of ferrocene (0.279 g, 1.5 mmol) and potassium *t*-butoxide (0.021 g, 0.188

mmol) in dry THF (15 ml) was cooled to -78 °C and *t*-BuLi (1.34 M in pentene, 2.24 mL, 3.0 mmol) was added dropwise. The reaction was left at -78 °C for 1 h, and DMF (0.257g, 0.27 mL, 3.5 mmol) was added slowly and the mixture was warmed to -40 °C and left for 20 min. H_2O (15 mL) was added, and then the organic solvent was evaporated. The residue was extracted with DCM (3 × 15 mL) and the combined extracts were washed with brine (25 mL), dried over $MgSO_4$, filtered, and concentrated in *vacuo*. The resulting residue was purified by column chromatography on silica gel (deactivated by addition of 4% w/w water, and eluting with petroleum [40-60] and DCM, sequentially) to yield the desired product as a purple solid (0.230 g, 72%).

Mpt 115-125 °C (lit.[102] 121 °C); ^{1}H NMR (400 MHz, $CDCl_3$): δ_H 9.98 (1 H, s, C*H*O), 4.82 (2 H, s, FcC*H*), 4.63 (2 H, s, FcC*H*), 4.30 (5 H, s, FcC*H*); ^{13}C NMR (101 MHz): δ_C 193.4 (*C*HO), 79.5 (Fc*C*CHO) 73.2 (4 × Fc*C*H), 69.6 (5 × Fc*C*H); ν_{max}(ATR)/cm^{-1} 3090 (m), 2835 (w), 2766 (w), 1675 (s), 1660 (s); *m/z* (TOF MS ES$^+$) 214.0074 (100%, $M^+.C_{11}H_{10}{}^{56}FeO$ requires 214.0076), 186 (54), 121 (51).

Ferrocenemethanol[104]

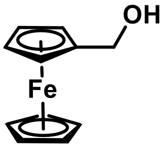

Ferrocene carboxaldehyde (2.140 g, 10 mmol) in dry methanol (25 mL) was cooled to 0 °C and sodium borohydride (0.757 g, 20 mmol) was added in three portions. After 1 h, the mixture was allowed to room temperature, then stirred overnight. Saturated ammonium chloride solution (20 mL) was added, and allowed to stir for thirty minutes, and the mixture extracted with EtOAc (3 × 20 mL), the combined extracts were dried over $MgSO_4$, filtered, and concentrated *in vaccuo* to give the title compound (2.132 g, 99%) as a yellow solid that did not require further purification.

Mpt 75-80 °C; ^{1}H NMR (400 MHz, $CDCl_3$): δ_H 4.34 (2 H, s, C*H*$_2$OH), 4.29 (2 H, s, FcC*H*), 4.23 (7 H, s, FcC*H*), 1.58 (1 H, s, O*H*); ^{13}C NMR (101 MHz, $CDCl_3$): δ_C 88.5

(Fc*C*CH$_2$), 68.3 (2 × Fc*C*H), 68.3 (5 × Fc*C*H), 67.9 (2 × Fc*C*H), 60.8 (*C*H$_2$OH); *m/z* (MS EI$^+$) 216.0233 (80%, M$^+$. $C_{11}H_{12}FeO$ requires 216.0232), 138 (100), 73 (20).

Ferrocenylmethyl-triethylene glycol ether[105]

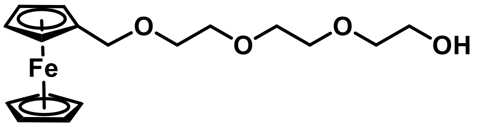

Triethylene glycol (4.505 g, 30 mmol) was mixed with ferrocenemethanol (1.295 g, 6 mmol) in dry DCM (3 mL) and Al(OTf)$_3$ (0.142 g, 0.3 mmol) was then added. The resulting mixture was stirred at room temperature for 6 hours and then diluted with 5% Na_2CO_3 solution (5 mL), and extracted with DCM (3 × 8 mL). The combined organic extracts were dried over $MgSO_4$, filtered, concentrated in *vacuo* and purified by column chromatography on silica gel (eluting with petroleum ether [40-60]/EtOAc, 1:1), yielding the desired product as a light brown oil (1.664 g, 80%).

^{1}H NMR (400 MHz, CDCl$_3$): δ_H 4.36 (2 H, s, FcC*CH$_2$*), 4.26-4.25 (2 H, m, FcC*H*), 4.17-4.15 (7 H, m, FcC*H*), 3.75-3.59 (12 H, m, C*H$_2$*O), 2.54-2.52 (1 H, m, O*H*); ^{13}C NMR (101 MHz): δ_C 83.4 (Fc*C*CH$_2$), 72.6 (*C*H$_2$), 70.7 (2 × *C*H$_2$), 70.4 (*C*H$_2$), 69.8 (4 × Fc*C*H), 69.6 (*C*H$_2$), 69.0 (*C*H$_2$), 68.7 (5 × Fc*C*H), 61.8 (*C*H$_2$OH); ν_{max}/cm^{-1} 3436 (s), 2869 (s), 1777 (m); *m/z* (TOF MS ES$^+$) 348.1018 (100%, M$^+$. $C_{17}H_{24}FeO_4$ requires 348.1019), 199.0 (4).

Ferrocenylmethyl-triethylene glycol hydroxyphthalimide

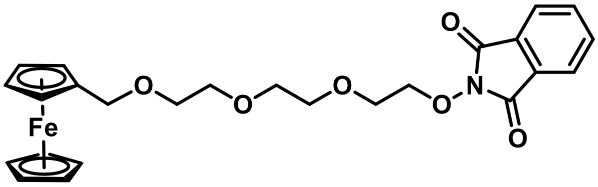

Ferrocenylmethyl-triethylene glycol ether (1.265 g, 3.6 mmol), triphenylphosphine (1.419 g, 5.4 mmol) and *N*-hydroxyphthalimide (0.881 g, 5.4 mmol) were added to anhydrous THF (10 mL) and cooled to 0 °C. Diisopropylazodicarboxylate (1.092 g, 5.4 mmol) in anhydrous THF (8 mL) was added dropwise to this solution. After 0.5 h, the reaction mixture was allowed to warm to room temperature and stirred overnight. Removal of the solvent and purification by column chromatography on silica gel (eluting with petroleum ether [40-60]/EtOAc, 2:1) yielded the desired product as brown oil (1.647 g, 93%).

^{1}H NMR (400 MHz, $CDCl_3$): δ_H 7.86-7.84 (2 H, m, ArC*H*), 7.77-7.76 (2 H, m, ArC*H*), 4.40-4.38 (2 H, m, FcCC*H*$_2$), 4.32 (2 H, s, FcC*H*), 4.24 (2 H, s, FcC*H*), 4.15 (7 H, s, 5 × FcC*H* and C*H*$_2$), 3.89-3.87 (2 H, m, C*H*$_2$), 3.69-3.66 (2 H, m, C*H*$_2$), 3.59-3.57 (2 H, m, C*H*$_2$), 3.55 (4 H, s, C*H*$_2$); ^{13}C NMR (101 MHz): δ_C 163.4 (2 × *C*=O), 134.4 (2 × Ar*C*H), 129.0 (2 × Ar*C*), 123.5 (2 × Ar*C*H), 83.4 (FcC*C*H$_2$), 77.2 (Fc*C*CH$_2$), 70.8 (*C*H$_2$), 70.6 (*C*H$_2$), 70.5 (*C*H$_2$), 69.6 (4 × Fc*C*H), 69.4 (*C*H$_2$), 69.3 (*C*H$_2$), 68.9 (*C*H$_2$), 68.5 (5 × Fc*C*H); ν_{max}/cm^{-1} 3506 (w), 3090 (w), 2863 (m), 1789 (m), 1727 (s), 1610 (w), 1467 (m); *m/z* (TOF MS ES$^+$) 511.2 (100%), 493.1184 (58, M$^+$. $C_{25}H_{27}FeNO_6$ requires 493.1182), 199.0 (19).

Ferrocenylmethyl-triethylene glycol hydroxylamine

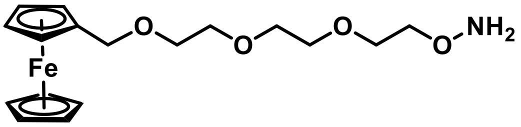

Ethanolamine (0.061 g, 1.0 mmol) in DCM (5 mL) was slowly added to a solution of ferrocenylmethyl-triethylene glycol hydroxyphthalimide (0.099 g, 0.20 mmol) in dry THF (10 mL) and the mixture was stirred at 45 °C for 28 h. The mixture was evaporated and purified by column chromatography on silica gel (eluting with EtOAc in petroleum [40-60], 25-100%), yielding the desired product as a dark yellow oil (0.056g, 77%).

ν_{max} (ATR)/cm^{-1} 3317 (w), 3095 (w), 2862 (m); ^{1}H NMR (400 MHz, $CDCl_3$): δ_H 5.51 (2 H, s, N*H*$_2$), 4.34 (2 H, s, 2 × FcC*H*), 4.24 (2 H, app t, *J* 1.8, FcCC*H*$_2$), 4.16-4.14 (7 H, m, 7 × FcC*H*), 3.85-3.83 (2 H, m, C*H*$_2$), 3.69-3.67 (2 H, m, C*H*$_2$), 3.66 (4 H, s, C*H*$_2$), 3.64-3.62 (2 H, m, C*H*$_2$), 3.60-3.58 (2 H, m, C*H*$_2$); ^{13}C NMR (101 MHz, $CDCl_3$): δ_C

83.2 (Fc*C*CH$_2$), 74.8 (FcC*C*H$_2$), 70.6 (*C*H$_2$), 70.5 (2 × *C*H$_2$), 69.6 (2 × Fc*C*H), 69.5 (*C*H$_2$), 69.0 (*C*H$_2$), 68.9 (*C*H$_2$), 68.6 (*C*H$_2$), 68.5 (2 × Fc*C*H), 68.4 (5 × Fc*C*H); ^{13}C NMR (101 MHz, Acetone-d$_6$): δ_C 84.1 (Fc*C*CH$_2$), 72.4 (FcC*C*H$_2$), 70.5 (*C*H$_2$), 70.4 (2 × *C*H$_2$), 69.3 (*C*H$_2$), 69.2 (2 × Fc*C*H), 69.1 (*C*H$_2$), 68.9 (*C*H$_2$), 68.3 (5 × Fc*C*H), 68.0 (2 × Fc*C*H); *m/z* (TOF MS ES$^+$) 402 (9%, MK$^+$), 386 (100, MNa$^+$), 364.1212 (26, MH$^+$. $C_{17}H_{26}{}^{56}FeNO_4$ requires 364.1211), 217 (5), 199 (6).

Ruthenocene[106]

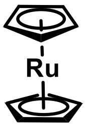

Dicyclopentadiene (25 mL) was rapidly distilled by a Vigreux column fitted with a distillation head at 210 °C under nitrogen and cyclopentadiene was collected in a dry ice-acetone receiver. After an approximate 5-mL forerun was collected and discarded, cyclopentadiene (0.99 g, 1.26 mL, 15 mol) was immediately added to ruthenium trichloride hydrate (0.26 g, 1 mmol) in absolute ethanol (12 mL). Meanwhile, zinc dust (10 g) was treated with 2% HCl solution (30 mL) for 1 min, filtered, and washed with 2% HCl solution (20 mL), water (3 × 30 mL), EtOH (3 × 20 mL), and Et$_2$O (3 × 20 mL), and left under the high vacuum. The freshly washed zinc dust (6.54 g, 0.10 mol) was added to the mixture in five portions and then stirred for 22 hours at RT. The mixture was filtered and the precipitate was washed with hot toluene (15 mL × 4). All of combined filtrates were dried over MgSO$_4$, filtered and evaporated. The residue was then passed through a plug of silica gel (eluting with 250 mL of toluene), giving the desired product as white crystalline solid (0.22 g, 95%).

Mpt 194-198 °C (lit.[106] 197-200 °C); ν_{max}(ATR)/cm^{-1} 3915 (w), 3083 (m), 2921 (m), 2852 (m), 2455 (m); ^{1}H NMR (400 MHz, CDCl$_3$): δ_H 4.58 (10 H, s, RcC*H*); ^{13}C NMR (101 MHz, CDCl$_3$): δ_C 70.0 (10 × Rc*C*H); *m/z* (MS EI$^+$) 231.9827 (100%, M$^+$. $C_{10}H_{10}{}^{102}Ru$ requires 231.9826), 204 (8), 167 (29), 141 (7).

Ruthenocene carboxaldehyde[102]

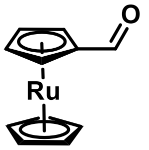

Ruthenocene (1.272 g, 5.5 mmol) and potassium *t*-butoxide (0.079 g, 0.7 mmol) were dissolved in dry THF (137 ml), cooled to -78 °C, and *t*-BuLi (1.3 M in pentene, 9.2 mL, 11.0 mmol) was added dropwise. The reaction was left at -78 °C for 0.5 h, then DMF (0.101 g, 13.8 mmol) was added slowly and the mixture was warmed to -40 °C, and left for 15 min. H_2O (50 mL) was added, and then the solvent evaporated. The residue was extracted with DCM (30 mL × 4) and the combined extracts were washed with brine (40 mL), dried over $MgSO_4$, filtered, and concentrated in *vacuo*. The resulting residue was purified by column chromatography on silica gel (deactivated by addition of 4% w/w water, and eluting with petroleum [40-60] and DCM, sequentially) to yield the desired product as a bright yellow solid (1.174 g, 82%).

Mpt 100-104 °C; ν_{max}/cm^{-1} 3094 (m), 2857 (w), 2763 (w), 1977 (s), 1672 (s), 1657 (s); ^{1}H NMR (400 MHz, $CDCl_3$): δ_H 9.74 (1 H, s, C*H*O), 5.10 (2 H, t, *J* 1.8, FcC*H*), 4.88 (2 H, t, *J* 1.8, FcC*H*), 4.67 (5 H, s, FcC*H*); ^{13}C NMR (101 MHz): δ_C 190.2 (*C*HO), 84.6 (Fc*C*CHO), 74.2 (2 × Fc*C*H), 72.1 (5 × Fc*C*H), 70.9 (2 × Fc*C*H); *m/z* (TOF MS ES$^+$) 259.9775 (73%, M$^+$. $C_{11}H_{10}{}^{102}RuO$ requires 259.9773), 232.0 (100), 204.0 (14), 177.9 (6), 166.9 (45), 140.9 (11), 113.9 (9).

Ruthenocenylmethanol[107]

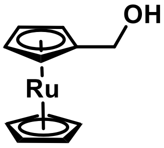

Ruthenocene carboxaldehyde (1.037 g, 4 mmol) in dry diethyl ether/MeOH (45 and 20 mL) was cooled to 0 °C and sodium borohydride (0.756 g, 20 mmol) was added in three portions. After 1 h, the mixture was allowed to room temperature, then stirred for 30 h.

Saturated aqueous ammonium chloride solution (40 mL) was added, allowed to stir for 0.5 h, and brine (30 mL) was added, allowed to stir for 5 minutes. The mixture was extracted with DCM (4 × 30 mL), the combined extracts were dried over $MgSO_4$, filtered, and concentrated *in vaccuo* to give the title compound (1.042 g, 100%) as a white solid that did not require further purification.

Mpt 75-80 °C; ν_{max}(ATR)/cm^{-1} 3244 (m), 3101 (m), 2927 (m), 2876 (m), 2104 (w), 1692 (w); ^{1}H NMR (400 MHz, $CDCl_3$): δ_H 4.70 (2 H, t, *J* 1.7, RcC*H*), 4.64 (5 H, s, RcC*H*), 4.57 (2 H, t, *J* 1.7, RcC*H*), 4.03 (2 H, d, *J* 5.7, C*H₂*OH), 1.13 (1 H, t, *J* 5.7, O*H*); ^{13}C NMR (101 MHz, $CDCl_3$): δ_C 95.4 (Rc*C*CH$_2$), 70.7 (4 × Rc*C*H), 70.4 (5 × Rc*C*H), 58.6 (*C*H$_2$OH); *m/z* (MS EI$^+$) 261.9926 (100%, M$^+$. $C_{11}H_{12}{}^{102}RuO$ requires 261.9932), 245 (61), 232 (65), 184 (18), 167 (58).

Ruthenocenylmethyl-triethylene glycol ether

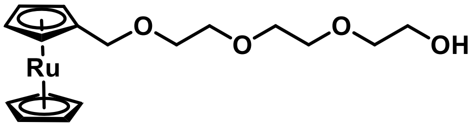

Ruthenocenylmethanol (0.941 g, 3.6 mmol) and triethylene glycol (2.703 g, 18.0 mmol) was dissolved in dry DCM (5 mL), and $Al(OTf)_3$ (0.085 g, 0.18 mmol) was then added. The resulting mixture was stirred at RT for 24 hours and then diluted with 5% aqueous Na_2CO_3 solution (10 mL), and extracted with DCM (4 × 10 mL). The combined organic extracts were dried over $MgSO_4$, filtered, concentrated in *vacuo* and purified by column chromatography on silica gel (eluting with EtOAc), yielding the desired product as a yellowish oil (1.156 g, 81%).

ν_{max}(ATR)/cm^{-1} 3360 (s), 2875 (m), 1637 (s); ^{1}H NMR (400 MHz, $CDCl_3$): δ_H 4.68-4.67 (2 H, app t, *J* 1.6, RcCC*H₂*), 4.55-4.54 (7 H, m, RcC*H*), 4.15 (2 H, s, RcC*H*), 3.77-3.73 (2 H, m, C*H₂*O), 3.71-3.69 (2 H, m, C*H₂*O), 3.68-3.65 (4 H, m, 2 × C*H₂*O), 3.64-3.62 (4 H, m, 2 × C*H₂*O), 2.54-2.51 (1 H, t, *J* 6.3, O*H*); ^{13}C NMR (101 MHz): δ_C 86.6

(Rc*C*CH$_2$), 72.5 (*C*H$_2$), 72.0 (2 × Rc*C*H), 70.7 (2 × Rc*C*H), 70.6 (*C*H$_2$), 70.6 (5 × Rc*C*H), 70.4 (*C*H$_2$), 69.1 (*C*H$_2$), 68.8 (*C*H$_2$), 61.8 (*C*H$_2$OH); *m/z* (TOF MS ES$^+$) 394.0725 (32%, M$^+$. $C_{17}H_{24}{}^{102}RuO_4$ requires 394.0718), 262 (42), 245 (100), 167 (44).

Ruthenocenylmethyl-triethylene glycol hydroxyphthalimide

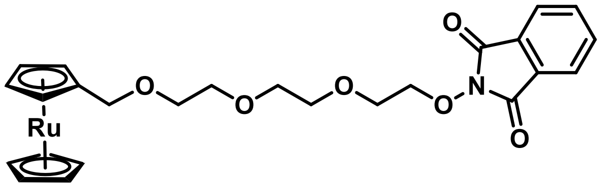

Ruthenocenylmethyl-triethylene glycol ether (0.590 g, 1.5 mmol), triphenylphosphine (0.525 g, 2.0 mmol) and *N*-hydroxyphthalimide (0.318 g, 2.0 mmol) were added to anhydrous THF (20 mL) and cooled to 0 °C. Diisopropylazodicarboxylate (0.404 g, 2.0 mmol) in anhydrous THF (9 mL) was added dropwise to this solution. After 0.5 h, the reaction mixture was allowed to warm to room temperature and stirred overnight. Removal of the solvent and purification by column chromatography on silica gel (eluting with 25-50% EtOAc in petroleum ether [40-60]) yielded the desired product as brown oil (0.641g, 79%).

ν_{max}/cm^{-1} 3095 (w), 2869 (m), 1790 (m), 1731 (s), 1467 (m); ^{1}H NMR (400 MHz, CDCl$_3$): δ_H 7.86-7.83 (2 H, m, ArC*H*), 7.78-7.75 (2 H, m, ArC*H*), 4.67-4.65 (2 H, m, RcCC*H*$_2$), 4.53 (7 H, s, RcC*H*), 4.40-4.38 (2 H, m, C*H*$_2$), 4.12 (2 H, s, RcC*H*), 3.89-3.87 (2 H, m, C*H*$_2$), 3.68-3.67 (2 H, m, C*H*$_2$), 3.59-3.57 (6 H, m, 3 × C*H*$_2$); ^{13}C NMR (101 MHz): δ_C 163.5 (2 × *C*=O), 134.4 (2 × Ar*C*H), 129.0 (2 × Ar*C*), 123.5 (2 × Ar*C*H), 86.8 (RcC*C*H$_2$), 77.2 (Rc*C*CH$_2$), 72.0 (2 × Rc*C*H), 70.8 (2 × *C*H$_2$), 70.7 (2 × Rc*C*H), 70.6 (5 × Rc*C*H), 70.5 (*C*H$_2$), 69.3 (*C*H$_2$), 69.1 (*C*H$_2$), 68.8 (*C*H$_2$); *m/z* (TOF MS ES$^+$) 539.0902 (16%, M$^+$. $C_{25}H_{27}{}^{102}RuNO_6$ requires 539.0883), 262 (33), 245 (100), 190 (16), 167 (39), 147 (28), 104 (27), 76 (22).

Ruthenocenylmethyl-triethylene glycol hydroxylamine

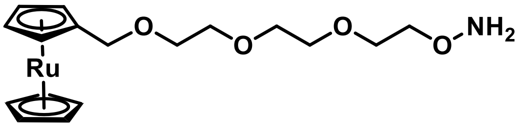

Ethanolamine (0.122 g, 2.0 mmol) was added to a solution of ruthenocenylmethyl-triethylene glycol hydroxyphthalimide (0.135 g, 0.25 mmol) in dry THF (8 mL) and the mixture was stirred at 50 ºC for 34 h. The mixture was evaporated and purified by column chromatography on silica gel (eluting with EtOAc in petroleum [40-60], 33-100%), yielding the desired product as a yellowish oil (0.075 g, 74%).

ν_{max} (ATR)/cm^{-1} 3313 (w), 3096 (w), 2864 (m); ^{1}H NMR (400 MHz, CDCl$_3$): δ_H 5.52 (2 H, br s, N*H*$_2$), 4.67 (2 H, app t, *J* 1.7, RcCC*H*$_2$), 4.55 (7 H, s, 7 × RcC*H*), 4.12 (2 H, s, 2 × RcC*H*), 3.87-3.85 (2 H, m, C*H*$_2$), 3.71-3.69 (2 H, m, C*H*$_2$), 3.68 (4 H, s, 2 × C*H*$_2$), 3.66-3.61 (4 H, m, 2 × C*H*$_2$); ^{13}C NMR (101 MHz, CDCl$_3$): δ_C 86.7 (Rc*C*CH$_2$), 74.8 (RcC*C*H$_2$), 72.6 (*C*H$_2$), 72.0 (2 × Rc*C*H), 70.7 (2 × Rc*C*H), 70.6 (*C*H$_2$), 70.6 (5 × Rc*C*H), 70.5 (*C*H$_2$), 69.6 (*C*H$_2$), 69.1 (*C*H$_2$), 68.9 (*C*H$_2$); *m/z* (TOF MS ES$^+$) 488 (23%), 472 (100), 448 (18, MK$^+$), 432.0728 (78, MNa$^+$. $C_{17}H_{25}Na^{102}RuNO_4$ requires 432.0725), 410 (29, MH$^+$), 245 (70).

But-3-ynyl *p*-toluenesulfonate[108]

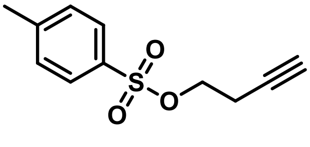

But-3-yn-1-ol (2.22 g, 31.6 mmol), triethylamine (3.84 g, 38.0 mmol), and 4-(dimethylamino)pyridine (0.08g, 0.64 mmol) were dissolved in DCM (36 mL) at 0 ºC, and *p*-toluenesulfonyl chloride (7.24 g, 38.0 mmol) was added in four portions. The reaction mixture was brought to RT and stirred for 18 h, aqueous HCl (0.5 M, 30 mL) was added, and the mixture was vigorously stirred for 20 min at RT. The reaction was extracted with DCM (3 × 20 mL), the combined organic layers washed with brine (3 ×

15 mL), dried over $MgSO_4$, filtered, and concentrated in *vaccuo* to afford but-3-ynyl *p*-toluenesulfonate (7.06 g, 100%) as a yellowish oil that did not require further purification.

ν_{max}/cm^{-1} 3292 (s), 2971 (s), 1738 (m); ^{1}H NMR (400 MHz, $CDCl_3$): δ_H 7.83-7.81 (2H, $(AX)_2$, ArC*H*), 7.38-7.36 (2H, $(AX)_2$, ArC*H*), 4.11 (2H, t, *J* 7.1, OC*H₂*), 2.60-2.56 (2H, td, *J* 7.1, 2.7, OCH_2CH_2), 2.48 (3H, s, CH_3), 1.98 (1H, t, *J* 2.7, C*H*); ^{13}C NMR (101 MHz, $CDCl_3$): δ_C 145.0 (ArC), 132.9 (ArC), 129.9 (2 × Ar*C*H), 128.0 (2 × Ar*C*H), 78.4 (CH*C*), 70.7 (*C*H), 67.4 (O*C*H₂), 21.6 (*C*H₃), 19.5 (OCH_2CH_2); *m/z* (ESI$^+$) 225.0593 (100%, MH$^+$. $C_{11}H_{13}O_3S$ requires 225.0585), 242 (10).

4-(Prop-2-yn-1-yloxy)benzaldehyde[109]

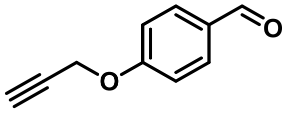

A mixture of 4-hydroxybenzaldehyde (1.22 g, 10 mmol), potassium carbonate (4.15 g, 30 mmol), and sodium iodide (0.15 g, 1 mmol) in dry acetonitrile (27 mL) was heated at reflux for 0.5 h, followed by addition of propargylbromide (1.93 g, 13 mmol). The reaction mixture was stirred overnight at reflux and the solvent was then evaporated. The residue was dissolved in water (20 mL) and extracted with EtOAc (3 × 15 mL). The combined extracts were washed with 0.5 M NaOH (20 mL), brine (20 mL), dried over $MgSO_4$, and filtered, and the solvent evaporated in vacuum to give the desired product (1.47 g, 92 %) that was used without further purification in the next step.

Mpt 76-81 °C; ^{1}H NMR (400 MHz, $CDC1_3$): δ_H 9.91 (1H, s, C*H*O), 7.86 (2H, $(AX)_2$, 2 × ArC*H*), 7.10 (2H, $(AX)_2$, 2 × ArC*H*), 4.79 (2H, d, *J* 2.4, C*H₂*), 2.55 (1H, t, *J* 2.4, C*H*); ^{13}C NMR (101 MHz, $CDCl_3$): δ_C 190.8 (*C*HO), 162.4 (Ar*C*O), 131.9 (2 × Ar*C*H), 130.6 (Ar*C*CHO), 115.2 (2 × Ar*C*H), 77.6 (HC*C*), 76.4 (H*C*C), 56.0 (*C*H₂O); *m/z* (EI$^+$) 160.0513 (30%, M$^+$. $C_{10}H_8O_2$ requires 160.0519), 131 (100), 121 (28), 103 (30), 77 (24).

Chapter 3 *In vivo* visualizing peptidoglycan in live bacteria using HAF488

3.1 Introduction

Bacteria present a wide diversity of shapes and sizes, and it has long been recognized that the determination of cell shape is highly consistent with the most of peptidoglycan (PG) cell wall biosynthesis and division model.[110] In rod-shaped bacteria, such as *Bacillus subtilis* and *Escherichia coli*, alternating elongation and division of the cell occurs. The elongation mode involves synthesis of lateral cell wall along a helical path while division is performed by the formation of septum across the shorter axis of the cell resulting in two identical daughter cells.[25] On the other hand, coccoid bacteria such as *Staphylococcus aureus* (*S. aureus*) appear to employ only one mode of cell wall synthesis at the mid-cell with the formation of a septum rather than alternating between elongation and division (Figure 3.1).

Although several models of cell growth have been successfully established, the relationship between PG dynamics and cell metabolism has remained elusive, despite the basic chemical structure of PG being well studied. Increasingly, studies require chemical or biochemical labelling approaches that enable the rapid incorporation and detection of stable labels or tags in specific sites of the PG components in real time, in a wide range of bacterial species, and in live cells. Genetically-encoded reporters such as green fluorescent protein (GFP) can be used to transfer the analysis of specific biological events or processes into an observable fluorescent signal without interfering with cellular metabolism, with such developments dramatically expanding the understanding of living organisms. Nevertheless, this genetically controllable approach may not always be possible in some areas, especially glycan and small-molecule metabolites.[111] Alternatively, a series of ligation reactions, referred as bioorthogonal chemistry, progressing rapidly under physiological conditions, without interacting with the surrounding molecules, enables the visualization of biomolecules that are impossible to tag with FP.

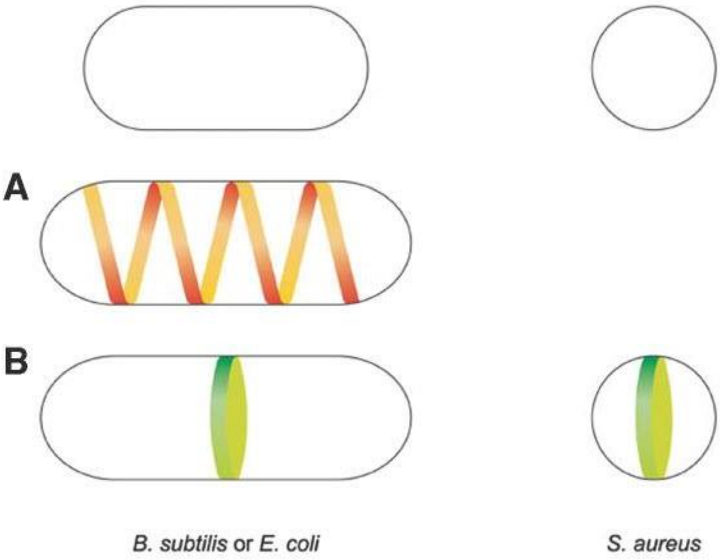

Figure 3.1 Different synthesis modes of new cell wall in differently shaped bacteria. Two proposed modes of cell wall synthesis: one is to elongate the lateral wall resulting from insertion of new peptidoglycan in a helical pattern **(A)**, and the other occurs insertion of new peptidoglycan at equatorial rings resulting in the division septum formation **(B)**. Ref 25 with permission from *the American Society for Microbiology*.[25]

3.2 Results

3.2.1 Labelling the peptide chain of PG

3.2.1.1 Incorporation of fluorescent amino acids into the peptide chain

A basic PG subunit contains a glycan backbone and a peptide chain (Figure 1.3). During PG biosynthesis process, subunits are crosslinked together by a peptide bond via the action of a transpeptidase. In *S. aureus* the peptide chain is assembled by sequentially incorporating both L-and D-amino acids via a series of ligases. As D-amino acids were rare in nature, it was envisaged that unnatural D-amino acids analogues (D-amino acids assembled with various functionalities) from the surrounding medium could be incorporated into the peptide side chain of PG during cell wall synthesis in live bacteria.[112-114] Therefore, this site-specific incorporation provides real-time spatiotemporal platform for deciphering cell wall mechanisms.

Fluorescent D-amino acids (FDAAs) used within this work were synthesised by B Cotterell and D Jenkinson in Jones lab. Relatively small fluorophores were linked with amine groups of D-amino acids to form the fluorescent amino acids HADA (7-hydroxycoumarin-3-carboxylic acid-3-amino-D-alanine), NADA (7-nitrobenzofurazan -3-amino-D-alanine) and SADA (7-nitro-2,1,3-benzothiadiazole-3-amino-D-alanine), respectively.

Herein, the initial work was carried out with the incorporation of three kinds of FDAA. FDAA was incubated with exponential-phase *S. aureus* WT cells in medium for just 5 minutes, avoiding excessive generations, which revealed structural insights using optical microscopy (Figure 3.2).

Based on the known PG biosynthetic mechanism, the FDAAs should be only incorporated into new synthesised PG, and the fluorescence signal will appear at the septal plane of cells. As shown in Figure 3.2 A, HADA treated cells grew in the expected pattern and exhibited strong septal labelling of entire cell population. However, some cells were also labelled at the peripheral cell wall. Recently cell wall biosynthesis in *S. aureus* has been shown to also occur at the cell periphery.[115,116] 7-Hydroxycoumarin-3-carboxylic acid is attached to D-amino acids via a relatedly weak peptide bond, which may be cleaved by enzymes, surrounding bioactive molecules and other metabolites, especially in a physiological environment. Therefore, the possibility that incorporated HADA was hydrolysed and resulted in unwanted or non-specific labelling of cell wall cannot be ruled out. To further verify this presumption, NADA and SADA, in which fluorophores and the D-amino acid are linked via a relatively stronger covalent bond, were incubated with whole cells using the same conditions of HADA labelling. Similar to labelling results with HADA; septa of the cells showed strong labelling while peripheral sections displayed a weaker fluorescence. The results support the hypothesis that preferential incorporation of D-amino acids are at the septal plane of division and that off septal biosynthesis occurs.

3.2.1.2 Vancomycin binding to the peptide chain of PG

3.2.1.2.1 Mechanism of vancomycin action

Vancomycin, the archetypal member of the glycopeptide antibiotic class, was discovered in the 1950s, isolated from a *Streptomyces* species found in soils in the USA, and is considered as the first of a series of chemically related antibiotics.[117] Over the years, it has been one of the most widely used and studied antibiotics.[118] Unlike most beta-lactam antibiotics such as methicillin that function by directly binding to and inactivating the bacterial transpeptidases, vancomycin inhibits cell wall synthesis at an earlier stage by binding to the C-terminal D-alanyl-D-alanine terminal dipeptides of PG precursors, not the enzyme (Figure 3.3).[119,120] This binding reaction therefore prevents the pentapeptide from being used for cell wall synthesis.

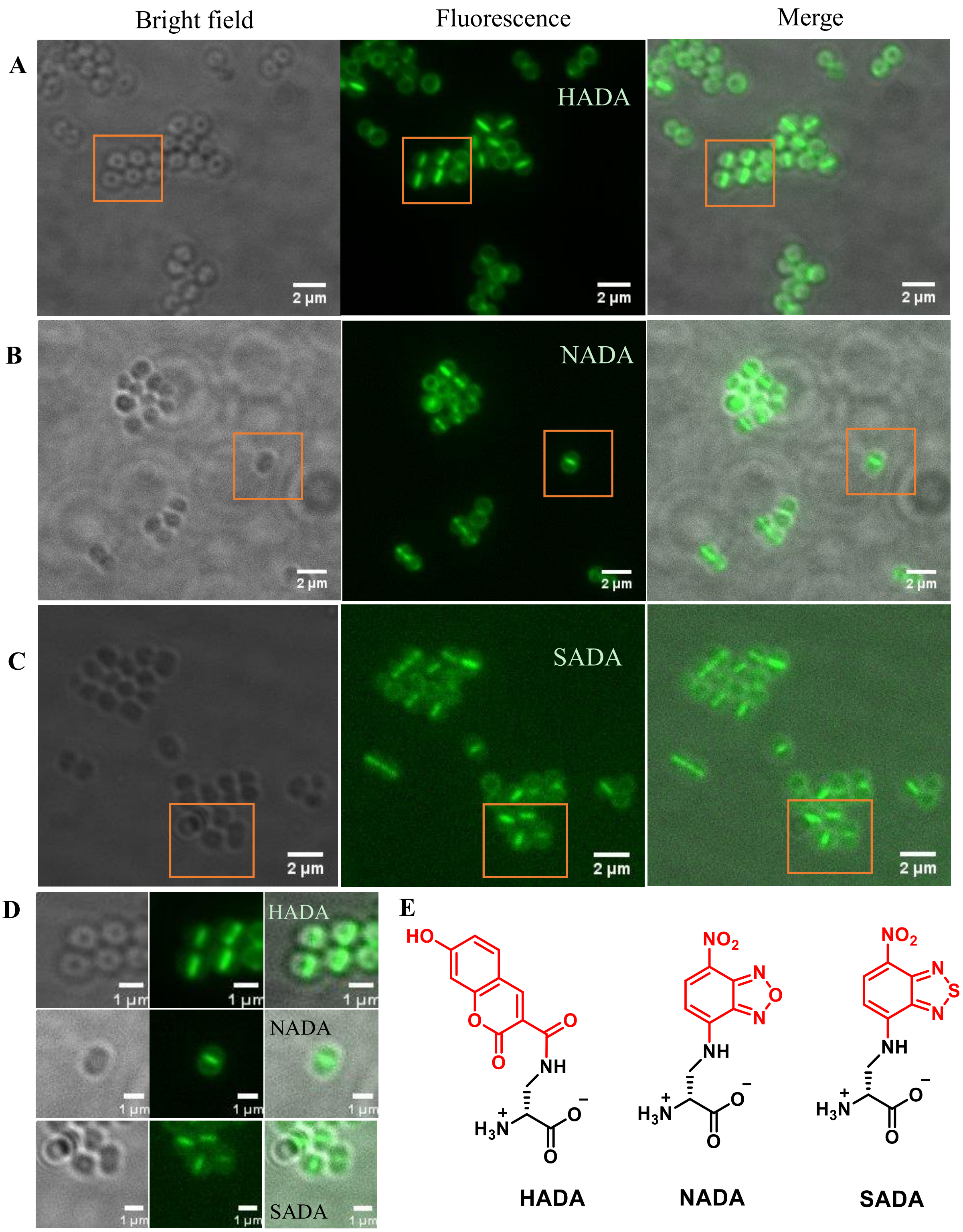

Figure 3.2 Fluorescent D-amino acid derivatives labelling of *S. aureus* cells. Exponential-phase live cells were treated with HADA **(A)**, NADA **(B)** and SADA **(C)**, respectively. **(D)** Enlarged images from the boxes were provided for better visualization of labelling pattern. **(E)** Chemical structures of FDAAs.

While vancomycin is clinically used for the treatment of a number of bacterial infections, extensive pharmacokinetic studies and biological mechanism analyses using this molecule are now widespread, including as a probe for super-resolution microscopy.[120] Due to highly specific vancomycin-binding mechanism, fluorescent derivatives have been developed that can specifically incorporate into nascent PG and, therefore, be used as a highly sensitive molecular probes to image PG.[37]

3.2.1.2.2 Preparing fluorescent derivative of vancomycin for *S. aureus* cells labelling

As shown in Figure 3.4A, there are two amines present in vancomycin (marked in red) that can be used as labelling sites for the incorporation of a functional group. The amine located on the disaccharide is relatively more reactive, and, more importantly, has no relevance to recognition between vancomycin and PG precursors.[121] On the basis of these findings, BODIPY (abbreviation for boron-dipyrromethene difluoride) and Alexa Fluor 647, were linked to this amine to generate fluorescent conjugates of vancomycin (VanF) with different excitation for PG multicolour imaging (See Chapter 2.9.1).

Initially, wild-type *S. aureus* was grown to exponential phase and labelled with a 1:1 mix of vancomycin: VanF for 5 minutes, then fixed with paraformaldehyde (PFA) and imaged by fluorescence microscopy (Figure 3.4). A range of fluorescent staining was observed, the most prominent labels were localised around the septum. However, at the same time, some cells were found with whole cell-wall labelling and a tiny minority with entire intracellular staining.

Intracellular staining suggests that the fluorescent label entered the cell, questioning cell wall integrity. It was envisaged that the cell fixing procedure was a prominent factor that might influence cell integrity and thus label penetration, considering the well-established successful usage of vancomycin.[37,122] In order to verify this hypothesis, three labelling strategies, termed as post-, no- and pre-fix, were established on the basis of the variation of fixing patterns (Scheme 3.1). According to the labelling strategies, test experiments were carried out with vancomycin-BODIPY in *S. aureus* cells. Figure 3.5 showed that in all cases, abundant labelling of cell wall occurred and the labelling phenotypes were similar to the previous work, which suggested that fixing methodologies have no effect on VanF labelling. Typically, probes were widely localized the entire cell surface but predominantly at the septum.

The labelling pattern with VanF can be followed through the cell cycle showing the characteristic septum formation, followed by a scission event resulting in an X- or Y-like conformation (Figure 3.6). The X-like conformation indicated the splitting was simultaneously initiated as a ring around the cell plane while the Y-like conformation suggested cell separation predominated from one side. Also, a faint band was sometimes found perpendicular to the bright septum which suggested the next orthogonal division plane had commenced. This observation was consistent with the previous findings.[25,123]

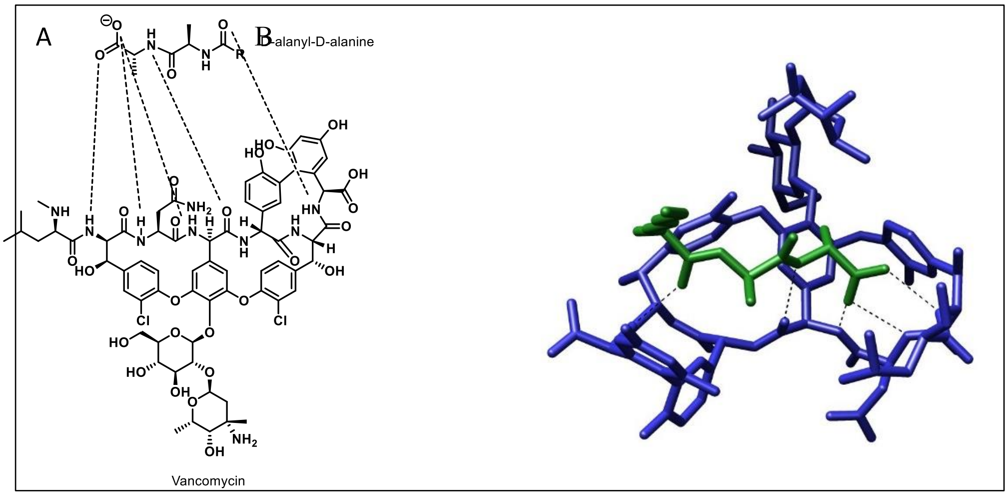

Figure 3.3 Mechanism of vancomycin action. (A) A non-covalent link between vancomycin and D-alanyl-D-alanine is through a network of five hydrogen bonds. **(B)** 3D structure (GNU Free Documentation License).

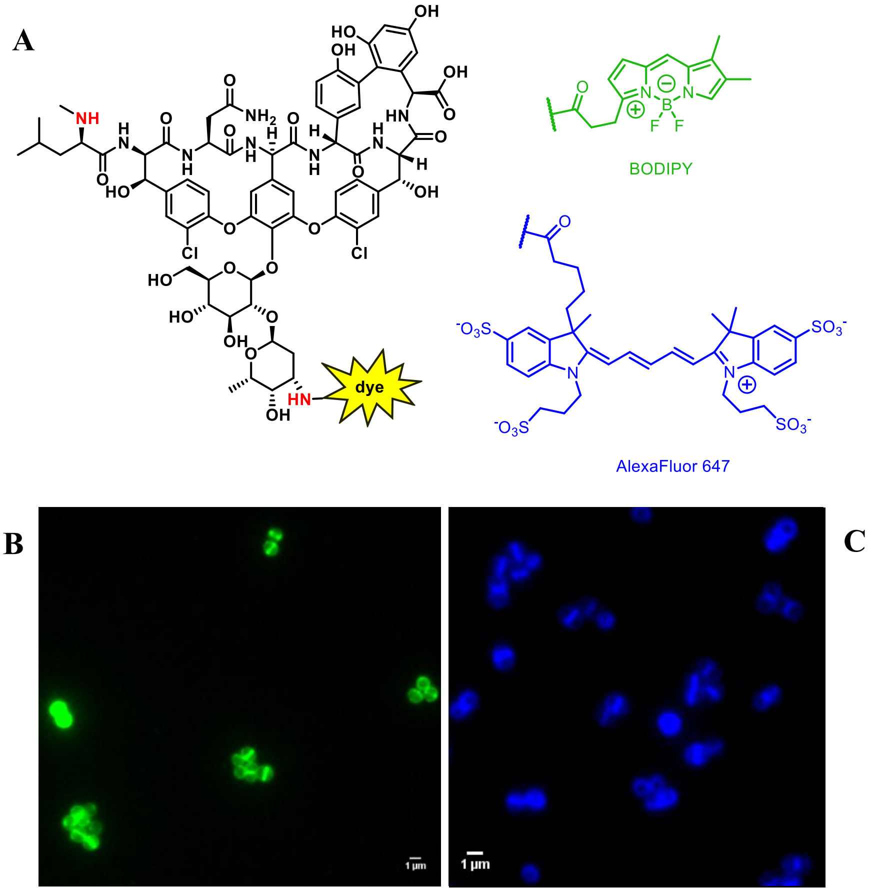

Figure 3.4 Fluorescent derivatives of vancomycin for *S. aureus* cell labelling. (A) Structures of derivatives and the position of derivatization. **(B-C)** cells were labelled with vancomycin-BODIPY (**B**) or -Alexa Fluor 647 (**C**), and fixed with PFA.

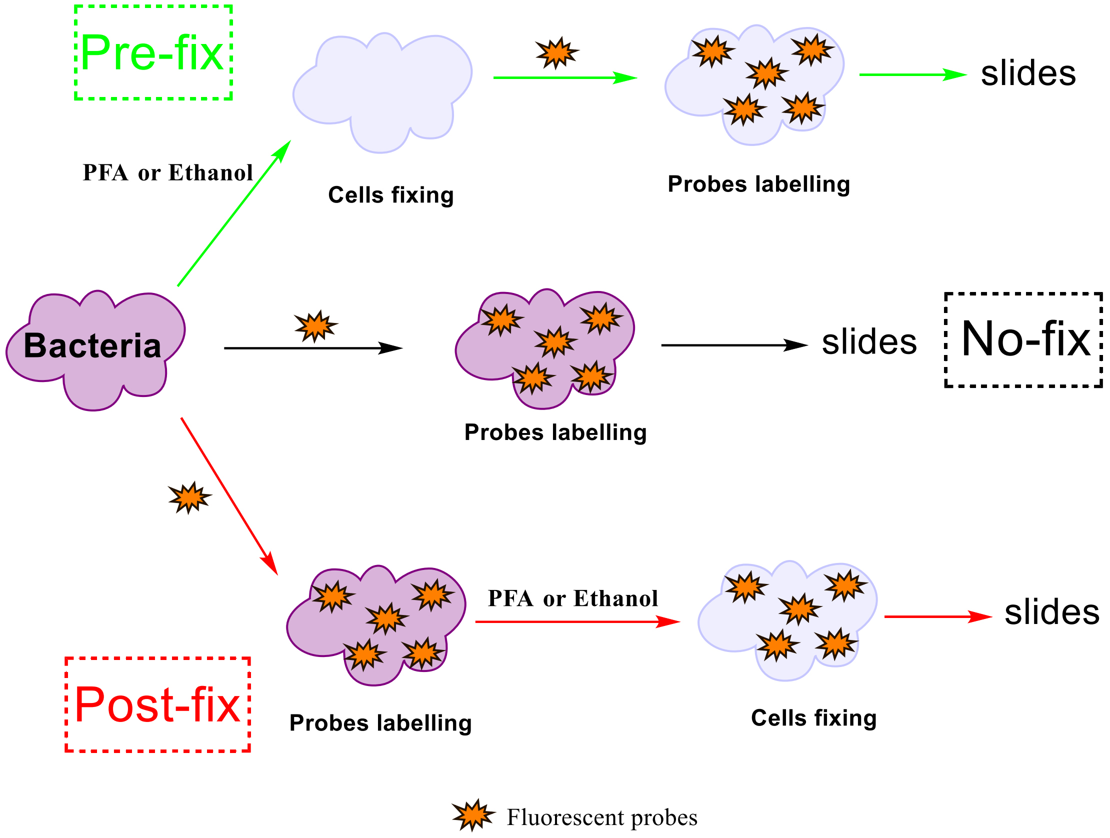

Scheme 3.1 Fixing strategies employed for cell labelling. Three possible labelling routes, termed post- (Red), pre- (Green) or no-fixing (Black), were used on the basis of the variation of conducting cell fixation. Pre-fixing: cells were fixed with PFA or ethanol, and labelled with probes; Post-fixing: cells were fixed after labelling with probes; No-fixing: labelled cells were directly imaged without fixing.

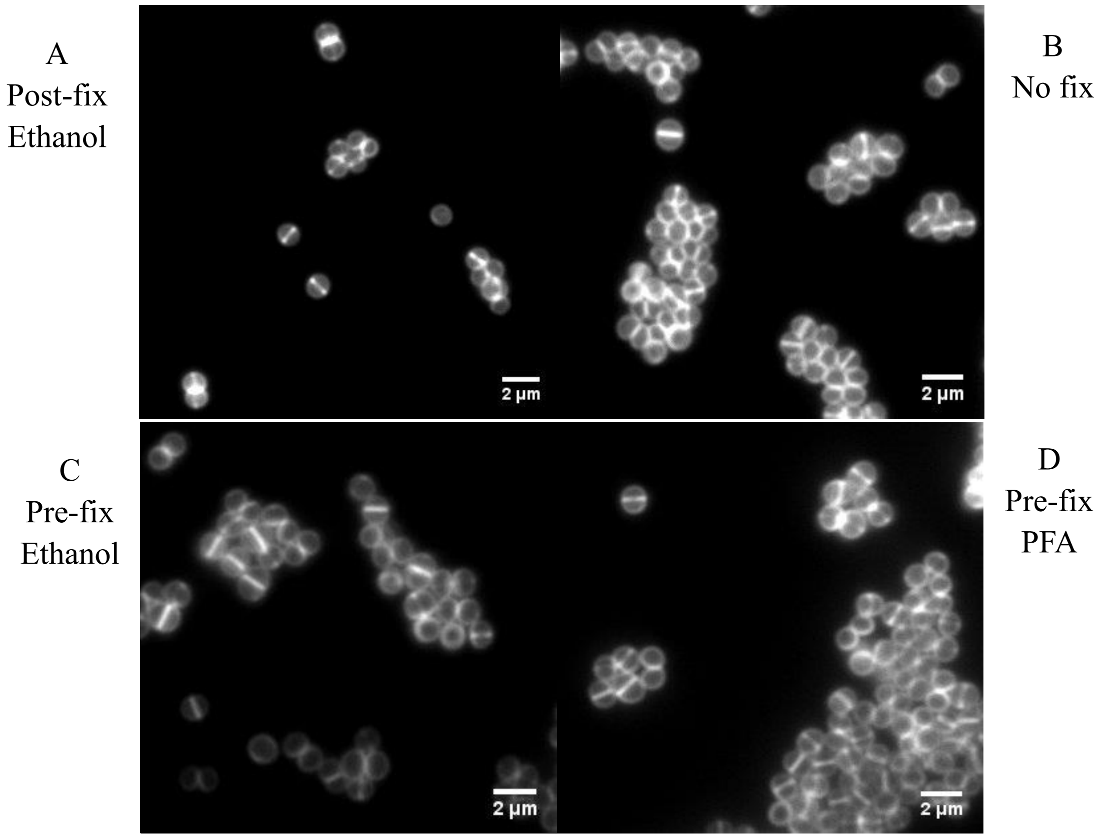

Figure 3.5 Vancomycin-BODIPY labelling of *S. aureus* cells using different fixing strategies. (A) Cells were labelled with VanF and then fixed with ethanol. **(B)** VanF-labelled cells were directly visualized without fixing. **(C-D)** Cells were pre-fixed with ethanol **(C)** or PFA **(D)** before labelling with VanF.

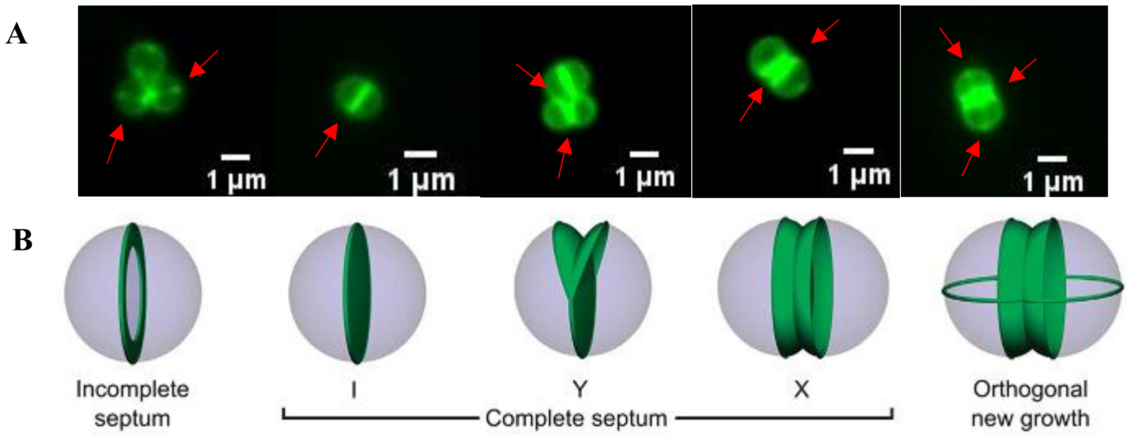

Figure 3.6 PG dynamics during cells separation in *S. aureus*. (A) Visualization of VanF-labelled cells at different stages. Red arrows: differential key targeting sites. **(B)** Schematic of cell wall synthesis and cell separation; Ref 37 with permission from Nature Publishing Group.[37]

3.2.2 Targeting glycan reducing termini of PG to analyse cell wall dynamics

The basic structure of PG consists of linear chains of glycans and side chains of peptides. Apart from imaging peptides as previously described, glycan is also an attractive target for studying dynamics of PG, which is a complex biological molecule surrounding the cell surface and plays an extremely important role in numerous physiological and pathological processes.[124]

As stated above, fluorescence imaging has been a powerful tool to decipher biological contexts using a variety of fluorescent probes. Whilst glycan is non-fluorescent by nature, well-designed fluorophores can be incorporated to allow the application of fluorescence imaging in cell wall analyses. Fluorophores, are a family of compounds that enable fluorescence emission upon excitation with special light source, which provide an elegant strategy to visualize cellular target structures. In this work, glycan labelling was targeted directly by chemoselective covalent ligation of fluorophores and the aldehyde functional groups at the reducing end of the polysaccharide in PG. The ligation of a ketone or aldehyde group with a hydrazide, hydroxylamine or amino thiol has found wide applications in biomolecule conjugation, protein modification and labelling of bacterial or mammalian cell surfaces (Figure 3.7).[125] For example, Paulson's group employed periodate to oxide cell-surface sialic acids on living animal cells, forming multi aldehyde handles for reaction with an aminooxy-biotin or dye tag by aniline-catalyzed oxime ligation.[126] Bindman and van der Donk readily introduced N-terminal ketones into various lanthipeptides followed by site-specific reaction with an aminooxy-derivatized fluorophore. The resulting fluorescent lantibiotics successfully demonstrated cellular localization within *Bacillus. subtilis*.[127]

Among these reactions, thiazolidine ligation is particularly useful in chemical synthesis of proteins that bear abundant cysteine residues, e.g., ligating two large peptides, but only few examples have been reported for live cell wall labelling or intracellular application due to the need for acidic reaction conditions and heavy metal catalysis.[128]

By contrast, imine-based reactions (oxime or hydrazone) have become an essential tool for development of *in situ* labelling in living organisms. In particular, oxime ligation has received much attention because it can be efficiently and chemoselectivly performed in aqueous conditions in a mild acidic environment and only release water as the side product. Moreover, compared to hydrazones and other imines, oximes are more resistant to hydrolysis due to the α-effect and resistance to protonation.[129] This extra stability is one of the key factors influencing labelling efficiency. Therefore, the idea presented herein is to label reducing terminus of PG through the oxime ligation formed by aminooxy functionalised fluorophores, e.g., Alexa Fluor 488 hydroxylamine (HAF488), with aldehyde groups (Scheme 3.2).

3.2.2.1 Optimization of HAF488 labelling methods

Initially, exponential-phase cells were fixed with PFA, then treated with HAF488 in 0.1 M sodium carbonate (pH 8.3) buffer giving a final concentration of 100 μg/mL. After incubation at room temperature for 1 h in the dark, the pellets were harvested and then prepared for analysis. It has been reported that oxime ligation is favoured under acidic solution but proceeds poorly or incompletely at neutral pH or at sub-millimolar concentrations.[130] However, aniline can work as a nucleophilic catalyst to dramatically accelerate the reaction.[131] Thus, addition of aniline during incubation with HAF488 was performed to observe if there was an impact on the efficiency of HAF488 labelling (Figure 3.8). It was found a large percentage of cells were stained entirely and the fluorescence was mainly distributed in the cytoplasm (Figure 3.8A). Meanwhile, as the red arrows show, a small number of cells were only labelled at the whole cell wall rather than cytoplasm, although showing much less fluorescence intensity than intracellular staining. Weak fluorescence was observed at the septa, which was almost overwhelmed by the strongly fluorescent intracellular staining (Figure 3.8A yellow arrows). In contrast, in the presence of aniline, a higher proportion of cells possessed intracellular staining and very faint labelling of cell wall and septa was observed (Figure 3.8B). This fact suggested that there was no need to use aniline as previously reported.

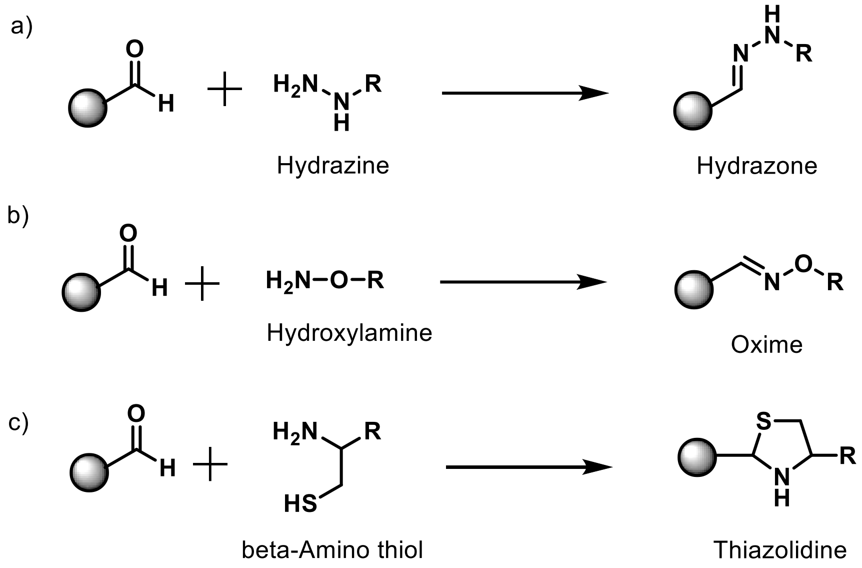

Figure 3.7 Emerging chemical methods for aldehyde ligation. Biomolecules bearing aldehyde groups can be selectively ligated to hydrazines **(A)**, hydroxylamines **(B)** or aminothiols **(C)** by formation of hydrazone, oxime or thiazolidine conjugates.

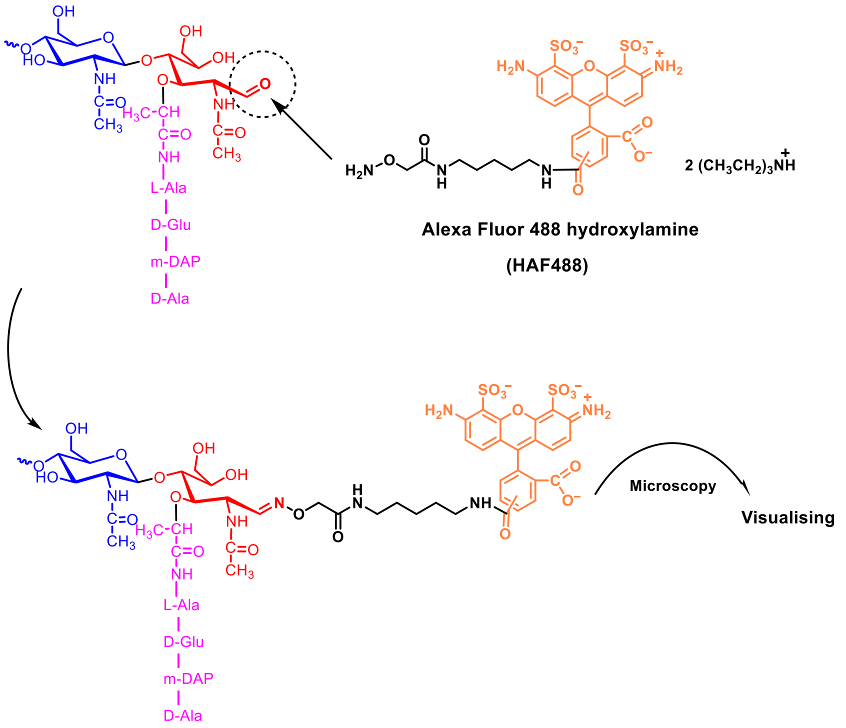

Scheme 3.2 Structure of hydroxylamine functionalised fluorophores and conceptual framework for PG labelling. The reducing termini of the cell wall were reacted with HAF488, resulting in loading dyes onto the cell surface, which allow for fluorescence imaging of the cell wall.

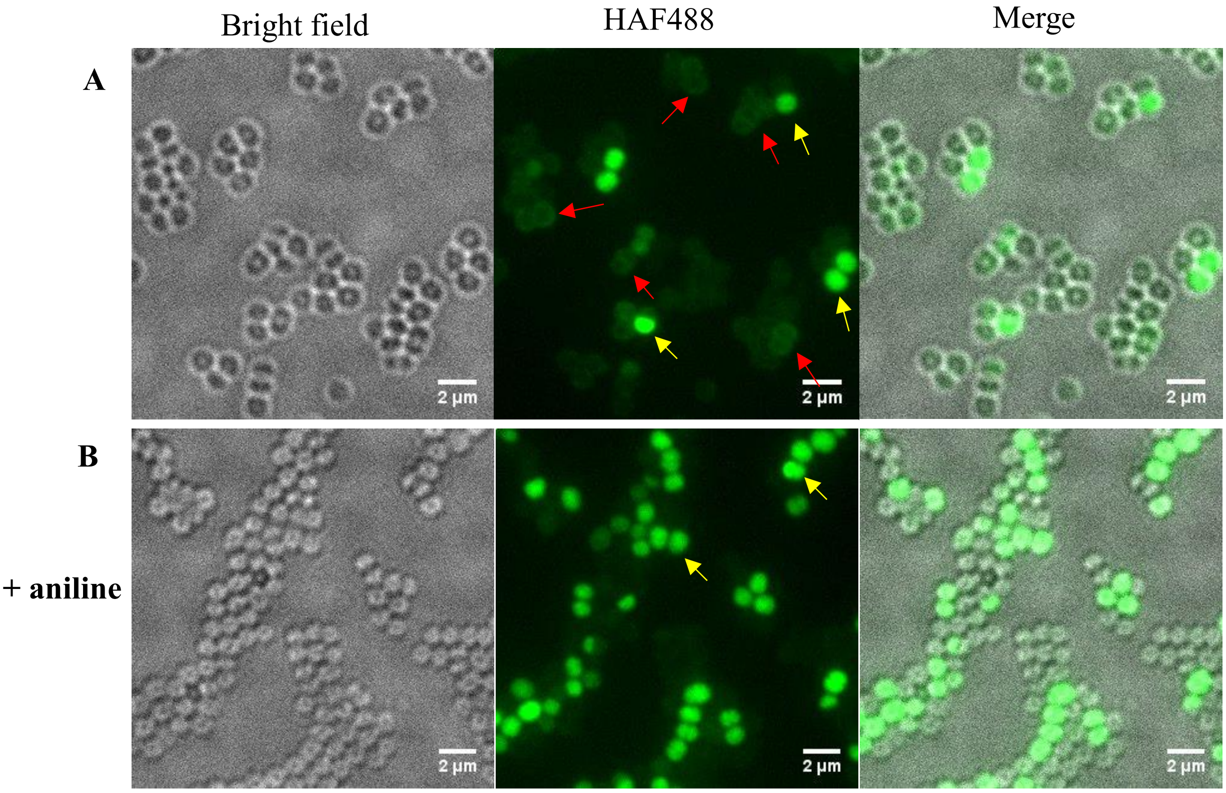

Figure 3.8 HAF488 labelling of reducing termini of PG in *S. aureus*. Cells were fixed with PFA and incubated with HAF488 without **(A)** or with aniline **(B)**. Red arrows: labelled sites; Yellow arrows: intracellular staining.

In order to check whether over-staining of cells was occurring, HAF488 solutions of different concentrations were used (final concentration of 25 or 50 µg/mL, respectively). Regardless of concentration, intracellular staining still occurred, while at low concentration the weak labelling of cell wall and septa that appeared in initial experiment was hardly observed (Figure 3.9A). A number of labelled cell walls and septa were clearly observable when using a concentration of 50 µg/mL HAF488 (Figure 3.9B red arrow), although intracellular staining still appeared and displayed brighter fluorescence (Figure 3.9B yellow arrow). The above results suggested that a HAF 488 concentration of 50 µg/mL was best and was chosen for further experiments. Moreover, whole cell staining occurred in all experiments, which suggested the dosage of fluorescent probes was not the main factor to impact the quality level of labelling.

3.2.2.1.1 Effect of the fixing methodology on HAF488 labelling

The fixing methodology was next taken into consideration. According to previous vancomycin labelling experiments, the similar fixing strategies were employed for HAF488 labelling (Scheme 3.3). The initial HAF488 labelling experiment (Figure 3.8 and 3.9) fixed cells using PFA, followed by incubating with HAF488 probes in 0.1 M sodium carbonate (pH 8.3) buffer which was in accordance with above mentioned “pre-fix”. However, PFA, possessing plenty of carbonyl groups, may result in unexpected cross reactions with the hydroxylamine moiety of the fluorescent probe, thereby leading to mislabelling or poor labelling. As an alternative, ethanol was used to fix cells, hopefully avoiding or reducing such unwanted reactions. Also, the basic environment used may be unsuited to oxime formation and thus the incubation buffer may be another key point. Considering cells were grown in Brain Heart Infusion medium (BHI) that is nearly neutral, it was used as an oxime-forming environment as an alternative to sodium carbonate buffer.

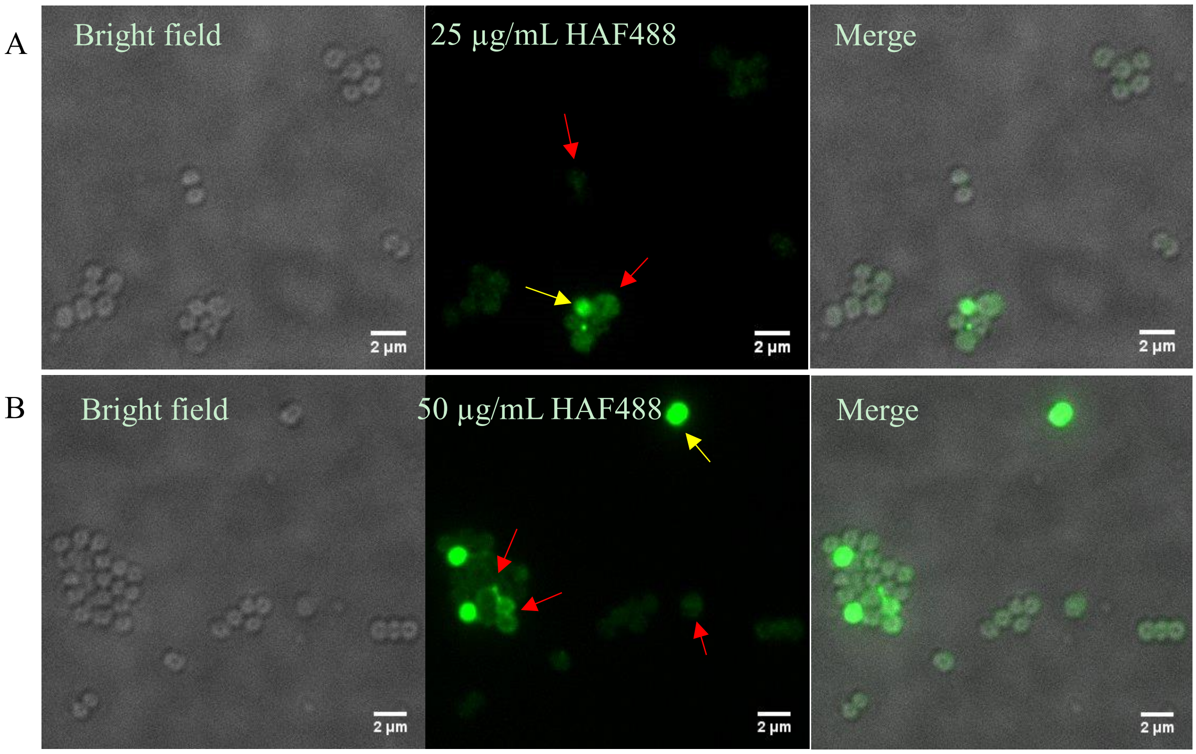

Figure 3.9 Comparison of using two different concentrations of HAF488. Fixed *S. aureus* cells were treated with HAF488 to a final concentration of 25 µg/mL **(A)** or 50 µg/mL **(B)**. Red arrows: specific labelling sites; yellow arrows: whole cell staining.

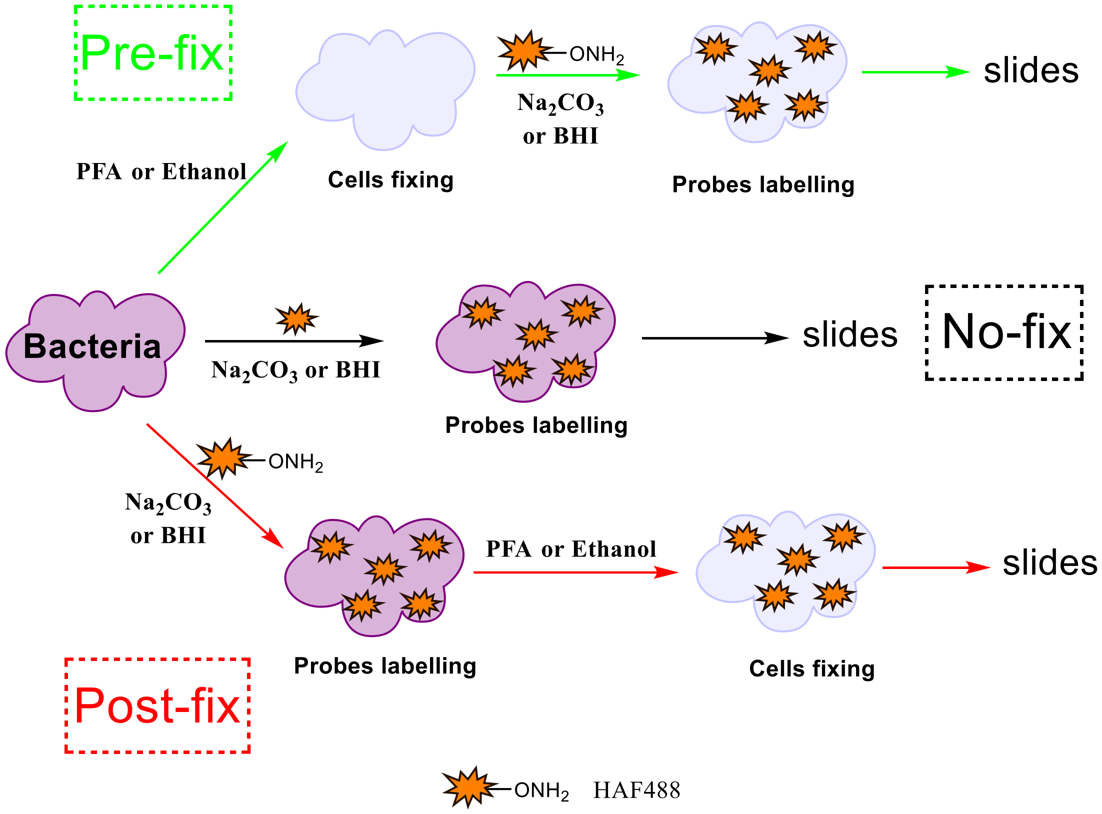

Scheme 3.3 Fixing strategies employed for HAF488 labelling. Three labelling routes, post- (Red), pre- (Green) or no-fixing (Black), were used on the basis of the variation of conducting cell fixation. Pre-fix (Green): cells were fixed with PFA or ethanol, and labelled with HAF488 in Na_2CO_3 or BHI; Post-fix (Red): cells were labelled with HAF488 before fixing; No-fix: HAF488 labelled cells were directly visualized.

Considering sodium carbonate buffer versus BHI as labelling buffer, it appeared only a faint fluorescence intensity could be observed in the cell wall whilst the cell intracellular staining increased (Figure 3.10). Conversely, cells fixed with ethanol rather than PFA exhibited weak labelling across the cell (Figure 3.10C and D). The unsatisfying results suggested the pre-fix strategy was unsuitable for HAF488 labelling.

This led to attempts to label cells without prior using fixing. Labelling without fixing ("no-fix") resulted in a reduction in intracellular staining and abundant labelling of the cell wall (Figure 3.11). Labelling in Na_2CO_3 buffer with HAF488 led to relatively uniform visualization of the entire cell wall and orientation details were lost, although some brighter "hot spots" could be observed which may mark division sites (Figure 3.11A yellow arrows). In contrast, when cells were incubated with probes in BHI, the ratio of signal to noise was enhanced and thus localization of HAF488 binding was much clearer, which exhibited predominant labelling at the division septum (Figure 3.11B red arrows).

The strategy of fixing after labelling ("post-fix") was then investigated (Figure 3.12) and the observation was consistent to the results of the 'no-fix' pattern: an abundant signal appeared at the whole cell wall but predominantly at the division septum. Although labelling in Na_2CO_3 buffer or BHI showed a similar pattern, BHI provided better contrast. Both fixing reagents worked well and the choice of fixing reagent had little effect on the quality of images. Compared with all fixing strategies, it was clearly shown that post-fix is more suitable for reducing termini labelling. Therefore, BHI and post-fix defined the most efficient solvent and labelling pattern for further optimization.

3.2.2.1.2 Optimization of labelling time

Given the inconvenience of the long labelling periods (60 min) used in the above experiments, optimization of the labelling time was investigated, in which the reaction temperature was set as 37 ºC to accelerate this process (Figure 3.13).

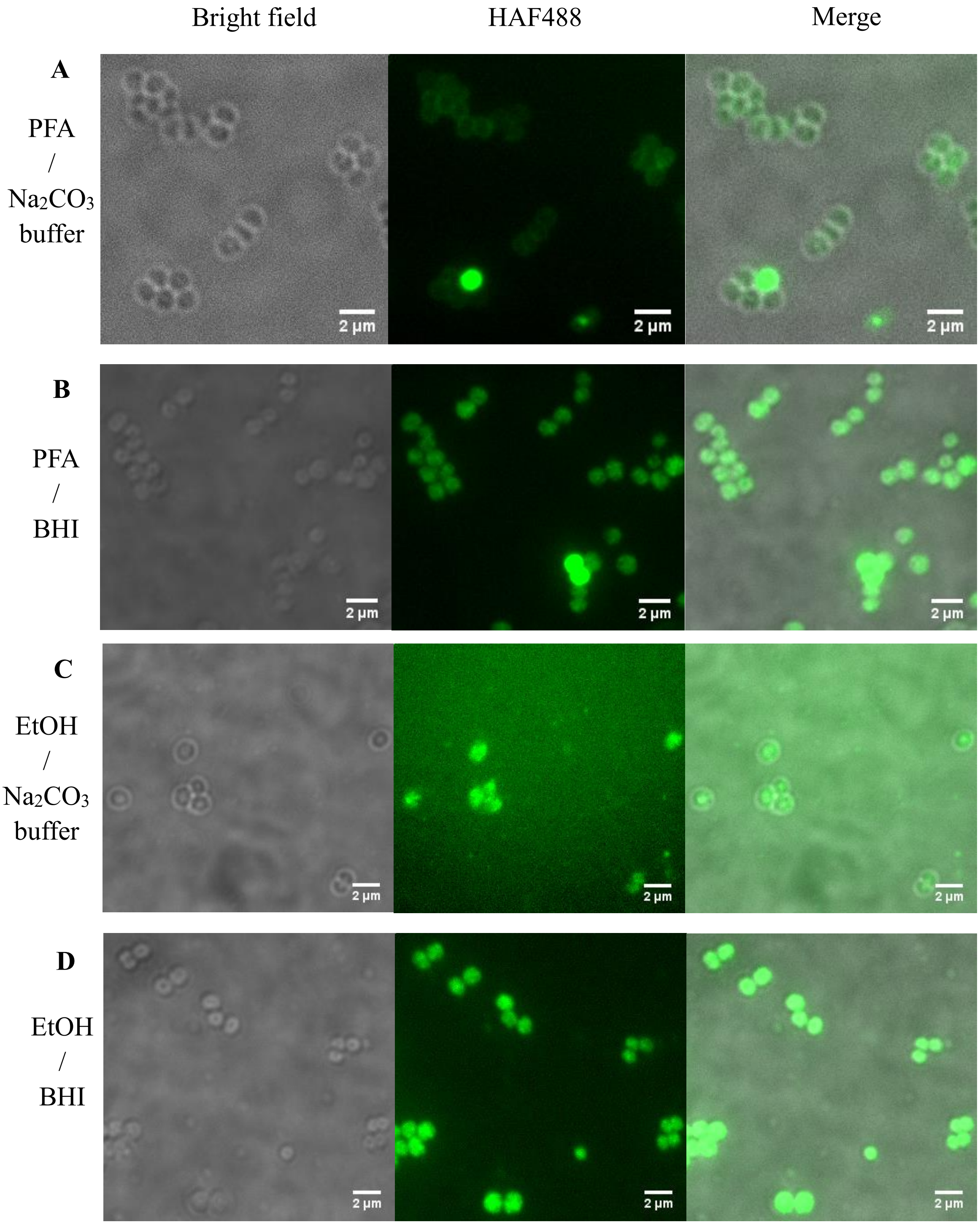

Figure 3.10 HAF488 labelling of *S. aureus* cells using the "pre-fix" strategy. Exponential-phase cells were fixed with PFA (**A** and **B**) or ethanol (**C** and **D**), and labelled with HAF488 in sodium carbonate buffer (**A** and **C**) or BHI (**B** and **D**), respectively, before microscopy observation.

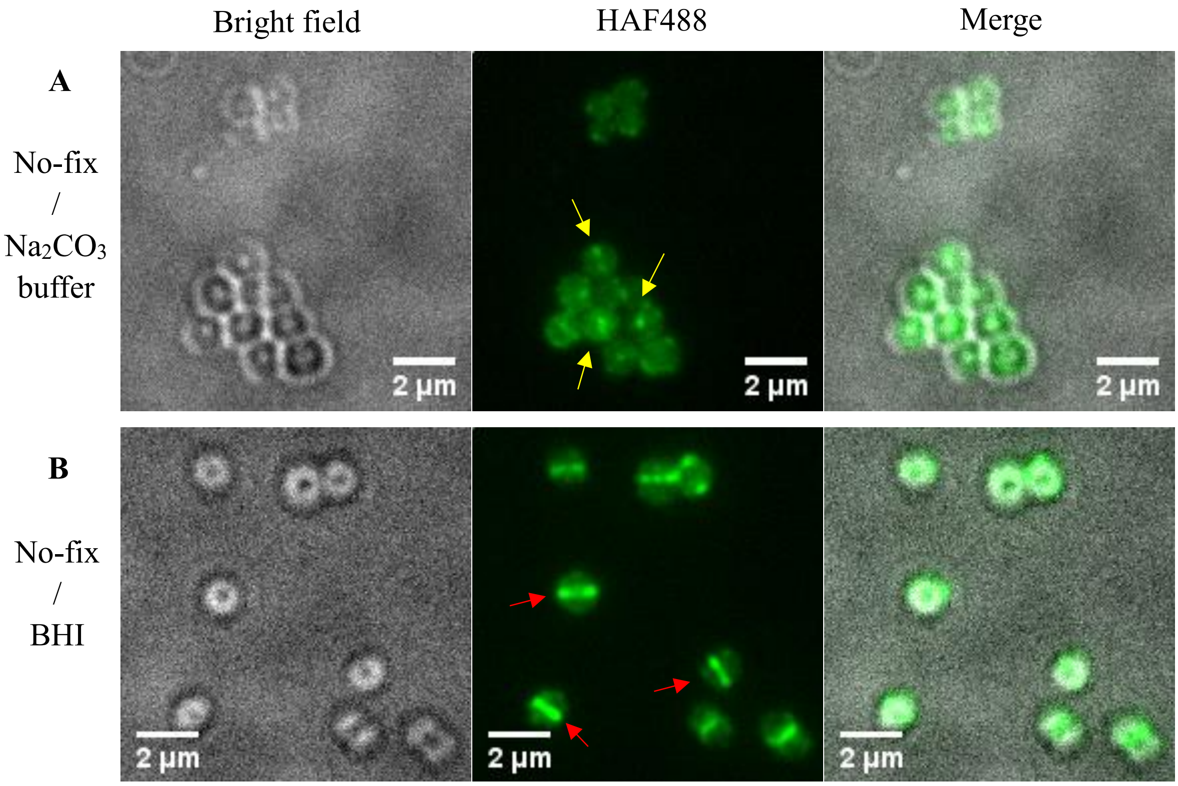

Figure 3.11 HAF488 labelling of *S. aureus* cells using the "no-fix" strategy. Freshly cultivated cells were incubated with HAF 488 in sodium carbonate buffer (**A**) or BHI (**B**), and directly used for microscopy observation after washing. Red arrows: septal labelling; yellow arrows: "hot spots".

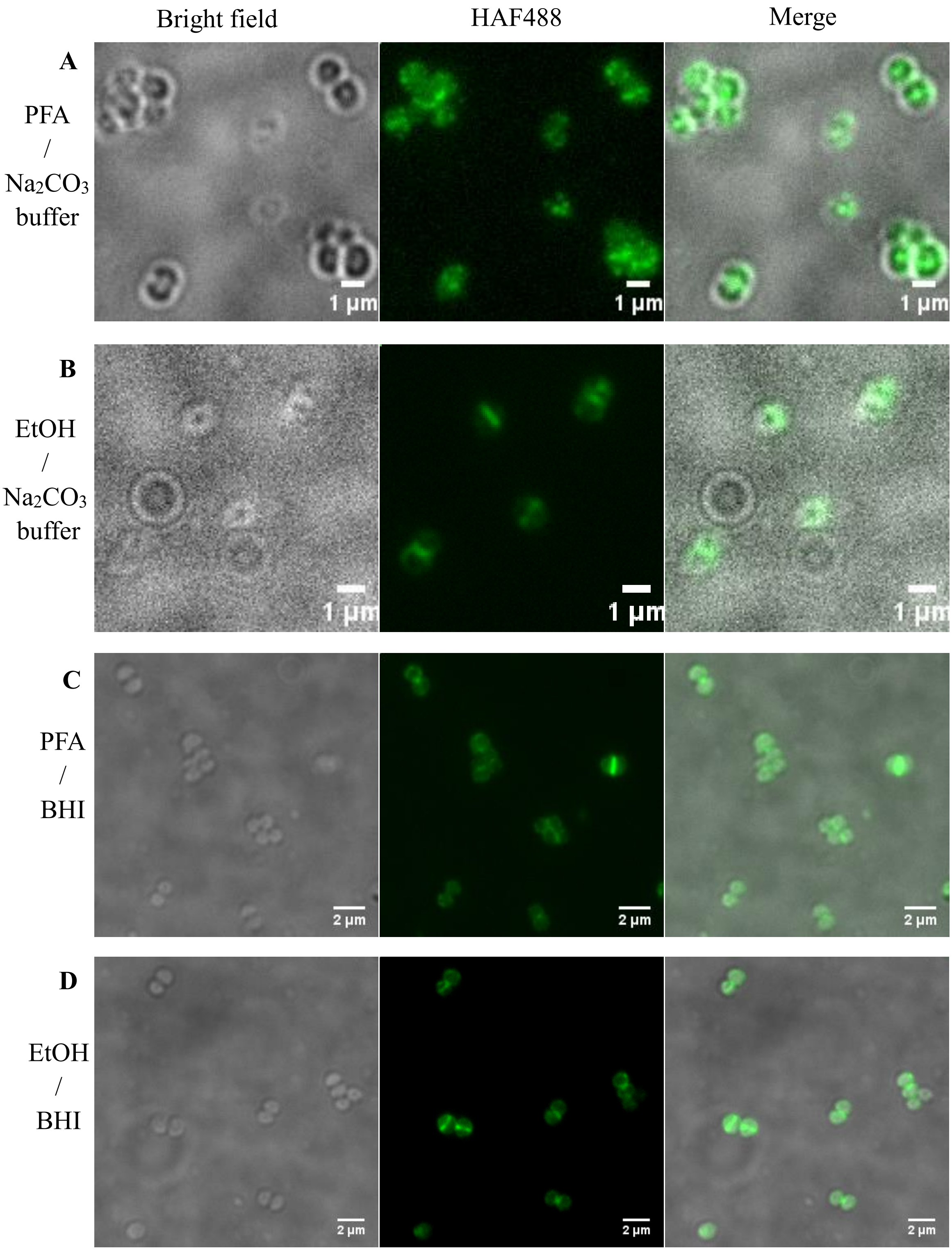

Figure 3.12 HAF488 labelling of *S. aureus* cells using the "post-fix" strategy. Cells were treated with probes in sodium carbonate buffer and fixed with PFA **(A)** or ethanol **(B)**, for microscopy observation; alternatively, cells were incubated with probes in BHI followed by fixing with PFA **(C)** or ethanol **(D)**,

Cells incubated in BHI without probes were imaged as a negative control (no dye) and those that were washed immediately after the addition of probes were used as the control of time 0. However, at time 0, a fluorescent signal still appeared at the cell wall, indicating that incorporation of the probe into PG was very fast. When monitored with respect to time, more fluorescence and strong septal labelling was observed, appearing saturated after 4 min labelling. In the case of 8, 15 and 30 min intervals, there was strong labelling but without significant difference. Therefore, 5 min was considered as the optimal reaction time.

3.2.2.1.3 Effect of the labelling buffer

It is worth noting that live cells are labelled in the growth media BHI and therefore cell will continue to grow while labelling, which makes it difficult to differentiate newly synthesised PG. To avoid this problem, it was necessary to find a new labelling buffer that ideally kept cells in physiologically relevant state and meets the requirements for oxime ligation at same time. Phosphate-buffered saline (PBS), a water-based neutral salt solution, was chosen for labelling, which is commonly used in biological research. As depicted in Figure 3.14, it can be seen that when incubated in PBS, cells were successfully labelled with HAF488 and the labelling was comparable to that in BHI, suggesting the replacement of labelling buffer has no determining effect. As a result, PBS was used as the optimized labelling buffer for further investigation.

3.2.2.1.4 Effect of reaction volume on HAF488 labelling

Although HAF488 labelling carried out, the labelling quality was incomparable to that of other probes labelling such as VanF. As a result, optimizations were continued to conduct. The effect of different reaction volumes on HAF488 labelling was determined, which was decreased from 1000 to 200 μL. It was found that a volume of 200 μL was best under all fixing methodologies (Figure 3.15). Results were consistent with the previous work carried out at a volume of 1000 μL, but gave an enhanced contrast and quality for HAF488 labelling. Therefore, the optimized labelling volume was 200 μL.

3.2.2.1.5 Effect of the probe amount on HAF488 labelling

The amount of HAF488 used for labelling in PBS was then optimized. Cells were dual labelled with HAF488 (5, 25, 50, 75 or 100 μg/mL) and VanF, and HAF488 labelling was carried out under optimized conditions, including a reaction volume of 200 μL, temperature of 37 ºC and a reaction time of 5 min (Figure 3.16). It was found that in the presence of 5 μg/mL of HAF488, the septum was successfully labelled and a faint signal appeared surrounding the peripheral cell wall. With increasing concentration of the probe, enhanced fluorescence could be observed. Using 50 μg/mL of HAF488, significant fluorescence were localised around the septum and the rest of the cell wall. In the case using 75 or 100 μg/mL of the probe, fluorescence intensity seemed no much difference, which suggested labelling efficiency reached a plateau. Therefore, 50 μg/mL was used as the optimized concentration of HAF488 for further investigations.

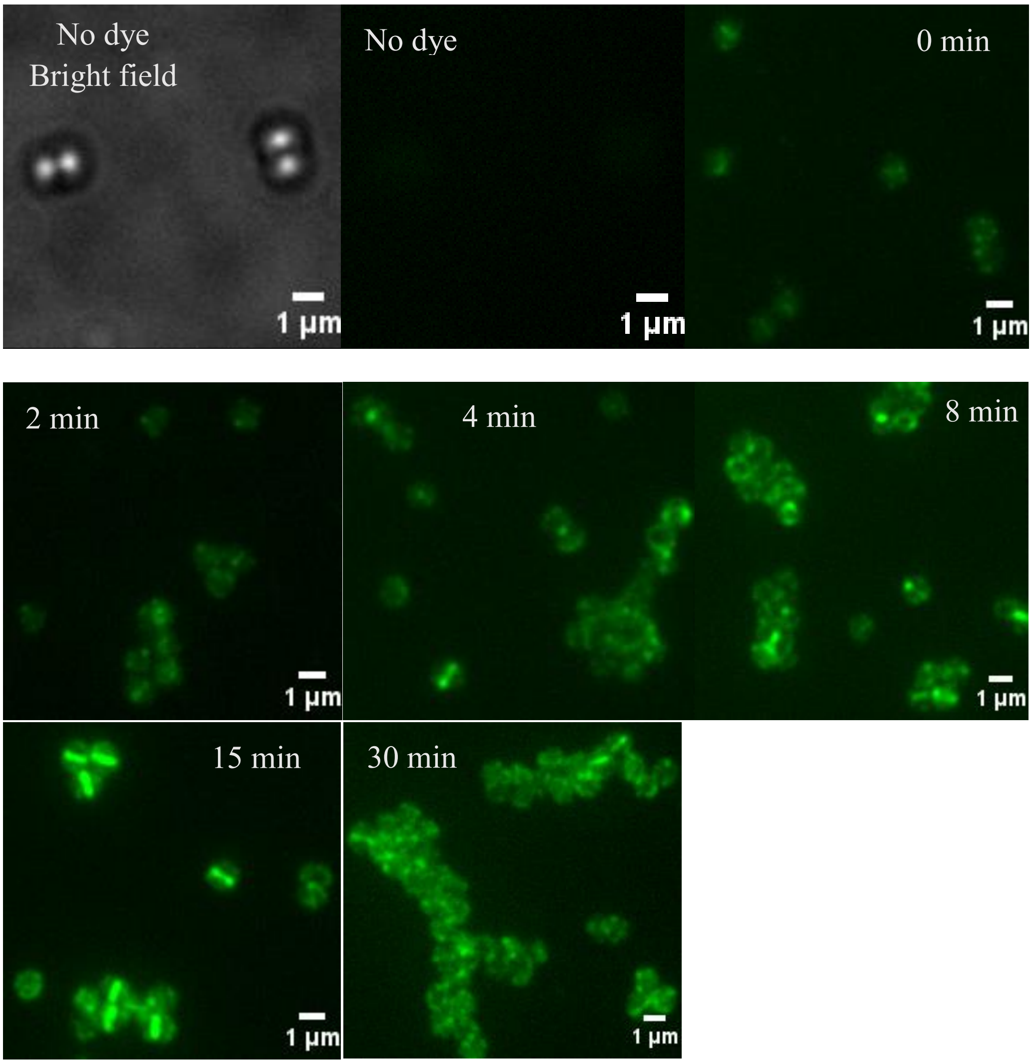

Figure 3.13 Effect of labelling time of HAF488 binding. *S. aureus* cells were incubated without the probe (no dye) and with the probe over different incubation time (0, 2, 4, 8, 15, 30 min) and then fixed with ethanol for imaging.

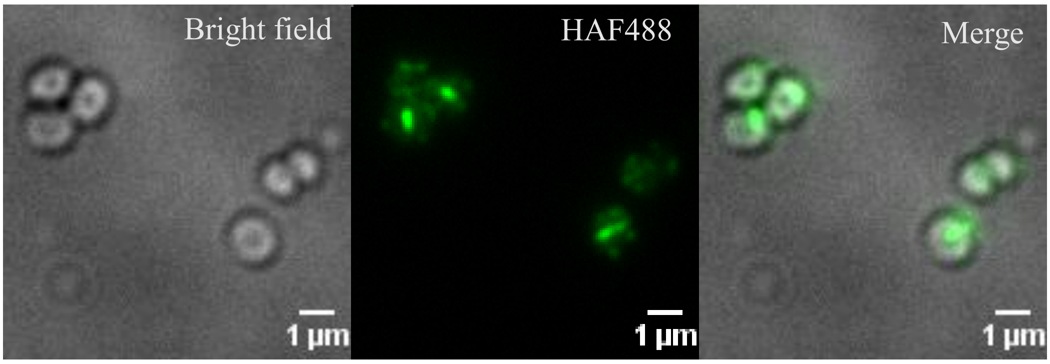

Figure 3.14 HAF488 labelling *S. aureus* in PBS. Cells were treated with HAF488 in PBS with a final volume of 1 mL at 37 ºC for 5 min and fixed with ethanol for imaging.

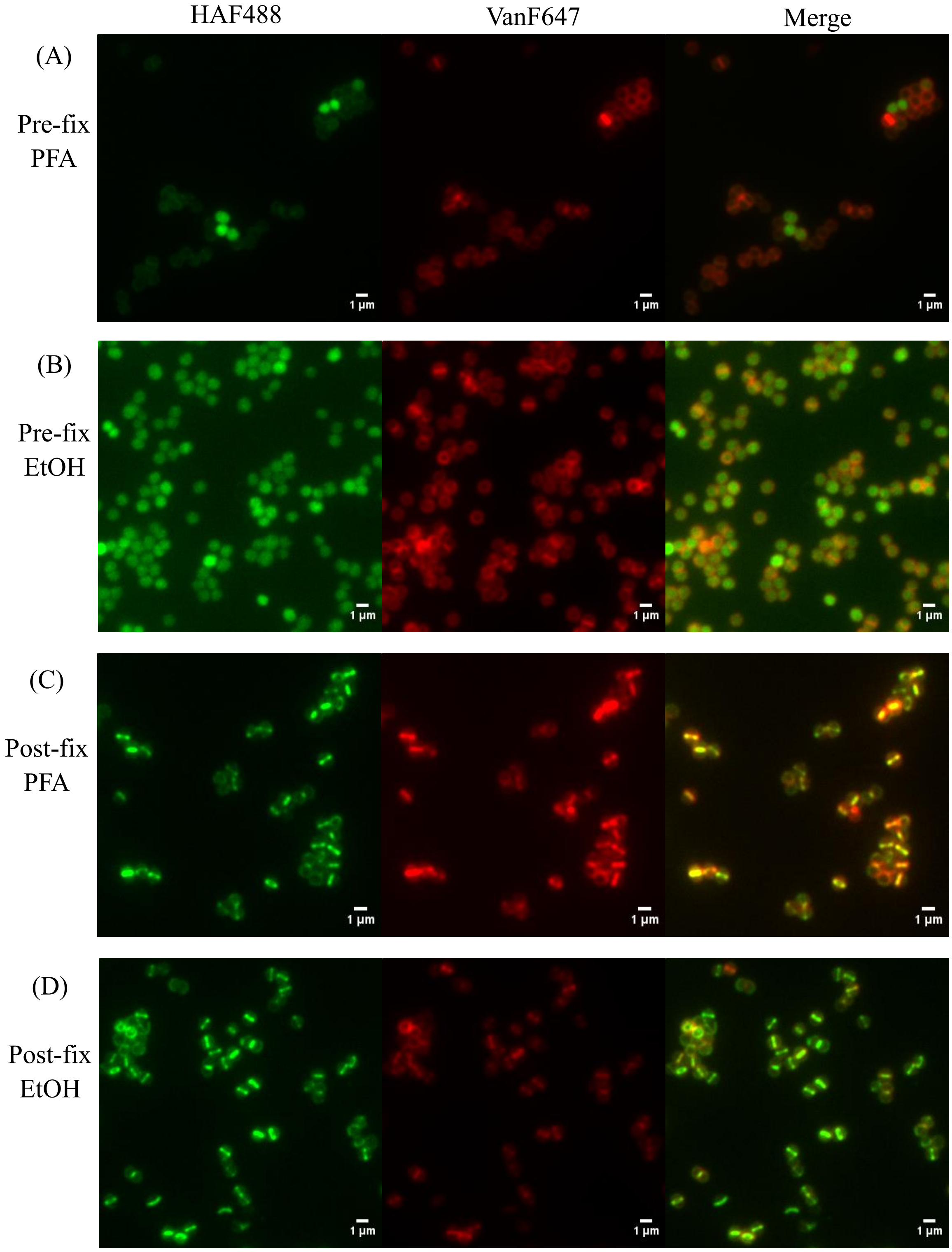

Figure 3.15 Effect of the reaction volume on HAF488 labelling. *S. aureus* cells were treated with HAF488 in PBS at a volume of 200 μL **(A and B)**; alternatively, cells were incubated with HAF488 in PBS at a volume of 200 μL, followed by post-fixed with PFA **(C)** or ethanol **(D)**. All cells were then labelled with VanF.

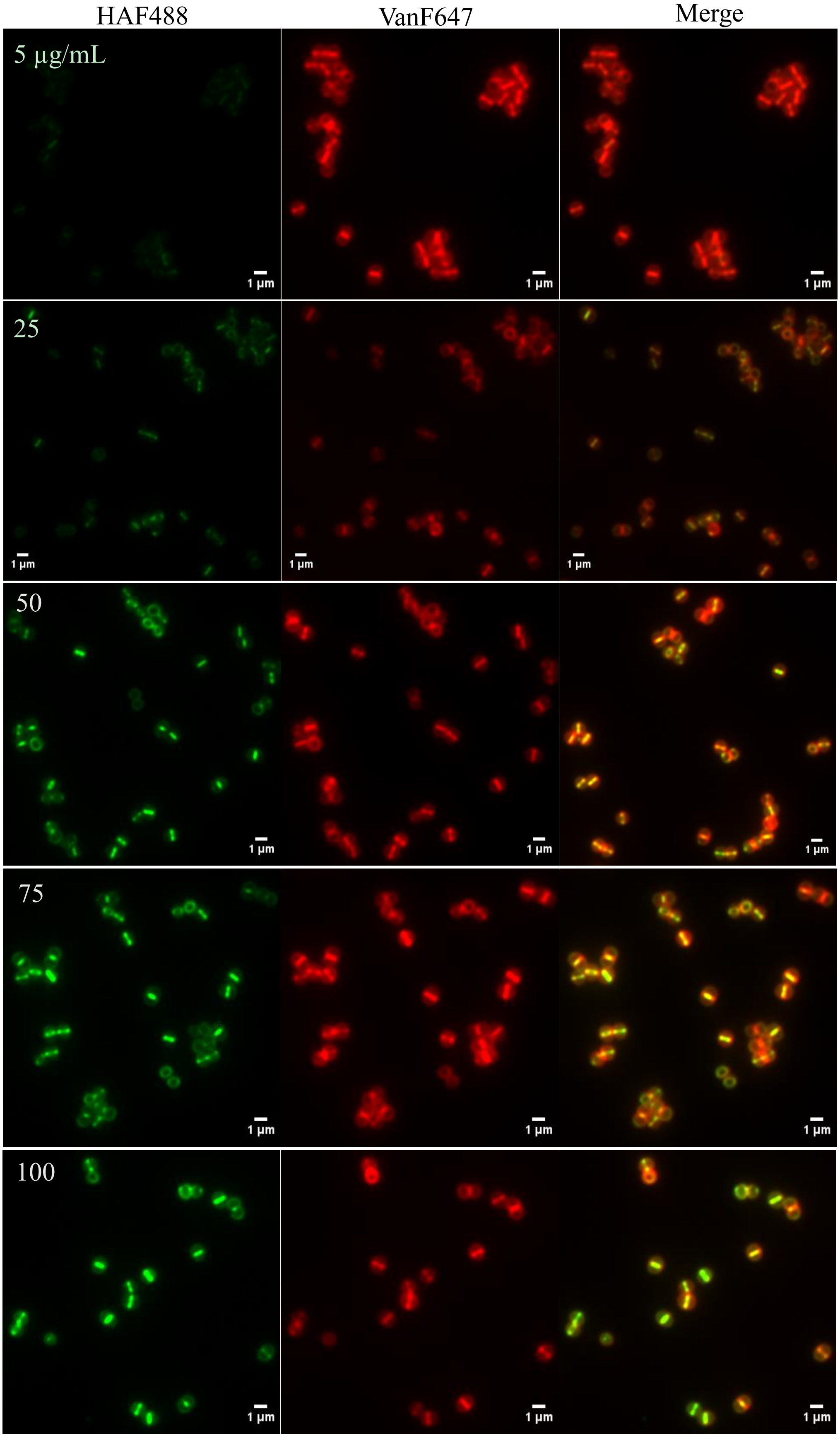
HAF488
VanF647
Merge
5 μg/mL
25
50
75
100
1 μm

Figure 3.16 Optimization of amount of HAF488 used for *S. aureus* cells labelling. Exponential-phase cells were resuspended in PBS with different amounts of HAF488 stock, producing a final volume of 200 µL (5, 25, 50, 75 or 100 µg/mL). After incubated at 37 ºC for 5 min, cells were harvested, washed and labelled with VanF, followed by fixing with ethanol for imaging. Green: HAF488; Red: VanF.

3.2.2.2 Verification of PG reducing termini labelling

3.2.2.2.1 Blocking of the reducing termini labelling using $NaBH_4$

Having developed a successful labelling system, it was important to determine whether the incorporation of probes was targeted at the reducing termini of PG. As the fluorescent probe was attached to PG by condensation with the aldehyde group in PG, the use of reagents that preferentially react with aldehydes was expected to remove these functional groups, thereby any subsequent addition of HAF 488 would not label cells (Scheme 3.4). In contrast, the target of vancomycin is the side chain of PG, so blocking the aldehyde of cell surface would have no effect on vancomycin labelling.

Initially, sodium borohydride ($NaBH_4$) was used as the blocking reagent to reduce the aldehydes to an alcohol. As expected, cells pre-treated by $NaBH_4$ were efficiently blocked and subsequent incubation of probes gave no fluorescence, suggesting the target of HAF 488 was the aldehyde from cell wall (Figure 3.17). Successful vancomycin co-labelling provided further evidence for the specificity. Compared to cells without $NaBH_4$ treatment, similar VanF labelling was observed implying $NaBH_4$ had no effect on cell integrity. This suggested that the labelling sites of HAF488 were aldehyde groups on the cell surface.

Further investigation of cell sacculi was conducted to verify whether those aldehyde groups labelled by HAF488 only belonged to cell wall PG, not other cell structures. Initially, WT sacculi were labelled following the same procedure as for live cells. It was clearly shown that sacculi were successfully labelled and fluorescence was observed as a uniform distribution surrounding the cell wall whereas VanF gave labelling across the cell wall but predominantly at the septum, similar to live cell labelling (Figure 3.18 A).

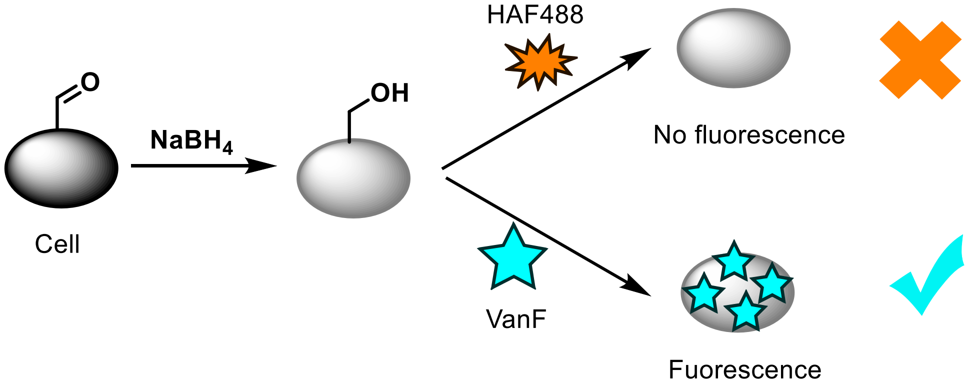

Scheme 3.4 Verification of reducing termini labelling. Via $NaBH_4$, the aldehyde group, HAF488 targeting site, will be reduced to alcohol, resulting in blocking of HAF488 binding. Conversely, $NaBH_4$ reduction had no effect on the side chain of PG, thus VanF labelling will occur as normal.

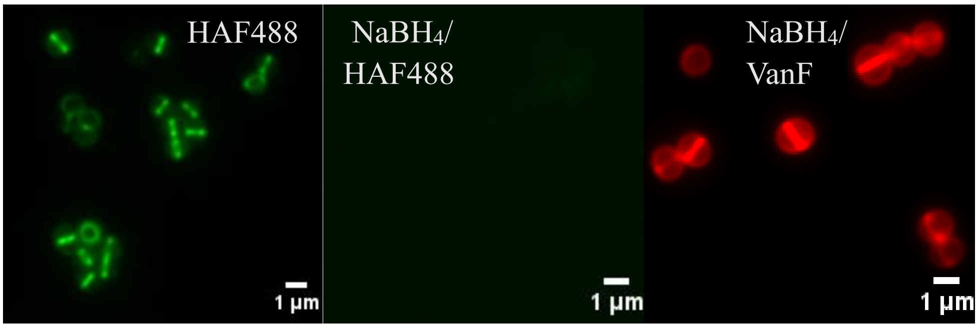

Figure 3.17 Blocking of HAF488 labelling using $NaBH_4$. Exponential-phase *S. aureus* cells were treated with freshly prepared $NaBH_4$ PBS buffer and washed with PBS at least three times, followed with labelling of HAF488 (Green) and VanF (Red).

It is worth noting that the HAF488 labelling pattern shown by sacculi was similar but not identical to that observed in live cells, and was more uniform around the cell wall. Importantly, the fluorescent intensity seemed to decrease and produce a relatively high background. The reason why the ligation efficiency decreased is not fully understood. One possibility is that live cells may give an environment conducive to oxime ligation. It was wondered that chemically whether longer reaction time helps recover high labelling quality in live cells. Strikingly, when the labelling time was increased to 16 h, a strong fluorescent signal was observed (Figure 3.18 B). Compared to the 5 min interval, this demonstrated lower background and higher quality images, suggesting sufficient oxime reaction occurred. As a control, sacculi were pre-treated with freshly prepared $NaBH_4$ PBS buffer and labelled with HAF488 and subsequently with VanF (Figure 3.18 C). The results clearly indicated that reduction of aldehyde groups in the cell wall resulted in no or faint HAF488 labelling whereas side chain of PG by VanF occurred unaffectedly. The results presented here experimentally supported the conclusion that HAF488 specifically labels the reducing terminus of cell wall PG.

All the above findings indicated that $NaBH_4$ is an excellent blocking reagent for reducing termini of PG and looks promising for further cell research as there is hardly any change in cell morphology. However, a fatal weakness is that $NaBH_4$ treatment can kill bacteria, meaning that continuous cell division and new PG incorporation studies are impossible using this method. A growth curve assay verified the growth limitation by $NaBH_4$ (Figure 3.19). To maximise the effect of blocking the reducing termini, $NaBH_4$ not only needs to be freshly prepared, but also repeated several times. Untreated cells were compared with those with 1-3 $NaBH_4$ treatments, and it was observed that all $NaBH_4$-treated cells had died. Therefore, it was necessary to find a new blocking reagent that did not disrupt the growth and division of cells.

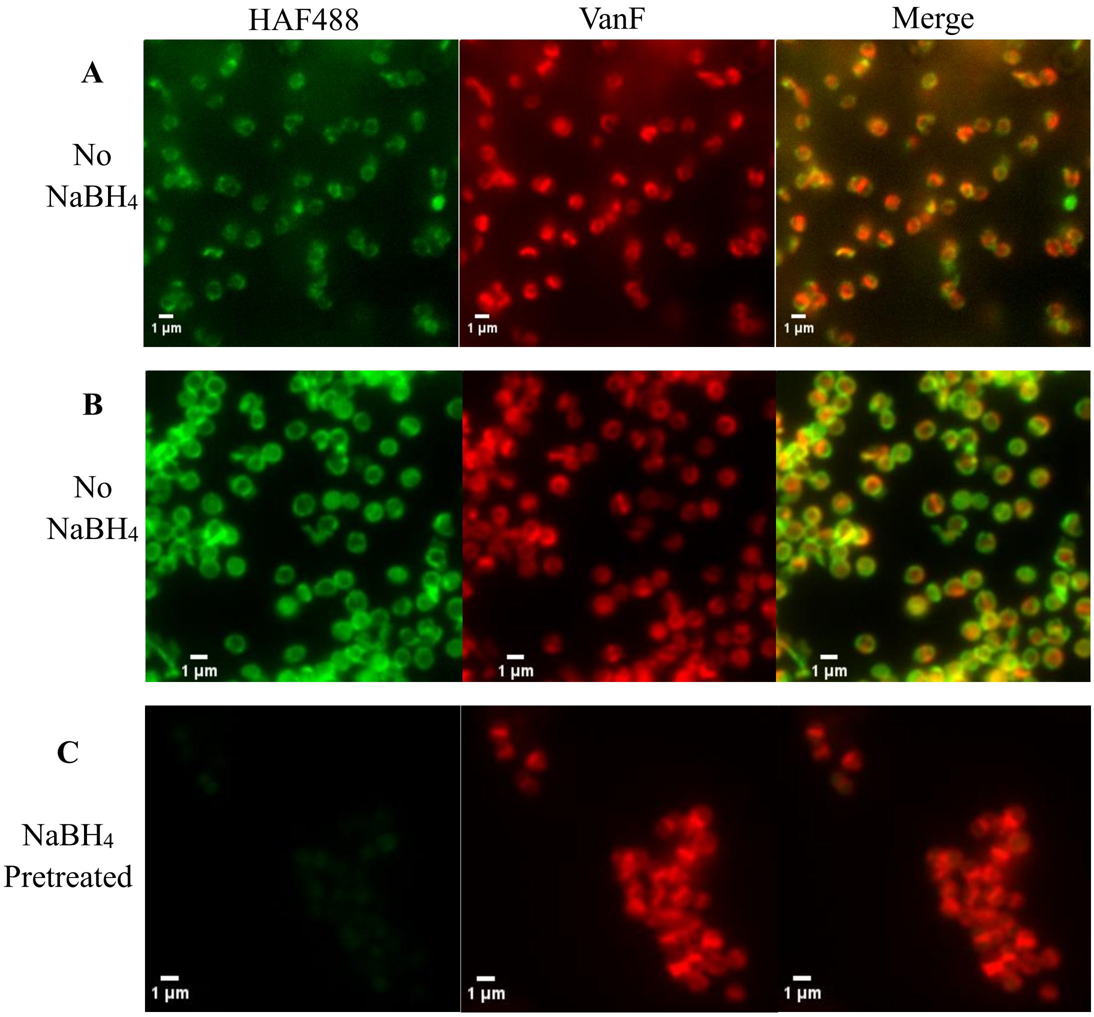

Figure 3.18 Dual labelling of blocked or unblocked *S. aureus* sacculi. Cell sacculi were incubated with HAF488 for 5 min (**A**) or 16 h (**B**), and then labelled with VanF; **(C)** Sacculi were treated with $NaBH_4$, followed by dual labelling with HAF488 (Green) and VanF (Red).

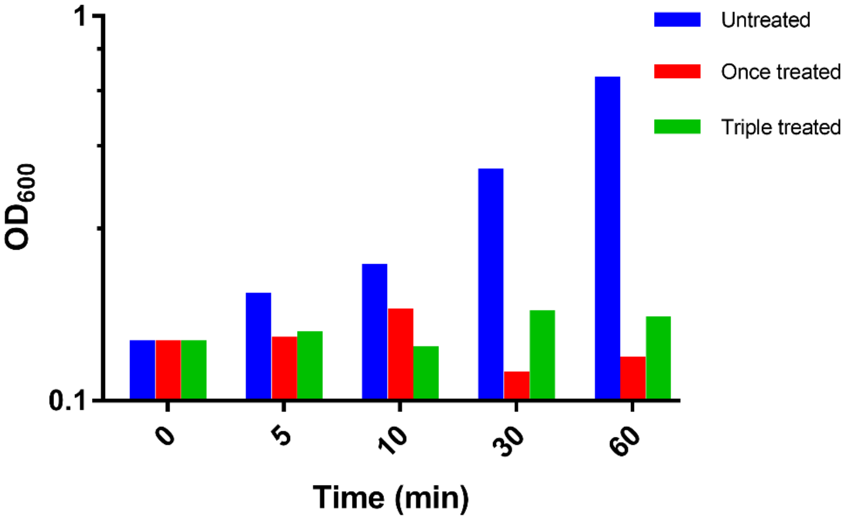

Figure 3.19 Growth of $NaBH_4$ treated and untreated *S. aureus* cells. Exponential-phase cells, with or without $NaBH_4$ pre-treating, were grown in TSB and the OD_{600} was monitored over 60 min.

3.2.2.2.2 Blocking of the reducing termini using hydroxylamine or its HCl salt

Similar to the labelling procedure of HAF488, hydroxylamine hydrochloride was used as a blocking reagent due to it containing the same functional group ($-ONH_2$) as found in probes. It was clearly shown that although HAF488 signal seemed to be slightly decreased compared to untreated cells, both HAF488 and VanF were successfully labelled, which suggested hydroxylamine hydrochloride did not significantly affect HAF488 labelling even at 200 μg/mL (Figure 3.20).

Hydroxylamine was used as an alternative blocking reagent to test HAF488 labelling (Figure 3.21). It was clearly observed that no fluorescent signal appeared after treatment with NH_2OH, followed by HAF488 labelling. Encouraged by the above results, the use of NH_2OH stock solution (50% w/v in H_2O) was optimised by exploring the dual labelling method on the basis of HAF488 and VanF (Figure 3.22). Compared with untreated cell labelling, the use of 0.055 mg/mL of NH_2OH resulted in a decrease of fluorescence of HAF488, although clear septum and surrounding cell wall labelling occurred. With increasing quantities of NH_2OH, the fluorescence of HAF488 decreased, and septum labelling nearly disappeared when using 27.5 mg/mL of NH_2OH. In good agreement with the results in Figure 3.21, 55 mg/mL of NH_2OH led to completely blocking the cell wall labelling and increased use of NH_2OH showed a similar observation. In addition, in all cases, cells were successfully labelled with VanF and the labelling pattern was consistent with the previous work without NH_2OH treatment, which confirmed that NH_2OH treatment had no significant influence on cell morphology. Therefore, 55 mg/mL of NH_2OH was used for further study.

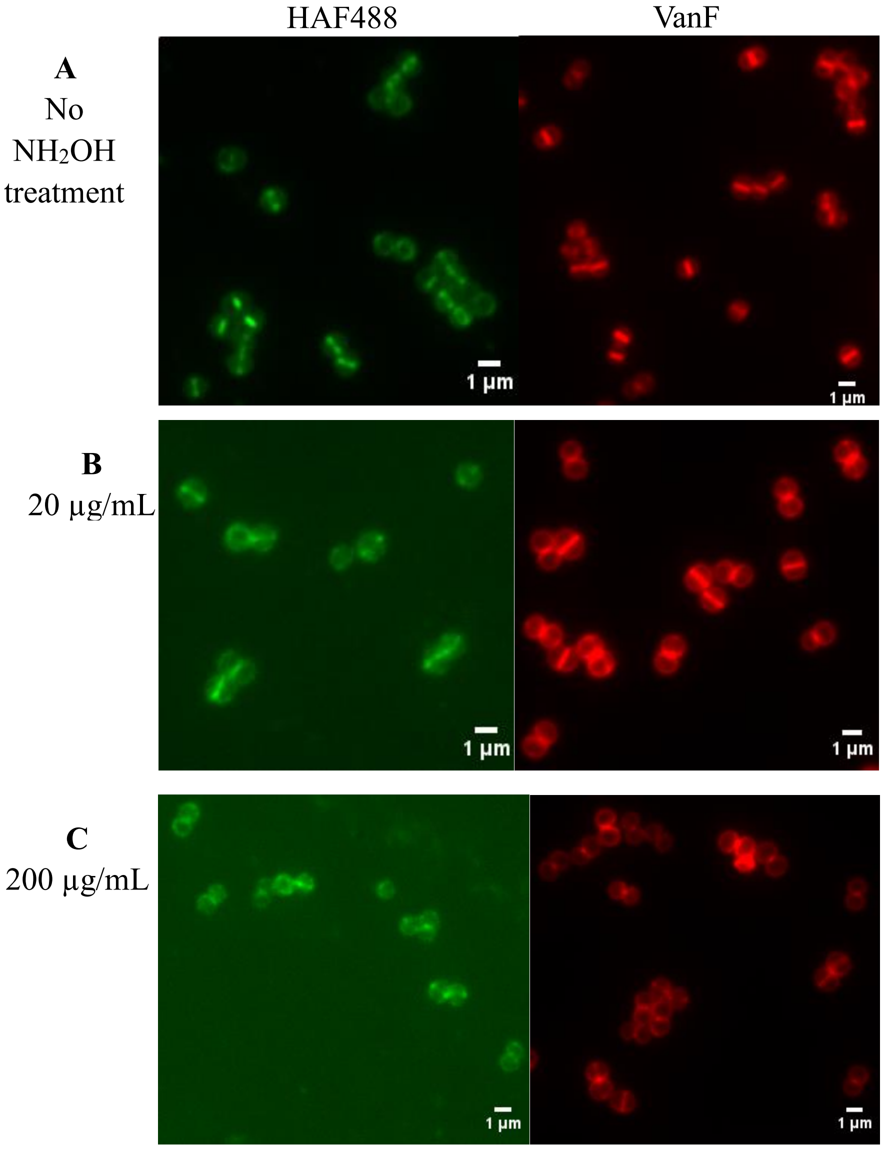

Figure 3.20 NH_2OH· HCl blocking *S. aureus* cells. Cells were pretreated with NH_2OH· HCl soluion, final concentration as 0 **(A)**, 20 **(B)** or 200 **(C)** µg/mL, followed with HAF488 or VanF labelling.

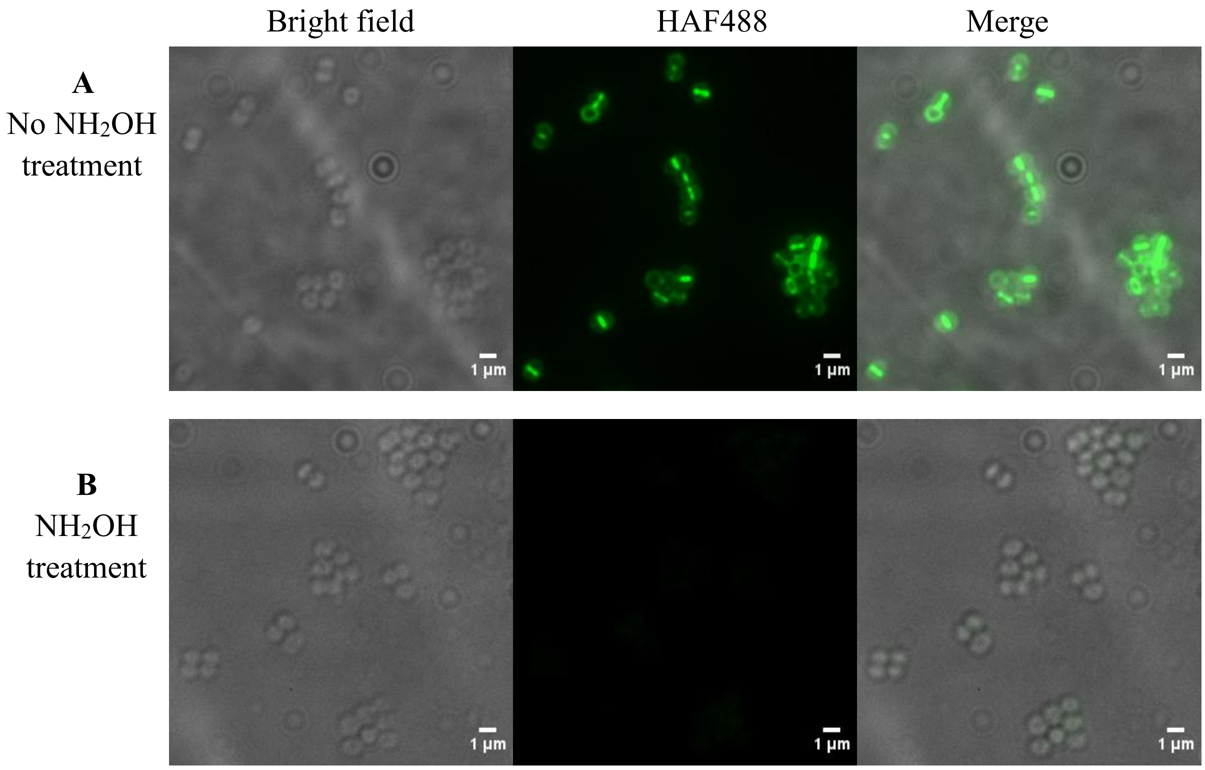

Figure 3.21 Initial test of NH_2OH blocking *S. aureus* cells. Cells were pretreated with or without NH_2OH (50% w/v in H_2O, 10 µL) and then labelled with HAF488.

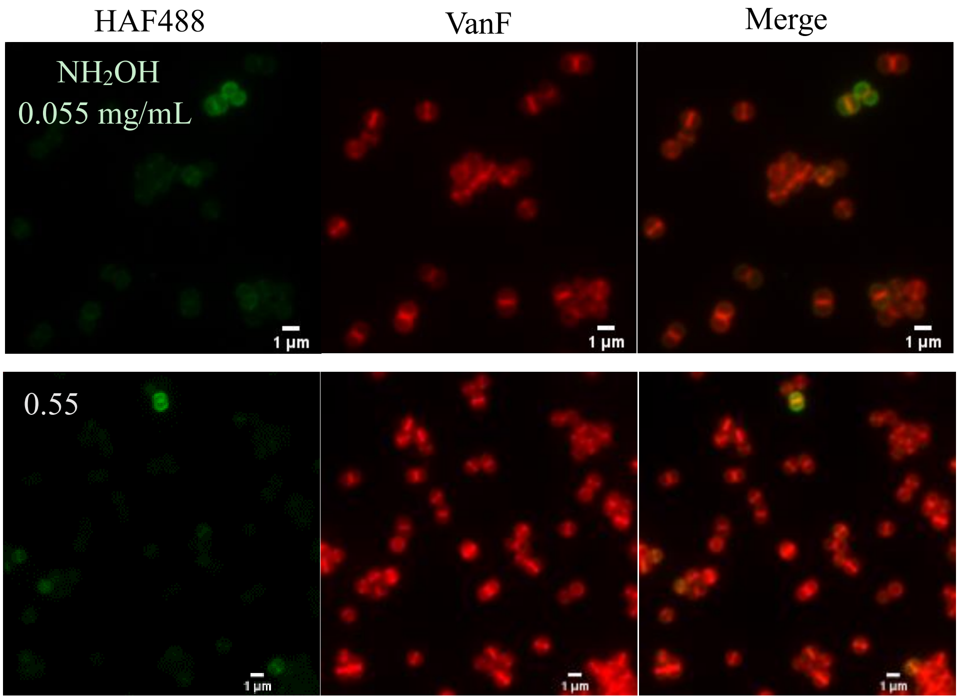

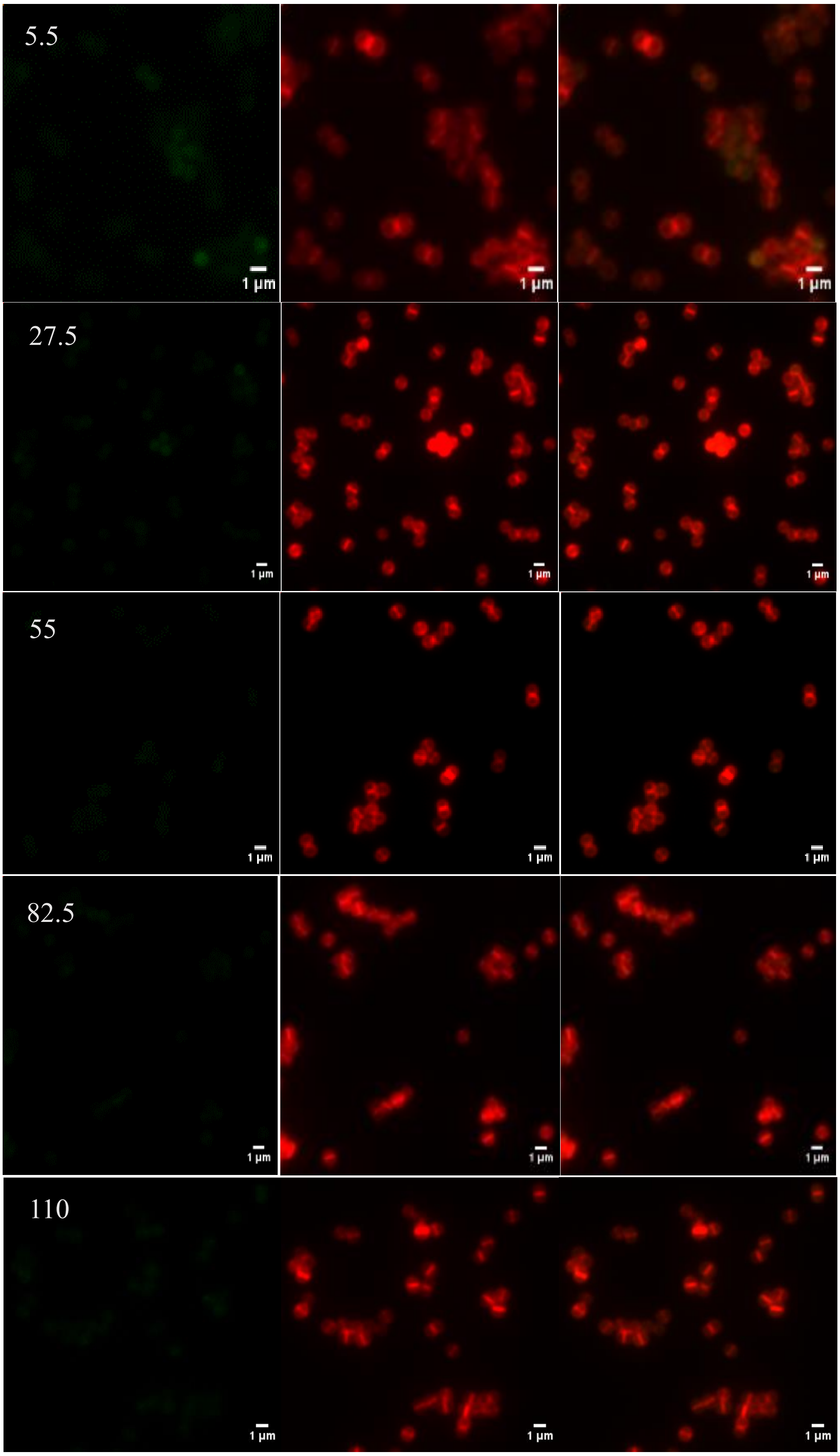

Figure 3.22 Effect of NH_2OH concentration on HAF488 labelling. Exponential-phase *S. aureus* cells were treated with different concentration of NH_2OH in PBS (0.055-110 mg/mL), and then labelled with HAF488 (Green) and VanF (Red).

3.2.2.2.3 Effect of NH_2OH on the growth and division of cells

As NH_2OH can successfully react at the reducing termini of cell walls, its effect on growth and division of cells was investigated. Initially, the growth curves of cells with or without NH_2OH treatment were assayed (Figure 3.23 A). Cells at an exponential phase were spun down and resuspended in PBS with or without NH_2OH for 5 min at 37 °C. After washing, the cells were cultivated and OD_{600} was recorded every half an hour. It was found that treatment of NH_2OH only slightly influenced the growth rates of bacteria cells. D-amino acid derivatives are only incorporated into live cells. Therefore, labelling NH_2OH-treated cells with HADA was conducted as a further marker for the test of toxicity of hydroxylamine. As shown in Figure 3.23 B, after NH_2OH treatment, HAF488 labelling exhibited no fluorescence whilst the cell wall was still obviously labelled with HADA, suggesting cells were alive. The results indicated that NH_2OH can successfully block the reducing termini without disturbing cells growth and allows for live cells imaging.

3.2.3 Analysis of glycan metabolism during cell growth and division

The growth and division of bacteria cells is a complex biological process governed by the synergistic action of numerous enzymes, highly involved in PG metabolism. To permit growth, PG has a dynamic structure, requiring polymerization of a Glc*N*Ac-Mur*N*Ac monomer, cleavage of glycan chains in old PG for insertion of PG precursors, and PG turnover. Labelling of the reducing termini of glycan chains with HAF488 has the potential to characterize dynamics of glycan and achieve detailed information. To analyse, two mutants of *S. aureus sagB* and *sgt mgt* were investigated as well as WT as control. SagB is a key glucosaminidase, that cleaves the glycan chains, and lack of it in the mutant results in a length increase of glycan chains in PG.[18,132] In *S. aureus*, one of crucial steps of PG assembly is polymerization of glycans to form a long PG chain which is controlled by transglycosylases or glycosyltransferases (GTs). Besides PBP2, there are two other characteristics: SgtA and monofunctional GT (MGT).[133]

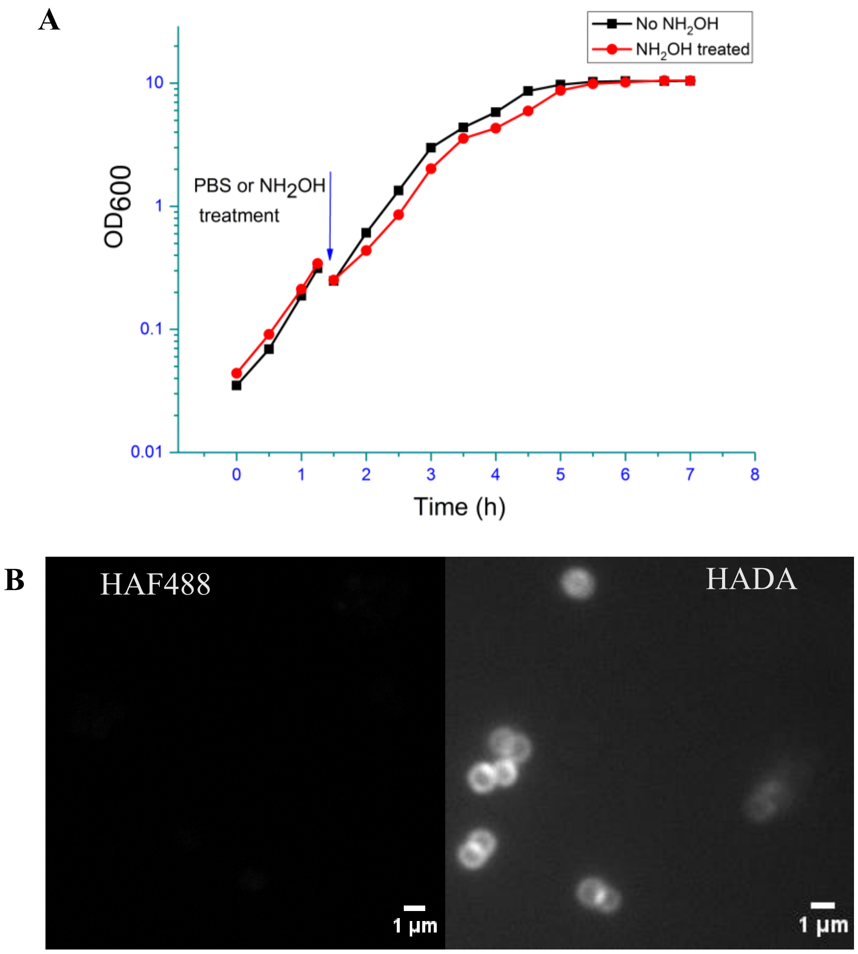

Figure 3.23 Effect of NH_2OH on *S. aureus* cell viability. (A) Exponential-phase cells strains were treated with NH_2OH in PBS (blocked) or PBS alone (unblocked) at 37°C for 5 min. After washing with PBS, cells were inoculated into TSB followed by incubation at 37°C. Bacterial growth was monitored by measuring OD_{600} and recorded at 1 hour-intervals. **(B)** NH_2OH treated cells were labelled with HAF488 or HADA for 5 min prior to microscopy.

Both a *sagB* and a *sgt mgt* mutant were available in the lab. Strains were pretreated with or without NH_2OH and later labelled with HAF488 (Figure 3.24). It was found that all were successfully labelled and displayed cell wall staining primarily at the septum while the periphery showed relatively weak fluorescence. To quantitatively analyse labelling effect, corrected total cell fluorescence (CTCF) of entire cells of the three strains were calculated and normalization performed by referring to the CTCF ratio of unblocked cells to their contrary blocked cells. The CTCF was determined using ImageJ software by calculating fluorescence readings for each cell within images as follows:[134]

$$CTCF = \text{Integrated density} - (\text{area of selected cell} \times \text{mean fluorescence of background readings})$$

As depicted in Figure 3.24 B, the normalized fluorescence intensity of the *sagB* mutant was significantly lower than that of WT, indicating that there were less reducing termini in the cell wall of the *sagB* mutant. This was consistent with previous reports that polymerized glycan strands are cleaved by SagB and lack of SagB generates longer glycan chains which means less recognition sites.[132] On the other hand, there was no distinct difference in entire cell fluorescence between WT and *sgt mgt*, suggesting in the absence of two GTs transglycosylation still occurred at the normal level. This finding is probably explained by the fact that neither of SgtA nor MGT is indispensable for cell well synthesis in *S. aureus*, and the strong catalytic power of PBP2 may mask changes induced by GTs being absent.[133]

It was worth noting that the labelling patterns of the strains seem to differ. In practical terms, HAF488 labelling of the *sagB* mutant exhibited relatively brighter fluorescence at the septa with weaker or faint labelling at the periphery (red arrows in Figure 3.24 A) in contrast to that of the WT. On the contrary, a broadly distributed staining pattern was observed throughout the entire cell wall in most *sgt mgt* cells (yellow arrows in Figure 3.24 A), and this labelling effect was not dramatically distinct between the septa and periphery. In order to investigate this hypothesis, the percentage (%) septal labelling was calculated and statistically analysed by an unpaired *t*-test with Welch's correction

(Figure 3.24 C). It was clearly shown that compared with the WT, the *sagB* mutant showed a high % septal labelling while a low % septal labelling in *sgt mgt* cells was observed.

3.2.4 Mutanolysin cleavage of PG chains

3.2.4.1 Growth of *S. aureus* cells with or without mutanolysin

Given the unique labelling of HAF488 at the reducing termini, it was suspected that release of more reducing termini by cleaving long glycan chains of PG might alter the distribution of fluorescence labelling. Mutanolysin, a PG hydrolase, specifically cleaves the β-1,4-glycosidic linkage of Mur*N*Ac-Glc*N*Ac in PG chains, which results in more reducing termini in the cell wall.[135] Thus, the effect of mutanolysin on WT cells was investigated. Initially, the sustainability of mutanolysin treatment was checked by analysis of a growth curve to guarantee the existence of intact cells. It has been reported that the lytic activity of mutanolysin is significantly increased in the presence of Mg^{2+}, therefore co-treatments with mutanolysin and $MgCl_2$ were also performed as control groups.[136] As shown in Figure 3.25, increasing the concentration or enhancing the enzyme activity did not kill cells and these live cells were capable of fluorescent labelling using HAF488.

3.2.4.2 Effect of mutanolysin on HAF488 labelling

Next, mutanolysin treated cells were labelled with HADA and HAF488 for fluorescent microscopy viewing (Figure 3.26). It was clearly shown that in all cases cells were successfully labelled with HADA, which also showed survival cells after enzyme treatment. This was consistent with a previous report that *S. aureus* living cells are mutanolysin-resistant.[136] As for the HAF488 channel, compared with cells without mutanolysin treatment, most of cells in all enzyme treated cases exhibited a similar labelling pattern and did not show an enhanced fluorescence as expected after mutanolysin treatment.

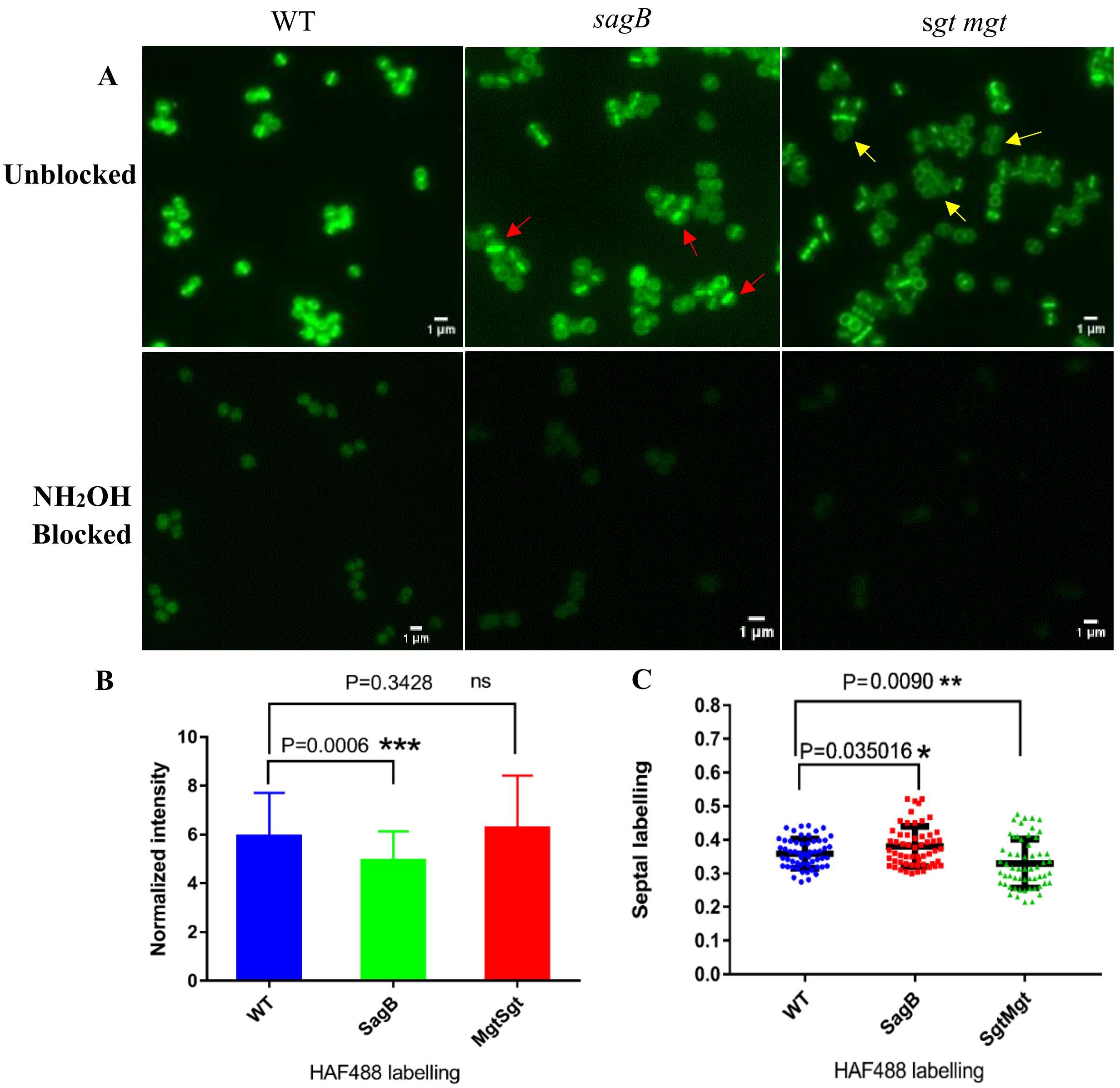

Figure 3.24 Analysis of *S. aureus* WT, *sagB* and *sgt mgt* cells labelling with HAF488. **(A)** Exponential-phase live cells, with or without NH_2OH blocking, were labelled with HAF488. Arrows: labelling features. **(B)** Histogram with mean ± SD (standard deviation) of normalized fluorescence intensity of entire cells on the basis of CTCF analysis. **(C)** Scatter diagram with mean ± SD of % septal labelling using HAF488 on the basis of CTCF analysis. P values were calculated by unpaired *t*-test with Welch's correction and statistical significance levels were shown as ns = not significant, $p > 0.05$; $*p<0.05$; $**p<0.01$; $***p<0.001$.

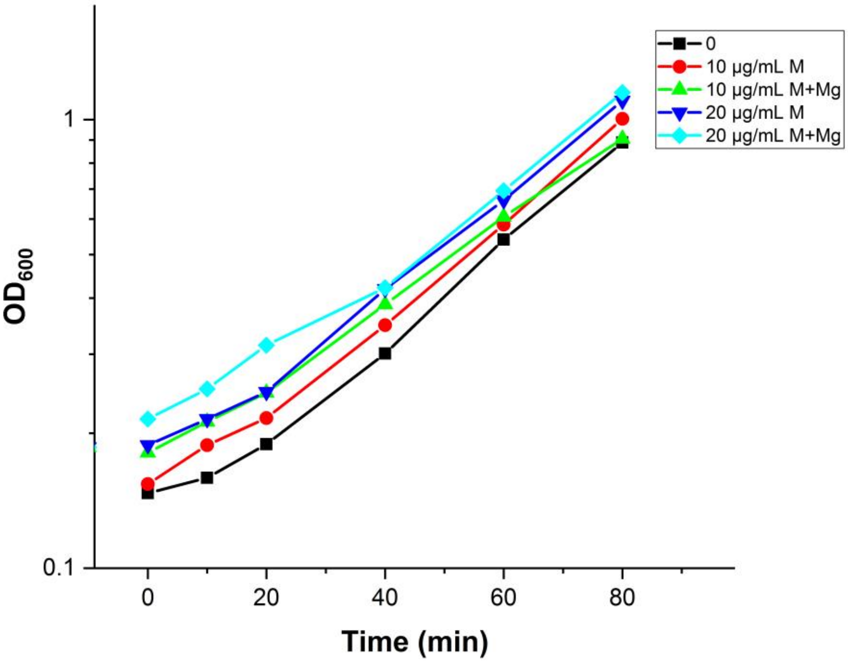

Figure 3.25 Growth of *S. aureus* cells with or without mutanolysin. Exponential phase live WT cells were resuspended in PBS, 10 μg/mL of mutanolysin in PBS with or without 100 mM $MgCl_2$, or 20 μg/mL of mutanolysin in PBS with or without 100 mM $MgCl_2$, respectively and OD_{600} was measured. After incubation at 37 °C for 0.5 hour, above cells were harvested, resuspended in TSB and the OD_{600} was measured over time.

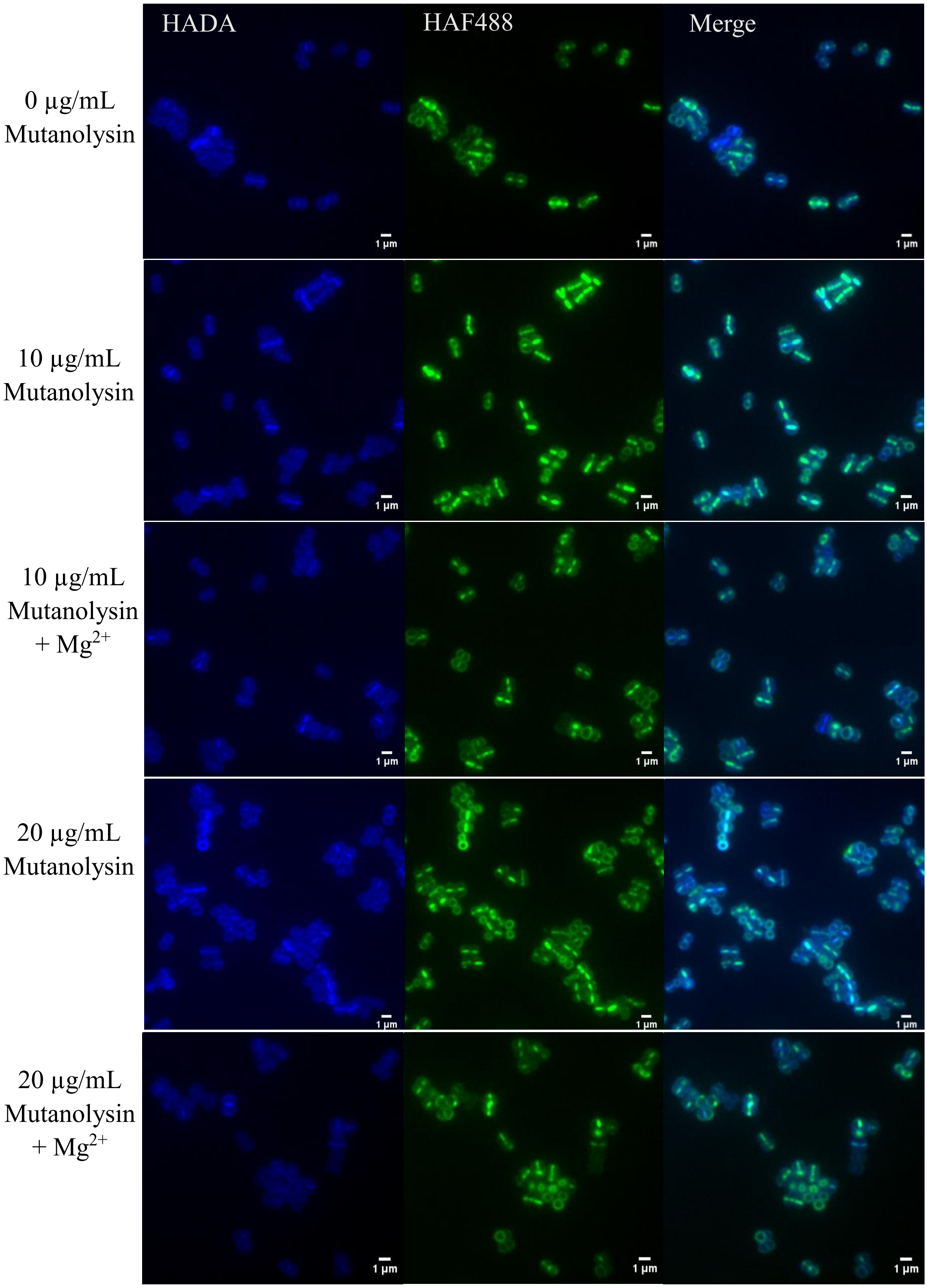

Figure 3.26 Effect of mutanolysin on HAF488 labelling *S. aureus* cells. Exponential-phase WT cells were treated with 0, 10 or 20 µg/mL of mutanolysin in PBS with or without 100 mM $MgCl_2$ at 37 ºC for 0.5 hour. Cells were labelled with HADA (blue) followed by HAF488 staining (green).

3.2.5 Analysis of newly synthesised PG with or without moenomycin treatment

It was difficult to distinguish nascent PG from mature cell wall by direct HAF488 labelling as they may be at the same targeting site. To better understand the distribution of new synthesised PG, mature PG of live cells were treated with NH_2OH using the above mentioned procedure and these blocked cells were regrown in media, which resulted in the formation of new reducing termini for probe labelling. As previously stated, transglycosylation of PG precursors to assemble PG is mediated by GTs and inhibition of GTs using an antibiotic such as moenomycin disturbs the growth of the cell wall.[137,138] The binding of moenomycin to PBP2 blocks elongation of the glycan chain and made more reducing termini free. Herein, the effect of moenomycin treatment during cells growth was investigated using the dual labelling methodology.

3.2.5.1 Analysis of newly synthesised PG of *S. aureus* WT cells

Initially, dual-labelling of blocked *S. aureus* WT cells were performed using HAF488 and VanF without moenomycin. It is clearly seen that HAF488 labelling increased and the distribution changed over time (Figure 3.27). More detailedly, at the early stage of the cell regrowth (5 min), HAF488 was mainly labelled at the periphery and similar to localisation of VanF labelling. When cells continued to grow, some showed a variation in HAF488 labelling from being focused on the periphery to surrounding the entire cell wall containing the septa, which still overlaid with VanF staining. The number of cells with entire septal labelling increased later. At 45 or 60 min, the HAF488 labelling displayed strong fluorescence at both the periphery and septa, while VanF staining preferred to the septa.

On the other hand, moenomycin-treated cells had faint fluorescence provided from HAF488, suggesting incubation with moenomycin was tremendously disruptive in cell growth and division (Figure 3.28). To analyse the influence of moenomycin on *S.*

aureus cells growth, the growth curve tests were carried out with WT cells and NH_2OH treated cells. In two cases, cells were found with significant growth inhibition after moenomycin treatment, especially after 15 min interval (Figure 3.29). These labelling results were further quantitatively analysed using a CTCF calculation. As shown in Figure 3.30, the CTCF of cells without treatment of moenomycin showed an increasing trend over time while treatment with moenomycin resulted in prevention of labelling. The CTCF difference between cells with or without moenomycin treatment was enhanced over time, which was consistent with the growth curve analysis.

3.2.5.2 Analysis of newly synthesised PG of *S. aureus* mutants

Further investigations were performed on two *S. aureus* mutants (*sagB* and *sgt mgt*) employing the same procedure as described above, which included NH_2OH blocking, cell regrowth and dual-labelling with HAF488 and VanF (Figure 3.31 and 3.33). The similar phenomenon was observed in newly synthesised PG in contrast to the old cell wall labelling (Chapter 3.2.3). The effect of moenomycin was also investigated. In both mutants, the growth imbibition occurred after moenomycin treatment. (Figure 3.32 and 3.34).

3.2.5.3 Analysis of HADA incorporation into HAF488 labelled cells

Another strategy was investigated that employed HAF488 to mark existing PG and subsequently regrown for a specific time followed by HADA labelling to localize newly synthesized PG (Figure 3.35). It was clearly shown that cells survived after HAF488 staining and fluorescence gradually faded over time while there was no significant effects on HADA labelling.

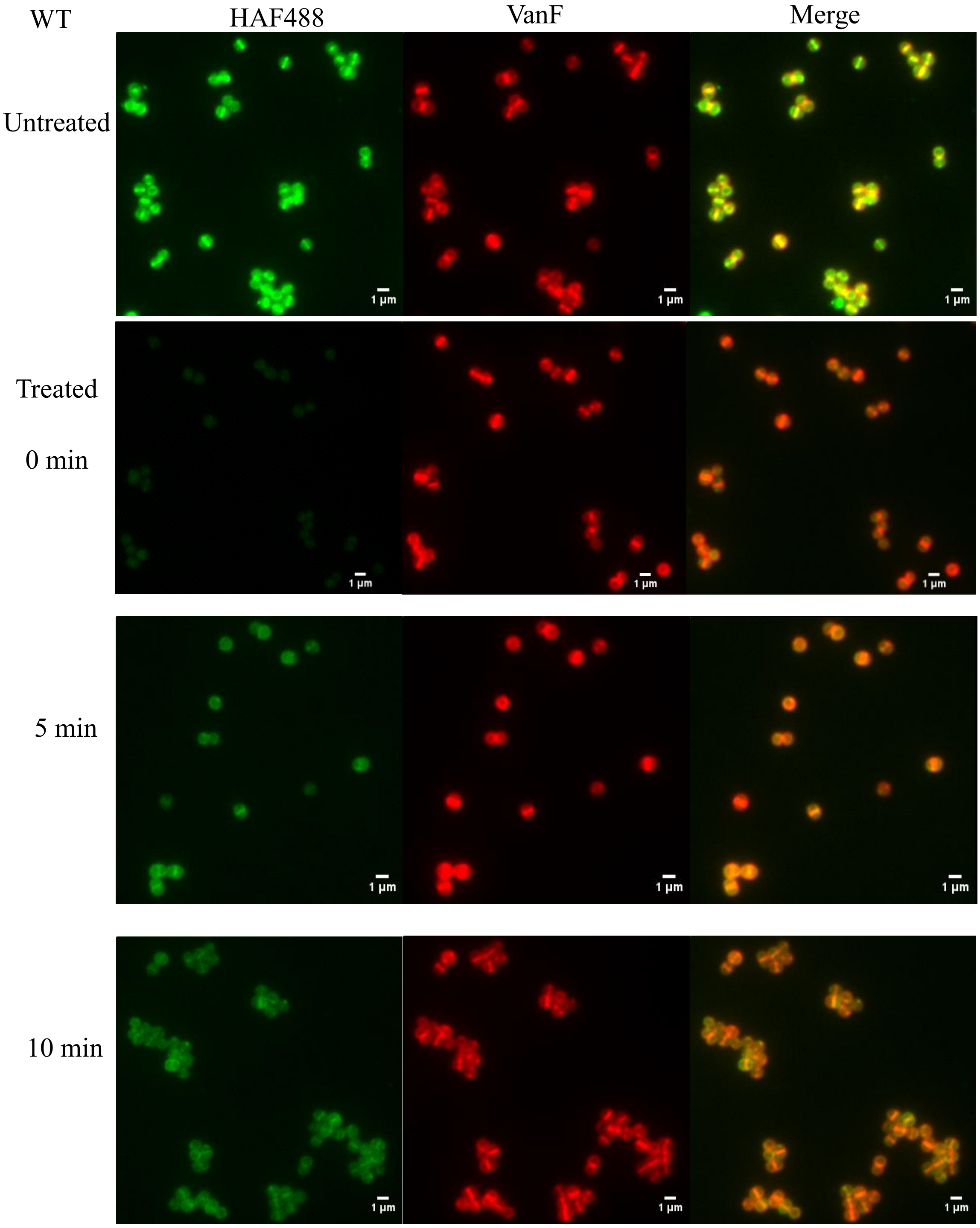
WT
HAF488
VanF
Merge
Untreated
Treated
0 min
5 min
10 min
1 µm

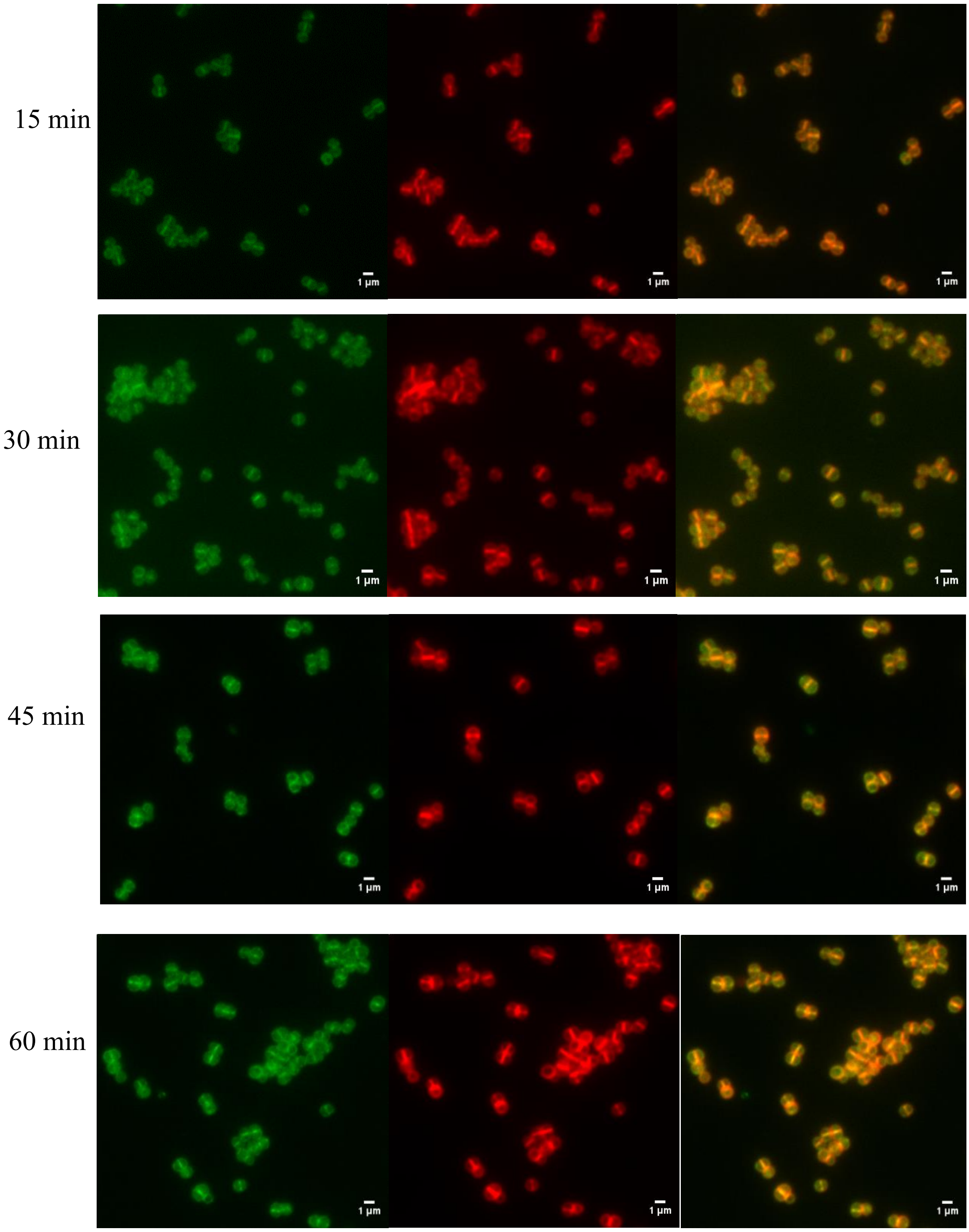

Figure 3.27 Dual labelling regrown *S. aureus* WT cells after NH_2OH treatment. Cells at exponential phase were blocked with NH_2OH and resuspended in TSB with shaking at 37 °C. After growing certain time (0, 5, 10, 15, 30, 45 and 60 min), cells were harvested and labelled with HAF488 followed by VanF staining.

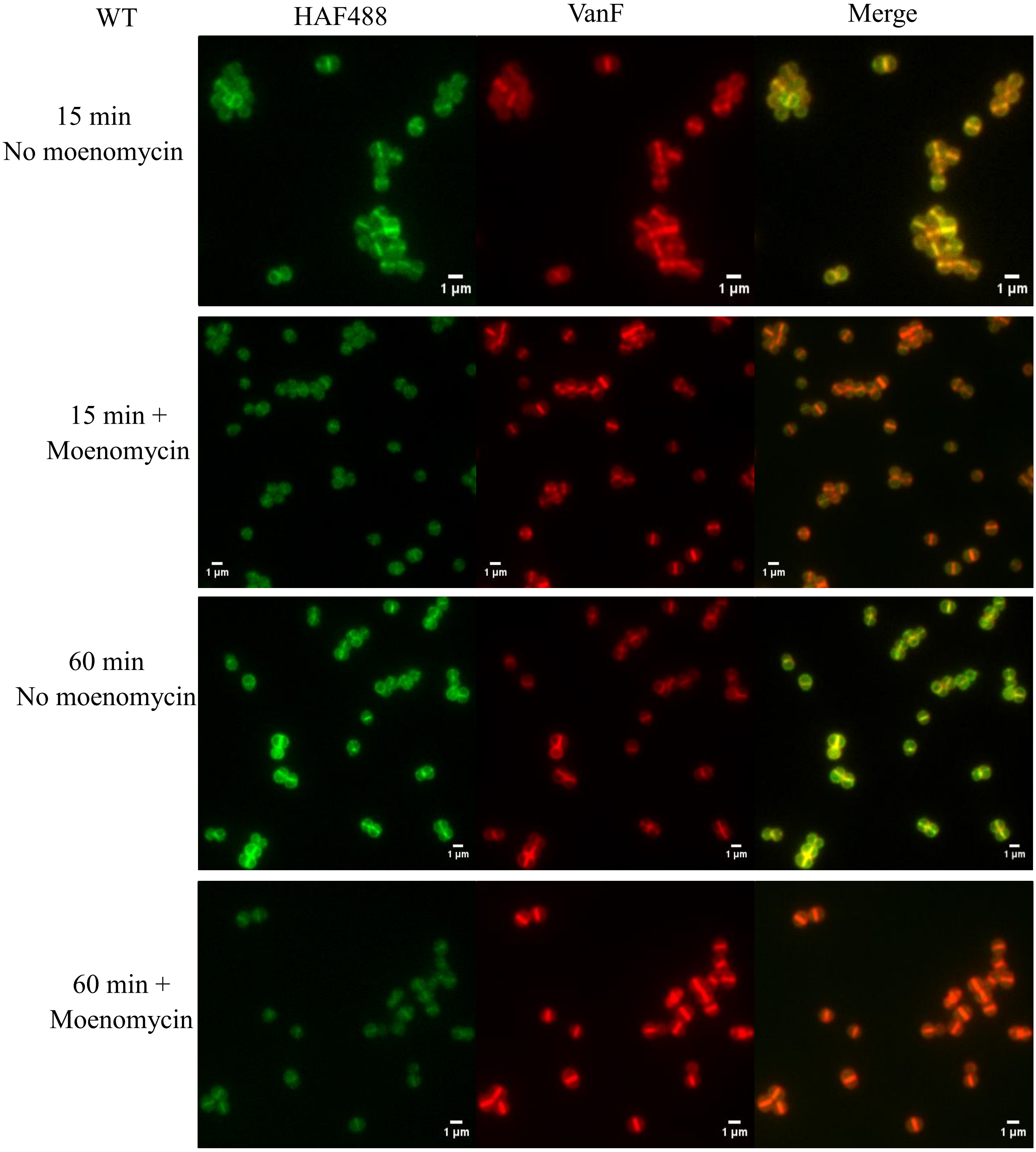

Figure 3.28 Effect of moenomycin on dual labelling of regrown *S. aureus* WT cells after NH_2OH treatment. Live WT cells at exponential phase were blocked with NH_2OH and resuspended in TSB with or without 5 µg/mL of moenomycin shaking at 37 °C. After growing 15 or 60 min, cells were harvested and labelled with HAF488 followed by VanF staining. Images were processed using an enhanced contrast for better visualization.

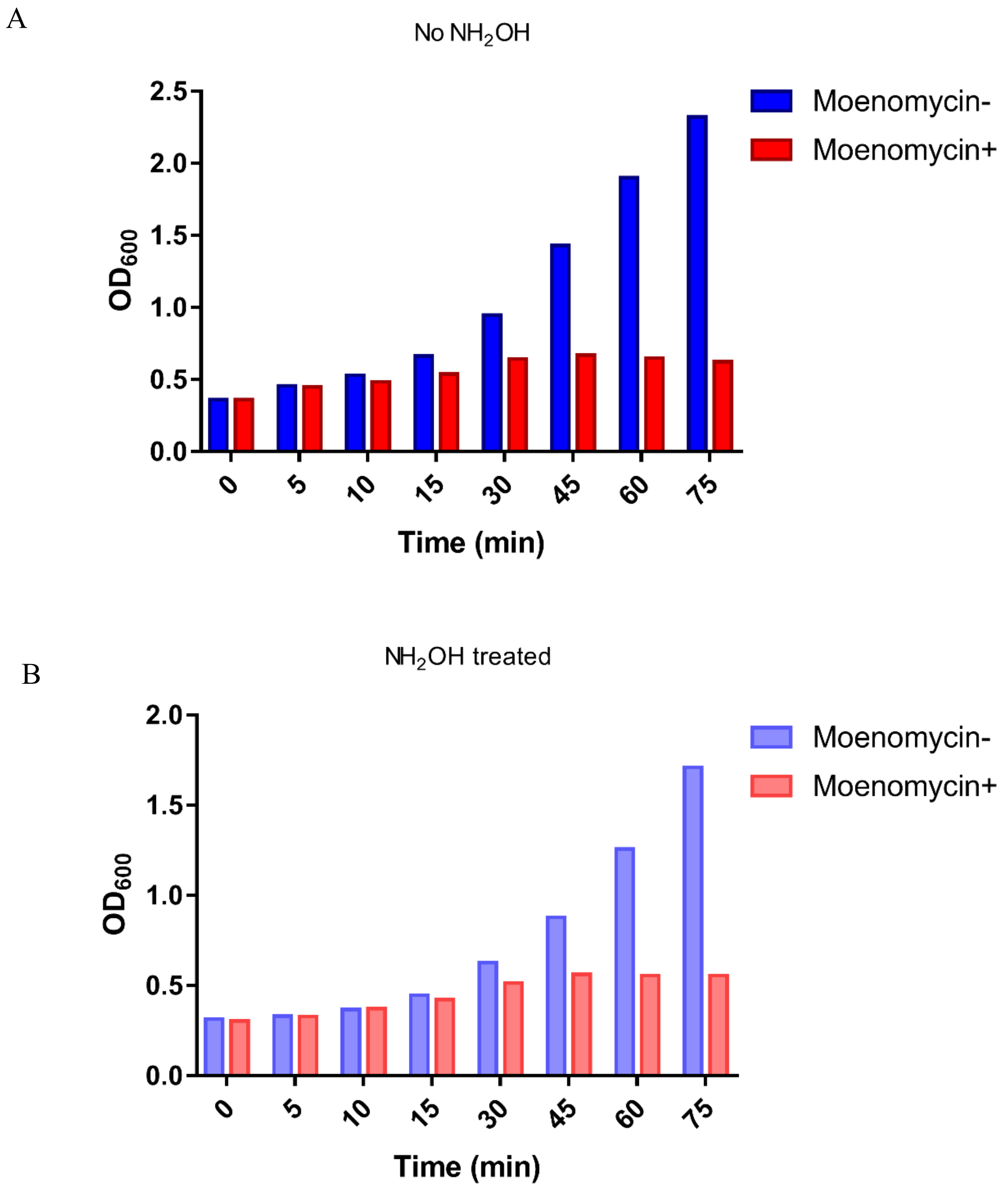

Figure 3.29 Growth of *S. aureus* cells with or without moenomycin. (A) Exponential phase WT cells were resuspended in TSB with or without 5 µg/mL of moenomycin shaking at 37 °C and the OD_{600} was measured over time. **(B)** NH_2OH treated exponential phase WT cells were resuspended in TSB with shaking at 37 °C and the OD_{600} was measured over time.

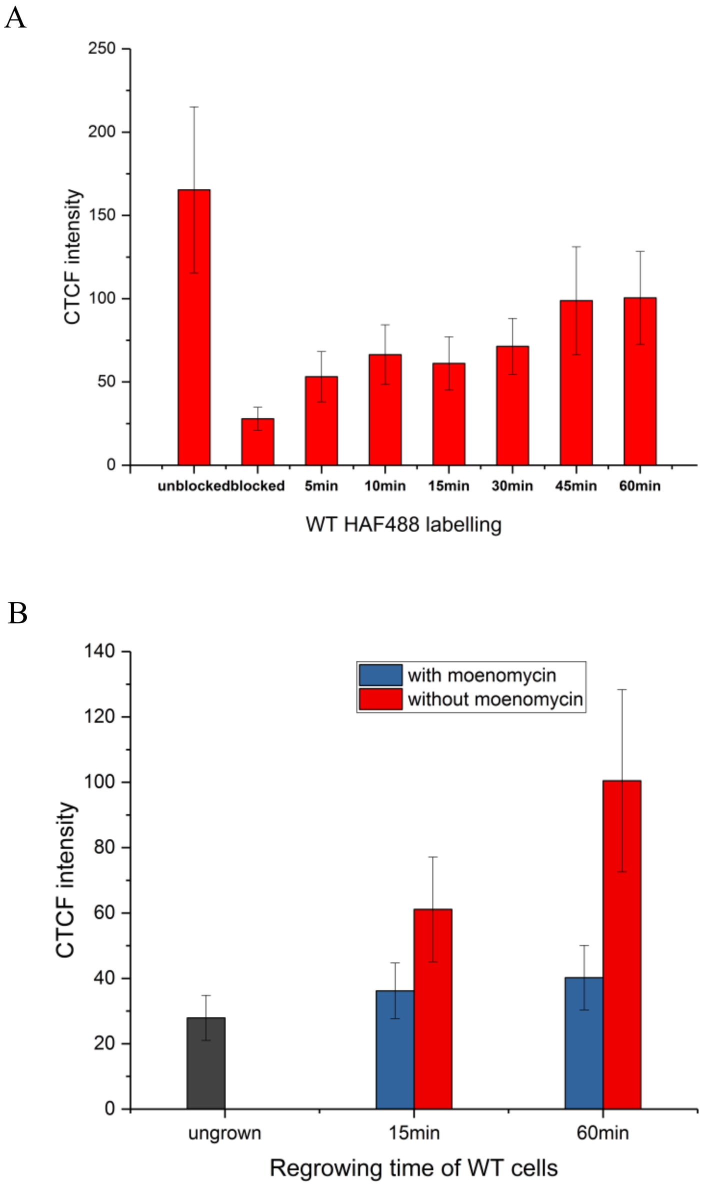

Figure 3.30 Quantification of HAF488 labelling of WT cells. (A) NH_2OH blocked WT cells were regrown for specified time and dual-labelled with HAF488 and VanF followed by CTCF calculation of HAF488 channel as mentioned above. (B) CTCF of blocked WT cells that grew with or without moenomycin were recorded and compared with blocked cells without regrowth.

In order to study the moenomycin effect, HAF488 labelled cells were grown with moenomycin over time and then labelled with HADA for 5 min (Figure 3.36). It was found that cell metabolism was inhibited and entire bright stripes of HAF488 were observed in most cells even after 60 min growth. With respect to HADA labelling, the pattern seemed to alter from labelling both septa and periphery but with strong preference at the septa, to now merely localising the periphery. To verify this observation, CTCF intensity derived from HADA labelling was statistically analysed, and the septal CTCF percentage in the entire cell wall staining (% septal labelling) was calculated for comparison. Considering the increasing of fading of HAF488, cells regrown for 15 min were chosen as models (Figure 3.37). As shown in Figure 3.37 A, the CTCF of the entire cell decreased after moenomycin treatment while surprisingly the intensity of septal labelling showed no significant difference, which finally gave an increased % septal labelling (Figure 3.37B). This suggested that moenomycin inhibited the peripheral labelling and PBP2 played a crucial role to regulate the incorporation of D-Ala to the off-septal cell wall.

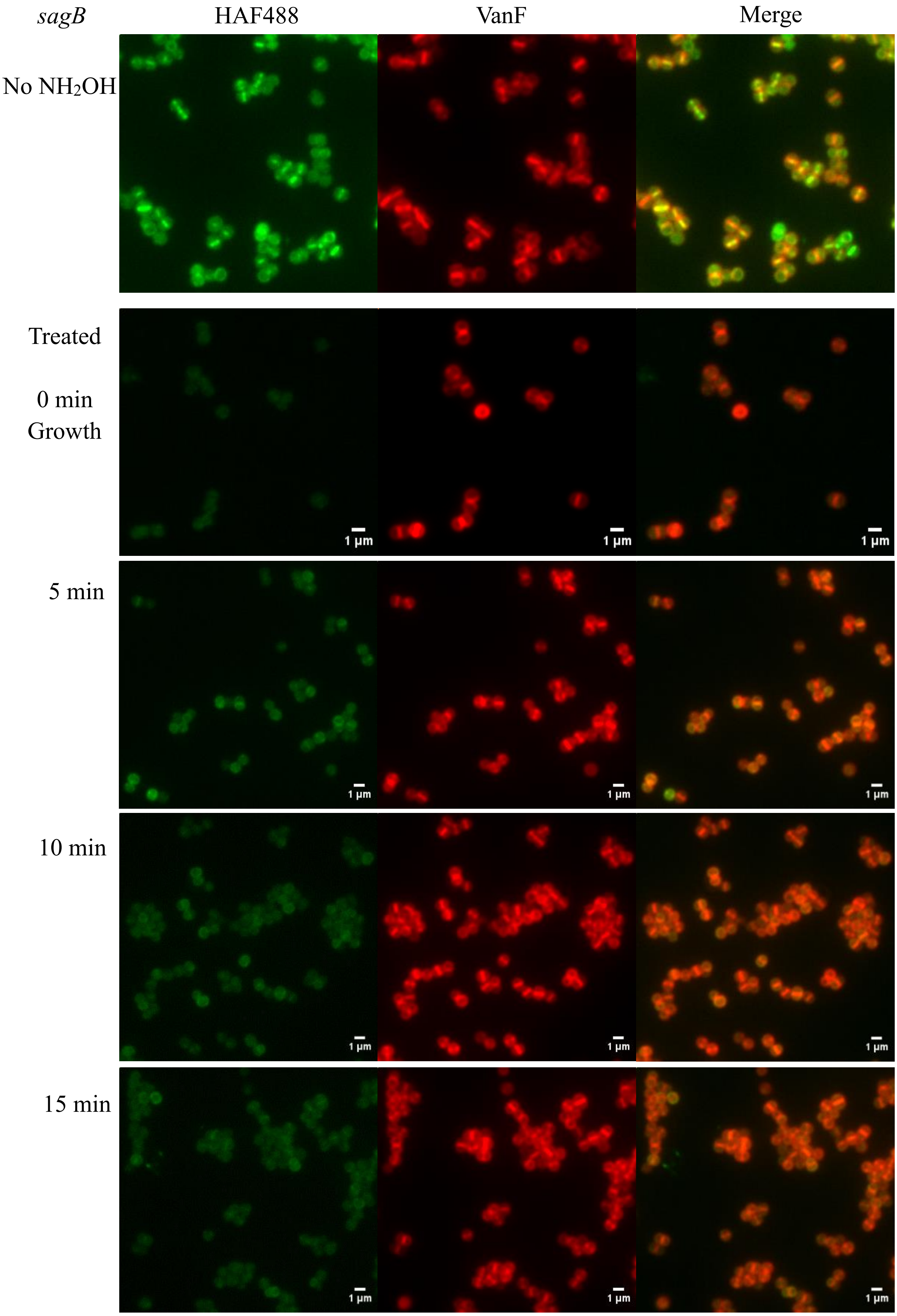
sagB
HAF488
VanF
Merge
No NH₂OH
Treated
0 min
Growth
5 min
10 min
15 min
1 μm

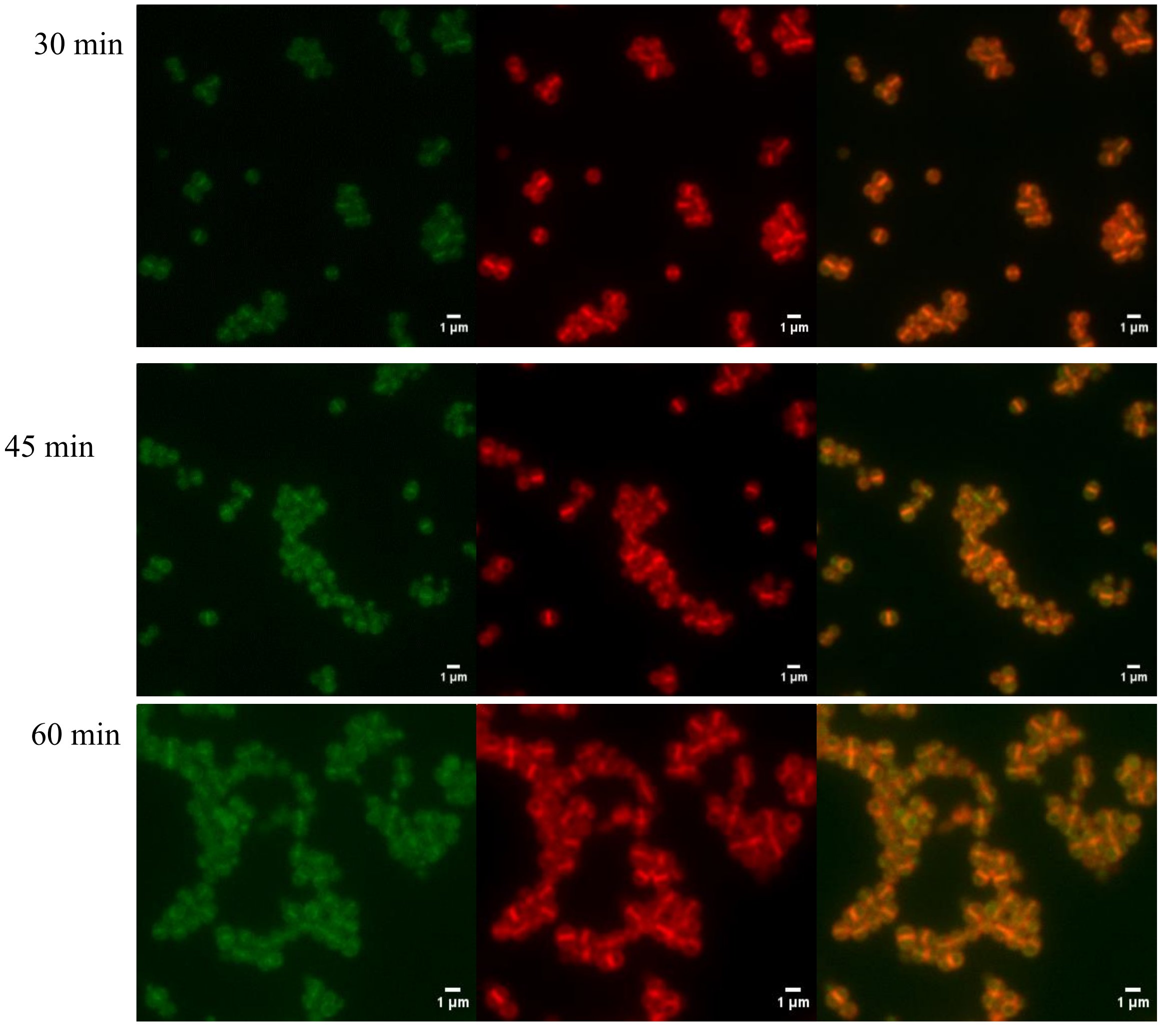

Figure 3.31 Dual labelling regrown *S. aureus sagB* mutant after NH_2OH treatment. Cells at exponential phase were blocked with NH_2OH and resuspended in TSB with shaking at 37 °C. Cells were harvested over time and labelled with HAF488 followed by VanF staining.

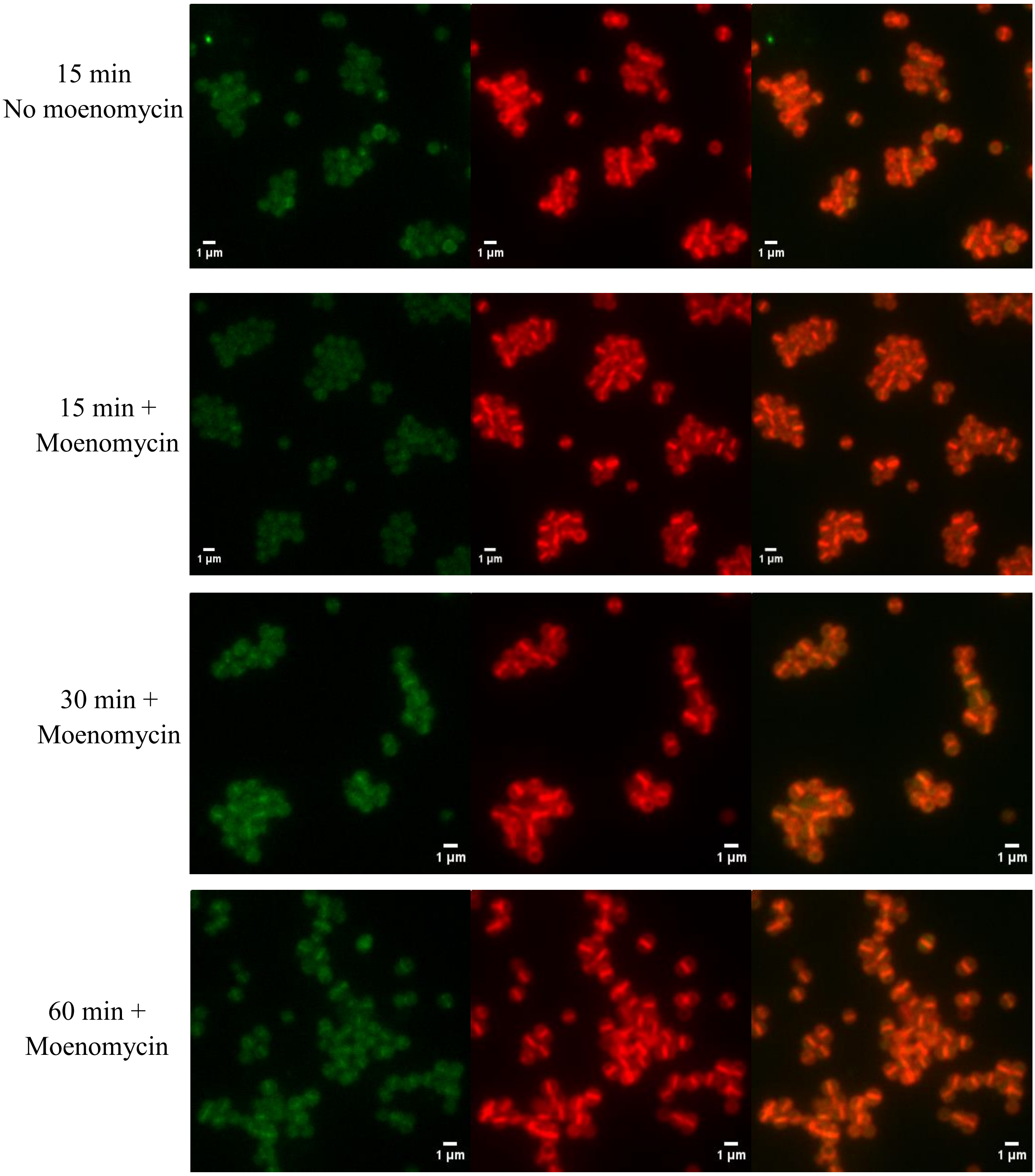

Figure 3.32 Effect of moenomycin on dual labelling of regrown *S. aureus sagB* mutant after NH_2OH treatment. Cells at exponential phase were blocked with NH_2OH and resuspended in TSB with or without 5 µg/mL of moenomycin shaking at 37 °C. Cells were harvested over time and labelled with HAF488 followed by VanF staining. Images were processed using an enhanced contrast for better visualization.

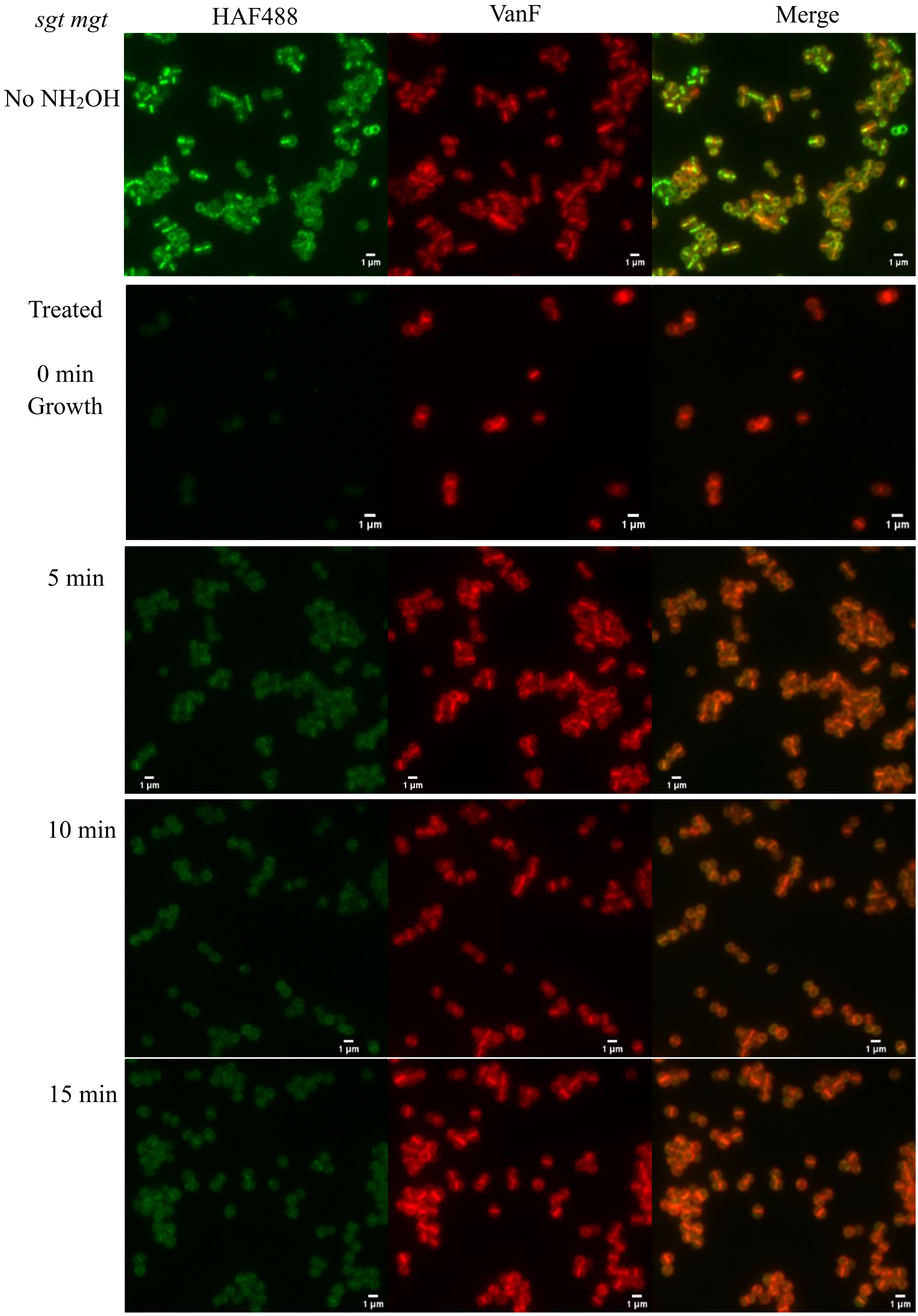
sgt mgt
HAF488
VanF
Merge
No NH₂OH
Treated
0 min
Growth
5 min
10 min
15 min
1 µm

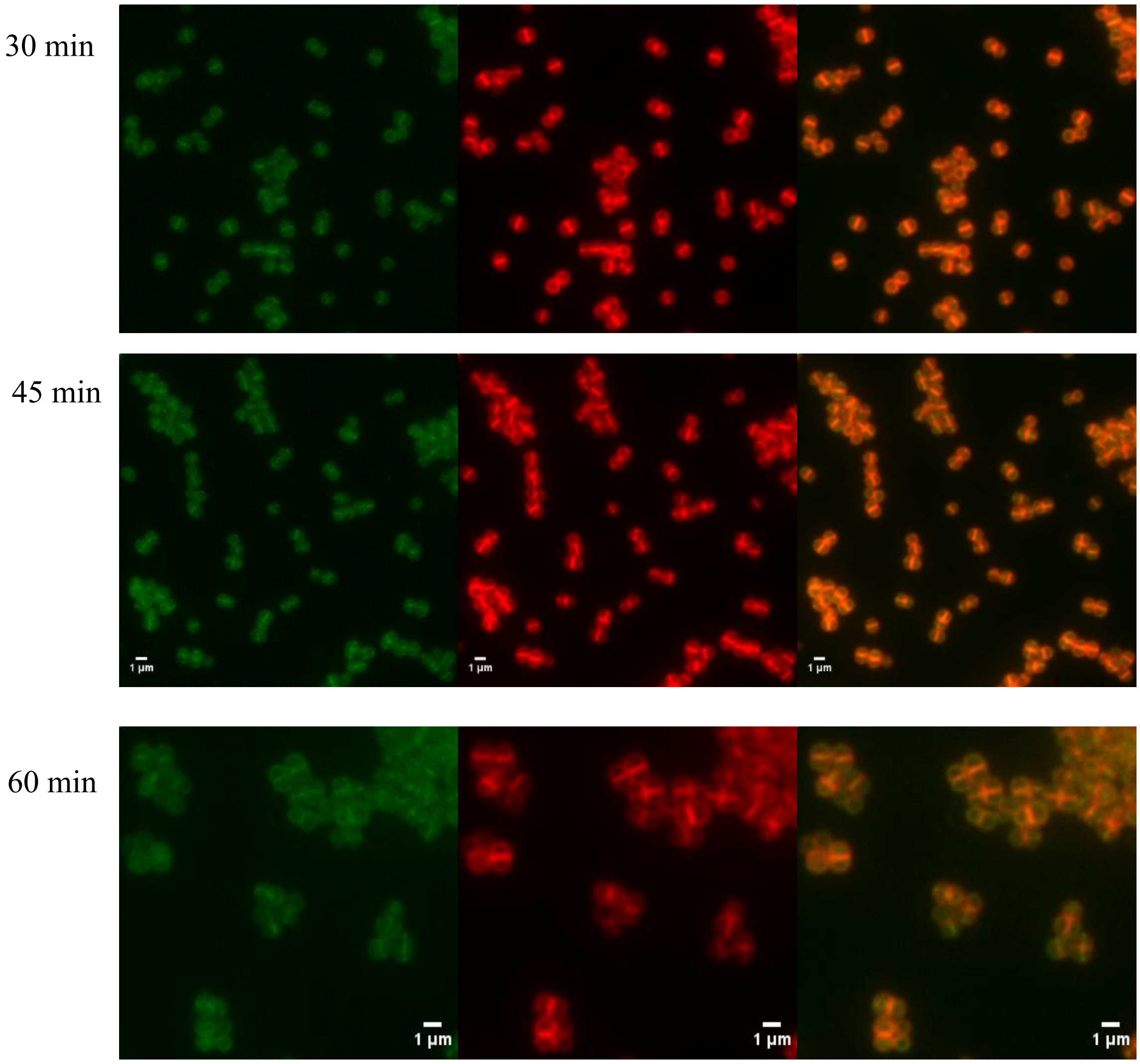

Figure 3.33 Dual labelling regrown *S. aureus sgt mgt* mutant after NH_2OH treatment. Cells at exponential phase were blocked with NH_2OH and resuspended in TSB with shaking at 37 °C. Cells were harvested over time and labelled with HAF488 followed by VanF staining.

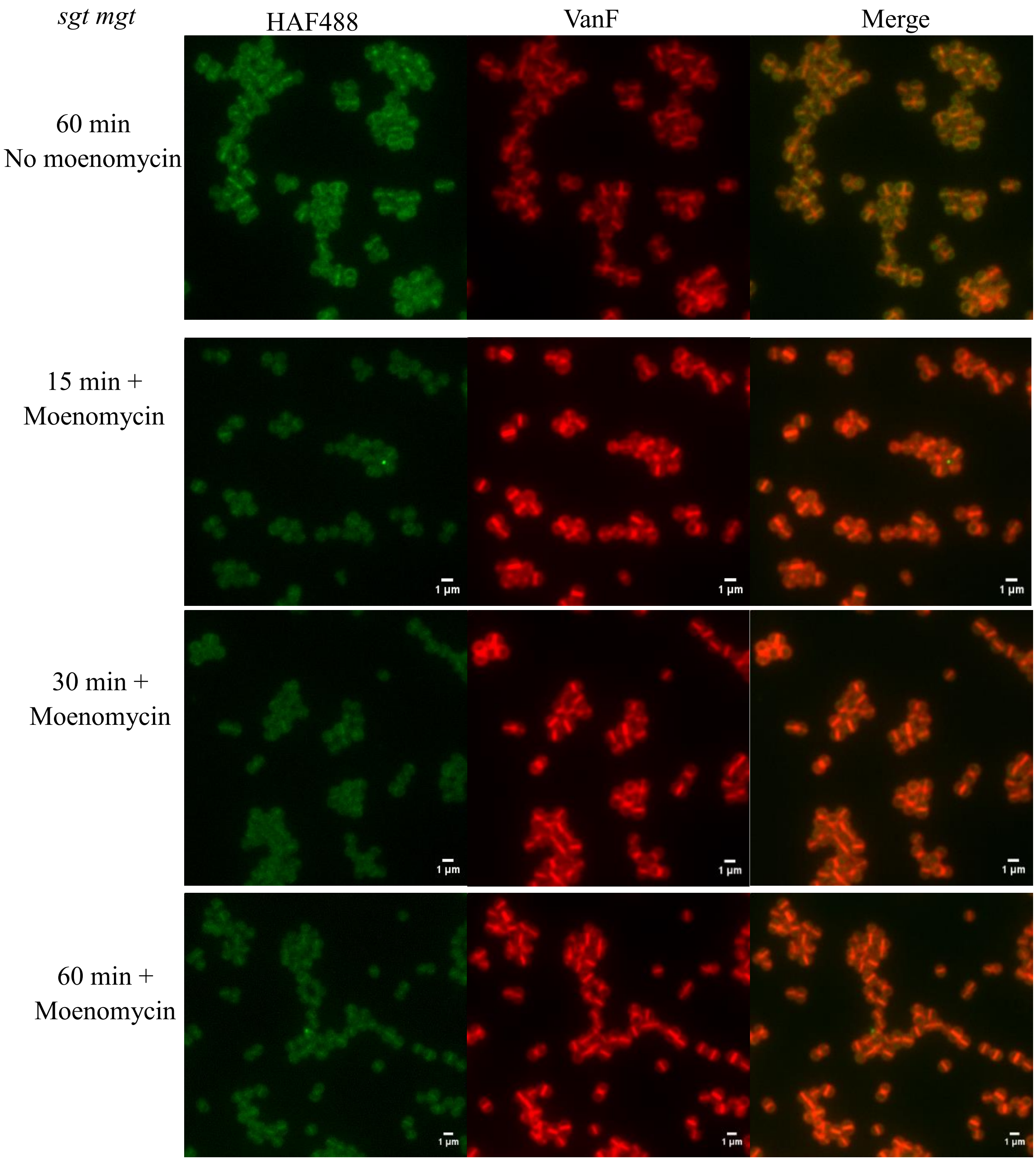

Figure 3.34 Effect of moenomycin on dual labelling of regrown *S. aureus sgt mgt* mutant after NH_2OH treatment. Cells at exponential phase were blocked with NH_2OH and resuspended in TSB with or without 5 µg/mL of moenomycin shaking at 37 °C. Cells were harvested over time and labelled with HAF488 followed by VanF staining. Images were processed using an enhanced contrast for better visualization.

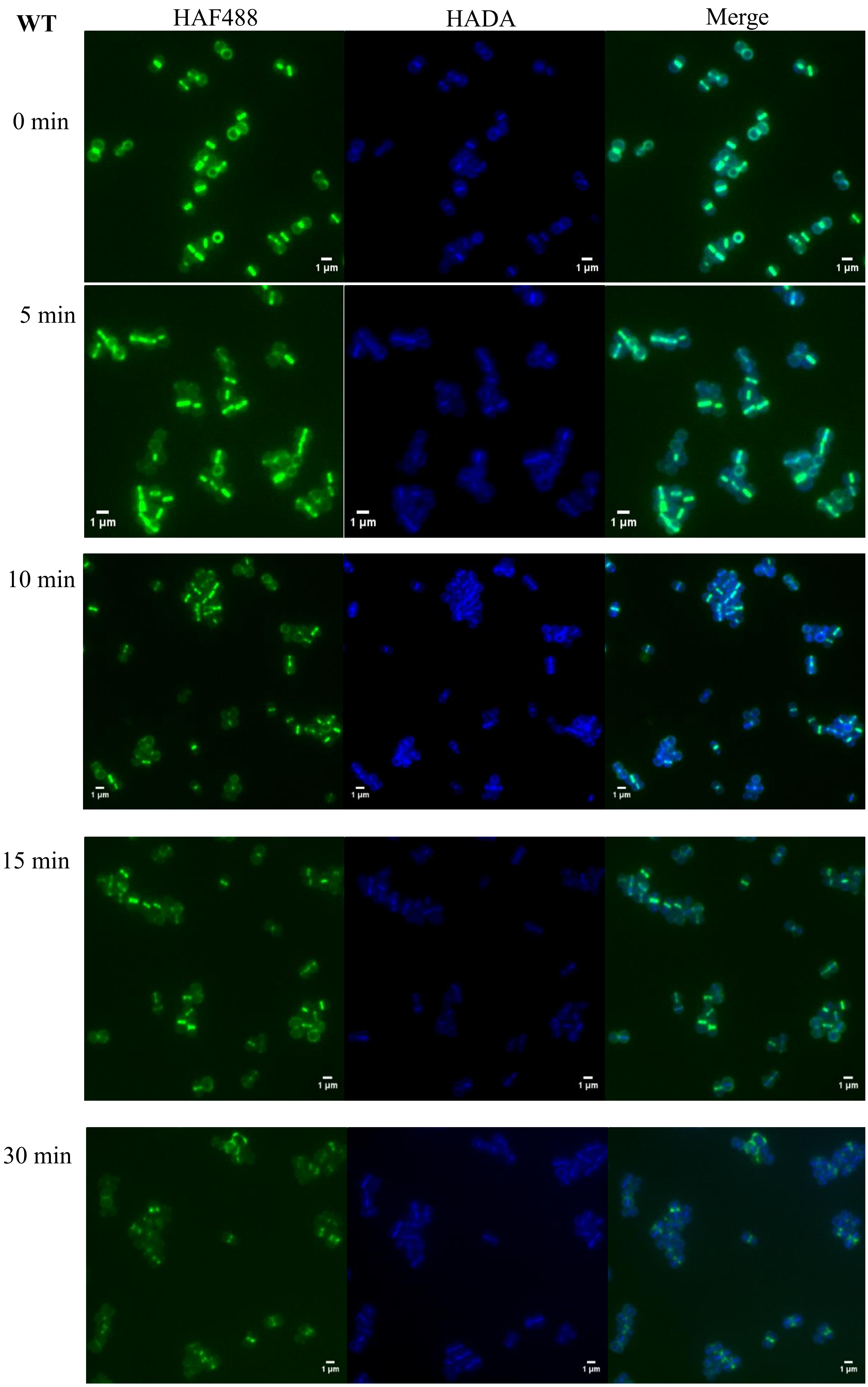
WT
HAF488
HADA
Merge
0 min
5 min
10 min
15 min
30 min
1 µm

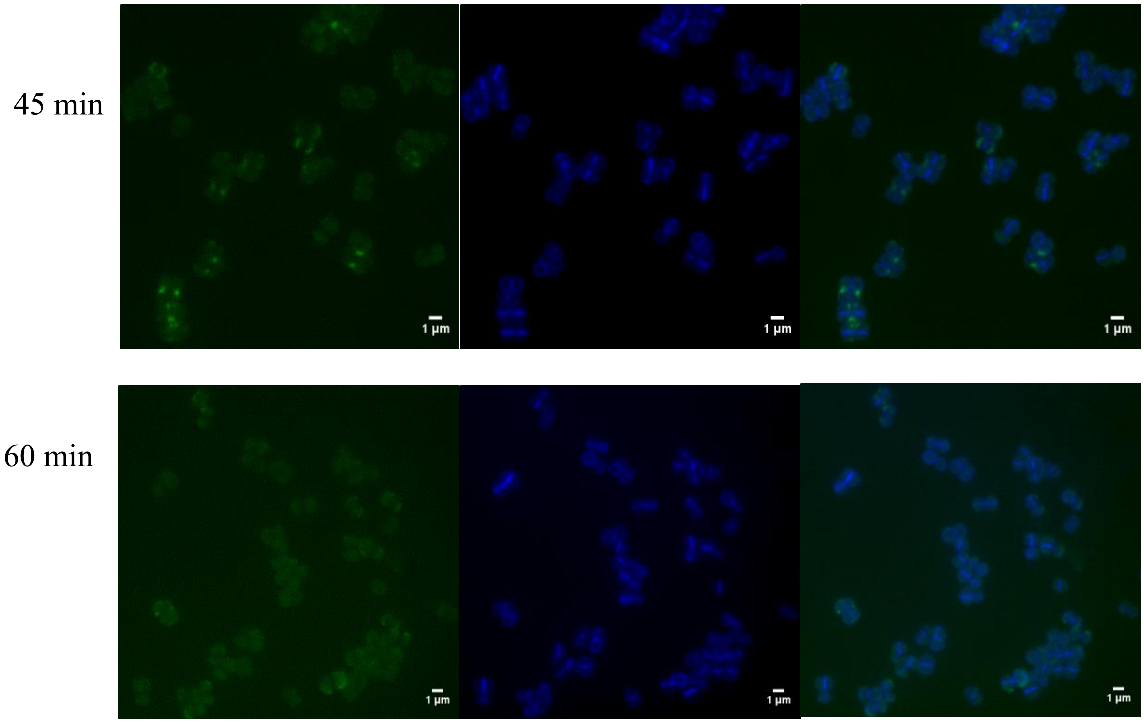

Figure 3.35 HADA labelling of regrown *S. aureus* WT after HAF488 labelling. Cells at exponential phase were labelled with HAF488 and resuspended in TSB with shaking at 37 °C. Cells were harvested over time and labelled with HADA for 5 min prior to microscopy.

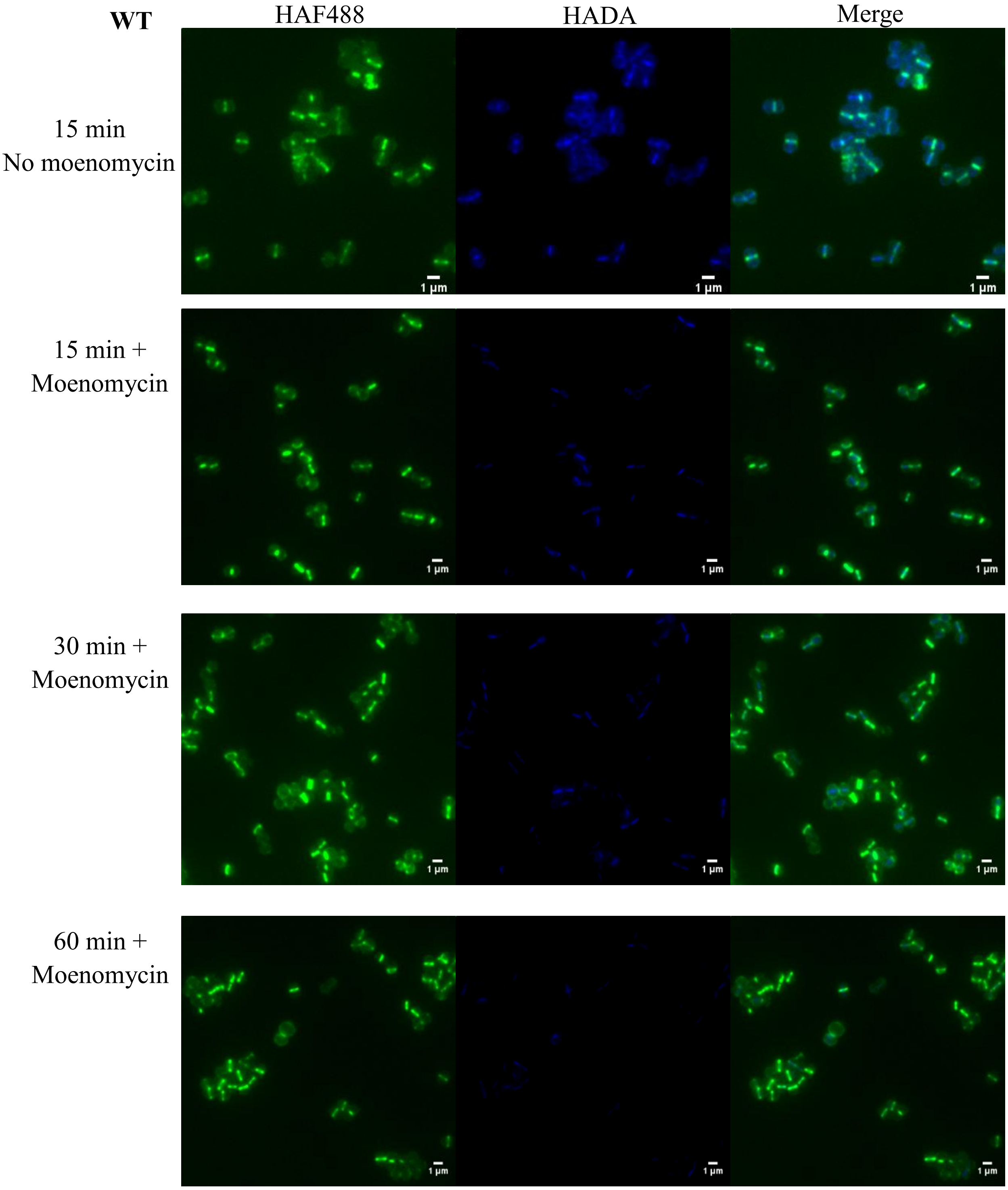

Figure 3.36 Effect of moenomycin on HADA labelling of regrown *S. aureus* WT after HAF488 labelling. Cells at exponential phase were labelled with HAF488 and resuspended in TSB with 5 μg/mL of moenomycin with shaking at 37 °C. Cells were harvested over time and labelled with HADA for 5 min prior to microscopy.

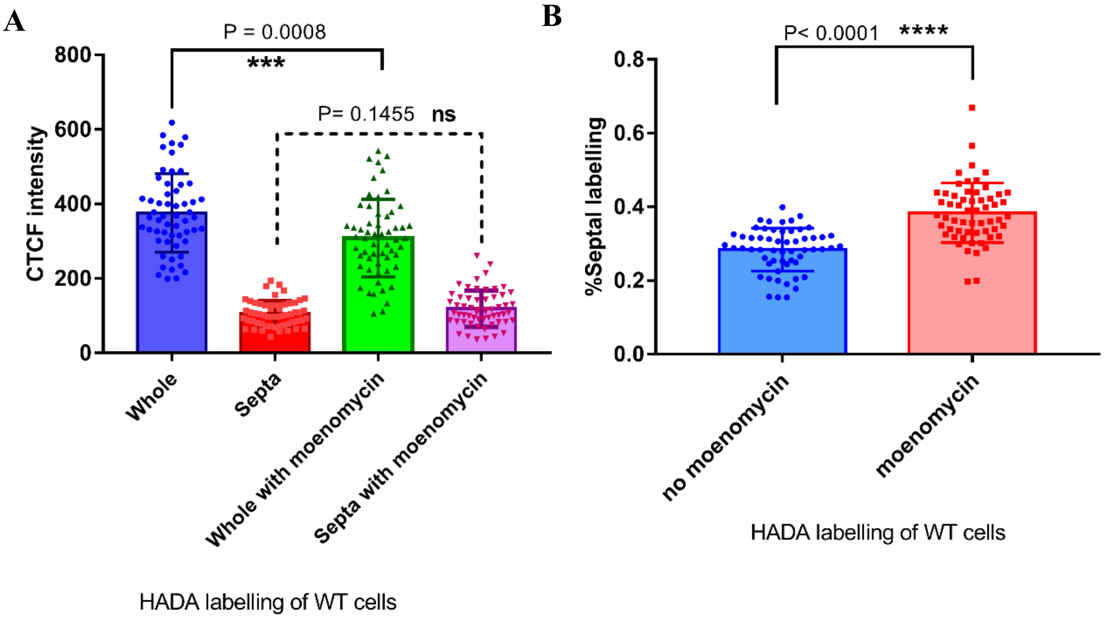

Figure 3.37 Quantifications of moenomycin effect on HADA labelling of WT cells. HAF488 labelled cells were regrown with or without moenomycin for 15 min followed by HADA staining. CTCF intensity of whole cells and septa was measured and statistically analysed. Comparisons of CTCF **(A)** and % septal labelling **(B)** were drawn using Scatter diagram with mean ± SD. P values were calculated by unpaired *t*-test with Welch's correction and statistical significance levels were shown as ns = not significant, p> 0.05; *p<0.05; **p<0.01; ***p<0.001; ****p<0.0001.

3.3 Discussion

3.3.1 Identification and evaluation of the probe suitable for reducing termini

To better understand cell dynamics, great efforts have been made toward real-time tracking of PG biosynthesis and remodelling by fluorescence imaging. Historically, fluorescent probes that can be specifically localized into cells have been widely used. Among the vast majority of studies used straightforward labelling strategies, chemical probes are routinely localized in the side chain of PG and direct visualization of specific sites within the glycan backbone using small molecular probes is rarely reported. As a result, in order to fill the gap, efforts herein were made to develop a suitable probe and establish a powerful labelling strategy for reducing termini of the glycan chain.

Before exploring HAF488, the reducing termini tagging probe, basic investigations of side chain labelling were conducted to unveil information of cell morphology, which were expected to be used as control to provide circumstantial evidence for later research of the reducing termini. Initial work was carried out by labelling exponential-phase *S. aureus* cells with well accepted fluorescent D-amino acids and fluorescent derivatives of vancomycin. Three kinds of FDAAs and two kinds of VanF were found to give a similar labelling profile with labelling at the septum and the cell periphery. This can be attributed to the commonly labelling mechanism involving the D-Ala residues. While having something in common, there were still some difference. Labelling the side chain with FDAAs is on the basis of a growth-dependent mechanism and FDAAs are incorporated into new synthesised PG. This suggests that preferential synthesis is at the septal plane of division and off-septal biosynthesis also occurs, which is consistent with published work.[115] However, for VanF labelling, it was a bit more complicated. VanF binds to the D-Ala-D-Ala residue. When cross-linked and uncross-linked PG is digested by carboxypeptidases, this results in the removal of terminal D-Ala residues.[25] However, unlike other Gram-positive bacteria, there is a scarcity of carboxypeptidases in *S. aureus*, giving a relatively high density of D-Ala-D-Ala residues left in the mature cell wall for fluorescent labelling.[139] Therefore, the peripheral VanF cell labelling can result from binding of both pre-existing and nascent D-Ala-D-Ala residues in the PG.

Having achieved the basic understanding of side chain labelling, optimization of HAF488 labelling was carried out and the side chain labelling probes were used as control. The fixing methodology was confirmed to play key role in HAF488 labelling and have no influence on VanF labelling. This difference was assumed to result from the variation of labelling sites. In the case of ethanol, fixation dehydrates surface ultrastructures and permeabilises cells, and therefore fluorescent probes may easily stain intracellular structures. When fixing with PFA, cross-linking formation from the reaction of PFA with the cell wall tends to shield or embed existing free aldehydes of PG, resulting in no or weak labelling. As a result, only post-fixing or no-fixing can be used for HAF488 labelling. On the contrary, D-Ala-D-Ala residues only appear in the cell wall, and both PFA-induced cross-linking and ethanol-induced dehydration did not alter the binding of vancomycin. By employing the optimized labelling strategies, the labelling quality of HAF488 was finally comparable to that of the side chain probes. The observation of the "┼"-like cross-labelling structure with HAF488 and the side chain probes confirmed the feasibility of HAF488 used for multi-labelling and the distinct labelling pattern of HAF488.

As stated above, it is challenging to find small-molecule fluorescent probes that directly label the glycan backbone. To date, the majority of labelling achievement pertaining to imaging the glycan of PG in bacterial cells has been conducted by using lectin-based probes such as dye-conjugated wheat germ agglutinin. Wheat germ agglutinin (WGA) is a lectin that binds to *N*-acetyl glucosamine residues throughout PG and teichoic acids, and therefore its fluorescent derivatives have been widely used for the cell wall imaging.[116,140] However, the probes had been reported to be limited to Gram-positive organisms and label only the outer wall without the septa distribution, due to their large sizes.[115,141] As shown in Figure 3.38A, WGA labelling merely occurred at the off-septal cell wall, although *N*-acetyl glucosamine is present throughout the cell wall. By comparison, HAF488 labelling was found with comparable quality to that of WGA labelling. Therefore, HAF488 has proven to be an extremely competitive small-molecule probe for the investigation of the reducing termini and is expected to shed new light into PG dynamics.

3.3.2 *In vivo* cell labelling using HAF488

After confirmation that HAF488 only labels the reducing termini of the cell wall, much experimental work was conducted via dual-labelling by HAF488 and the side chain probes, including comparison of *S. aureus* WT and mutants, tests of mutanolysin or moenomycin effect, and investigation of newly synthesised PG.

As expected, the lack of SagB resulted in decreased HAF488 labelling, which was confirmed by CTCF quantification. The *sgt mgt* mutant was equally labelled as compared to WT by HAF488, and the observation was in good agreement with the previous finding that lack of them has no major effect upon glycan chain length or PG composition in *S. aureus*.[142] In the *sagB* strain, due to a lack of cleavage of mature PG, long glycan chains in the periphery decreased the labelling effect, but at the septa incorporation of newly synthesised PG still occurred, resulting in a high % septal labelling. With respect to *sgt mgt* cells, there were several possible explanations for lack of phenotype. As enzymes act in concert within the cell, removal of SgtA and MGT may affect PBP2 activity. Another possibility was assumed to the localization of SgtA and MGT. PBP2 has been considered to exclusively act at the septum where the major amount of the cell wall synthesis occurs.[143] As a result, the peripheral synthesis has to recruit other GTs, probably SgtA and MGT. SgtA and MGT may be important in glycan strand synthesis at the cell periphery. Lack of them led to less polymerization of the glycan at the periphery.

Investigation of mutanolysin effect was conducted. However, both the growth test and HADA imaging conformed that *S. aureus* cells are mutanolysin-resistant. A similar labelling pattern of HAF488 was found in all cases, which suggested mutanolysin seems to exclusively act in *in vitro* degradation and has no effect on live cells.

New synthesised PG was also investigated via the strategy of using NH_2OH blocking and subsequently labelling after growth. The experiments were carried out with *S. aureus* WT, *sagB* and *sgt mgt* strain. Although there were no new finding by comparison of the strains due to the limited imaging resolution, cells from a variety of growth stage were characterised (Figure 3.39 A). Pre-treatment with NH_2OH blocked the reducing termini of the cell wall and prevented existing PG from specific HAF488 labelling. After short time growth (ie, 5 min), there was the appearance of new reducing termini. As cells continued to grow, labelling increased at the septum and the cell periphery. After 60 min, the majority of cells were successfully labelled with HAF488 at both the periphery and the septa with relatively identical fluorescence intensity, which was distinct from the septal preference in the VanF labelling pattern. A schematic depiction of the dynamics of the cell wall metabolism on the basis of HAF488 labelling of newly synthesised PG was hypothetically drawn (Figure 3.39 B). To allow cell growth, cleavage of the old cell wall occurs and the stiffness of the cell wall changes, resulting in expansion of the cell. Over time reducing termini increasingly appear at the cell periphery, due to wall hydrolysis and/or synthesis. After growth, septum formation is initiated, leading to eventual cell division.

Finally, both visualization and the CTCF analysis confirmed that moenomycin has significant effect on the incorporation of D-Ala. The inhibition experienced several phases: supressing the peripheral synthesis, affecting the septal action, and completely killing cells.

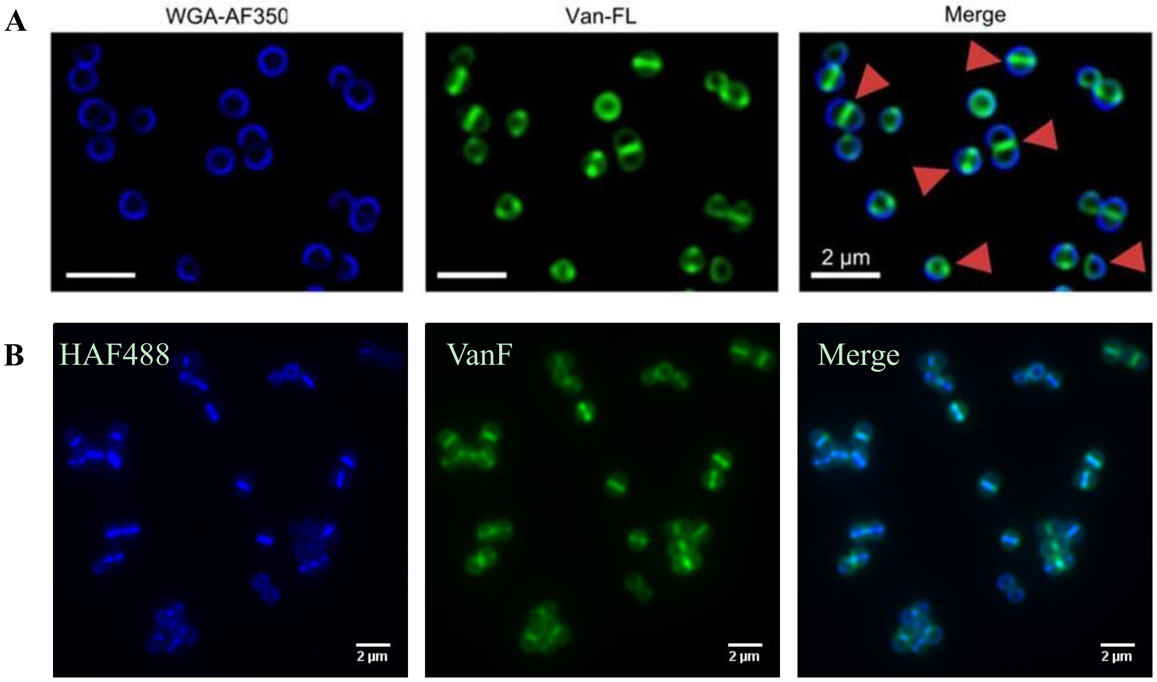

Figure 3.38 Comparison of WGA and HAF488 labelling of *S. aureus* cells. (A) Cells were dual-labelled with dye-conjugated WGA (Blue) and VanF (Green). Arrowheads show the difference between two probes. Image from published work in our laboratory Ref 18 with permission from *American Society for Microbiology*.[18] **(B)** Dual labelling using HAF488 and VanF was carried out.

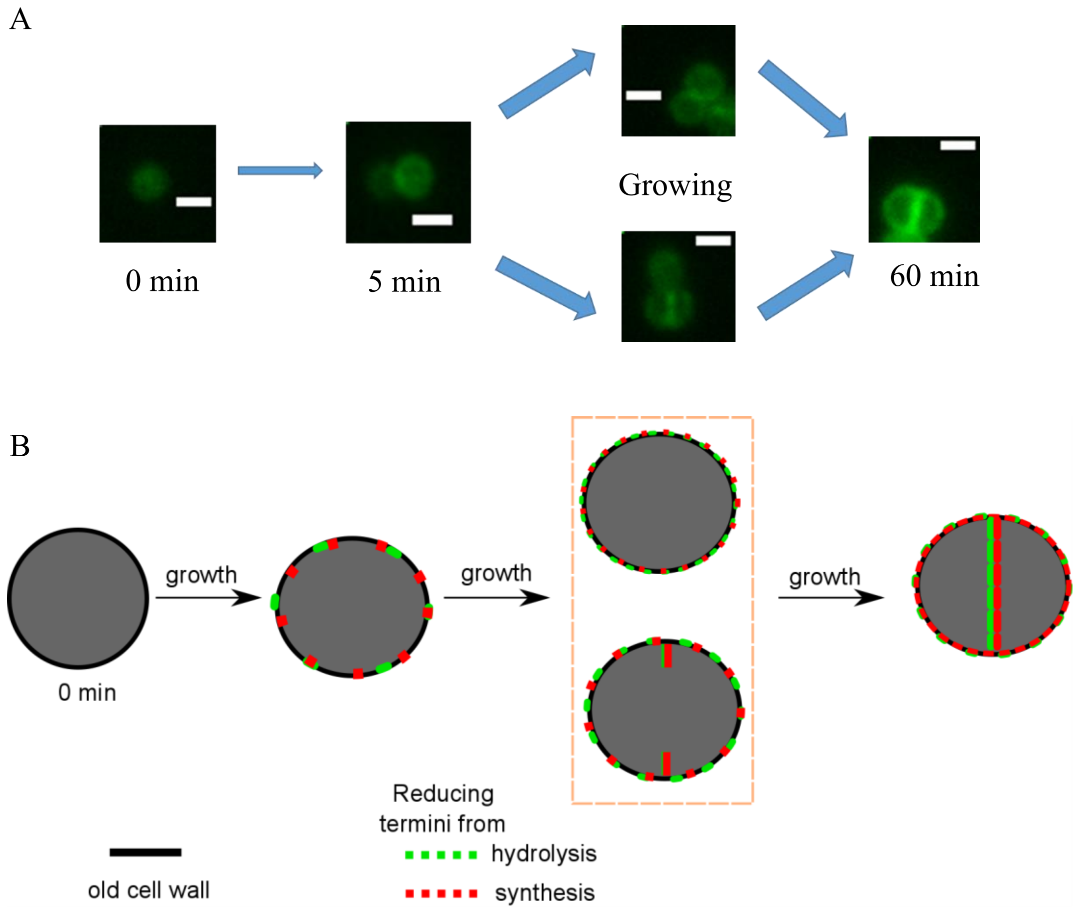

Figure 3.39 *S. aureus* cell wall dynamics after NH_2OH blocking. (A) Cells with NH_2OH pre-blocking were grown on in TSB and then labelled with HAF488. Representatively HAF488 labelled cells were chosen. Scale bars were 1 µm. **(B)** Schematic demonstration of the molecular basis for the appearance of new reducing termini in PG during the cell cycle.

Chapter 4 Development of multi-functional azide-probes for cell wall research

4.1 Introduction

In the previous chapter, HAF488 was successfully used for reducing termini labelling. However, due to the image resolution being curtailed by the diffraction limit, it was difficult to gain more insight into cell dynamics. Thus, super-resolution microscopy was to be applied to solve more biologically relevant questions. The problem with HAF488 is that its fluorophore is not compatible with super-resolution approaches such as STORM. Thus, in this chapter, it was proposed to generate a new suite of probes that are both usable in super-resolution microscopy and for live cell labelling.

Over the last several decades, the emergence of bioorthogonal reactions endowed by chemists have opened up new ways for using innovative probes bearing diverse functionalities in live cells, that allows dynamic tracking in their native state with high specificity and fast kinetics.[144,145] Among all of the widely used bioorthogonal reactions, click chemistry has attracted enormous interest as a versatile labelling method.[146,147] A click chemistry reaction is a 1,3-dipolar cycloaddition between an azide and a terminal alkyne to form a stable triazole, first defined by Sharpless.[148] Copper(I) salts are used as catalysts to accelerate the click reaction rate and enhance the regioselectivity, hence this reaction is also called a copper-catalyzed azide-alkyne cycloaddition (CuAAC) (Figure 4.1A).[149] While CuAAC routinely occurs *in vitro*, labelling in cells is problematic due to the toxic effects of copper, therefore much effort has been devoted to enhance the biocompatibility of the click reaction, leading to the development of strain-promoted azide-alkyne cycloaddition (SPAAC) (Figure 4.1B). SPAAC takes the advantage of cyclooctyne and successfully achieves a fast reaction with azides with no use of copper.[150]

PG, as the focused target, consists of polysaccharides and amino acids, and presents a variety of functional groups such as aldehydes that provide opportunities for modification and conjugation of cellular probes. Oxime-based ligation was employed for PG labelling because of its high efficiency, low cost and non-toxic byproduct (water) formation. The success of HAF488 labelling in my previous work proves the suitability of oxime-based ligation in PG research. In addition, an elegant strategy to functionalize the probe with a clickable moiety makes it possible to selectively bind a variety of modalities suitable for super-resolution microscopy, EM or AFM. As a result, multi-functional probes were prepared and these provided a range of approaches for information collecting and elucidation of cell wall dynamics.

4.2 Results

4.2.1 Design and prepare multifunctional probes for reducing termini labelling

Incorporation of a clickable moiety and hydroxylamine groups for oxime ligation were envisaged as the initial means towards the goal of preparation of cellular probes. Considering the poor water-solubility of imaging modalities, polyethylene glycol (PEG), a family of hydrophilic polymers of ethylene oxide, widely used in biological research, was applied as the framework of new probes.[151,152] Apart from aiding water-solubility, PEG also endows high flexibility for chemical modification and reduces nonspecific binding between probes and surrounding untargeted biological issues.[153] Moreover, antigenicity and immunogenicity, major barriers to cell labelling, can be decreased or even eliminated with the help of PEG.[154] It was worth mentioning that, because of its high reactivity, the hydroxylamine group was protected until the final stages of this synthesis. Summarily, the design and synthesis of new probes was strategized as shown in Scheme 4.1.

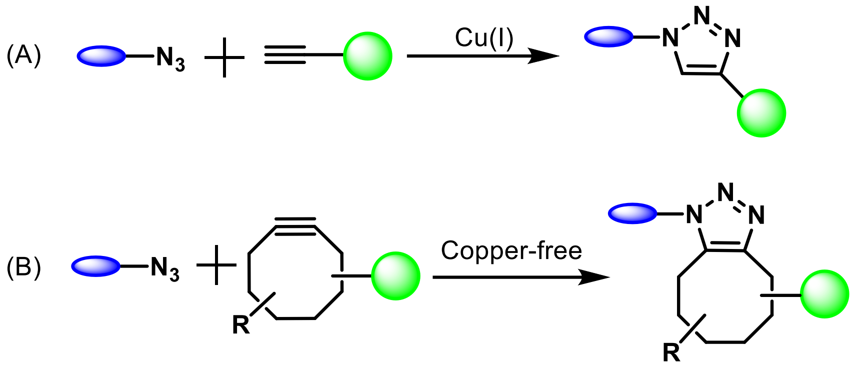

Figure 4.1 Click reactions for selectively labelling biomolecules. An azide and an alkyne or a cyclooctyne undergo cycloaddition through a copper(I) catalyst (A) or by relieving the ring strain of a cyclooctyne without the catalyst (B). As a result, biomolecules with a clickable moiety are labelled with probes functionalized with the complementary clickable moiety

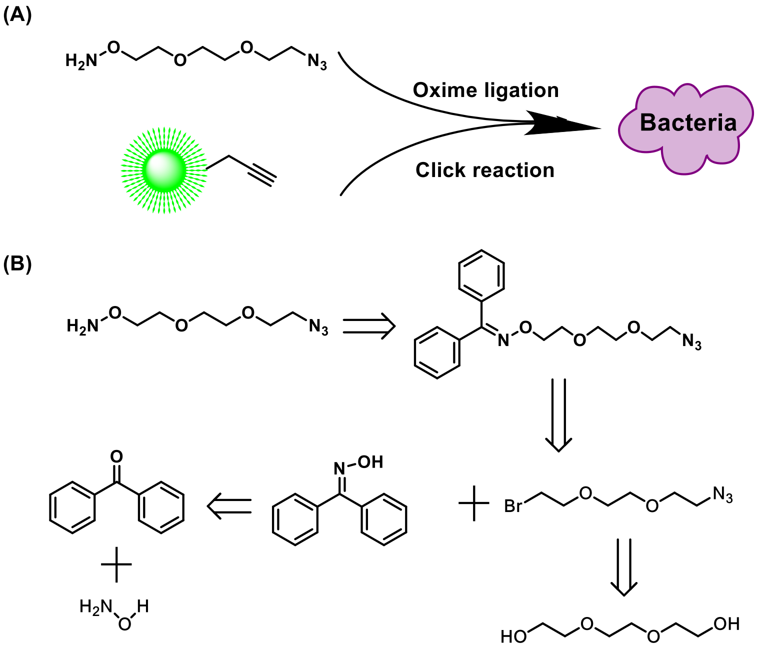

Scheme 4.1 Design and preparation of probes for cell imaging. (A) Strategy of cell labelling by oxime ligation and click reactions, the new liker specifically incorporates imaging modalities (Green) into the reducing termini of cell walls; **(B)** retrosynthesis of the azide-linker.

4.2.1.1 Synthesis of the azide probe from benzophenones and triethylene glycol

Initially, a benzophenone oxime surrogate of hydroxylamine was targeted. After several attempts according to previous work with minor modifications (Table 4.1),[155,156] a promising result was achieved by reacting ketone, $NH_2OH{\cdot}HCl$ and NaOH in a molar ratio of 1/1.5/1.5 at room temperature for 24 hours, followed by heating at 80 °C until ketone was completely consumed.

Having obtained the oxime precursor, the PEG dibromide was readily prepared as an intermediate followed by S_N2 substitution to incorporate an azide moiety (Table 4.2). Commercially available triethylene glycol (TEG) was treated with carbon tetrabromide (CBr_4) and triphenylphosphine (PPh_3) via an Appel reaction, giving the dibromide at 80% yield. Next, sodium azide was reacted with excess of the TEG dibromide in dimethylformamide (DMF) in an attempt to form the monosubstituted azide TEG bromide (N_3-TEG-Br). However, this failed and no mono azide product was formed. One possible reason may be the poor solubility of the inorganic azide in DMF. To test this presumption, azide was added into preheated DMF and heating continued until it was completely dissolved before the addition of TEG dibromides. Unfortunately, similar results were attained. 18-Crown-6 was used to selectively bind metal cations and thereby release free azide ions, which may accelerate azide substitution but this did not improve the outcome. Use of other solvents suggested essentially no N_3-TEG-Br was formed, as determined by ^{1}H NMR spectroscopy.

4.2.1.2 Updated routes for synthesis of the azide probe

Frustrated by these failures, effort was transferred to design a new synthetic strategy to prepare the monosubstituted azide TEG (Scheme 4.2). In the first route, TEG was reacted with 1.1 equivalent of tosyl chloride to form the mono tosylate, which was reacted with sodium azide. Initially, according to previous work with minor modification,[157] TEG was treated with sodium hydroxide in a mixture of THF and water followed with addition of tosyl chloride. However, formation of ditosylate and other unwanted compounds occurred and column chromatography on silica gel was needed to give the desired product (48% yield) (Table 4.3). Recently, Bouzide reported a simple protocol for monofunctionalization of symmetrical diols via tosylation mediated by silver oxide (Ag_2O) and a catalytic amount of potassium iodide (KI).[158] Two comparative experiments were performed at different temperatures following Bouzide's method. It was found tosylation at 0 °C afforded the highest yield with no need of further purification, confirmed by the ^1H NMR spectrum. Monotosylated TEG was then reacted with sodium azide in a different solvent to form the target azide compound (N_3-TEG-OH), with acetone/water and sodium iodide (NaI) being preferable reacting conditions (Table 4.4).

In an alternative route starting from commercially available 2-[2-(2-chloroethoxy)ethoxy]ethan-1-ol (Cl-TEG-OH), N_3-TEG-OH may be made in one step in water or DMF, respectively (Table 4.5). Both procedures worked, but better in water. Compared with the previous route, it was found that the second route only took one step which is direct and convenient. More importantly, the two-step yield in the first route was about 34% and this was much lower than 76% of the second. Consequently, the second route was used as primary choice for prepare of N_3-TEG-OH.

With the azide moiety successfully introduced, interest was then focused on incorporation of a hydroxylamine moiety via a Mitsunobu reaction on the azide-TEG in the presence of PPh_3 and diisopropyl azodicarboxylate (DIAD), affording the intermediate product (N_3-TEG-ONPhth) in a yield of 80%. Subsequent deprotection occurred in ethanolamine instead of commonly used hydrazine, releasing phthalimide and affording the desired product (NH_2O-TEG-N_3) with a high yield (92%), as shown in Scheme 4.3.

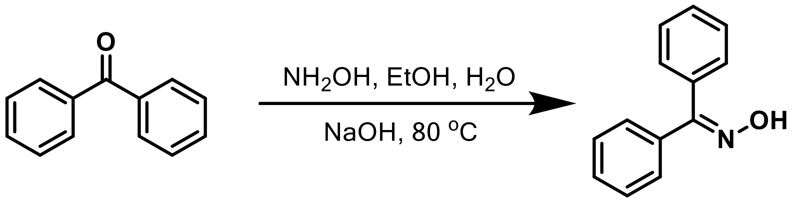

Amount of $NH_2OH{\cdot}HCl$	Amount of NaOH	Temperature	Volume ratio of EtOH and H_2O	Yield%
2 eq	1.3 eq	80 °C	1.4	-[a]
1.5 eq	1.5 eq	80 °C	9	-[a]
1.5 eq	1.5 eq	RT to 80 °C	9	95[b]

Table 4.1 Synthesis of benzophenone oxime. Reaction conditions: benzophenone and hydroxylamine HCl salt were completely dissolved in the solvent before addition of NaOH. The mixture was reacted at RT or 80 °C for 24-48 hours. a: after recrystallization, the product still contained with tiny by-products and was used directly for the next step; b: referred to the isolated product.

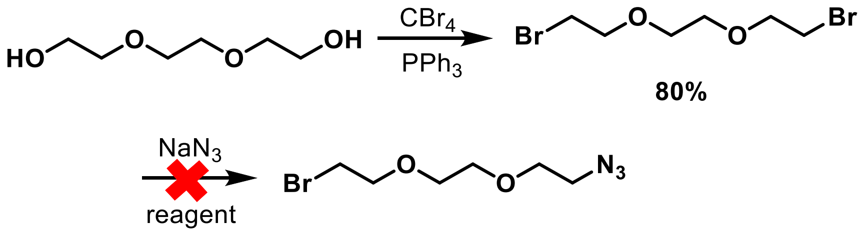

Reagent	Conversion %[a]
DMF	<5
Preheated DMF	<5
DMF and 18-crown-6	<5
Ethanol	<5
H_2O	<5

Table 4.2 Azide monosubstitution using two steps. Reaction conditions: first step: The PPh_3 THF solution was added dropwise to the mixture of TEG and CBr_4 in dry THF at 0 °C. After 1 h, the mixture was warmed to room temperature and stirred overnight; second step: sodium azide was added to the TEG dibromide solution and refluxed for 8-24 h. a: determined by analysis of the crude ^{1}H NMR spectrum.

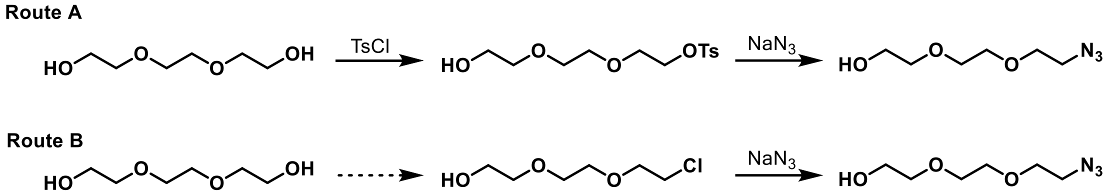

Scheme 4.2 New synthetic strategies to prepare monosubstituted N_3-TEG-OH via two steps. One hydroxyl group of TEG was turned into a better leaving group; OTs **(A)** or Cl **(B)**, followed by reaction with sodium azide.

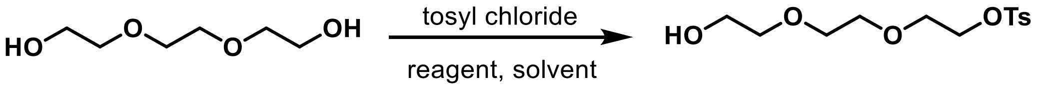

Reagent	Solvent	Temperature (°C)	Yield %[c]
NaOH [a]	THF/H_2O	0	48
Ag_2O, KI [b]	DCM	0	82
Ag_2O, KI [b]	DCM	50	34

Table 4.3 Synthesis of monotosylated TEG. Reaction conditions: a: TsCl (1.1 equivalents) in THF was added dropwise to the mixture of TEG (1 equivalent) in THF and NaOH (3 equivalents) water solution at at 0 °C, followed by warmed to RT and reacted for overnight; b: Ag_2O (1.5 equivalents), TsCl (1.1 equivalents), and KI (0.2 equivalents) were added to a solution of TEG (1 equivalent) in anhydrous CH_2Cl_2 at 0 °C, followed by reacted at 0 or 50 °C for 5 h. c: referred to the isolated product.

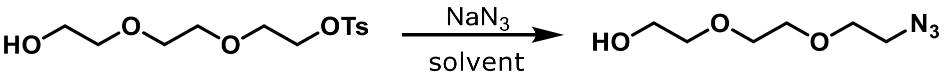

Solvent	Yield %[a]
DMF/H_2O (4:3)	40
Acetone/H_2O (1:1) and NaI	42

Table 4.4 Preparation of N_3-TEG-OH from monotosylated TEG. Reaction conditions: NaN_3 (2.5 equivalents) was added to the monotosylated TEG (1 equivalent) solution and the mixture was reacted at 60 °C for 10-18 hours. a: referred to the isolated product.

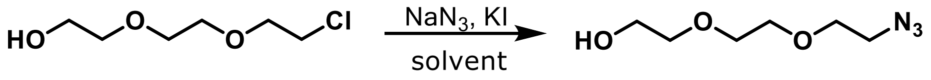

Solvent	Yield %[a]
H_2O	76
DMF	59

Table 4.5 Preparation of N_3-TEG-OH from Cl-TEG-OH. Reaction conditions: NaN_3 (2.5 equivalents) was added to the Cl-TEG-OH (1 equivalent) solution with KI (0.2 equivalent) and the mixture was reacted at 80-100 °C for 10-18 hours. a: referred to the isolated product.

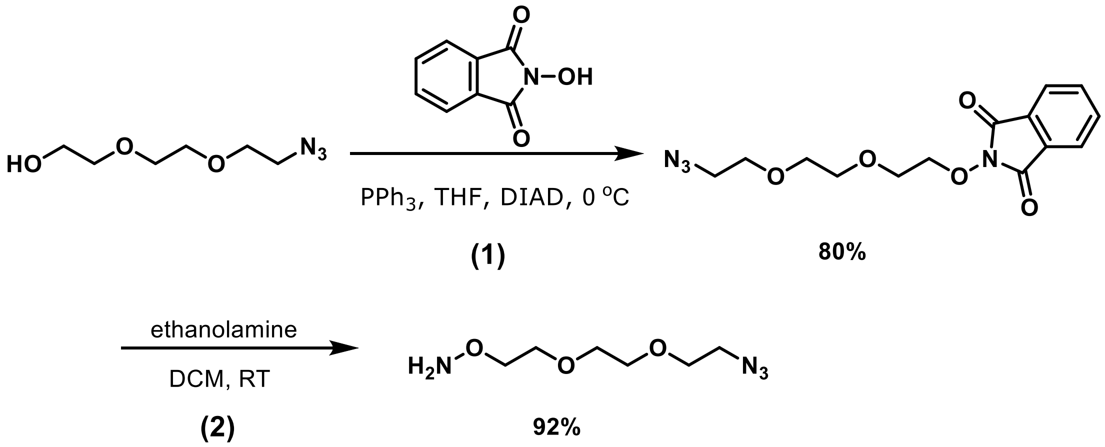

Scheme 4.3 Preparation of NH_2O-TEG-N_3. Reaction conditions: (1) DIAD (1.5 equivalents) in dry THF was added dropwise to the mixture of the mixture of N_3-TEG-OH (1 equivalent), hydroxyphthalimide (1.5 equivalents) and PPh_3 (1.5 equivalents) in dry THF at 0 °C followed by warmed to RT and reacted overnight; (2) ethanolamine (2.1 equivalents) was slowly added to N_3-TEG-ONPhth (1 equivalent) in DCM and the mixture was stirred at RT overnight.

4.2.1.3 Chemical test of the azide probe

With the functionalized TEG linker in hand, a model reducing terminus was targeted to test the ligation efficiency of the linker (Scheme 4.4). The synthetic route for the preparation of the model involved two steps starting from benzylation of *N*-acetylglucosamine (Glc*N*Ac) followed by partial debenzylation, releasing the aldehyde group. Following a widely-cited traditional approach, Glc*N*Ac was treated with BaO, $Ba(OH)_2$ and benzyl bromide (BnBr) to benzylate the hydroxyl groups as represented in Table 4.7.[159] Unfortunately, the crude product was very complex even after partial purification by recrystallization. During this experiment, in the ice-bath the reaction mixture froze solid over time. Thus, an experiment was performed at room temperature, expecting a better outcome. No target compound was formed with lower mass return. Then sodium hydroxide and sodium hydride was used and it was found in some case target compound could be formed, but some impurities were hard to remove even if processed by recrystallization and column chromatography on silica gel (Table 4.6).

4.2.2 Fluorescence imaging of reducing termini of cells

4.2.2.1 Analysis of the feasibility of bacterial labelling using click reactions

Initially, the feasibility of the click reaction in bacteria was investigated (Figure 4.2). According to the previous achievement of FDAAs labelling, azide modified D-alanine (3-azido-D-alanine, ADA) was applied to incorporate the azide functionality into cell walls, followed by a click reaction with the Alexa Fluor® 647 dye with an alkyne (Alkyne647). A series of experiments were performed, including directly labelling cells with ADA, ADA labelling NH_2OH-blocked cells after regrowth, and dual labelling cells with ADA and HAF488. It was clearly shown that in all cases a Cu(I)-catalysed click reaction successfully labelled cells with the dye. In addition, reaction in the click buffer mixture for 30 min had no significant influence on HAF488 labelling, which suggested the feasibility of multiple iterative labelling based on click reactions.

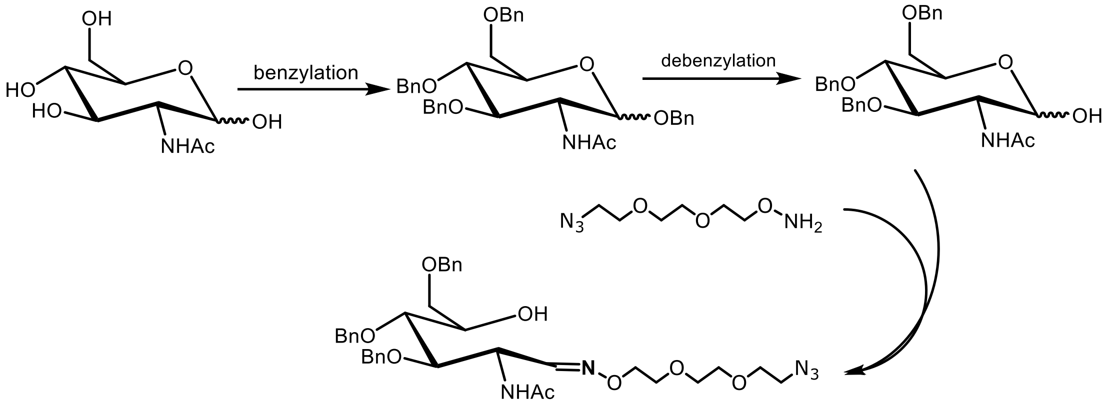

Scheme 4.4 Chemical test of NH_2O-TEG-N_3. Via two steps, specifically protected Glc*N*Ac, a mimic of PG components, would be achieved. Subsequently, NH_2O-TEG-N_3 were expected to react with the aldehyde moiety of the mimic and the resulting oxime could be investigated using NMR and MS.

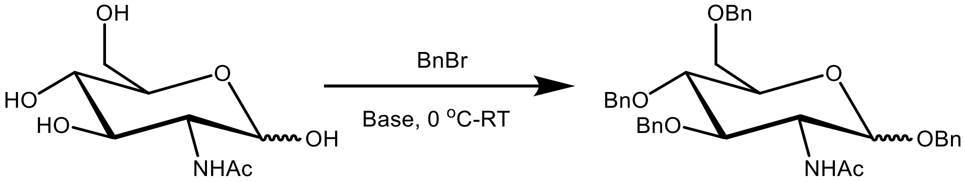

Base	Solvent	Temperature	Yield
$Ba(OH)_2$, BaO [a]	DMF	0 °C-RT	No reaction
$Ba(OH)_2$, BaO [a]	DMF	RT	No reaction
NaOH [b]	DMF	0 °C-RT	-[d]
NaOH [b]	DMF	RT	-[d]
NaOH (powder) [b]	DMF	RT	-[d]
NaH [c]	THF/DMSO (1:5)	0 °C-RT	-[d]
NaH [c]	THF/DMSO (1:5)	RT	-[d]
NaH [c]	DMF	0 °C-RT	-[d]
NaH [c]	DMF	RT	-[d]

Table 4.6 Synthesis of benzyl Glc*N*Ac. Reaction conditions: The mixture of Glc*N*Ac (1 equivalent), BnBr (5-10 equivalents) and base in dry solvent were reacted for 6-24 h. a: $Ba(OH)_2$ (2 equivalents), BaO (9 equivalents); b: NaOH (10 equivalents); c: NaH (6 equivalents); d: the product was very complex even after purification by recrystallization and column chromatography on silica gel.

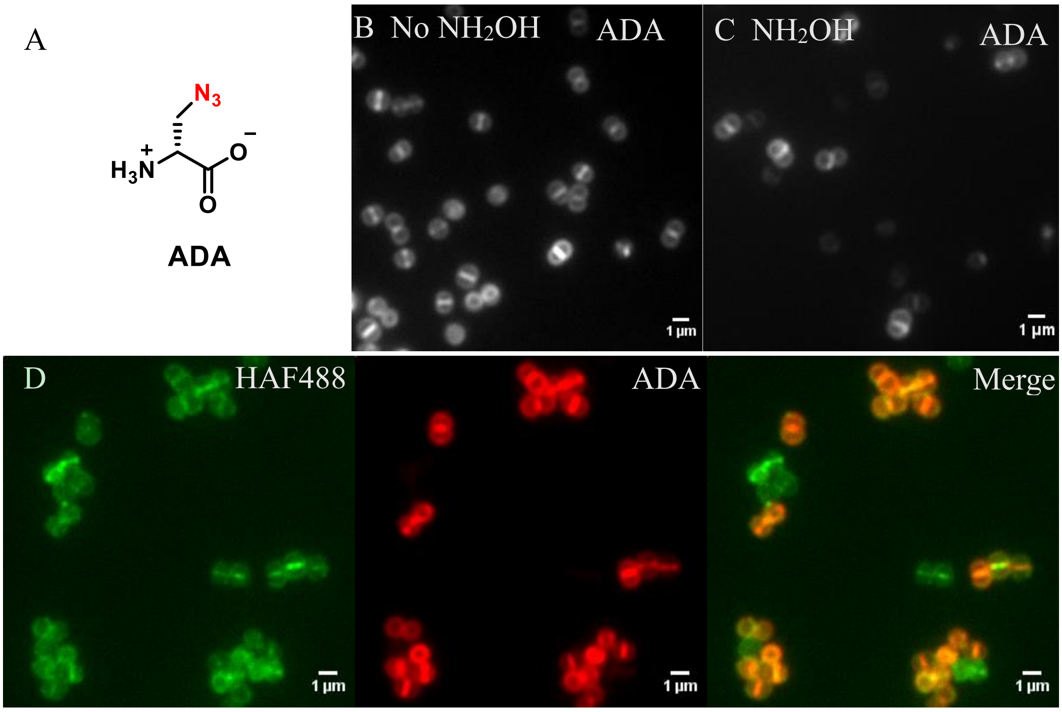

Figure 4.2 Analysis of biocompatibility of the click reaction during cell labelling. **(A)** Chemical structure of ADA. **(B)** Exponential-phase *S. aureus* WT were treated with ADA in TSB (500 µM) at 37 °C for 5 min, washed and reacted with Alkyne647, followed by fixing. **(C)** NH_2OH-pretreated cells were resuspended in TSB at 37 °C for 10 min and then labelled with ADA and Alkyne647 via a Cu(I)-catalysed click reaction before fixation. **(D)** Cells were dual labelled with ADA and HAF488 (Green), followed by the click reaction with Alkyne647 (Red) and fixation.

4.2.2.2 Optimising the conjugation strategy for the azide-probe

4.2.2.2.1 Effect of the click reaction parameters

Optimization of labelling cells using the clickable TEG probe were conducted. Considering the functional structure similarity between the new probe and HAF488, a similar labelling procedure was employed where exponential-phase *S. aureus* WT cells were incubated with the clickable TEG probe in BHI with a final volume of 1 mL at 37 ºC for 5 min and HAF488 labelling was also simultaneously carried out as a control. Alkyne-terminated Alexa Fluor® 488 (Alkyne488) was first used to label the azide incorporated cells using a copper-catalysed click reaction, which was consistent with HAF488. It was found that cells were successfully labelled with HAF488 (Figure 4.3 A) while the TEG probe failed to label cells (Figure 4.3 B), where a majority of cells were completely stained and a tiny minority showed faint labelling (Red arrows).

As the feasibility of bacteria labelling using click reactions has been successfully validated (Chapter 4.2.2.1), other factors probably contributing to the labelling failure were investigated. Chemically, there were two options for cell labelling on the basis of click reaction strategies, termed post- and pre-click (Scheme 4.5). Compared with HAF488, the extremely small size and biologically relevant properties of TEG probably had a big effect on the permeability of cell wall, which contributed to the staining of whole cells. In contrast to post-click labelling performed above (Figure 4.3 B), pre-click labelling, where a click reaction was carried out to ligate the probe before labelling cells, could form an active probe with strong similarity on structure and size to HAF488. Therefore, pre-click labelling was next employed. As depicted in Figure 4.3 C, in this way cells were successfully labelled with new probes and exhibited a similar pattern to HAF488 labelling. All this suggested that the order of conducting the click reaction played a crucial role in the labelling of reducing termini.

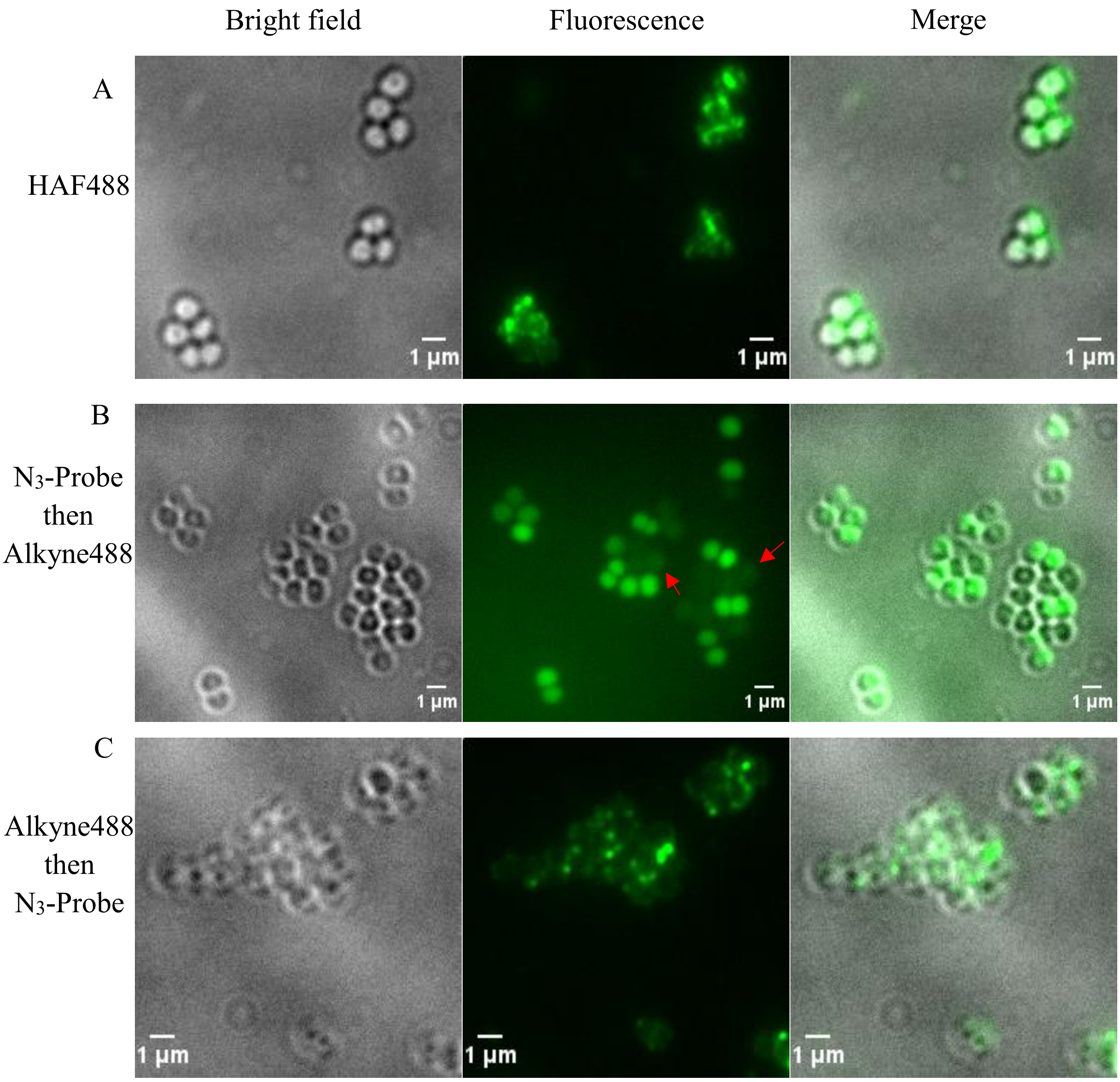

Figure 4.3 Effect of click reaction methodology on cell labelling. Cells were incubated in BHI with HAF488 **(A)** or NH_2O-TEG-N_3 **(B)** stock at a final volume of 1 mL at 37 °C for 5 min, and washed. Azide incorporated cells were reacted with Alkyne488 in the presence of $CuSO_4$ and click additive in the click buffer at RT for 30 min. **(C)** Click reaction between NH_2O-TEG-N_3 and Alkyne488 occurred under the same conditions and cell pellets were then resuspended in the resulting mixture at 37 °C for 5min. All samples were fixed with ethanol for imaging at bright field and 488 fluorescence channel. Arrows: characteristic labelling features.

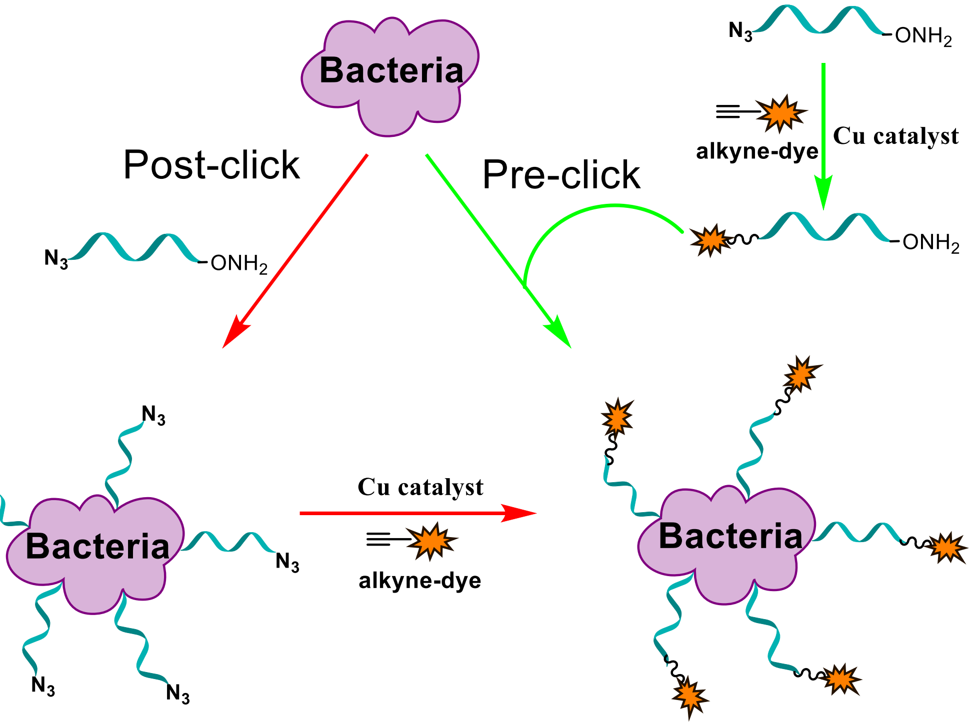

Scheme 4.5 Click reaction strategies for cell labelling. Two possible labelling routes, termed post- (Red) or pre-click (Green) labelling, were used on basis of the order of conducting click reactions. Post-click labelling: cells were treated with the azide-probe followed by a click reaction with alkyne-dyes; Pre-click labelling: the azide-probe and an alkyne-dye underwent a click reaction and the resulting complex was used for cell labelling.

Apart from the order of conducting the click reaction, copper salts may be another critical influence on the labelling results. In the click reaction, copper salts are routinely applied to accelerate the reaction process, but they have considerable toxicity to cells. This suggests that labelling in live cells probably would be problematic. In the previous test of the feasibility of click reactions in bacteria, the cell states should not be effected by the click reaction, as the cells had been assembled with azide groups prior to the click reaction. Therefore, a compensatory test was investigated using dual labelling with a clickable dye and fluorescent amino acid TADA (tetramethylrhodamine 3-amino-ᴅ-alanine), which not only checked the survival status of cells after copper treatment, but also provided complementary information of cell structures. In addition, the TEG probe labelling buffer was replaced from culture to PBS in order to avoid cell growth. As shown in Figure 4.4, labelling results were consistent with previous work (Figure 4.3) and the order of conducting the click reaction was still crucial, in which pre-click labelling was preferred. Fluorescent amino acids were successfully incorporated into cell walls in both cases, which suggested that cellular activity was maintained at the normal level and the copper salt used was non- or low toxic to *S. aureus*. All observations indicated that the main factor contributing to the labelling results was the order of conducting click reactions rather than the use of copper catalyst.

4.2.2.2.2 Effect of the oxime reaction volume on cell labelling

Following previous work with HAF488 labelling, reaction with the NH_2O-TEG-N_3 probe was carried out in PBS at a final volume of 200 μL rather than 1 mL, followed by a post-click reaction with the dye (Figure 4.5). Meanwhile, VanF was applied to replace TADA as the contrast label in order to exclude the possibility of culture effects on cell morphology. Surprisingly, the labelling protocol provided a high-quality Alkyne488 labelling. To avoid false positives, this same labelling work was repeated several times and similar results were achieved, although whole cell staining was inevitably found again in a fraction of cells (data not shown). Two probes showed different labelling phenotypes in some cells. For instance, the cell displayed strong VanF labelling at the septum and had begun or was about to begin splitting (dashed boxes in Figure 4.5). As for the Alkyne488 signal, labelling was observed at both the septum and a less bright band at an orthogonal orientation that was considered as the upcoming septum for the next generation. This finding was consistent with the previous pre-fix work (Figure 4.4 B). All results indicated that the oxime reaction volume played a crucial role in the reducing termini labelling and the post-click method was also capable of live cell labelling.

4.2.2.2.3 Effect of concentrations of dye and azide probe on cell labelling

Before further studies of *S. aureus* cell morphology, optimisation of labelling conditions was carried out, including concentrations of dye and azide probe. Initially, cells were tested with increasing concentrations of dye from 0.25 to 25 µg/mL (Figure 4.6). It was clearly shown that in all cases cells were successfully labelled, but when 2.5 µg/mL of dye was used, a better contrast was achieved. As labelling at a concentration of 15 or 25 µg/mL gave a similar result, 2.5 µg/mL was the optimal concentration of Alkyne488. Optimisation of concentrations of azide probe used for labelling were next investigated using the optimal concentration of Alkyne488. As depicted in Figure 4.7, in the case of using 500 or 750 µM of azide probe, cells were labelled with high contrast and the fluorescence intensity seemed to have reached a plateau. Therefore, 500 µM of azide probe was sufficient for labelling cells via a click reaction.

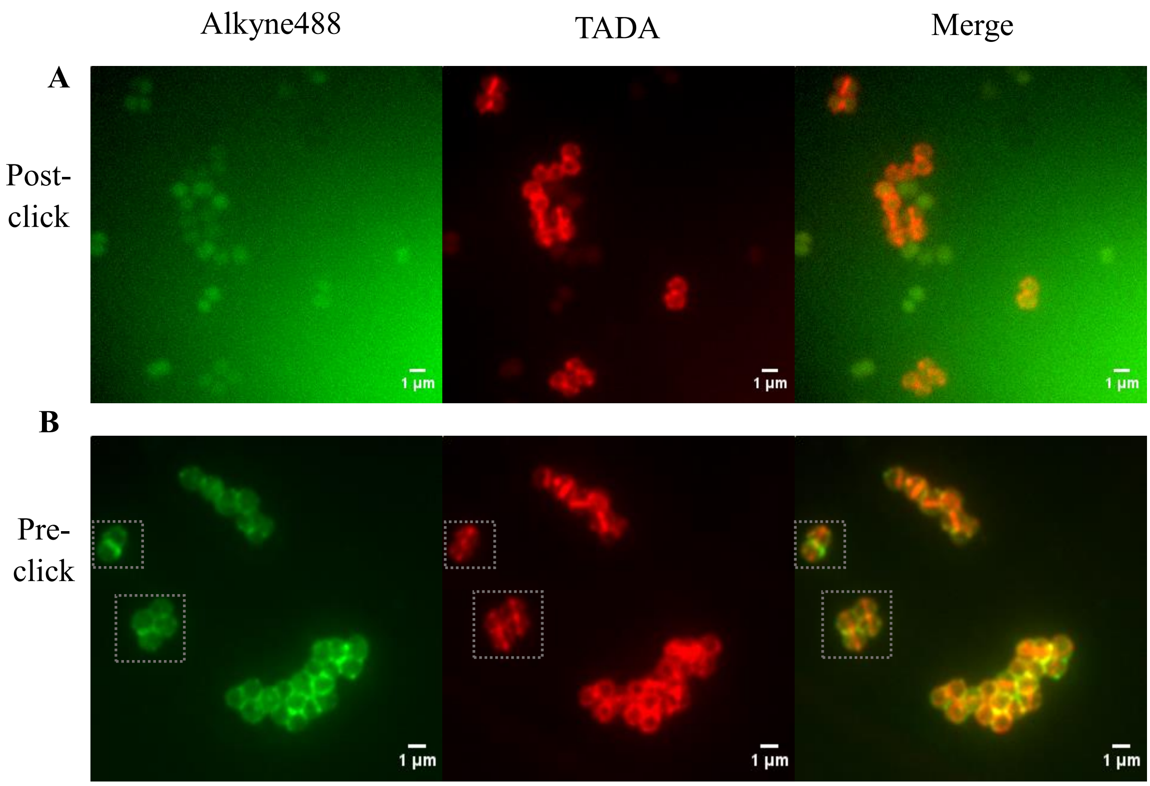

Figure 4.4 Test of cell viability after post- or pre-click labelling. Cells were labelled with NH_2O-TEG-N_3 and Alkyne488 in either the post- (**A**) or pre-click (**B**) pattern. The treated cells were incubated with TADA in TSB at 37 °C for 5 min. All samples were fixed for imaging. Green: Alkyne488; Red: TADA. Dashed boxes: cross-labelling “┼”-like structures.

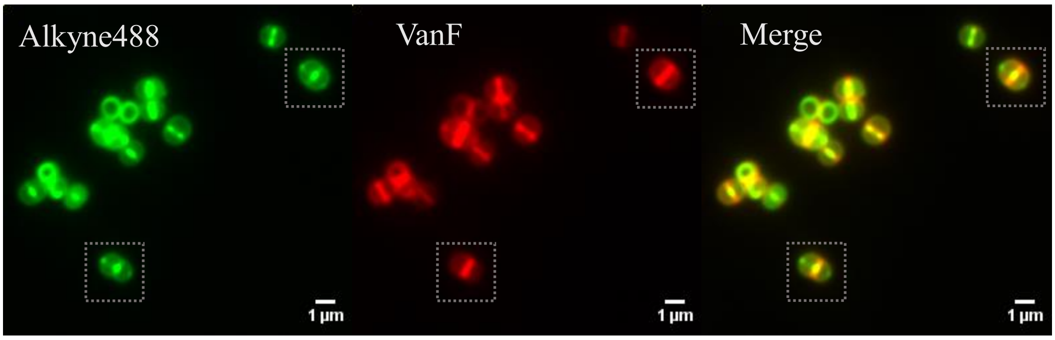

Figure 4.5 Dual labelling of cells using TEG probe in a decreased reaction volume and VanF. Cells were incubated with NH_2O-TEG-N_3 in PBS at a final volume of 200 µL and subsequently reacted with Alkyne488 (Green) in the post-click method. The treated cells were labelled with VanF (Red) before fixing with ethanol for imaging. Dashed boxes: cross-labelling “┼”-like structures.

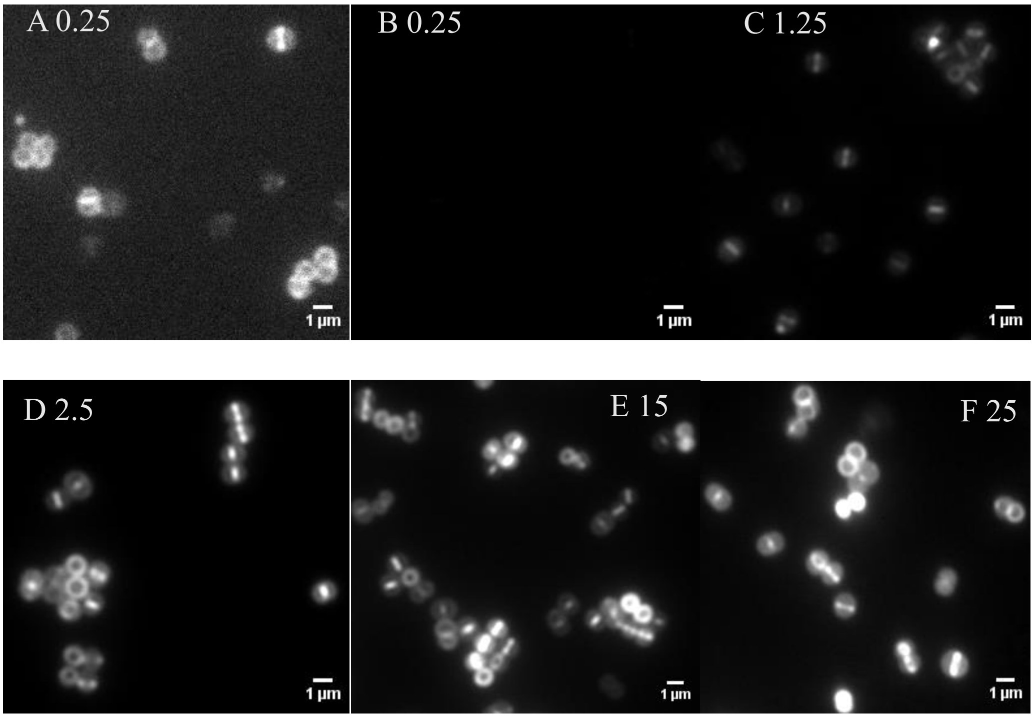

Figure 4.6 Optimising dye concentrations used for cell post-click labelling. Cells were incubated with azide probe in PBS at a final volume of 200 µL and subsequently post-click reacting with Alkyne488. (**A**) 0.25 µg/mL, high contrast; (**B**) 0.25 µg/mL; (**C**) 1.25 µg/mL; (**D**) 2.5 µg/mL; (**E**) 15 µg/mL; (**F**) 25 µg/mL.

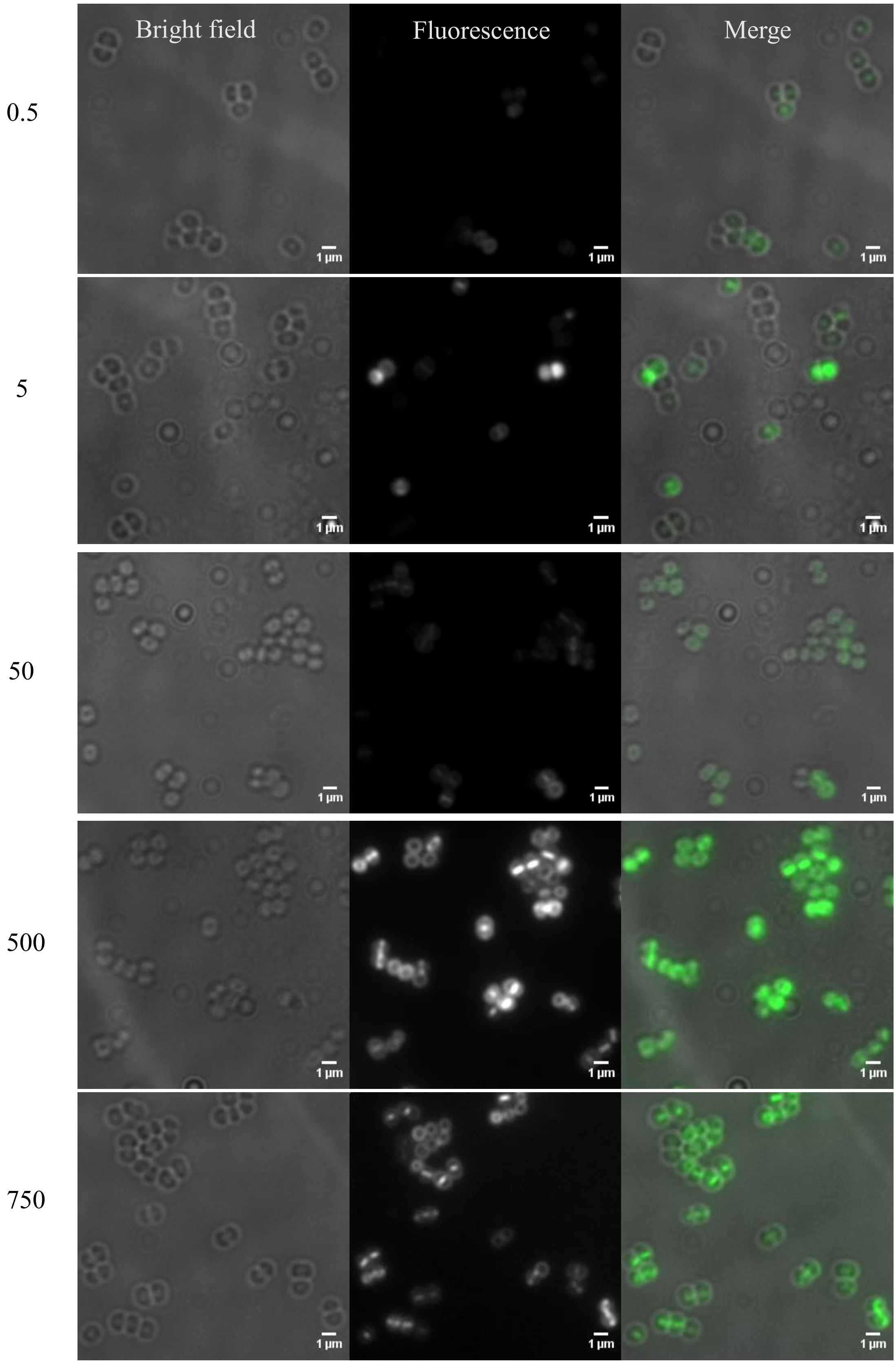

Figure 4.7 Optimising azide-probe concentrations used for cell labelling. Cells were incubated with azide probe in PBS at different concentrations before post-click reaction with Alkyne488 (2.5 µg/mL), at 0.5, 5, 50, 500 or 750 µM.

4.2.2.3 Verification of the localization of the azide probe/alkyne-dye

Once all optimisation of labelling strategy had been carried out, localisation of the azide probe was verified to determine whether the target site was strictly confined to PG rather than other components of the cell wall. To exclude this possibility, the cell wall was extracted and purified, and the generated PG was then dual-labelled with azide probe/ Alkyne488 and VanF (Figure 4.8). A clear fluorescence signal was observed from Alkyne488 in the case of 5 min labelling and it was sufficient to characterize structural features of cells. When PG was labelled for long time, images with high contrast were achieved. Both cases displayed some cells, where a VanF signal appeared at the septum and Alkyne488 was broadly distributed throughout the cell periphery. This observation was consistent with previous results of live cell labelling (Figure 4.5). All results suggested that the azide probe was incorporated at the reducing termini of PG rather than other sites of the cell.

4.2.2.4 Labelling of a range of bacterial PG reducing termini

4.2.2.4.1 Comparison of WT and *sagB* strain labelling

As mentioned in the previous chapter, SagB is a key glucosaminidase and lack of it results in an increase of glycan chains length in PG, which subsequently affected the labelling phenotype of reducing termini. The azide probe was used to determine if the *sagB* mutant alters labelling in comparison to the HAF488 (Figure 4.9). Compared with WT cell labelling, the HAF488 signal in the *sagB* mutant seemed to weaken and the labelling pattern changed from mainly localising throughout the cell wall septum (main labelling region) and periphery, to tightly restricted at the septum without the peripheral labelling. However, the changes were not very obvious before quantitative analysis. When cells were labelled with the azide probe, the changes of the labelling pattern were relatively clear, probably due to the high signal-to-noise ratio provided by the azide probe. This observation is consistent with the conclusion in the previous chapter of

HAF488 labelling where the cell walls of the *sagB* mutant have less reducing termini and lack of SagB probably results in deficiency or decrease of the peripheral labelling.

4.2.2.4.2 *B. subtilis* labelling

Another bacterium (*Bacillus subtilis*) with different glycan content was next investigated. *B. subtilis*, an aerobic, sporulating Gram-positive bacterium, is widely applied as the bacteria model for biological research and a cell factory for production of many industrial enzymes and proteins.[160,161] As a canonical rod-shape bacteria, *B. subtilis* has very different PG from *S. aureus* cells with the length of glycan chains being up to 5 μm, which suggested that the distribution of reducing termini is different.[162] Compared with *S. aureus* cells, *B. subtilis* displayed fairly weak fluorescence with both probes and this indicated that *B. subtilis* presents a small amount of reducing termini, in accordance to the existence of long glycan chains (Figure 4.10). Surprisingly, there was an obvious difference in the labelling phenotype between HAF488 and Alkyne488 incorporated via the post-click reaction. As depicted in Figure 4.10 A, HAF488 labelling was broadly localised throughout the cell wall and the staining structures were observed as blob-like features. These features seemed to have similar fluorescence but there are rare "special blobs" that were super bright or dark. On the contrary, Alkyne488 labelling showed integrated bands or bright foci that were obviously differentiable with adjacent structures (Red arrows in Figure 4.10 B). In addition, a small amount of cells had whole staining and were much brighter. Based on previous experience, one possibility that led to the differences was the click reaction method. To exclude this possibility, the pre-click labelling procedure was carried out to incorporate Alkyne488. Similarly to the post-click labelling, the pre-click labelling stained the cell wall as features of bands or bright foci rather than blob-like structures observed in HAF488 labelling. All these suggested that in this strategy, the click procedure had only a small influence and the difference in the labelling phenotype between HAF488 and Alkyne488 was probably attributed to different chemical and physical properties of the probes.

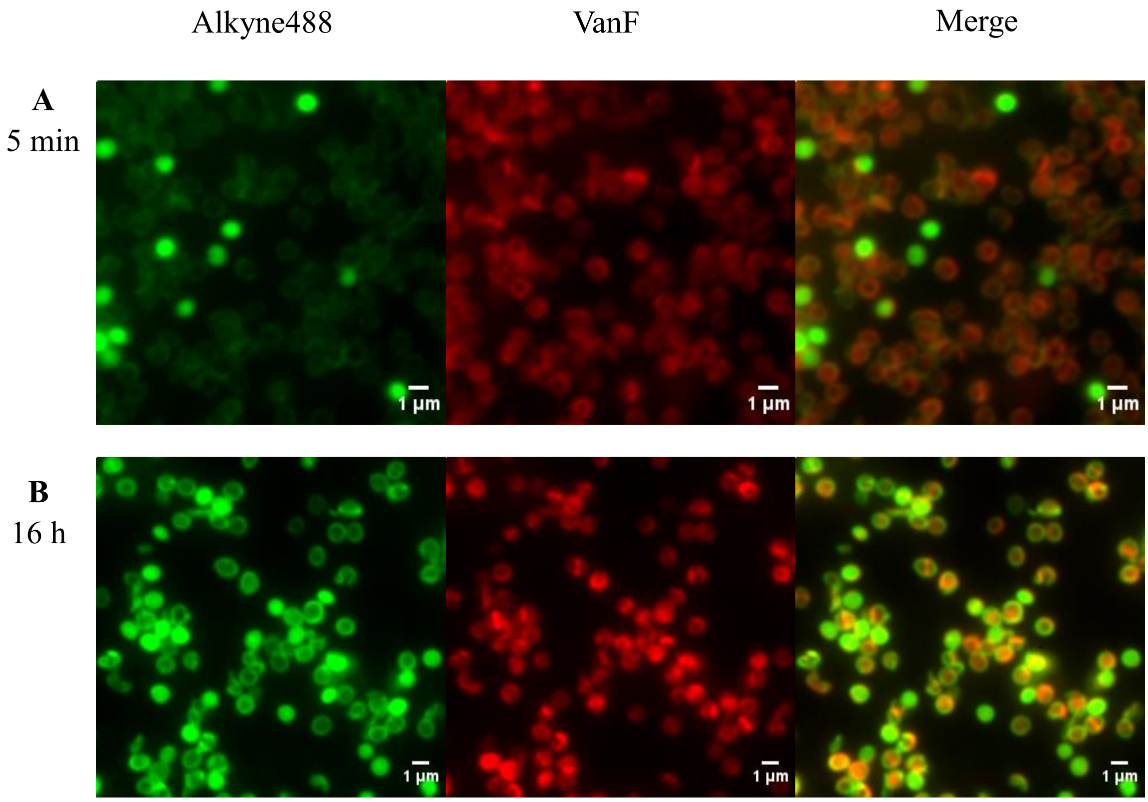

Figure 4.8 Dual labelling of purified PG using azide probe and VanF. PG was extracted from exponential-phase *S. aureus* WT cells, purified and incubated with azide probe for 5 min (**A**) or 16 h (**B**) followed by click reaction with Alkyne488 (Green) and labelled with VanF (Red).

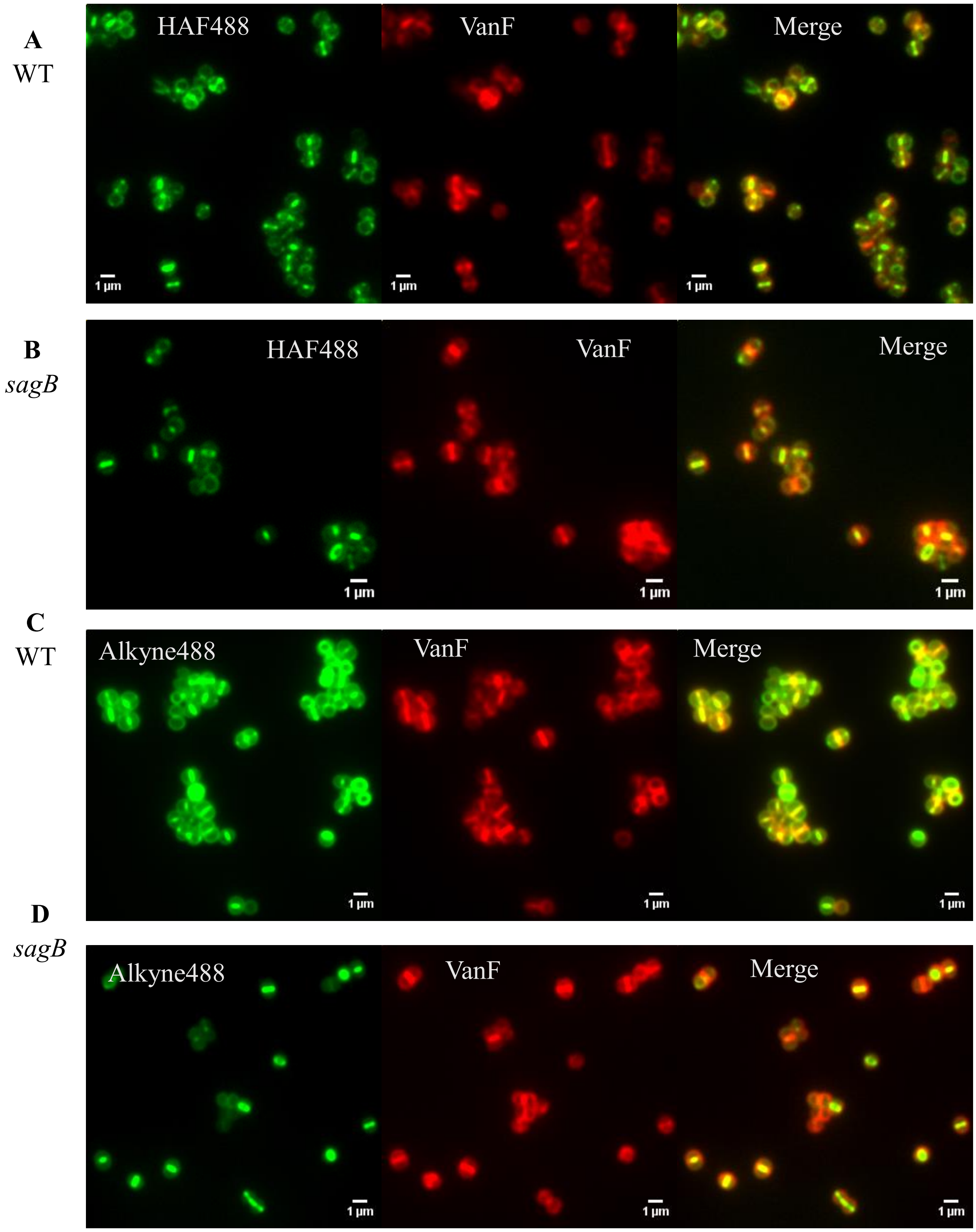

Figure 4.9 Dual labelling of live cells using HAF488 or azide probe and VanF. *S. aureus* WT (**A** and **C**) or *sagB* mutant (**B** and **D**) cells were labelled with HAF488 or azide probe for 5 min. Azide probe-labelled cells were reacted with Alkyne488 by click reaction. All treated cells were stained with VanF.

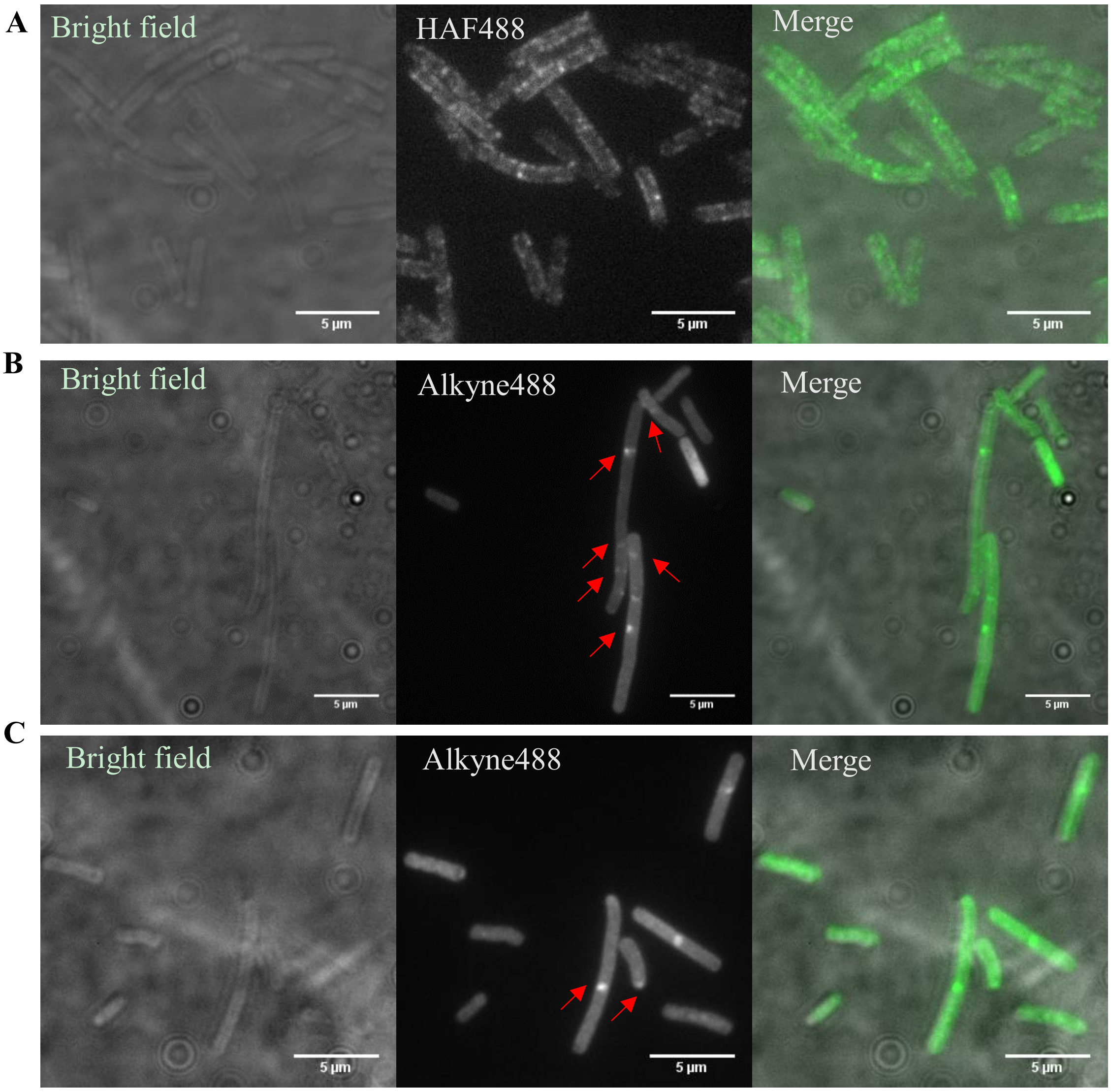

Figure 4.10 Labelling of *B. subtilis* cells using HAF488 or azide probe. (A) Exponential-phase cells were labelled with HAF488 in PBS at 37 °C for 5 min. Cells were labelled with azide probe and Alkyne488 in the post- **(B)** or pre **(C)** -click pattern. Red arrows: characteristic labelling features.

4.2.2.5 Characterisations of newly synthesised PG

Bacterial cell growth and division are closely associated with PG metabolism. Tracking of newly synthesised PG has been shown to be a powerful tool to better understand this close relationship.[25] Reducing termini labelling, as an investigative strategy, provides the possibility to gain new insights into cell dynamics. Reducing termini normally appear in mature cell walls and also occur by hydrolysis of PG during cell growth and division. As previously stated, distinguishing nascent PG from the mature cell walls is not possible by direct HAF488 labelling. Treatment with NH_2OH blocks mature PG of live cells and subsequent new growth generates new reducing termini for probe labelling. Therefore, a dual-labelling strategy was developed based on HAF488 and the azide-probe, in which one probe was used for the mature cell wall and the other was for new reducing termini (Scheme 4.6).

Initially, based on the labelling order, two complementary experiments were carried out, which were referred to HAF488-Alkyne647 and Alkyne647-HAF488 labelling on the basis of the order of labelling (Figure 4.11). Meanwhile, the recovery of PG labelling was also checked by growing labelled cells for 30 min before labelling cells with the other probe. It was found that HAF488 labelling provided abundant signal, but the subsequent azide probe/Alkyne647 labelling failed, which suggested that all the reducing termini had been occupied by HAF488. The background signal in Alkyne488 labelling was likely nonspecific, as all bright cells or structures had lost their characteristic features such as the septum with distinct brightness. After 30 min growth, the HAF488 signal was faded whilst the Alkyne647 signal appeared and displayed a different localisation pattern to HAF488. This indicated that the recovery of Alkyne647 signal was due to new PG synthesis and/or hydrolysis.

However, on the other hand, when cells were first labelled with Alkyne647, followed by HAF488 treatment led to a variety of labelling patterns that should be “dark”. For instance, some cells were completely unlabelled, some underwent entire cell staining, and some displayed a weak but recognizable septal labelling. As shown in Figure 4.11D, 30 min growth resulted in a change in labelling localisation. Although the background signals seemed high, cross-septum labelling features were observed, and these also occurred in grown on cells that were labelled with the inverse probe order (Figure 4.11B). Compared with the HAF488-Alkyne647 order of labelling, the Alkyne647-HAF488 order displayed imaging results with low contrast and high background signals. The low fluorescence signal was probably due to the steric hindrance of big size of the HAF488 dye on the reaction of the alkyne dye. As the click reaction of Alkyne647 and azide loaded cells was carried out after HAF488 labelling, HAF488 may shield the small molecule azide from interaction with alkyne dye, resulting in decrease of fluorescence signal. Inefficient washing and slide preparation could lead to high background signal. Summarily, the HAF488-Alkyne647 order of labelling not only exhibited a strong signal but also gave complete saturation of reducing termini in the cell wall. Therefore, the HAF488-Alkyne647 order of labelling was applied in further studies of newly synthesised PG.

As depicted in Figure 4.12, HAF488 pre-labelled cells were grown in TSB and newly formed PG was labelled with the azide probe/Alkyne647. With the passage of time, the HAF488 fluorescence signals gradually weakened and were distributed at a variety of locations of new cell wall. On the other hand, Alkyne647 labelling changed from dark to bright due to the cell growth and division. Cross-septum labelling features were increasingly found. After regrowth, the HAF488 labels were found as a variety of conformations, including “I” (orange arrows), “V/Y” (red arrows), “X” (blue arrows), and “C” (purple arrows). “I” shapes were the most commonly found, especially in the early regrowth stage, which most likely came from the septum of mother cells. The corresponding Alkyne647 labels in same cells appeared at the off-septal cell wall and/or the perpendicular bands as an ongoing septum of the next generation, which indicated sequentially orthogonal planes formed for cell division. As for “V” and “Y” shapes, cells were partially split and off-septal cell wall labelling disappeared, probably due to PG turnover in which fluorescent old PG was cleaved and mixed with new PG. As a result, the fluorescence intensity was decreased and the weak initial signal at the off-septal cell wall lessened. In a 5min pulse labelling experiment, Alkyne647 labelling was homogeneously distributed throughout the cell wall periphery and the old septum in a “V” shape cell. “V” shape cells in the 15 and 30 min pulse labelling were observed without off-septal localization as previously, but the phenotype of Alkyne647 labelling was changed from homogeneous distribution to heterogeneous localization at both the periphery and the orthogonal new septum. Hydrolysis of old cell wall results in reducing termini being uniformly localized. However, later Alkyne647 labelling mainly resulted from reducing termini associated with nascent PG synthesis, producing a strong but inhomogeneous fluorescence. In the “X” shape cells the labelling phenotype was remarkably similar to that of “Y” shape cells. The “C” shape cells resulted from the old septum reconstruction during cell wall remodelling and more biological detail was hard to be provided due to the disappearance of fluorescence.

4.2.2.6 Effects of moenomycin on reducing termini appearance

To further study reducing termini localization during cell wall hydrolysis, moenomycin was used and the effect on probe labelling was investigated. The antibiotic moenomycin blocks transglycosylation of PG precursors by binding to PBP2 and the formation of reducing termini during synthesis is therefore inhibited. As shown in Figure 4.13, after treatment of moenomycin, cells did not display a clear change in fluorescence intensity over time after blocking. This was distinct from untreated cells in Figure 4.12, as cell growth was inhibited. Alkyne647 labelling, in the presence of moenomycin, exhibited a broadly distributed pattern without a clear signal at the septum. This suggests that after moenomycin treatment, hydrolysis serves as the main path to reducing termini formation.

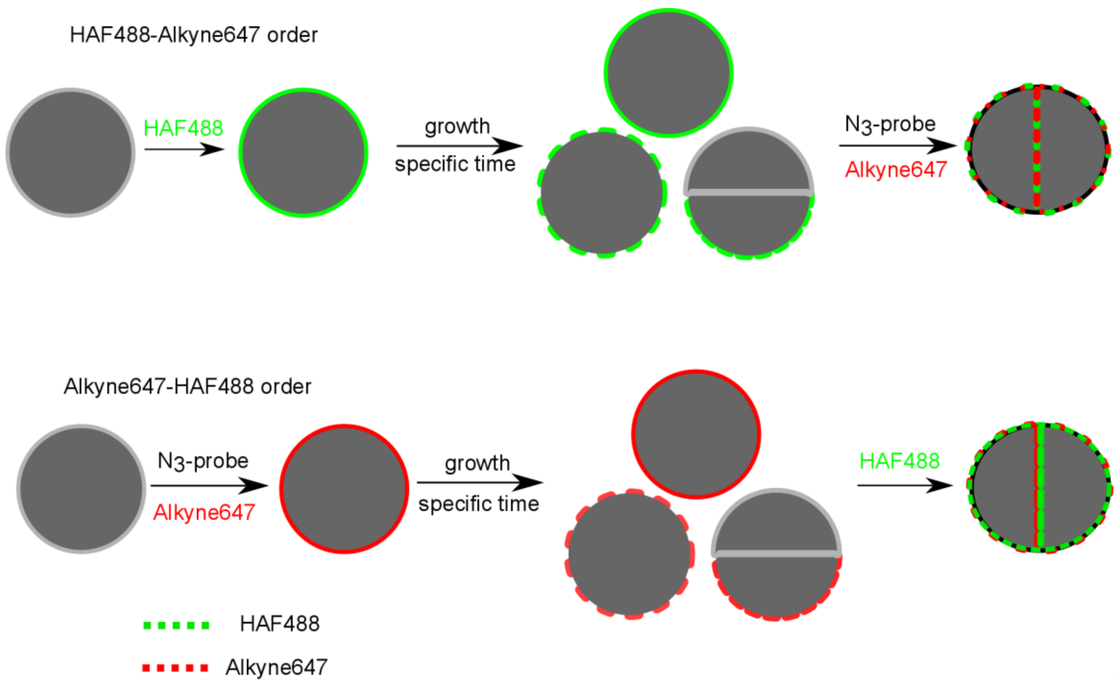

Scheme 4.6 Strategies used to distinguish mature and new cell wall associated to reducing termini. HAF488-Alkyne647 order: exponential-phase cells were labelled with HAF488 and grown on for specific times. New cell wall reducing termini were then labelled via the click reaction of azide probe and Alkyne647. Alkyne647-HAF488 order: cells labelled with azide probe/Alkyne647 were grown on followed by HAF488 staining.

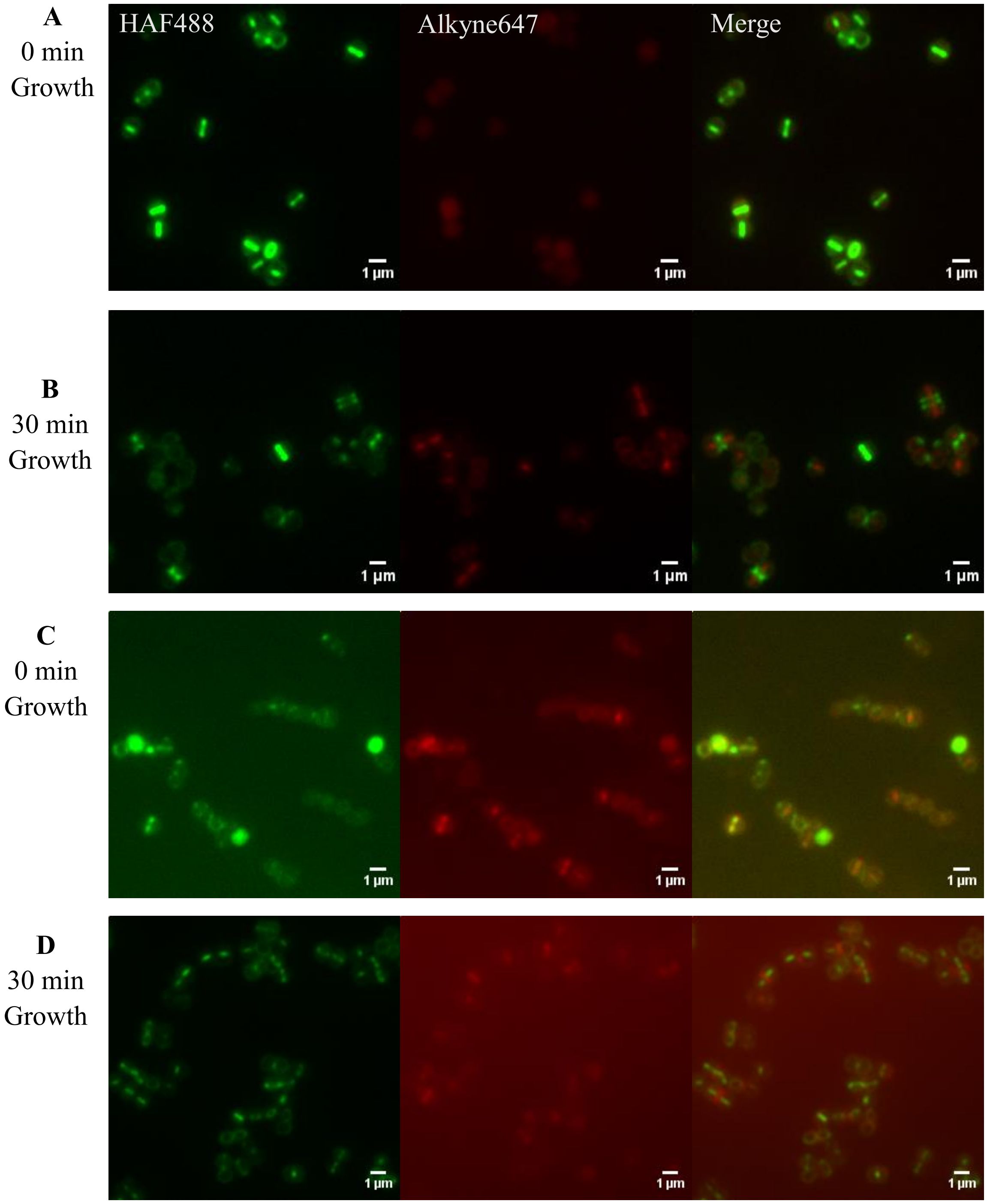

Figure 4.11 Labelling of *S. aureus* cells using HAF488 and azide probe. (A) Exponential-phase cells were labelled with HAF488 and then directly labelled with azide probe/Alkyne647 in the post-click pattern. **(B)** HAF488 labelled cells were grown in TSB at 37 °C for 30 min before labelled with azide probe/Alkyne647. **(C)** Cells were labelled with azide probe and HAF488, followed by click reaction with Alkyne647. **(D)** Azide probe labelled cells were grown for 30 min before labelled with HAF488, followed by click reaction with Alkyne647.

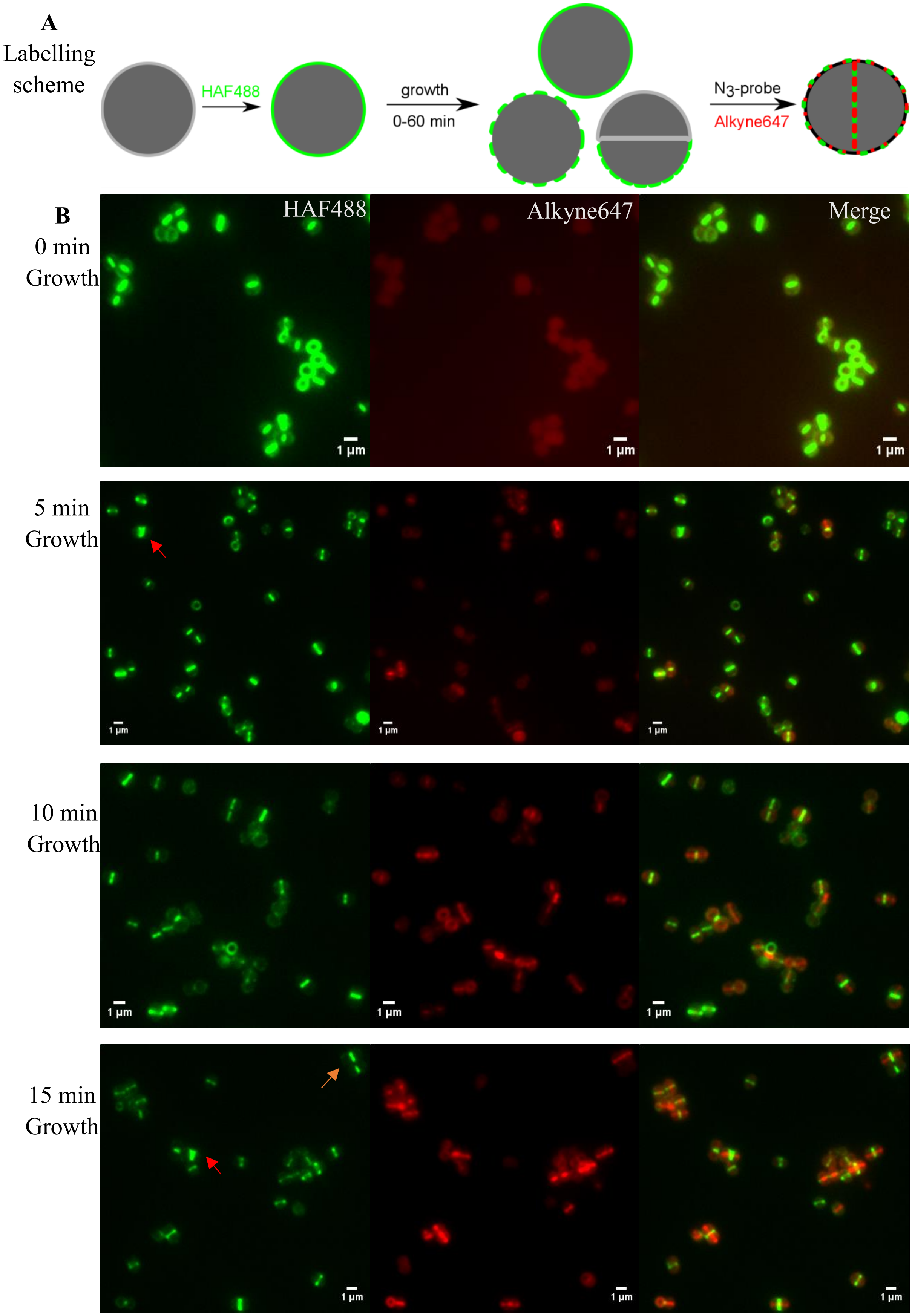
A
Labelling scheme
HAF488
growth
0-60 min
N3-probe
Alkyne647
B
0 min Growth
HAF488
Alkyne647
Merge
1 μm
5 min Growth
10 min Growth
15 min Growth

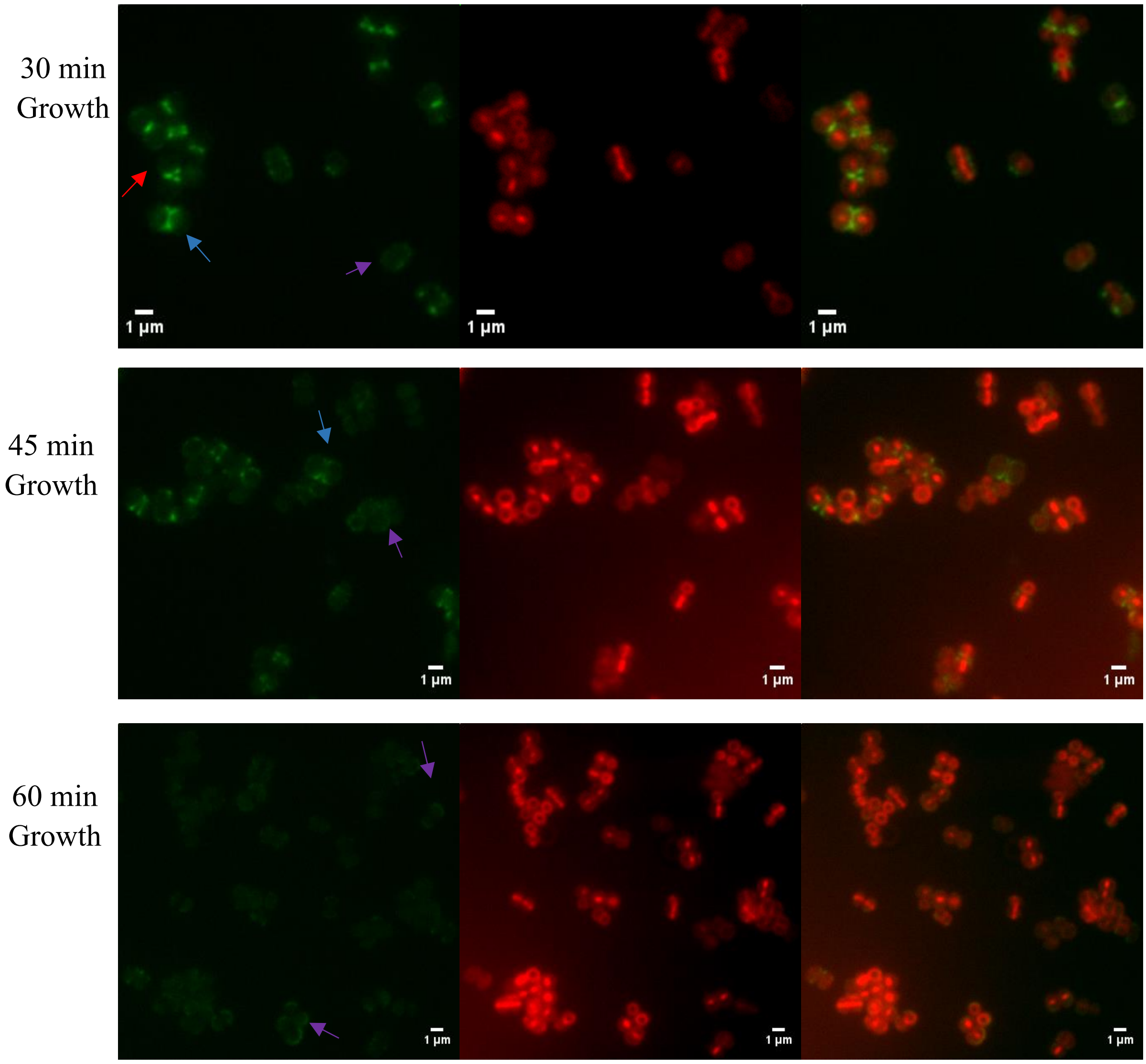

Figure 4.12. Regrowth and Alkyne647 labelling of HAF488 labelled *S. aureus* WT cells. **(A)** The labelling scheme. Cells in exponential phase were labelled with HAF488 (Green), and grown on in TSB for specific times (0, 5, 10, 15, 30, 45 and 60 min) followed by azide probe/Alkyne647 (Red) in the post-click mode. **(B)** Time interval images. Arrows: characteristic labelling features, "I" (orange arrows), "V/Y" (red arrows), "X" (blue arrows), and "C" (purple arrows).

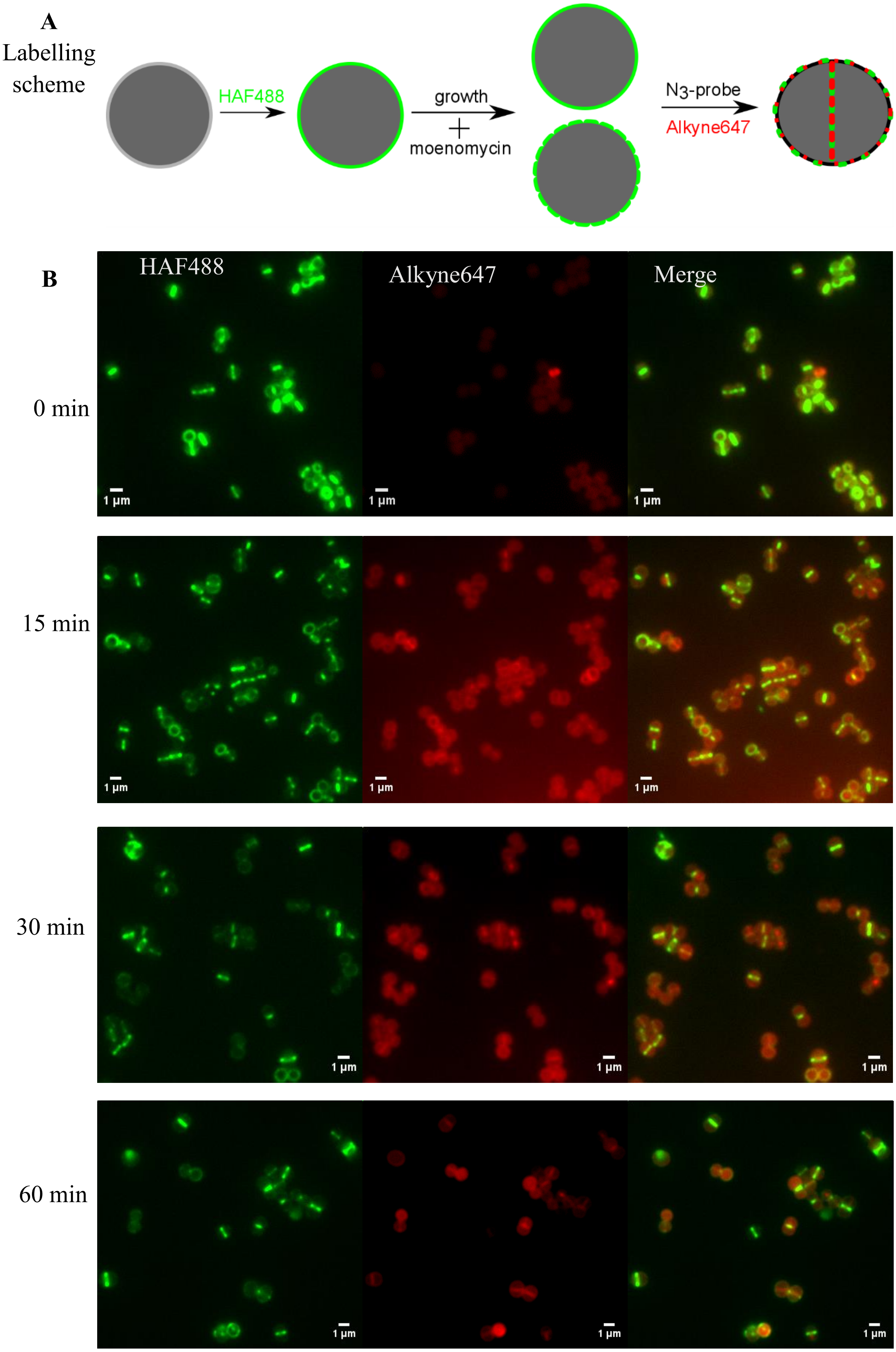
A
Labelling scheme
HAF488
growth
+
moenomycin
N3-probe
Alkyne647
B
HAF488
Alkyne647
Merge
0 min
15 min
30 min
60 min
1 µm

Figure 4.13 Moenomycin effects on Alkyne647 labelling of HAF488 labelled *S. aureus* WT cells. **(A)** The labelling scheme. Cells in exponential phase were labelled with HAF488 (Green), and grown on in TSB with 5 µg/mL of moenomycin for specific times (15, 30 and 60 min) followed by azide probe/Alkyne647 (Red) in the post-click mode. **(B)** Time interval images.

4.2.3 Super-resolution fluorescence imaging of reducing termini of cells

In the previous chapters, a number of probes were prepared to label the bacterial cell wall for fluorescence imaging. As a result, partial PG dynamics were deciphered and biological information of cell growth and division was collected. However, a better understanding of this complex biological context was limited by the resolution of optical microscopy used. The advent of super- resolution microscopy has open up new path for elucidating microbiology at the cellular level, which includes structured illumination microscopy (SIM) and stochastic optical reconstruction microscopy (STORM).[163]

4.2.3.1 SIM imaging

Multicolour three-dimensional (3D) super resolution imaging such as SIM, has been developed as an extremely powerful tool for cellular structure investigation, which enables simultaneous visualisation of multiple targets for determination of single cell dynamics.[164] For instance, Fleurie *et al.* investigated the cell division sites, and the formation and dynamics FtsZ rings in *Streptococcus pneumoniae* using 3D-SIM imaging.[165] Inspired by these achievements, organic probes were designed and employed to label *S. aureus* cell walls in this work, as visualization in 3D-SIM with much higher precision would allow more understanding of cell morphology and dynamics.

4.2.3.1.1 Triple-labelling bacterial cells with HAF488, HADA and Alkyne647

Initially, cells were, in turn, labelled with HAF488, HADA and azide probe/Alkyne647, which successively targeted reducing termini of mature PG, newly synthesised PG and newly formed reducing termini (Figure 4.14). Triple-colour probes successfully labelled cells and showed differential distribution. Over time, HAF488 labelling decreased and Alkyne647 signal was gradually enhanced whereas the intensity of HADA labelling was relatively steady and localization of the probe was also consistent. Although both HADA and azide probe/Alkyne647 were designed to strategically label newly formed target sites of the cell wall, the distribution of two probes was not identical. Both probes labelled throughout the entire cell wall but with a preference for the septum. However, the HADA signal was homogeneously distributed at the septum whilst for Alkyne647 labelled the septal middle zone most (Grey dashed boxes in Figure 4.14). Addition of moenomycin to the triple labelling was examined. Figure 4.15 shows that after treatment of moenomycin, the downward trend of HAF488 signal was countered and Alkyne647 labelling exhibited a broadly distributed pattern. However, HADA labelling was restricted to the septum rather than throughout the entire cell well, suggesting that moenomycin inhibits the incorporation of D-ala in the cell periphery, which was consistent with the observation in Chapter 3.

4.2.3.1.2 Dual-labelling bacterial cells with Alkyne647 and NHS555

In order to further characterise the different phenotypes, cells were labelled with the NHS ester of Alexa Fluor® 555 (NHS555), which reacts with the amine group within the cell surface. Initially, cells were treated with NH_2OH and grown on for 30 min before dual-labelled with Alkyne647 and NHS555 (Figure 4.16). It was found that while cells were successfully labelled with Alkyne647, NHS555 labelling failed in both SIM and diffraction limited microscopy imaging, and intracellular staining occurred. There were several possible causes of failure including NH_2OH treatment and the fixing methodology. A series of preliminary experiments were carried out, including cells without any chemical treatment and NH_2OH-blocked cell with or without regrowth, were labelled and fixed using different strategies (Scheme 4.7).

A
Labelling
scheme

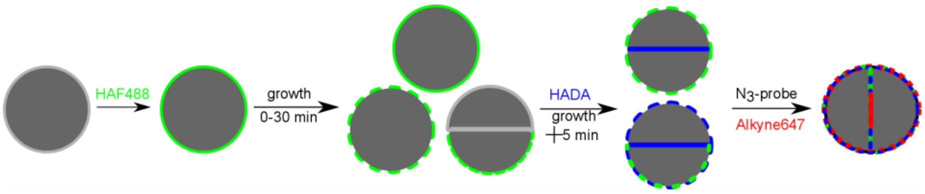

B

Control
No growth
with
HADA

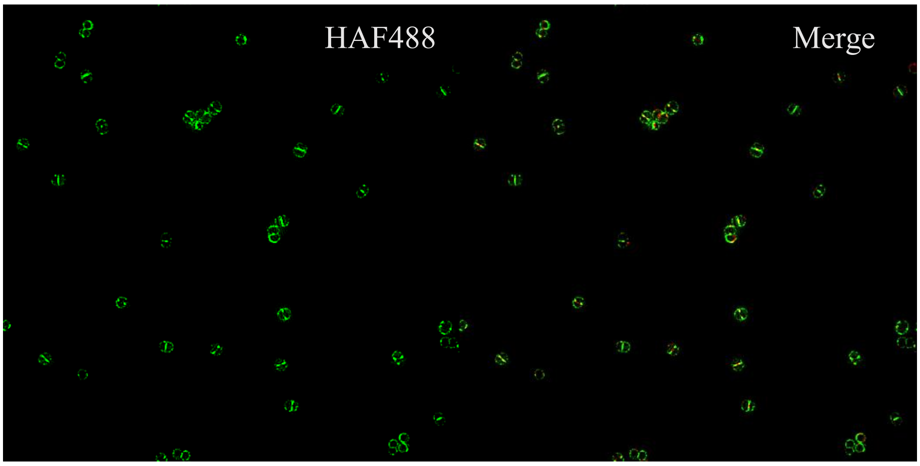

0 min plus

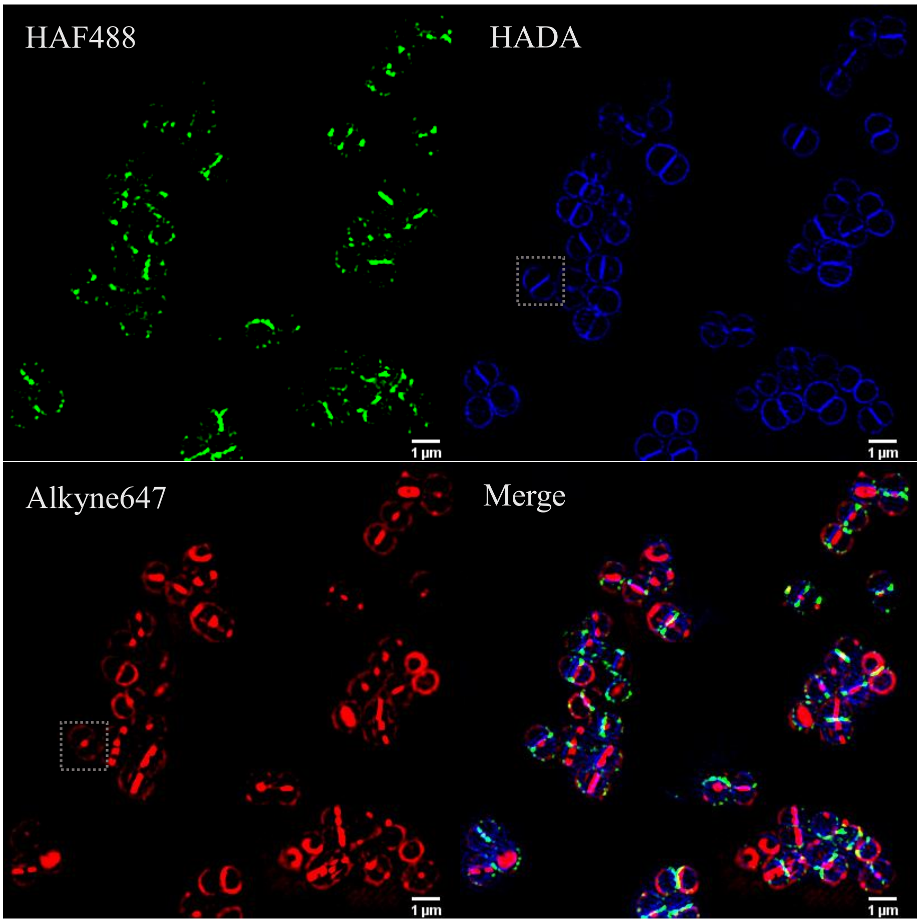

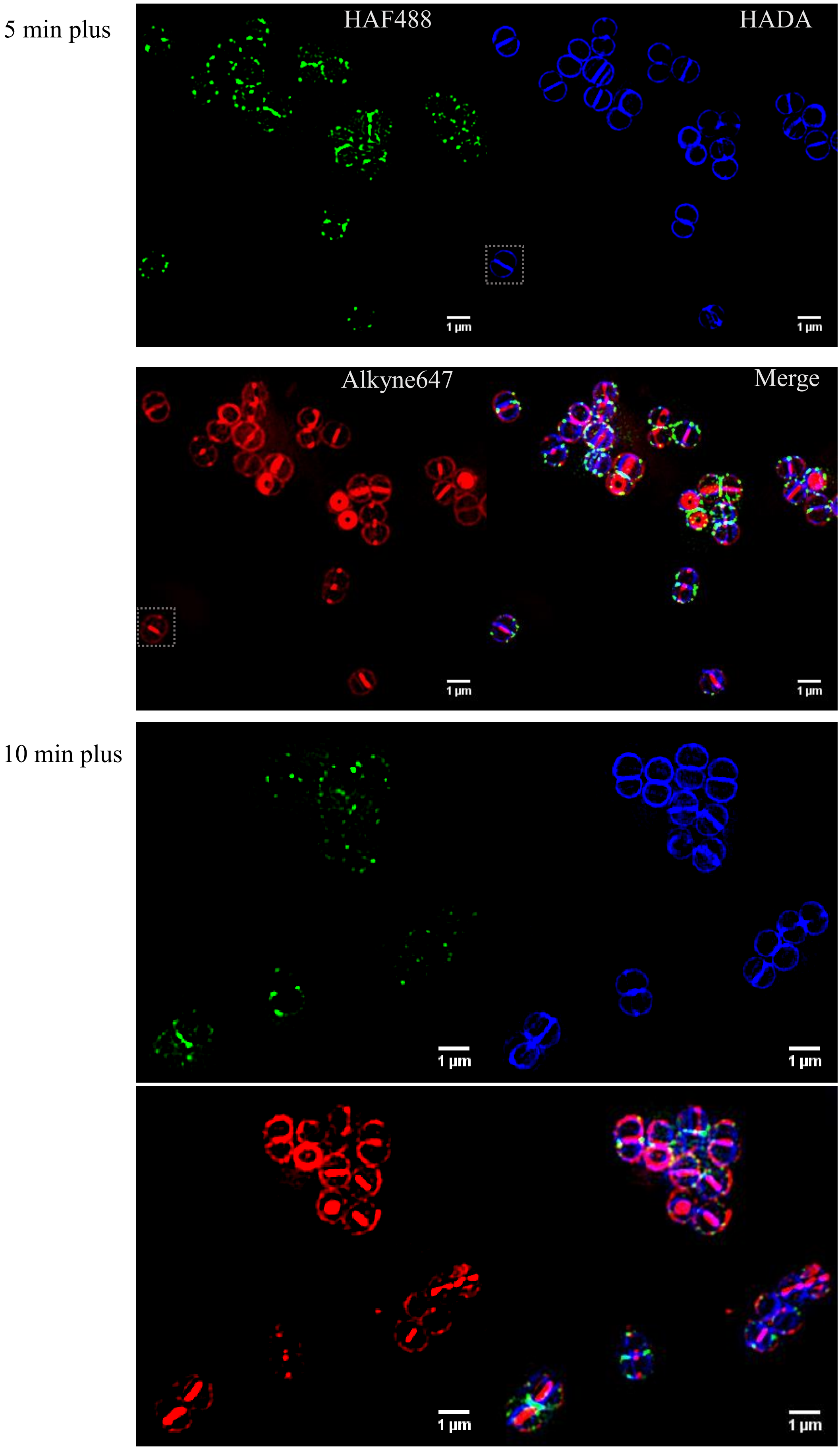
5 min plus
HAF488
HADA
1 µm
1 µm
Alkyne647
Merge
1 µm
1 µm
10 min plus
1 µm
1 µm
1 µm
1 µm

15 min plus

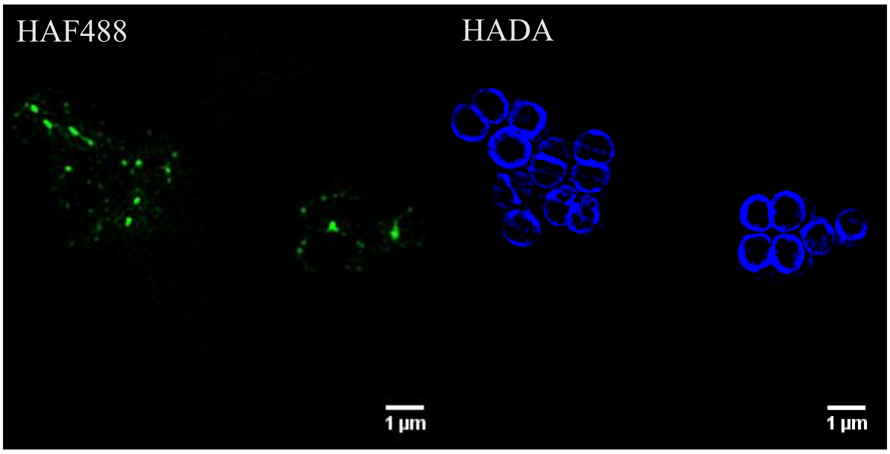

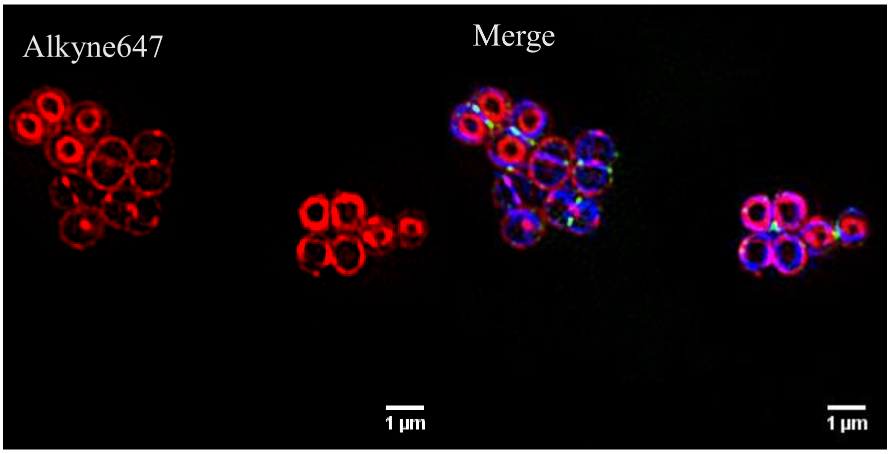

30 min plus

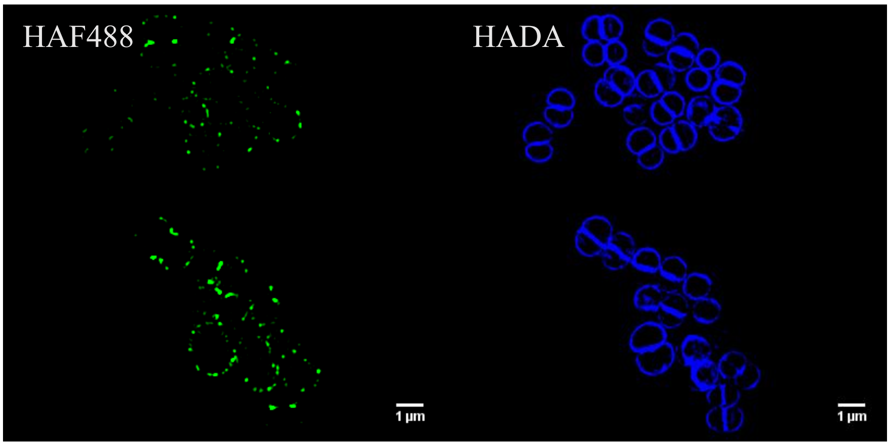

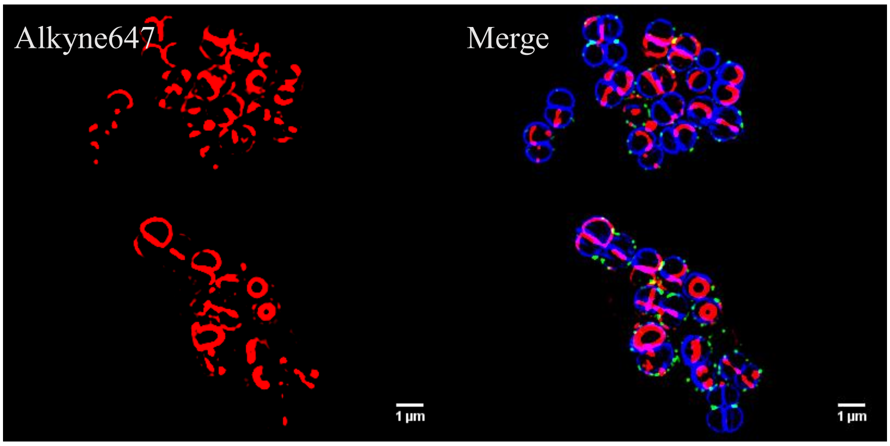

Figure 4.14 SIM visualization of triple labelled *S. aureus* WT cells. **(A)** The labelling scheme. Cells in exponential phase were labelled with HAF488 (Green), and grown on in TSB for specific times (0, 5, 10, 15, 30, 45 and 60 min), followed by addition of HADA for a further 5 min labelling (Blue). After harvesting, pellets were labelled with the azide probe/Alkyne647 (Red) post-click. As a control, HAF488-labelled cells were directly labelled with azide probe/Alkyne647 without further growth or HADA treatment. **(B)** Time interval images. Dashed boxes showed the different septal labelling pattern of HADA and Alkyne647.

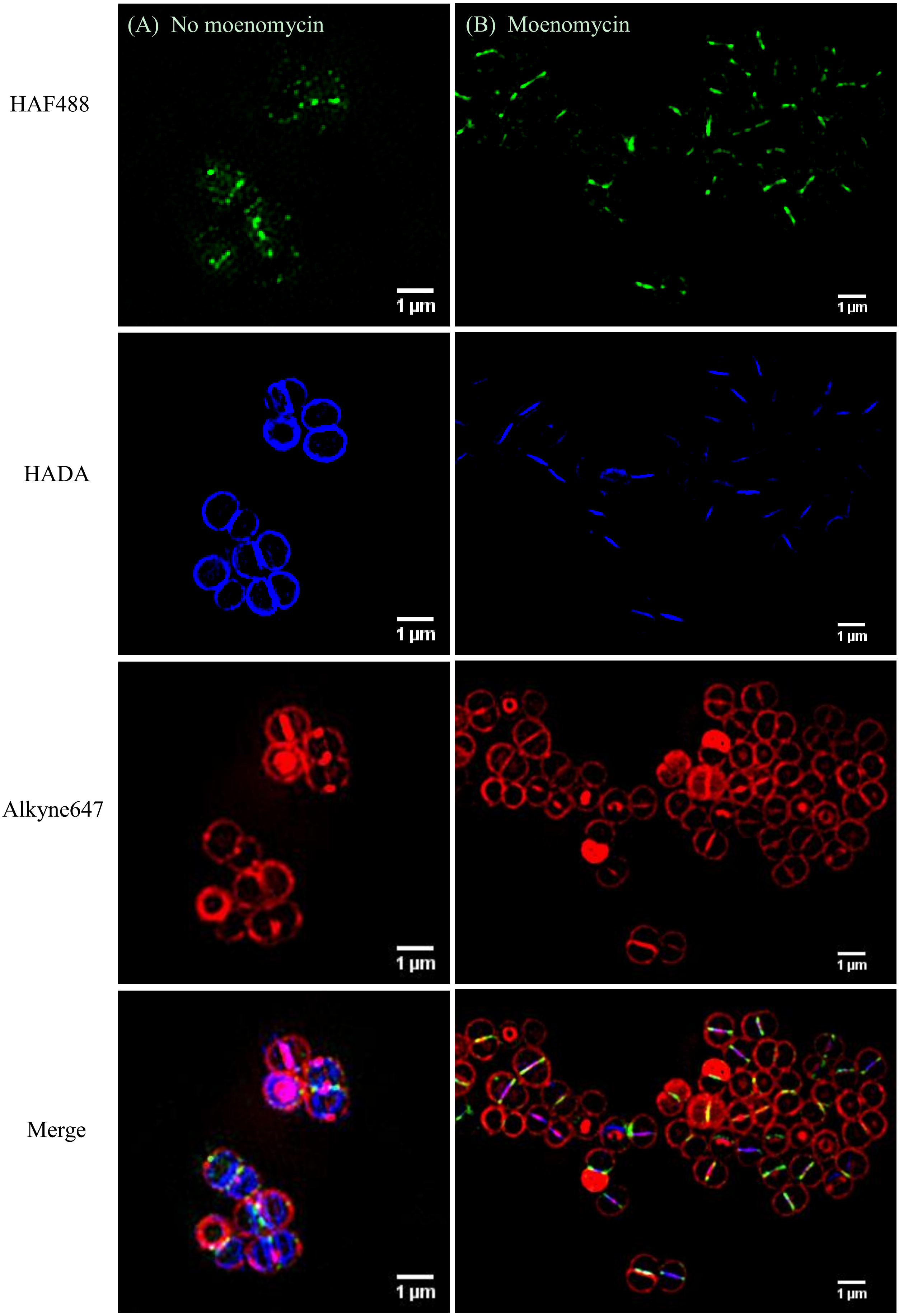
(A) No moenomycin
(B) Moenomycin
HAF488
HADA
Alkyne647
Merge
1 µm

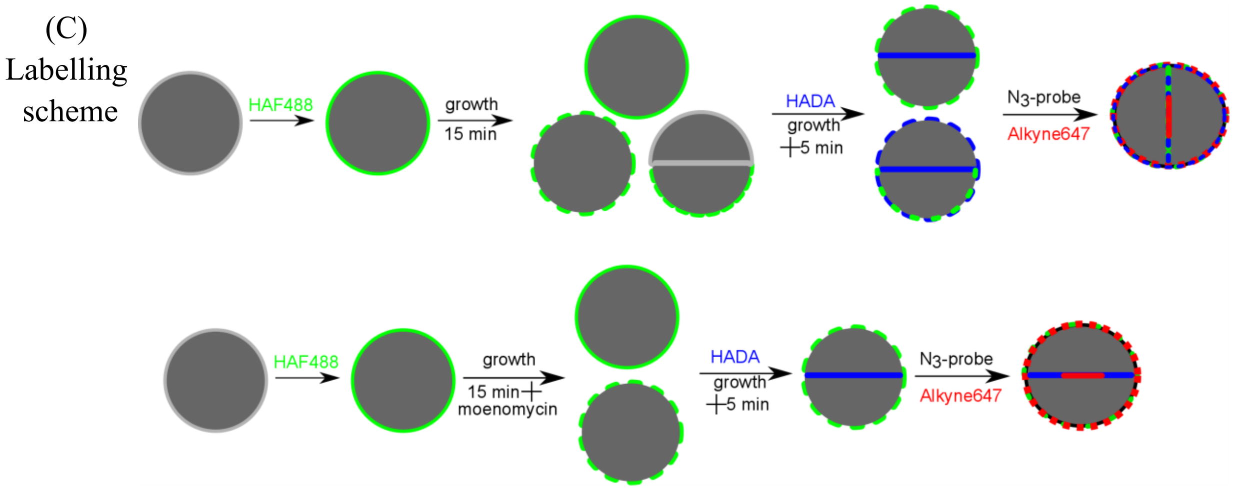

Figure 4.15 SIM visualization of triple labelled *S. aureus* WT cells with moenomycin treatment. Cells in exponential phase were labelled with HAF488 (Green), and grown on in TSB without **(A)** or with **(B)** 5 µg/mL of moenomycin for 15 min, followed by addition of HADA for further a 5 min labelling (Blue). Treated cells were labelled with azide probe/Alkyne647 (Red) post-click. **(C)** The labelling scheme.

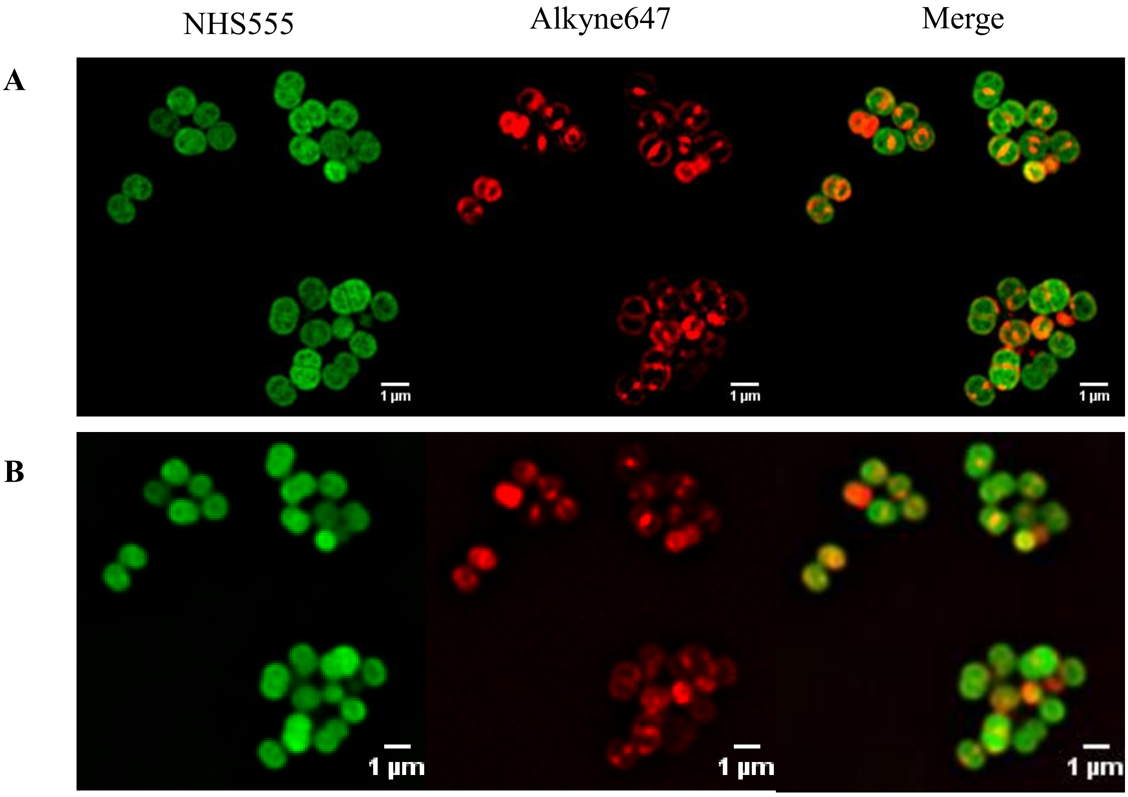

Figure 4.16 Growth and labelling of NH_2OH-blocked cells with Alkyne647 and NHS555. Cells in exponential phase were blocked with NH_2OH, and grown on at 37 °C for 30 min. After harvesting, cells were labelled with azide probe/Alkyne647 (Red) in the post-click strategy and fixed with ethanol followed by NHS555 (Green) staining. **(A)** SIM visualization and **(B)** wide-field imaging.

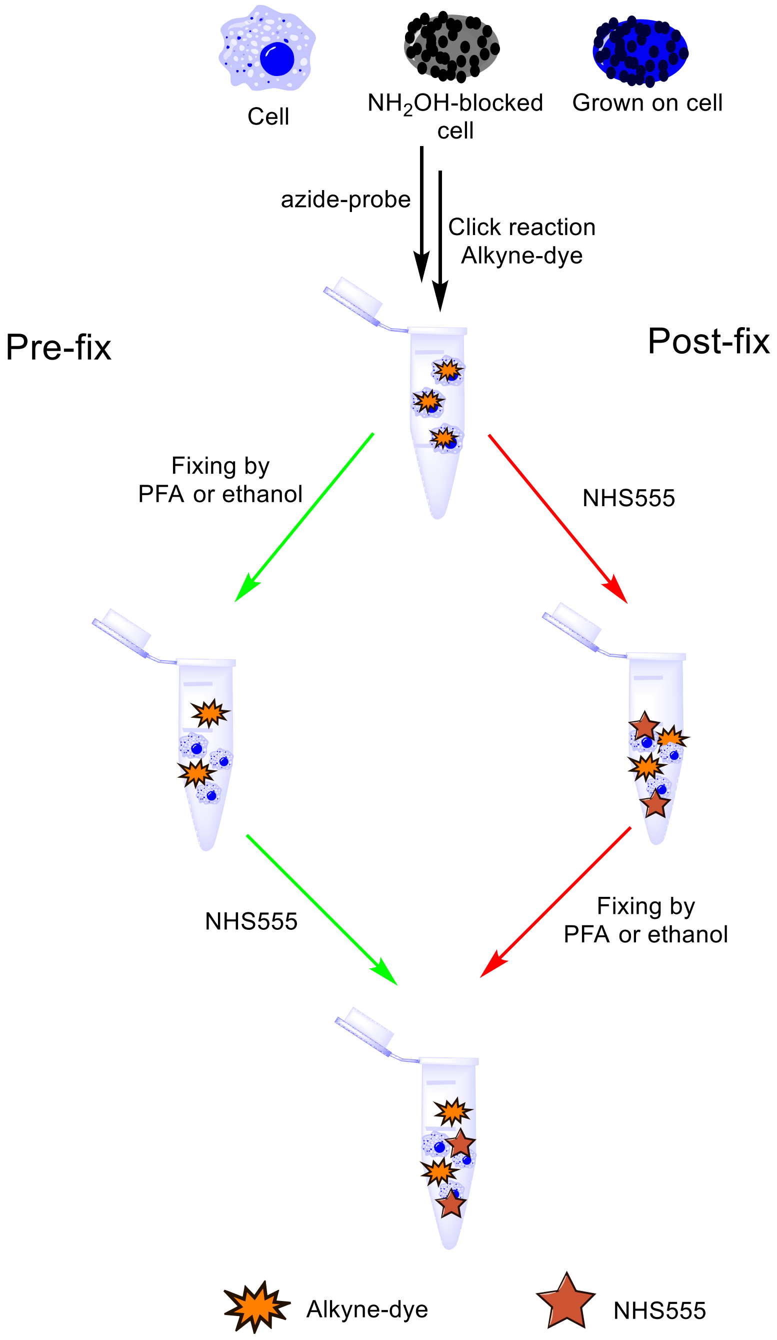

Scheme 4.7 Fixing strategies for dual-labelling cells with alkyne-dye and NHS-dye. Two possible labelling routes, termed pre- (Green) or post- fix (Red) labelling, were used. Pre-fix labelling: cells were labelled with the azide-probe followed by a click reaction with alkyne-dyes. Treated cells were fixed with PFA or ethanol before labelling with NHS555 (5 min). Post-fixing labelling: cells were labelled with the azide-probe/alkyne-dyes and NHS555 (5 min). Treated cells were fixed with PFA or ethanol.

As shown in Figure 4.17, changes in the fixing strategy had no significant effect on Alkyne647 labelling cells without NH_2OH treatment. However, NHS555 labelling displayed a variation accompanied with the fixing changes. When cells were post-fixed, both PFA and ethanol gave clear staining results. In the case of pre-fixing, ethanol fixing resulted in the same observation with SIM imaging as shown in Figure 4.16 and intracellular staining appeared again while PFA fixing provided comparable labelling results with that from post-fixing. NH_2OH-blocked cells with (Figure 4.18) or without (Figure 4.19) growing on showed a similar labelling observation to cells without NH_2OH treatment. All results indicated that the fixing strategy was the key factor affecting NHS555 staining rather than NH_2OH treatment.

On the basis of the test results, post-fixing in ethanol was used for the next dual-labelling of cells with Alkyne647 and NHS555. Initial work was carried out with *S. aureus* WT cells using SIM imaging. As depicted in Figure 4.20, in most cells the periphery had a similar distribution of both probes, which suggested that they were attached to the cell wall. The effect of moenomycin on Alkyne647 and NHS555 labelling was next investigated (Figure 4.21). As SagB is a key glucosaminidase and lack of it results in a length increase of glycan chains in PG, the effect of the *sagB* mutant with and without moenomycin was investigated using two probes labelling (Figure 4.22 and 4.23). In both cases, the labelling phenotypes were consistent with the observation in WT cells.

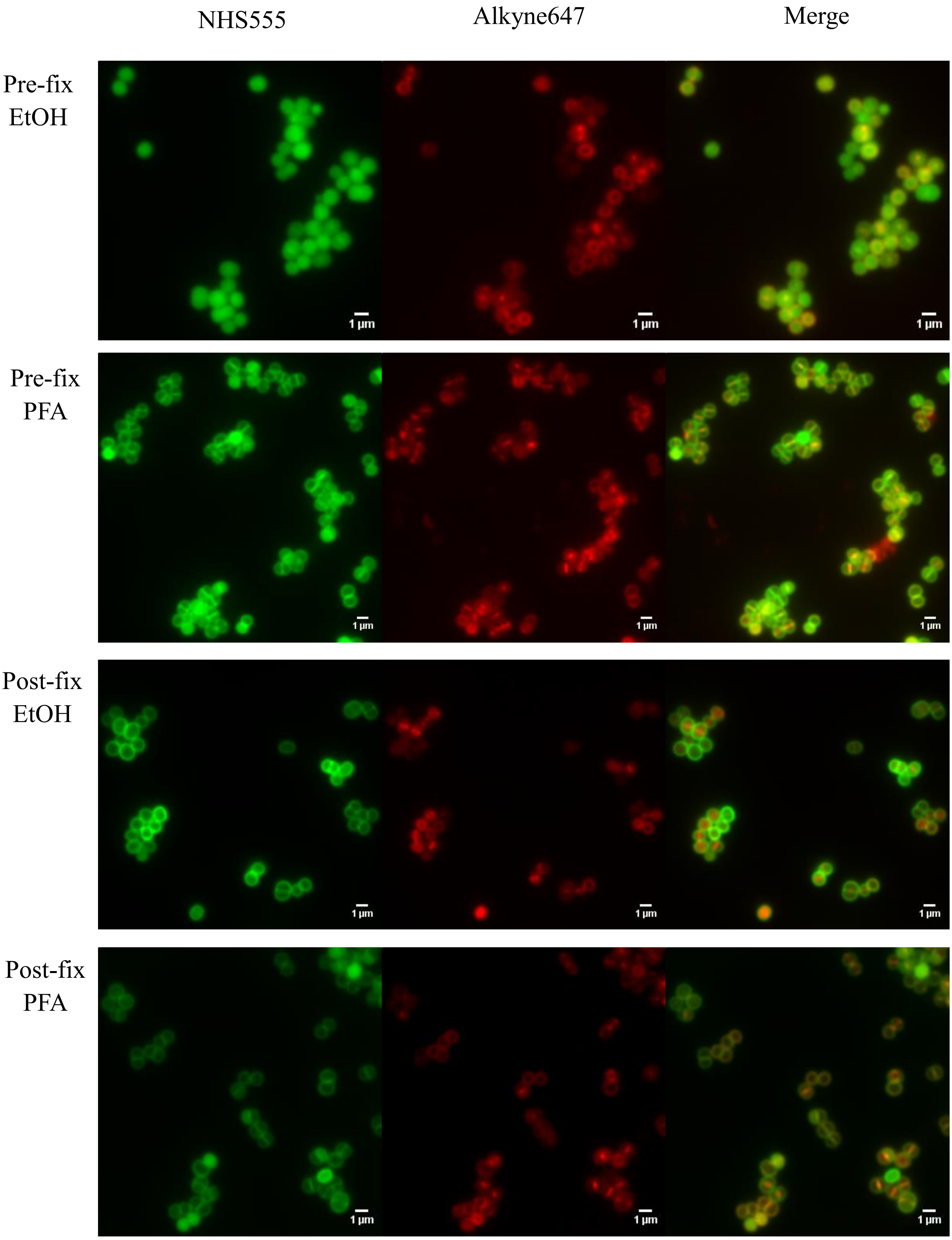

Figure 4.17 Effects of the fixing strategy on labelling cells with Alkyne647 and NHS555. Cells in exponential phase were labelled with azide probe/Alkyne647 (Red). Labelled cells were fixed with ethanol or PFA before (pre-fix) or after (post-fix) NHS555 (Green) staining.

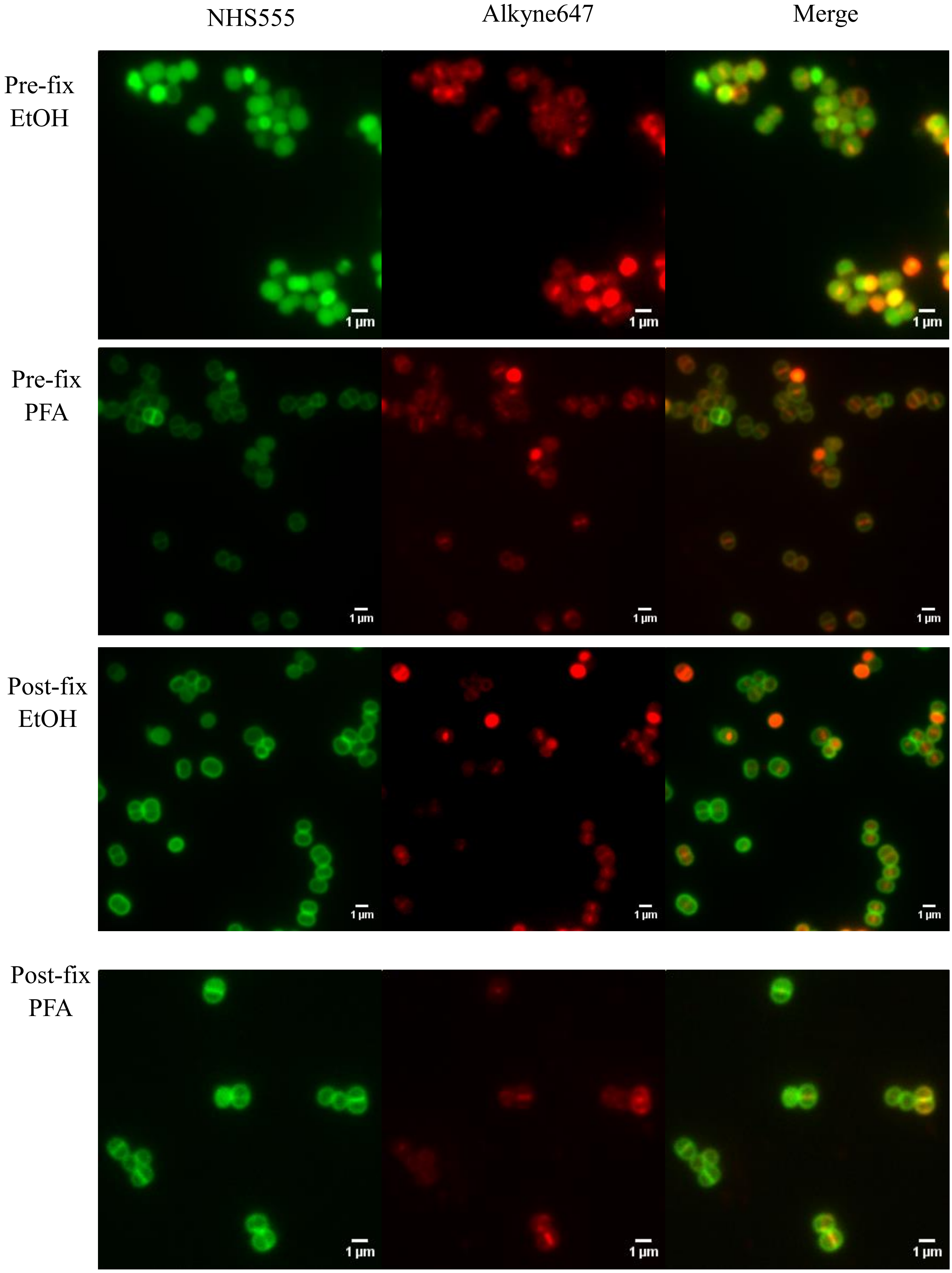
NHS555
Alkyne647
Merge
Pre-fix EtOH
Pre-fix PFA
Post-fix EtOH
Post-fix PFA
1 µm

Figure 4.18 Effects of the fixing strategy on labelling grown on NH_2OH-blocked cells with Alkyne647 and NHS555. Cells in exponential phase were treated with NH_2OH and grown on at 37 °C for 30 min before labelling with azide probe/Alkyne647 (Red). Labelled pellets were fixed with ethanol or PFA before (pre-fix) or after (post-fix) NHS555 (Green) staining.

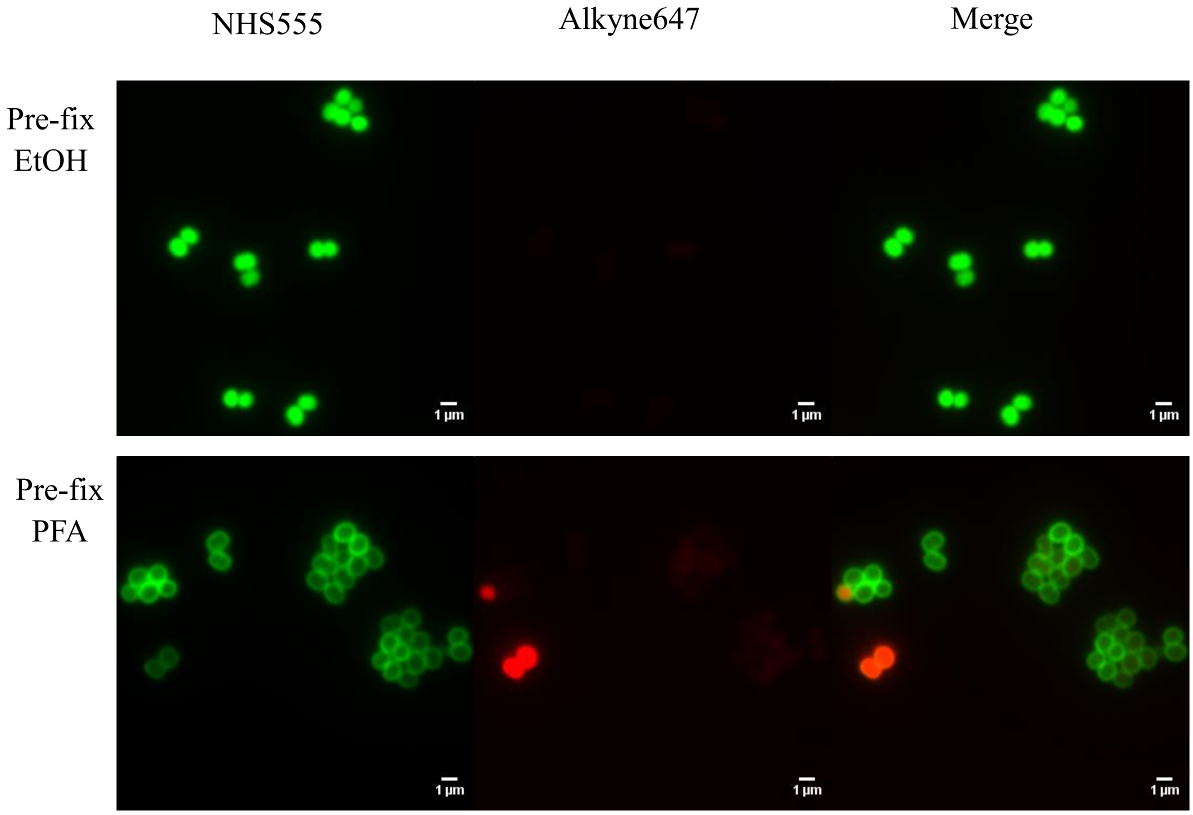

Figure 4.19 Effects of the fixing strategy on labelling NH_2OH-blocked cells with Alkyne647 and NHS555. Cells in exponential phase were treated with NH_2OH and directly labelled with azide probe/Alkyne647 (Red). Treated cells were fixed with ethanol or PFA before (pre-fix) NHS555 (Green) staining.

(A) Labelling scheme

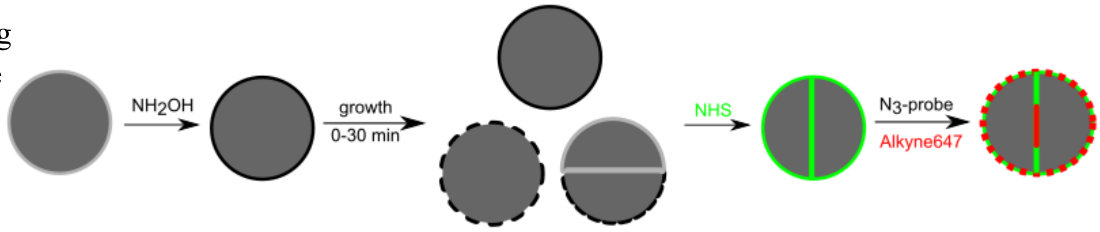

(B)

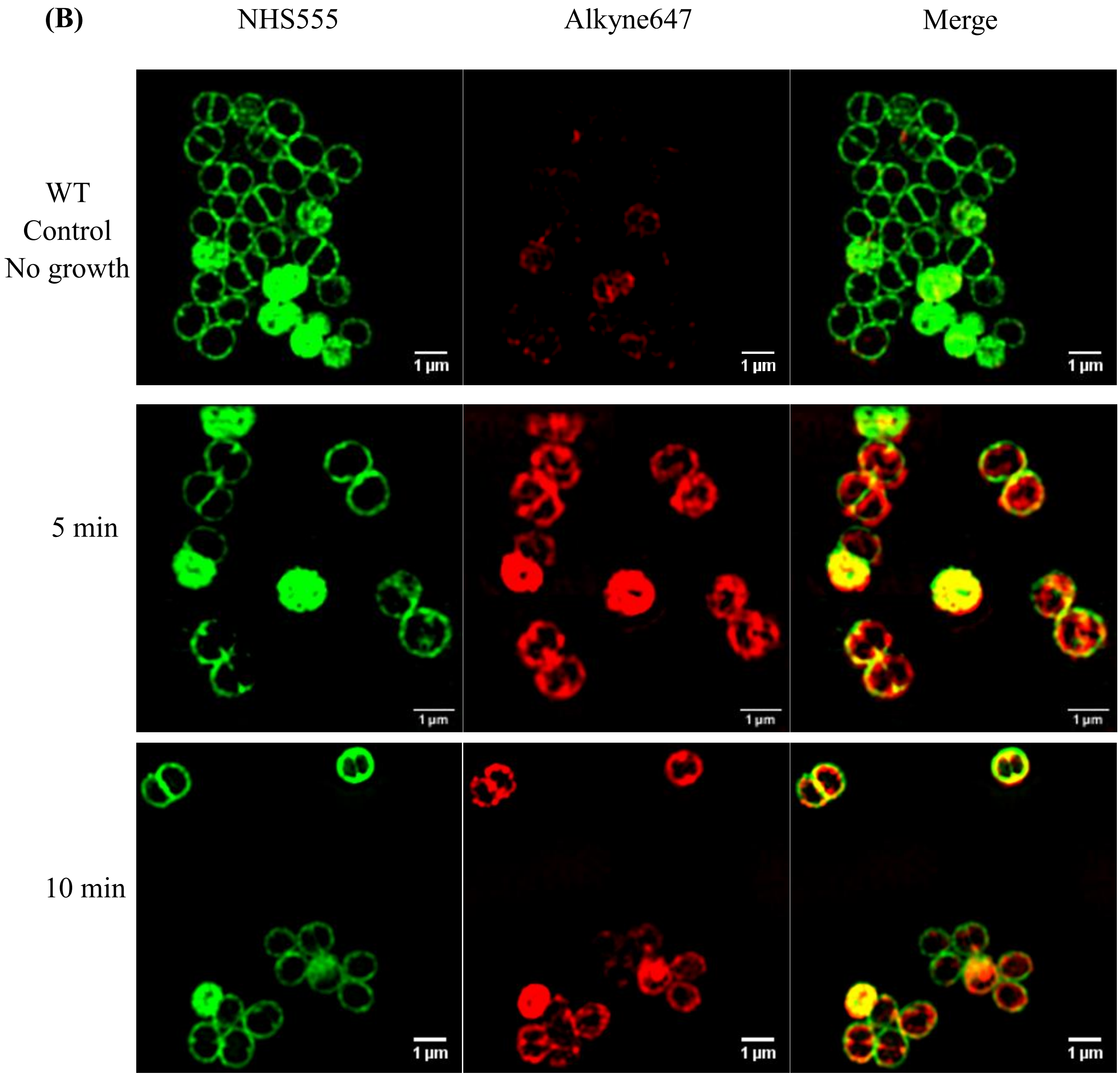

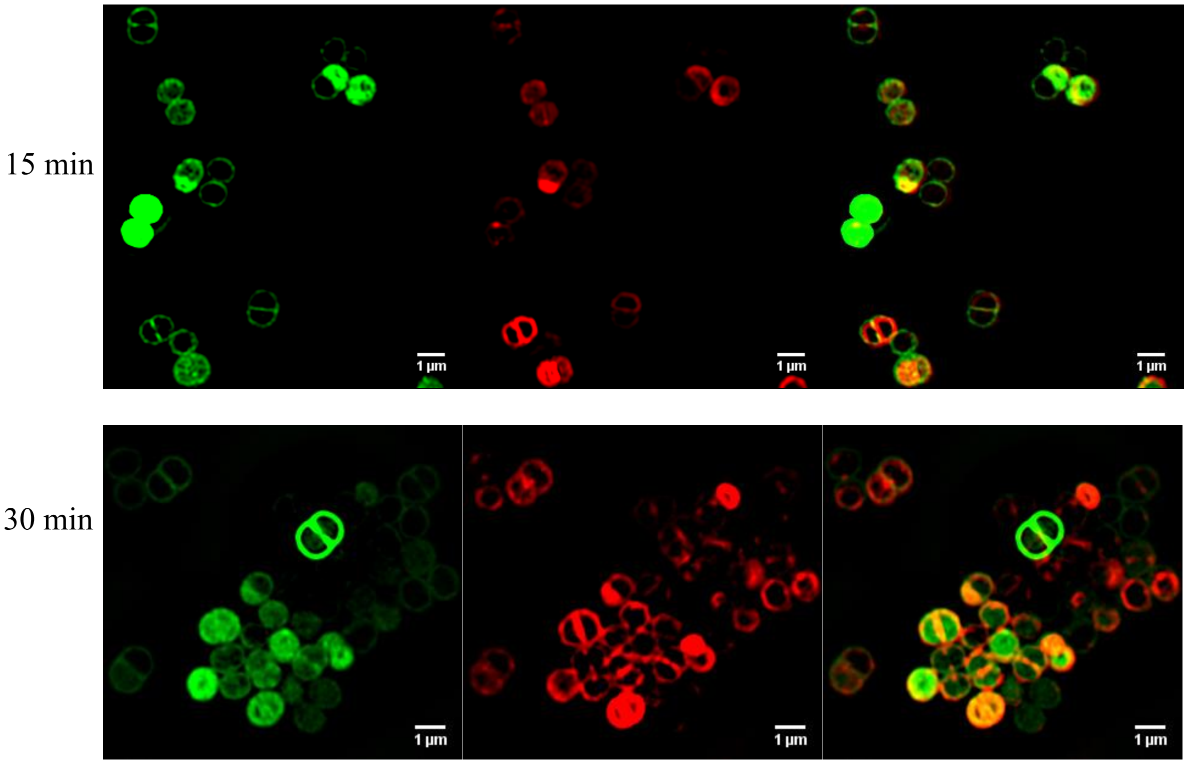

Figure 4.20 SIM visualization of grown on WT cells labelled with Alkyne647 and NHS555. **(A)** The labelling scheme. Cells in exponential phase were treated with NH_2OH and grown on in TSB for specific times (0, 5, 10, 15 and 30 min). After harvesting, cells were labelled with azide probe/Alkyne647 (Red) and NHS555 (Green). Treated cells were fixed with ethanol. **(B)** Time interval images.

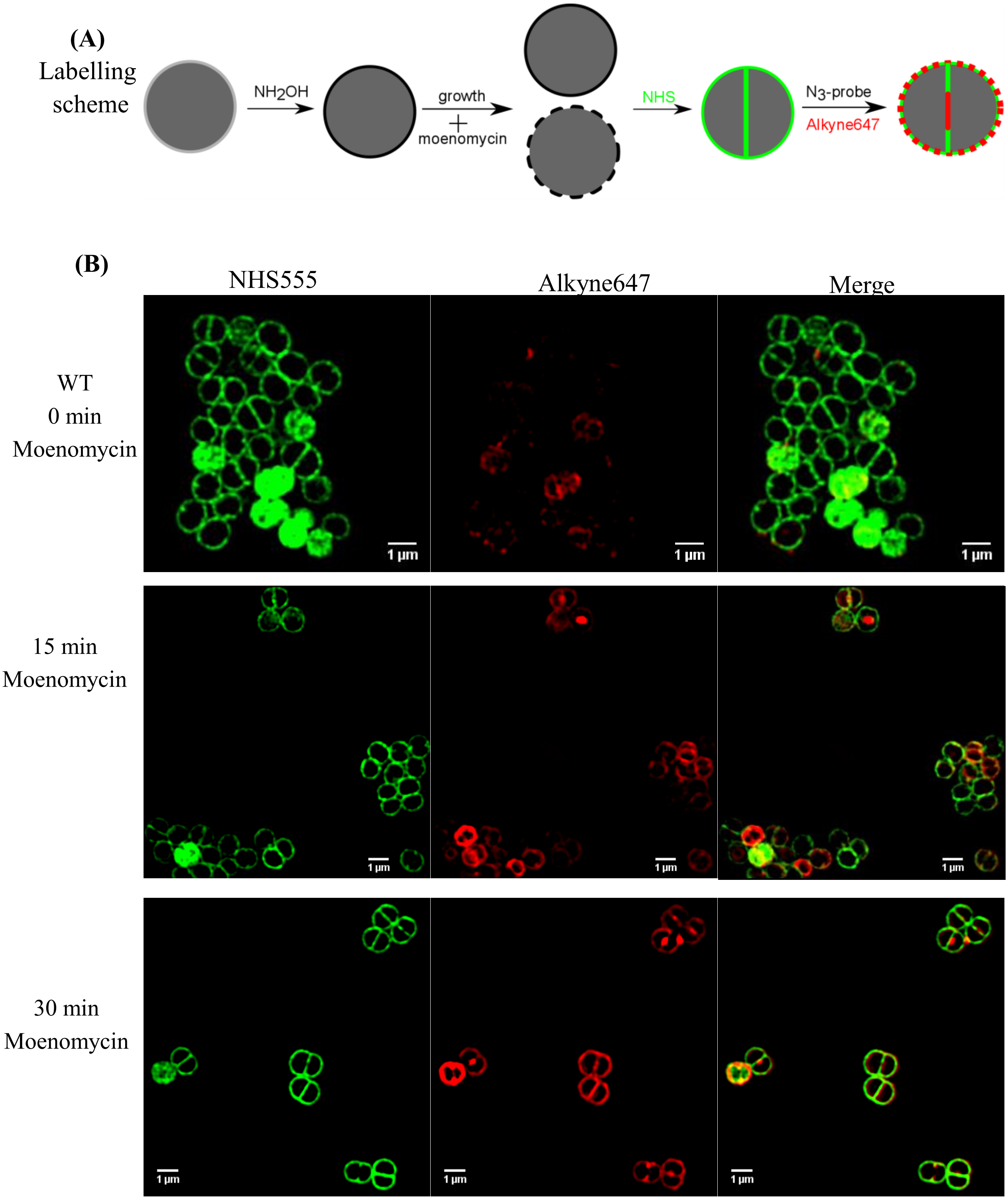

Figure 4.21 SIM visualization of moenomycin treated grown on WT cells labelled with Alkyne647 and NHS555. **(A)** The labelling scheme. Cells in exponential phase were treated with NH_2OH and grown on in TSB with 5 µg/mL of moenomycin for 0, 15 or 30 min. After harvesting, cells were labelled with azide probe/Alkyne647 (Red) and NHS555 (Green). Treated cells were fixed with ethanol. **(B)** Time interval images.

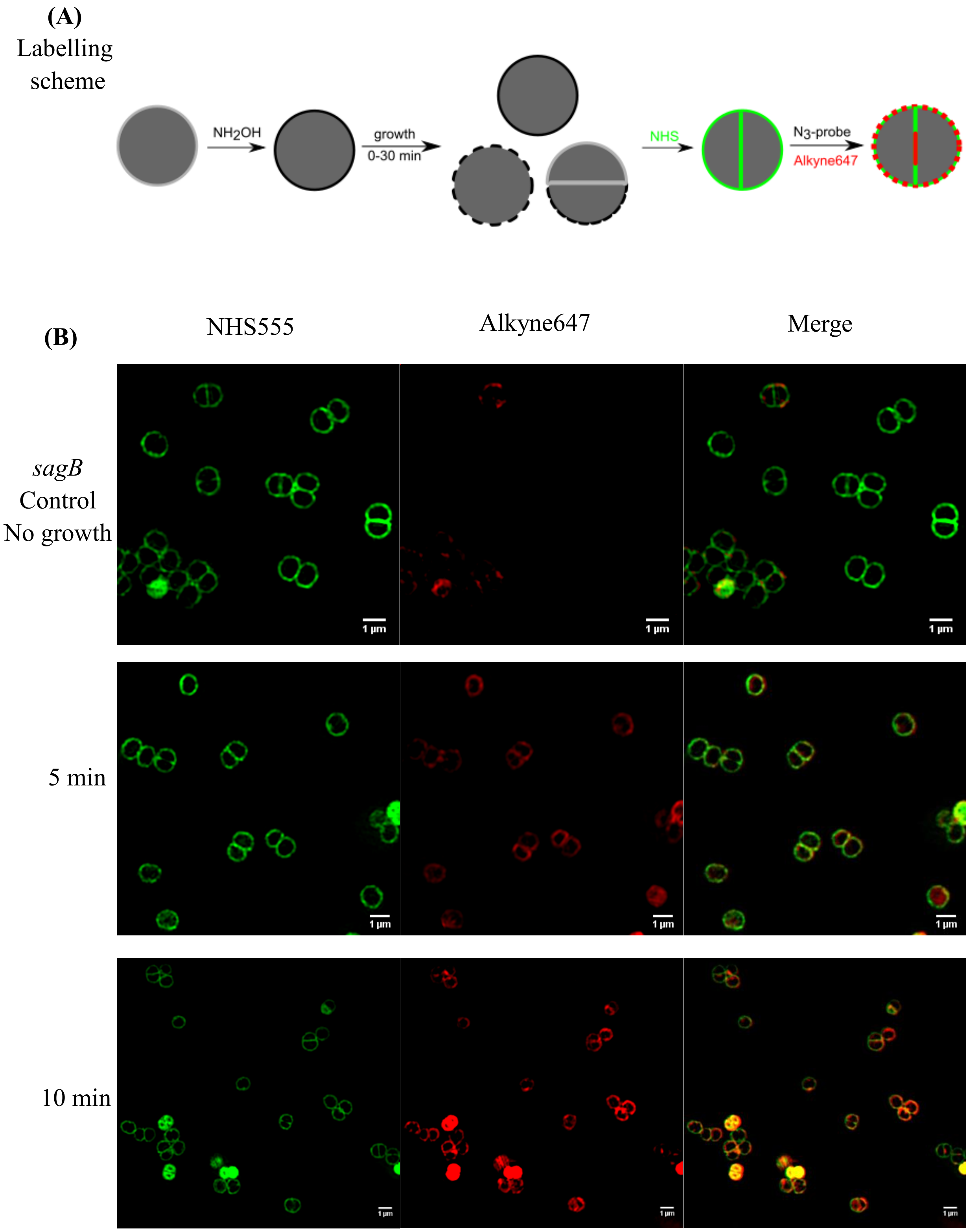
(A)
Labelling scheme
NH2OH
growth
0-30 min
NHS
N3-probe
Alkyne647
(B)
NHS555
Alkyne647
Merge
sagB
Control
No growth
5 min
10 min
1 µm

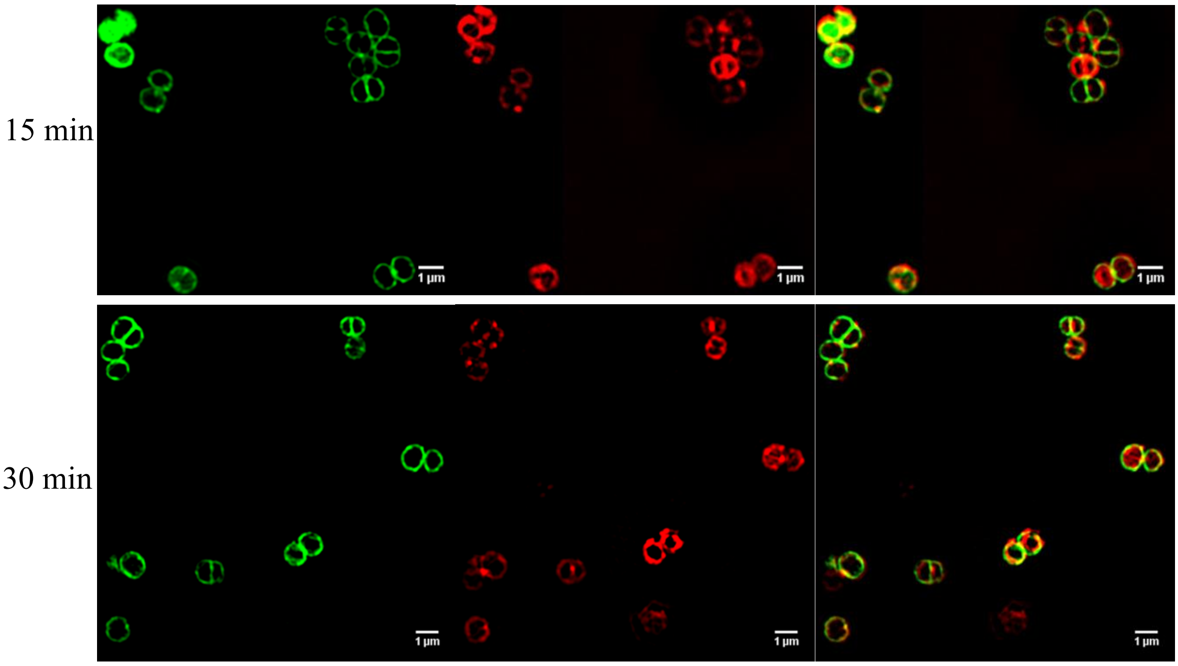

Figure 4.22 SIM visualization of grown on *sagB* cells labelled with Alkyne647 and NHS555. **(A)** The labelling scheme. Cells in exponential phase were treated with NH_2OH and grown on in TSB for specific times (0, 5, 10, 15 and 30 min). After harvesting, cells were labelled with azide probe/Alkyne647 (Red) and NHS555 (Green). Treated cells were fixed with ethanol. **(B)** Time interval images.

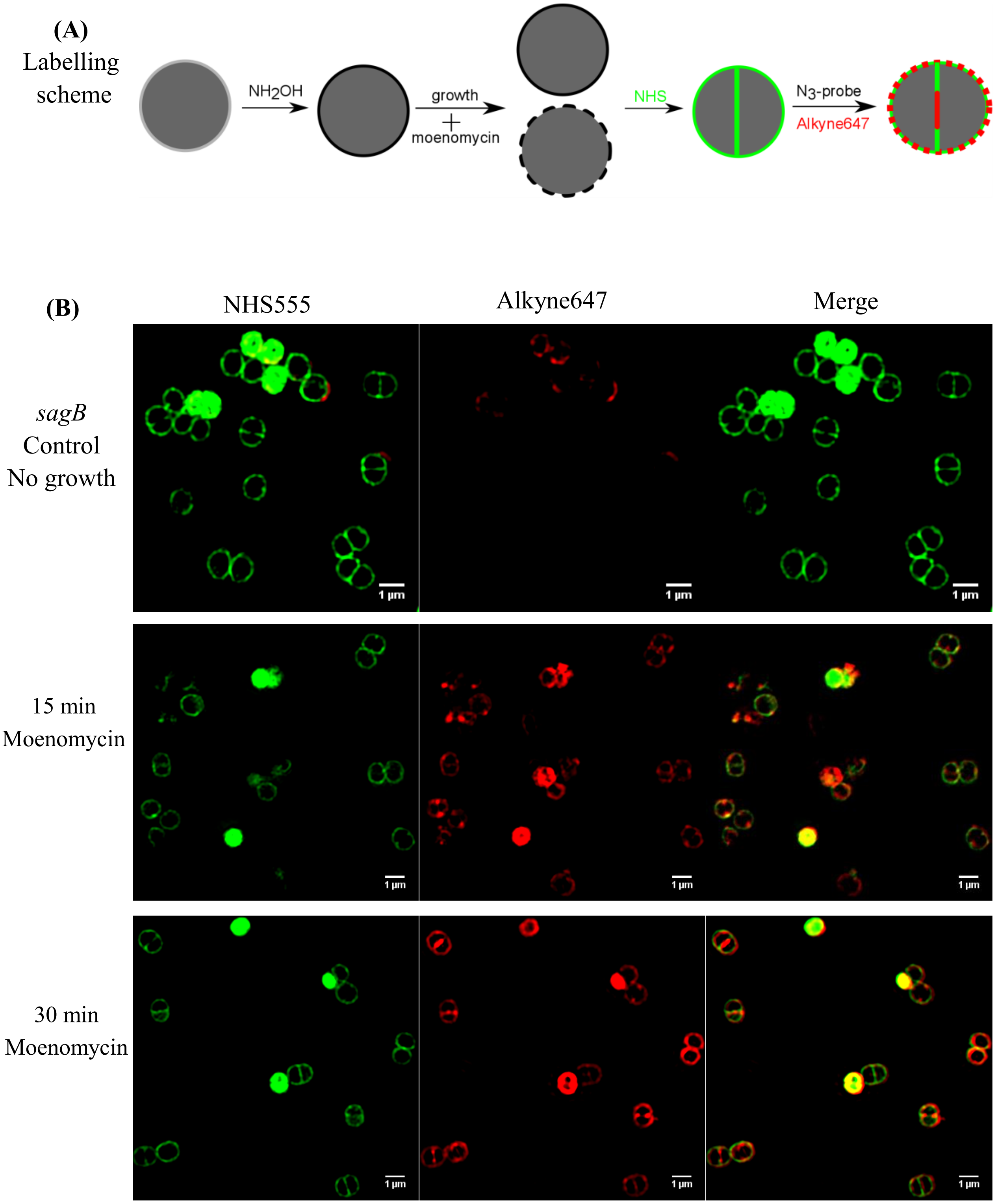

Figure 4.23 SIM visualization of moenomycin treated grown on *sagB* cells labelled with Alkyne647 and NHS555. **(A)** The labelling scheme. Cells in exponential phase were treated with NH_2OH and grown on in TSB with 5 µg/mL of moenomycin for 0, 15 or 30 min. After harvesting, cells were labelled with azide probe/Alkyne647 (Red) and NHS555 (Green). Treated cells were fixed with ethanol. **(B)** Time interval images.

4.2.3.2 STORM imaging

As above mentioned, SIM, as a powerful tool, has been widely applied in the research of the dynamics of living systems. However, the resolution of SIM can merely be improved by a factor 2 compared with that obtained by conventional confocal microscopy, which has restricted the application of SIM.[55] On the other hand, stochastic optical reconstruction microscopy (STORM) enables the direct visualization of the subcellular distributions of molecules of interest reaching 10-25 nm of lateral resolution and providing new insights into the details of the dynamics of cells.[166] For instance, nucleoid-associated proteins facilitate the organization of bacterial chromosomes and tracking the subcellular distributions of these proteins in live bacteria has been achieved using STORM, which contributes a better understanding of 3D architecture of the *E. coli* chromosome.[167] Inspired by these achievements, STORM was herein applied to investigate the dynamics of the cell wall in *S. aureus*.

Initially, the STORM compatibility of the azide probe was tested using Alexa Fluor 647, a well-studied dye suitable for STORM.[168] The reducing termini of *S. aureus* cell wall were labelled with the azide probe and Alkyne647 was attached via a click reaction, followed by 3D-STORM imaging in GLOX buffer with MEA (Figure 4.24). The STORM image clearly showed that the reducing termini were successfully labelled and the probe preferentially labelled the septum. This suggested the new azide-probe can be used as a STORM probe for deciphering the dynamics of bacterial cells.

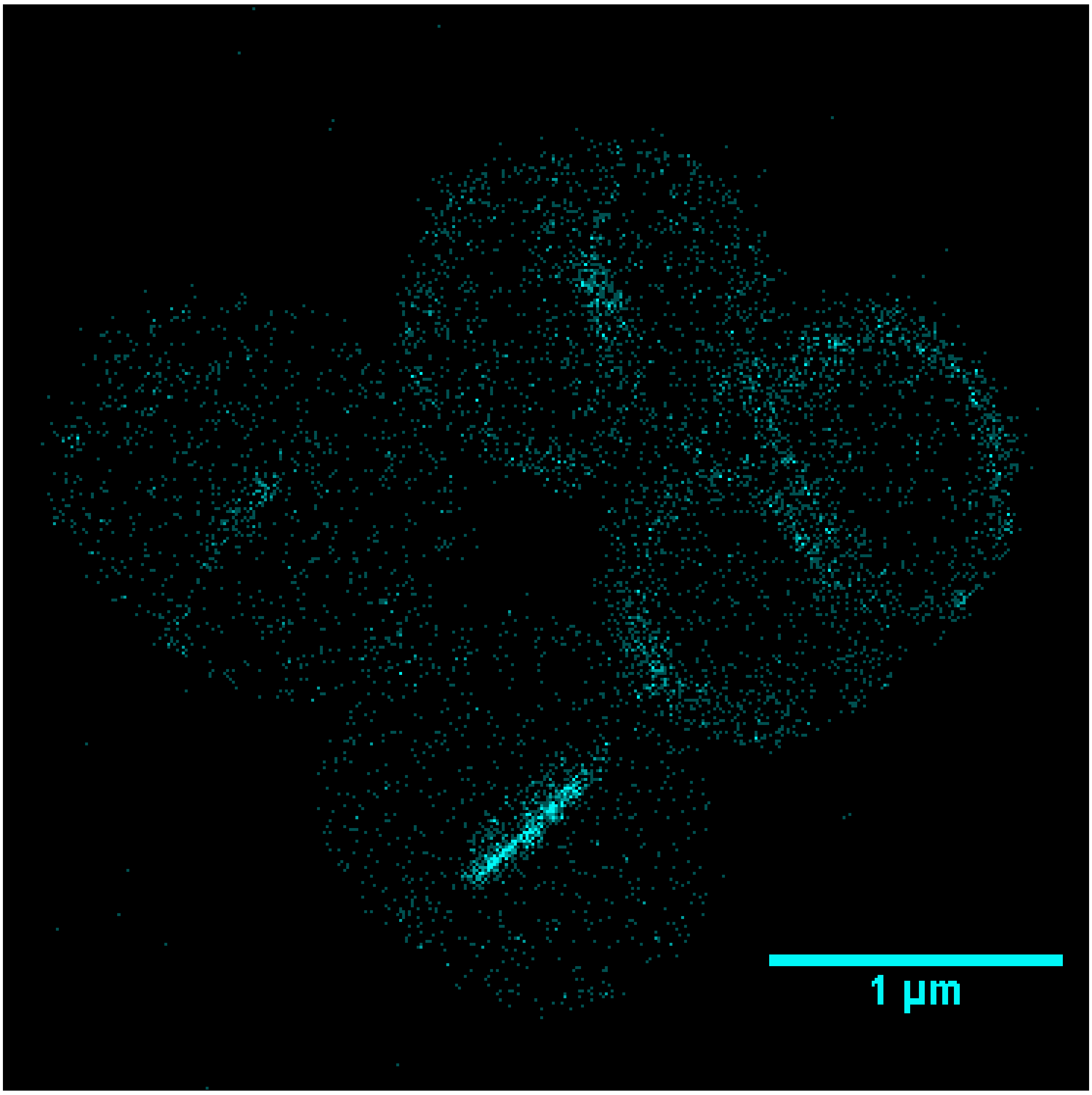

Figure 4.24 dSTORM visualization of *S. aureus* cells labelled with Alkyne647. Cells in exponential phase were labelled with azide probe/Alkyne647 and fixed with ethanol.

4.2.4 EM imaging of cells using clickable gold nanoparticles

While fluorescence microscopy in conjunction with specific fluorescent tags are extremely popular among researchers for studying biological molecular and cellular processes, comparable resolution at the atomic or molecular level is difficult to achieve. The development of electron microscopy (EM) has opened up new opportunities for detailing morphology and ultrastructure of cells, and achieving a deeper understanding of cellular processes.[169] An electron microscopy image with morphological information is attributed to the contrast difference generated by the differential electron scattering between the respective components within biological specimen and/or between specimen and the surrounding environment. In order to provide enhanced contrast and selectivity, electron-dense labels are routinely used, such as gold nanoparticles (AuNPs). As a consequence, immunogold staining has been well accepted and employed for EM visualization of proteins using specific antibodies before gold particle-secondary antibody conjugates are in turn attached. However, the extended applications of this strategy are limited due to a lack of suitable antibodies, and therefore the development of a robust approach that allows location of electron-dense labels within cellular targets with high specificity is required.[170] Herein, the copper(I)-catalyzed click reaction was employed for incorporation of gold nanoparticles to the reducing termini of the bacteria cell wall, which is a potent coupling strategy with high biocompatibility.

For visual inspection of the reducing termini, initial test was carried out with two types of alkyne functionalized gold nanoparticles with different sizes (5 or 30 nm). Via a click reaction, alkyne functionalized AuNPs were attached to the *S. aureus* cell wall with pre-loaded azide-probe, and subsequently, TEM analysis was performed to decipher the morphological information (Figure 4.25). The 5 nm AuNPs localized at the outer edge of dark regions and minor portions were also observed at the periphery of the cell. However, in the case of 30 nm AuNPs labelling, a handful of the particles were found as aggregates on the cell surface. To test if the binding of AuNPs resulted from the reducing termini labelling rather than non-specific attachment, $NaBH_4$ was applied to reduce the aldehyde group within the cell wall for inhibition of from the reducing termini binding. As shown in Figure 4.26, after treatment with $NaBH_4$, there were no observations of AuNPs in both cases, which suggested that AuNPs binds to the reducing termini of the cell wall.

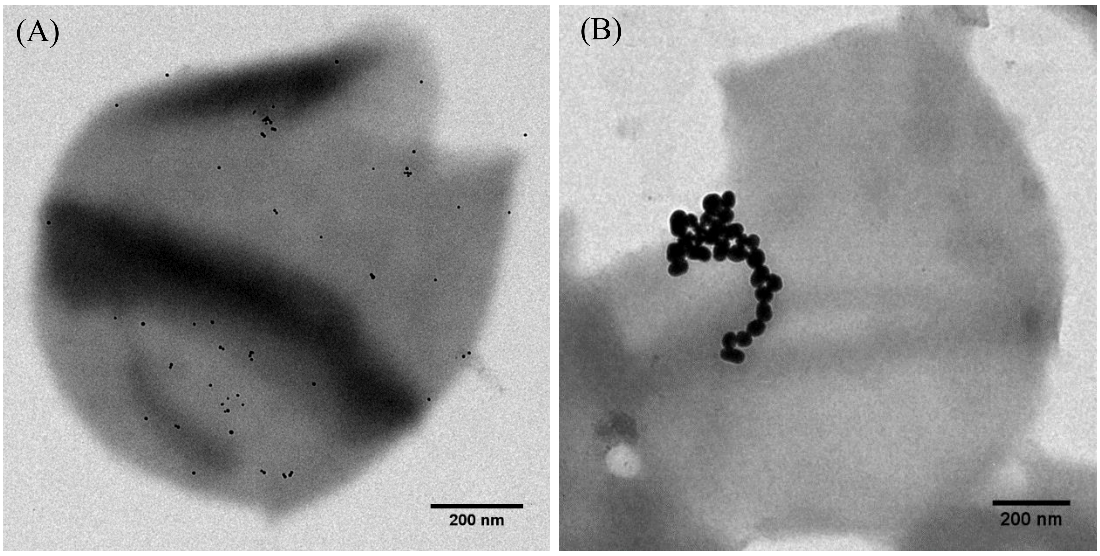

Figure 4.25 TEM visualization of WT cells labelled with AuNPs. *S. aureus* cell sacculi were labelled with the azide probe, followed by a click reaction with alkyne functionalized AuNPs possessing 5 **(A)** or 30 **(B)** nm in size. Treated sacculi were imaged by TEM.

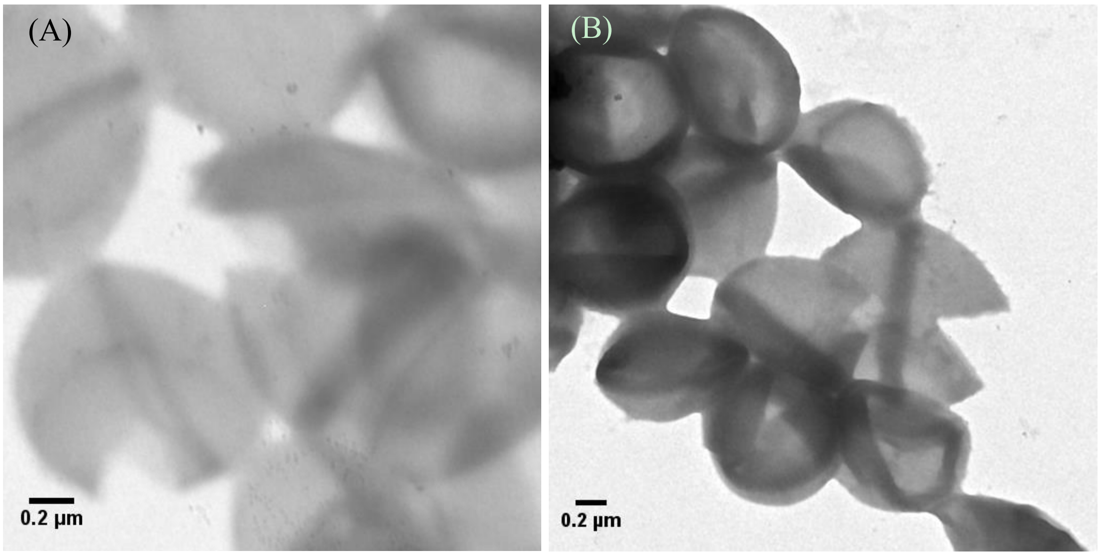

Figure 4.26 $NaBH_4$ effects on labelling cells with AuNPs. *S. aureus* cell sacculi were treated with $NaBH_4$ before labelled with the azide probe and alkyne functionalized AuNPs possessing 5 **(A)** or 30 **(B)** nm in size. Treated sacculi were imaged by TEM.

4.3 Discussion

4.3.1 Probe preparation and the development of labelling protocols

PG has aldehydes at the reducing termini that provide opportunities for conjugation of cellular probes and the study of cellular processes. The success of HAF488 labelling in previous work proves the suitability of aldehyde-active probes for PG labelling. Consequently, the initial strategy was to design new aldehyde-active probes functionalized with hydroxylamine groups and a clickable moiety. After several attempts, a successful synthetic route was established, which started from inexpensive Cl-TEG-OH and generated the azide-probe with 56% overall yield. Subsequent *in vivo* cellular and sacculi imaging using diffraction limited FM, SIM, STORM and EM confirmed the broad biocompatibility and feasibility of the new synthetic probe.

The labelling strategy was investigated before the study of cell dynamics, including feasibility of the *in vivo* click reaction, the order of conducting click reactions, and oxime ligation conditions. It was found that the click reaction strategy and the reaction volume of ligation played crucial roles in cell labelling results. Another exciting finding was that the Cu(I)-catalyzed click reaction can be used for both *in vivo* and *in vitro* cellular labelling, and the copper salt used was non- or low toxic to *S. aureus*. Previous work related to copper biotoxicity was mainly performed on human or mammalian cells.[171,172] Compared with eukaryotic cells, bacteria probably possess strong resistance to metal ions. For example, in Tirrell's lab, Cu(I)-catalyzed click reaction was employed using alkynyl amino acid and fluorogenic dye with azide to label newly synthesized proteins in *Escherichia coli* cells.[173] In addition to the tolerance to metal ions, a synergistic effect from the addition of copper chelating ligands provided another possibility for cell survival, although the commercially available click reaction buffer kit used in this work was sealed and ingredients like chelating ligands were unknown. These ligands were found to play multiple-roles in click reactions such as stabilizing Cu(I), increasing the reaction rate and in particular reducing or even eradicating the cytotoxicity of catalysts.[174,175] Finally, cells were merely treated with the copper containing mixture for 5 or 30 mins that was shorter than that of previously reported (ie, 2 hours), resulting in avoiding the cytotoxicity.

4.3.2 Multiple imaging modes for understanding cell wall dynamics

First of all, optimization and investigation of quality and feasibility of azide probes in fluorescence microscopy was carried out. On the basis of above established labelling protocol, high-quality fluorescence images with biological information were obtained. The probe was confirmed to be comparable with the pre-existing HAF488 and thus has the potential for reducing termini labelling. In addition, the azide probe could be used for dual labelling experiments and its localization was not identical with that of the side-chain labelling probe (D-amino acid analogues or VanF), in which cross-labelling features were observed (Figure 4.27). For instance, when the azide probes were localized at the cell wall periphery, the TADA signal appeared at the septum.[37] Apart from true localization of probes, this was probably due to further cell growth changing probe distribution after the azide probe labelling, as TADA labelling occurred in the culture at 37 °C. The observation of cross-labelling features in new dual labelling experiments using the azide probe and VanF excluded the possibility of further growth effects (Figure 4.27B).

PG dynamics of the *S. aureus sagB* mutant and *B. subtilis* were investigated. SagB is a key glucosaminidase and lack of it leads to a length increase of glycan chains in PG.[18] As a result, the reducing termini labelling was decreased. It was also found that the mutant lacked the peripheral cell labelling. This suggested SagB plays a crucial role in PG hydrolysis at the periphery. With respect to *B. subtilis*, the reducing termini labelling was clearly decreased in contrast to the *S. aureus* WT cells, which is supported by the fact that *B. subtilis* has much longer glycan chains.[162] Apart from the difference in the length, the distribution of reducing termini was also different. HAF448 showed, a punctate pattern along the cylindrical cell wall that was similar to the previously reported staining pattern using fluorescent antibiotics.[176]

The distribution of new reducing termini in *S. aureus* was also investigated. HAF488 pre-labelled cells were grown on and newly formed reducing termini were labelled with the azide-probe/Alkyne647. Over time the old cell wall was cleaved and the HAF488 labelling was re-localized as characteristic features, termed as “I”, “Y/V”, “X”, and “C” conformations (Figure 4.28), which revealed the dynamics of PG. In addition, the observation of the cross-labelling features at variety levels provided a direct visualization of remodelling of PG associated with the cell cycle.

New insight was also provided as to the understanding of the role of hydrolysis in the cell wall remodelling by moenomycin treatment. Of note, moenomycin inhibits bacterial growth through blocking transglycosylation. As a result, the appearance of new reducing termini labelling after treatment could be only explained by hydrolysis.

Finally, the feasibility of the new azide probe in super resolution imaging was examined. SIM and STORM provided similar, but much clearer imaging modes than diffraction limited microscopy. For instance, SIM showed a macroscopic convincing evidence that moenomycin leads to the lack of the peripheral labelling of FDAAs, which was consistent with my previous work in Chapter 3.

TEM imaging of the reducing termini was also carried out. Although, the labelling efficiency, especially in the case of 30 nm AuNPs, was not satisfactory, probably due to aggregation of AuNPs, which was easily judged from the colour change, there were still characteristic features. The obvious dark regions were considered as septa or ribs left after division, which confirmed the applicability of the synthetic probe in EM imaging. This provided complementary information to fluorescence imaging for the study of cell dynamics.

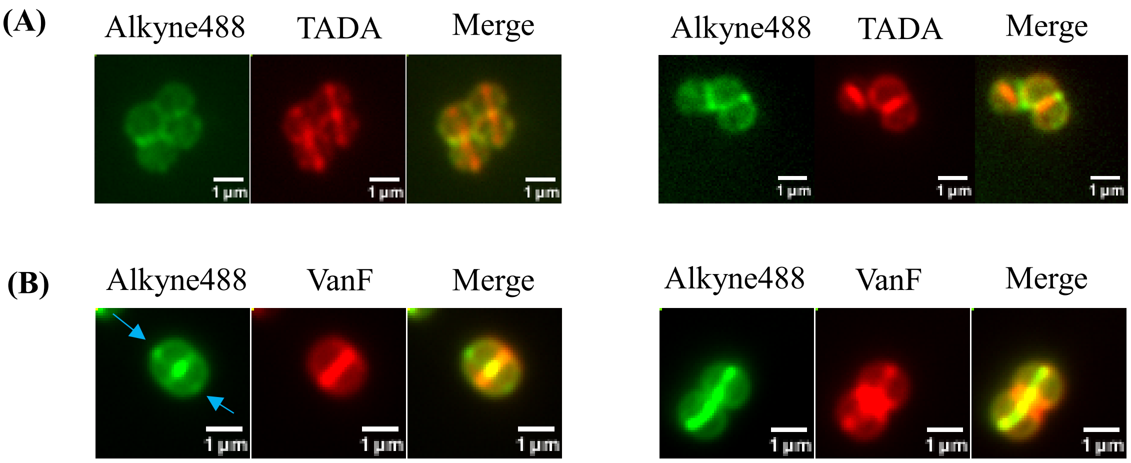

Figure 4.27 Cross-labelling features in dual-labelling strategies. *S. aureus* WT cells were labelling with azide-probe/Alkyne488 and then stained with TADA **(A)** or VanF **(B)**. Arrows: increased reducing termini sites.

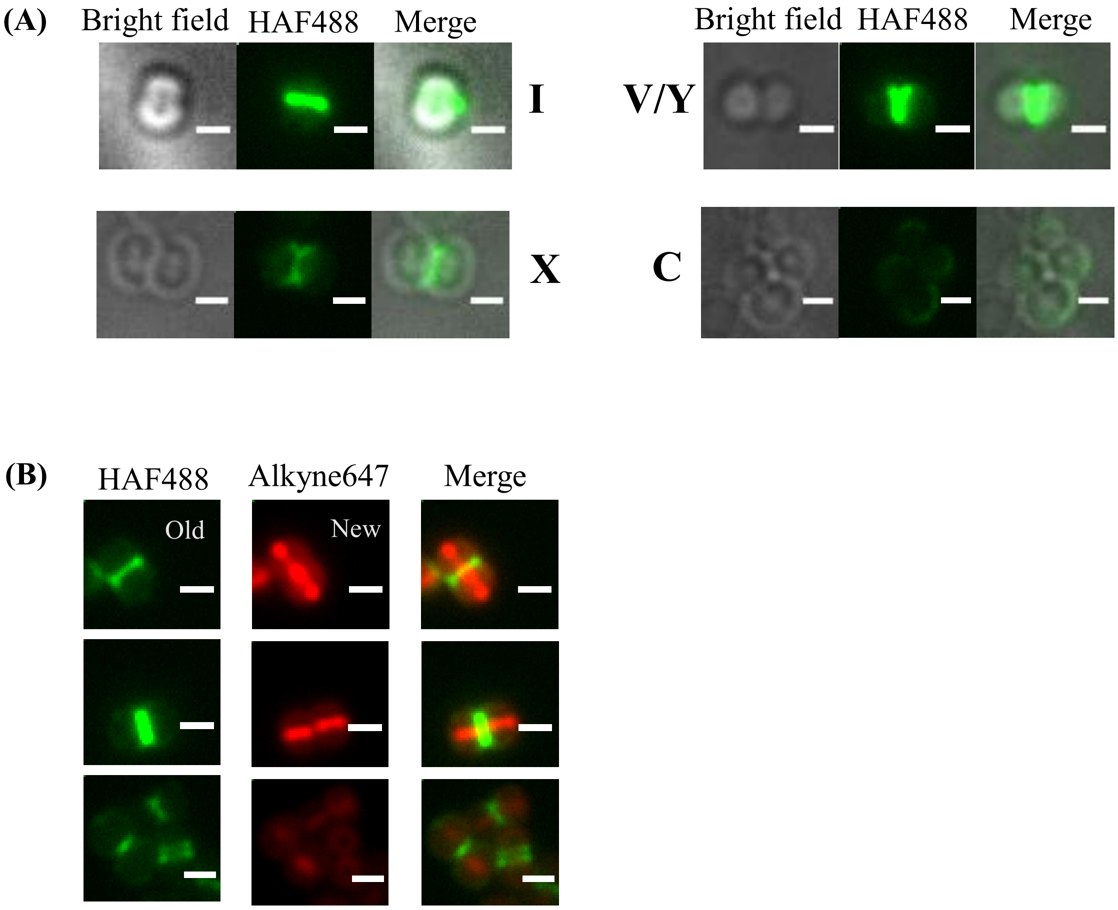

Figure 4.28 Reducing termini dynamics associated with the cell cycle in *S. aureus*. Cells in exponential phase were treated with HAF488 (Green) and grown on in TSB. After harvesting, cells were labelled with azide probe/Alkyne647 (Red). **(A)** HAF488 labelling changed from “I”, to “Y/V”, “X”, and “C” conformations. **(B)** Cross-labelling features at different levels from old and new PG. scale bar: 1 µm.

Chapter 5 Development of metallocene probes for cell wall research

5.1 Introduction

Fluorescent probes have been widely applied as investigative tools for bacteria cell imaging as described in previous chapters.[177,178] Despite such success, as a result of the optical diffraction limit, fluorescent microscopy only provides visualisation of large structures and is incapable of precise subcellular or molecular localization. The emergence of super-resolution microscopy has enabled improved image resolution to 20-100 nm, but this still barely meets the size requirements of biological molecular targets ranging from 0.1 to 10 nm. Another limitation of fluorescence imaging is unexpected quenching of probes resulting from the micro-environment of biological samples. In contrast, the sub-nanometer resolution provided by electron microscopy (EM) is sufficiently high to ascertain bacterial morphology. Therefore, EM is as an alternative approach to examine bacterial ultrastructure. For more detailed investigations of cell wall dynamics, labels that allow precise localization of targets and distinct visualisation by EM are desirable.

Metallocenes are organometallic compounds with a metal ion between two π-bonded cyclopentadienyl (Cp) rings and their discovery has greatly advanced organometallic chemistry. The investigation of metallocenes originated from an accidental discovery of *bis*(η^5-cyclopentadienyl)iron, ferrocene, from which the common name metallocene is derived. In 1951, ferrocene was discovered unintentionally by two researchers at Duquesne University when they performed a coupling of anhydrous ferric(II) chloride and a Grignard reagent of cyclopentadienyl magnesium bromide, attempting to prepare fulvalene.[179] This crystalline compound showed remarkable stability when exposed to air, high solubility in organic solvents but insolubility in aqueous solvents. Initially, the formation of ferrocene was mistakenly considered as covalent binding of cyclopentadienide anions and ferrous ion (Figure 5.1 A). However the correct structure of ferrocene was elucidated as a “sandwich compound” by two independent research groups and further confirmed using infrared (IR), NMR spectroscopy and X-ray crystallography (Figure 5.1 B).[180-184] Due to these achievements, the 1973 Nobel Prize in Chemistry was awarded to this field. Over time, more and more compounds with a similar structure that consist of transition metal and two Cp rings have been developed and named as metallocenes, including ferrocene, cobaltocene, osmocene, chromocene, ruthenocene and nickelocene. As a result of this special structure, metallocenes possess a variety of intrinsic properties such as redox-activity, and have attracted considerable interest, being widely applied in chemistry and materials science, including organic catalysis, energy conversion, electrochemical sensing, and molecular electronics.[185-188]

There have been increasing reports about using metallocenes in biological and medical studies since ferrocenyl polyamines were found to bind to tumour cell surfaces and show antitumour activity.[189] Metallocenes have been incorporated into polymers, DNA and peptides for cell and intracellular sensing based on electrochemical properties of metallocenes.[190,191] Also, metallocene peptide bioconjugates have been used in an MIC (Minimum inhibitory concentration) test against *Escherichia coli*, *Pseudomonas aeruginosa*, and *Staphylococcus aureus*, showing good antibacterial properties.[192] Despite widespread reports of the biological and medical applications of metallocenes, few investigations have employed metallocenes for cell morphology and dynamics research. Metallocenes have great potential in studying the cell wall, especially with the help of EM. Transition metals contain a high density of electrons in the centre of metallocene making themselves potential candidates for development as probes for EM imaging. Meanwhile, the two Cp rings provide ample opportunities for incorporation of multi-functional groups to label cells. Furthermore, a variety of chemical and physical properties derived from their sandwich structure such as their kinetic stability and high accessibility of ligand substitutions facilitate imaging work in EM. These concepts provided a steer to investigate the development of a new EM probe based on metallocenes for cell wall labelling.

5.2 Results

5.2.1 Design and synthesis of new metallocene probes

A variety of metallocenes have been synthesized, including ferrocene, cobaltocene, osmocene, chromocene, ruthenocene and nickelocene.[193] In spite of the similar sandwich structure, metallocenes show diverse stabilities with different transition metals. For example, compared with ferrocene, cobaltocene and nickelocene are more easily oxidised due to an increased number of electrons. However, transition metals found in ferrocene, ruthenocene, and osmocene have achieved the electronic configuration of noble gases and therefore these three metallocenes show particularly high stability.[194] Most literature reports involving biological and medical studies have employed derivatives of ferrocene or ruthenocene. As a result, ferrocene and ruthenocene were chosen as the core components of the proposed EM probes.[195,196] Also, cells survive in natural aqueous environments, but bare metallocenes are insoluble in aqueous solvents. Therefore, TEG was introduced to enhance the solubility of metallocenes and aid their flexibility in cell labelling. Furthermore, a common approach for labelling the cell wall is to recognize aldehyde groups from the reducing termini of PG, therefore hydroxylamine was used as a ligating group (Scheme 5.1).

5.2.1.1 The synthetic strategy on basis of dimethylaminomethylferrocene

The first synthetic strategy involved formation of a ferrocenyl ammonium salt as an intermediate from commercially available dimethylaminomethylferrocene. The aromatic-like structure and quaternization of dimethylaminomethylferrocene results in formation of a good leaving group and thus a hydroxyphthalimide-protected primary alcohol should readily perform S_N2 nucleophilic substitution, yielding ferrocene-TEG conjugates. For this purpose, several approaches were considered for the synthesis of hydroxyphthalimide-TEG (PhthNO-TEG).

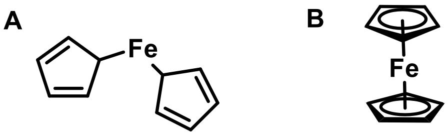

Figure 5.1. Ferrocene structure. **(A)** Original incorrect notion: when ferrocene was first synthesised, the compound was determined as the complex formed by covalent binding of cyclopentadienide anions and ferrous ion. **(B)** Correct structure: the real structure was afterward published as sandwich-like feature.

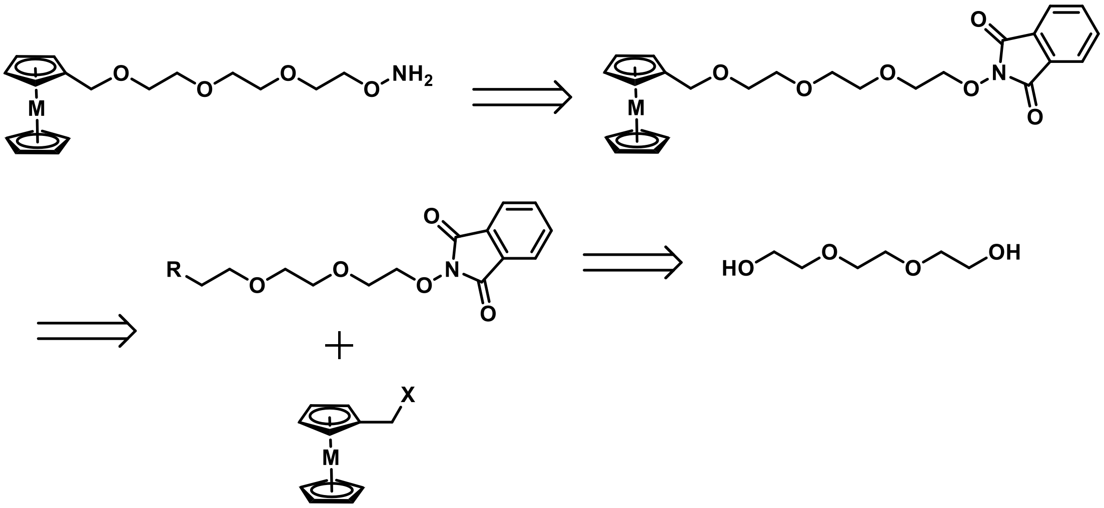

Scheme 5.1 Retrosynthesis of metallocene probes. Through a straightforward route, metallocene probes were envisaged to be prepared from commercially available triethylene glycol, which involved with several steps of substitutions and deprotection. X or R: -OH, -OTs, -Cl, -Br, or -I group.

Initially, *N*-hydroxyphthalimide was reacted with 2-[2-(2-chloroethoxy)ethoxy] ethanol (Cl-TEG) in the presence of a base and sodium iodide catalyst to access PhthNO-TEG (Table 5.1). It was found that base option was the key determinant: strong (NaH) and weak ($NaHCO_3$) bases resulted in failure, hydroxide provided an extremely low yield and the use of carbonate slightly improved the yield (Table 5.1 entry 1-7). To enhance the solubility of iodide catalyst, an organic salt (TBAI) was substituted for sodium iodide (NaI), but it showed no effect (Table 5.1 entry 8). TEG with different leaving groups were prepared and tested (Table 5.2). 2-[2-(2-Iodoethoxy)ethoxy]ethanol (I-TEG) was synthesized by the reaction of Cl-TEG and NaI in acetone heated at reflux for 2 days, giving 96% yield. Mono-tosylated TEG was obtained by means of Ag_2O mediated tosylation as described above. Subsequently, nucleophilic displacement occurred, but the results were unsatisfactory. It should be pointed out that in each case a complex mixture of by-products appeared and it was hard to completely purify products by column chromatography on silica gel, and repeated purifications were needed.

As an alternative approach, a Mitsunobu reaction of TEG and *N*-hydroxyphthalimide in the presence of triphenylphosphine (PPh_3) and diisopropyl azodicarboxylate (DIAD) was used and allowed straightforward access to mono-hydroxyphthalimide protected TEG on a 5 g scale in a 90% yield after purification by column chromatography on silica gel (Scheme 5.2).

Having obtained PhthNO-TEG, synthesis of ferrocene-TEG conjugates were next investigated. Trofimov's group has developed an efficient method for the synthesis of propargyloxymethylferrocene by the reaction of propargyl alcohol with dimethylaminomethylferrocene ($FcMeNMe_2$) in the presence of dichloroethane and NaOH in almost quantitative yield.[197] Also, it was reported that iodomethane was employed for formation of a ferrocenyl ammonium salt intermediate for subsequent nucleophilic substitution to functionalize ferrocene with long chains.[198,199] Inspired by this work, two modified approaches were attempted and the starting $FcMeNMe_2$ underwent quaternization with dichloroethane or iodomethane followed by S_N2 nucleophilic substitution of PhthNO-TEG (Scheme 5.3). Unfortunately, in both cases TLC showed incomplete consumption of dimethylaminomethylferrocene even if using an excess of PhthNO-TEG. All of the crude ^{1}H NMR spectrums suggested there was rare formation of the desired product.

5.2.1.2 The synthetic strategy employing the Mitsunobu coupling

Given previous successes with the Mitsunobu coupling, focus was shifted to conjugate ferrocenemethanol (FcMeOH) with PhthNO-TEG. The synthesis of FcMeOH was achieved in a two-step protocol, starting with monolithiation of the commercially available Fc to afford ferrocene carboxaldehyde (FcCHO) in 72% yield according to a previous report.[102] The reduction of the aldehyde with $NaBH_4$ in MeOH generated FcMeOH (99% yield), which was subsequently used for Mitsunobu coupling. Although the same procedure was employed as successfully described above, the results were unsatisfactory; the starting materials were unconsumed and only traces, if any, of the target compounds were detected.

5.2.1.3 The synthetic strategy using the S_N2 nucleophilic substitution of FcMeOH

The possibility of reacting FcMeOH as a nucleophile with an electrophilic conjugate of Cl-TEG and hydroxyphthalimide moiety (Cl-TEG-ONPhth) was explored next (Table 5.3). The synthesis of Cl-TEG-ONPhth was achieved by a Mitsunobu reaction of Cl-TEG with hydroxyphthalimide with a 76% yield.

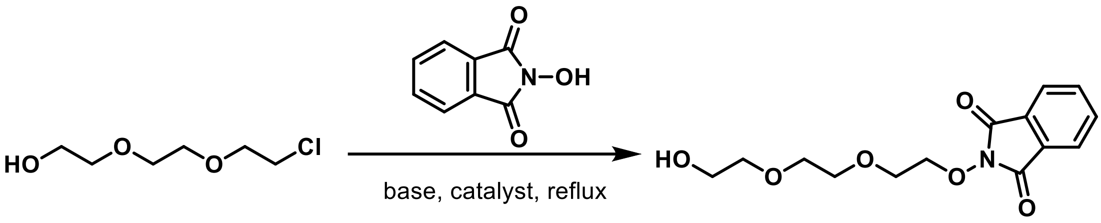

Entry	Base	Solvent	Catalyst	Yield %[c]
1	Na_2CO_3[a]	MeCN	NaI	none
2	NaH[b]	MeCN	NaI	none
3	KOH	DMF	NaI	<15
4	KOH	DMSO	NaI	<15
5	NaOH	DMF	NaI	<28
6	$NaHCO_3$	DMF	NaI	none
7	Na_2CO_3	DMF	NaI	<38
8	Na_2CO_3	DMF	TBAI	<40

Table 5.1 Synthesis of PhthNO-TEG from Cl-TEG. Reaction conditions: 1.3 equivalent of hydroxyphthalimide and 2 equivalents of base in dry solvent was refluxed 0.5 h followed by the addition of 10 mol% catalyst and Cl-TEG (1 equivalent) and refluxed for overnight. a: 3 equivalent; b: 1.5 equivalent; c: referred to the isolated product.

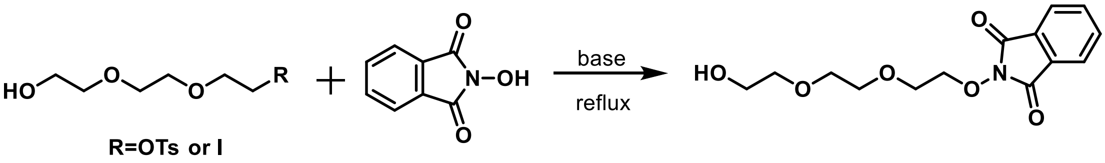

Entry	R	Base	Solvent	Yield %[a]
1	I	KOH	DMF	30
2	OTs	KOH	DMF	26
3	OTs	Na_2CO_3	DMF	35

Table 5.2 Synthesis of PhthNO-TEG from TEG with different leaving groups. Reaction conditions: 1.3 equivalent of hydroxyphthalimide and 2 equivalents of base in dry solvent was refluxed for 0.5 h followed by the addition of R-TEG (1 equivalent) and refluxed for overnight. a: referred to the isolated product.

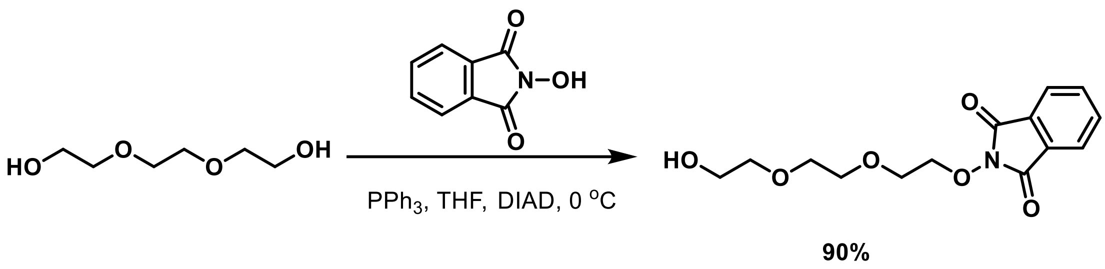

Scheme 5.2 Synthesis of PhthNO-TEG in a Mitsunobu reaction. Conditions: DIAD was added dropwise to the mixture of TEG, hydroxyphthalimide and PPh_3 in dry THF at 0 °C followed by warmed to RT and reacted for overnight.

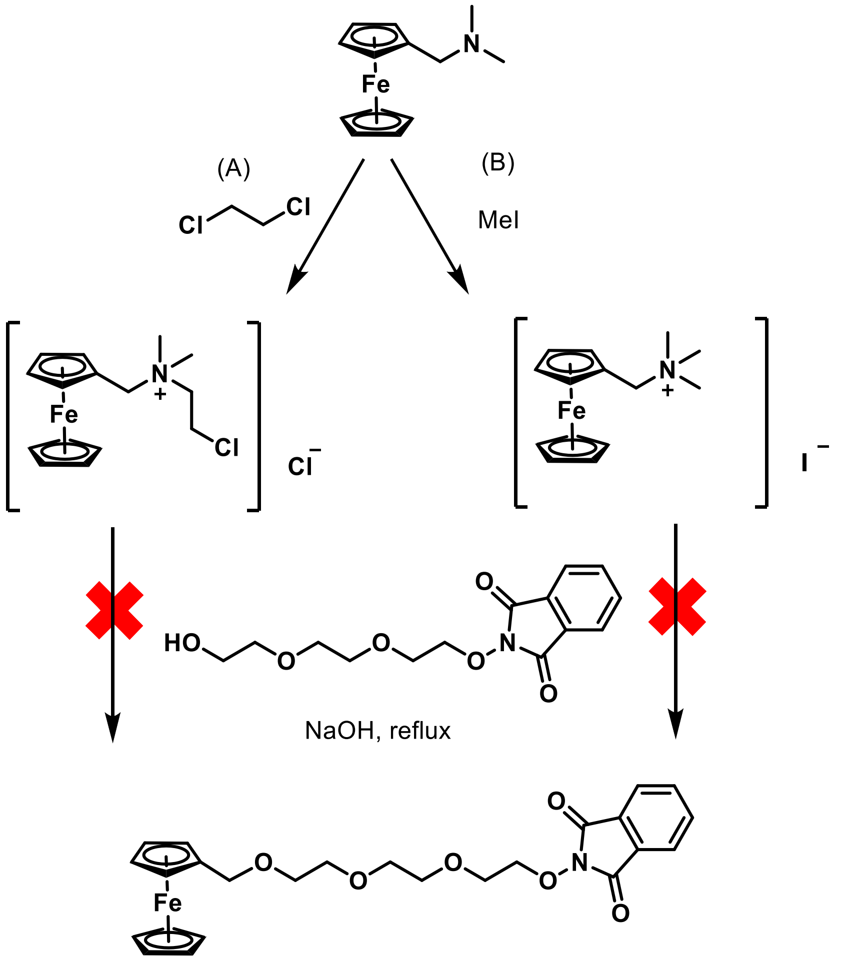

Scheme 5.3 Attempted synthesis of ferrocene-TEG conjugates. Reaction conditions: (A) the mixture of $FcMeNMe_2$ and dichloroethane were reacted at 100 °C for 1.5 hour followed by the addition of NaOH and TEG in toluene, which were refluxed for 12 hour. (B) The mixture of $FcMeNMe_2$ and iodomethane in acetonitrile were refluxed for 1 hour followed by the addition of NaOH and TEG, which were refluxed for 48 hours.

Initially, two kinds of well-used bases (Na_2CO_3 and NaH) were chosen. However, the crude ^{1}H NMR spectrum displayed multiple impurities (Table 5.3 entry 1-3). Wurm's group has reported the reaction of FcMeOH and epichlorohydrin in the presence of tetrabutylammonium bromide (TBAB) in a mixture of benzene and a 50% NaOH solution, giving a yield up to 80%.[200] An attempt to replicate this with minor modifications was performed, in which toluene was substituted for benzene, but the results showed no much difference (Table 5.3 entry 4).

Another approach was considered for the formation of ferrocene-TEG conjugates; conversion of FcMeOH into an electrophile by tosylation and nucleophilic displacement with PhthNO-TEG. It was found that using the traditional method that reacted FcMeOH with TsCl in the presence of triethylamine (Et_3N) and 4-dimethylaminopyridine (DMAP) did not generate the desired Fc tosylate, probably due to the high reactivity of the product, forming *bis*ferrocenyl methyl ether, which was consistent with previous research.[201]

5.2.1.4 The synthetic strategy on basis of the S_N1 reactions

In recent years, the condensation of FcMeOH with long chain alcohols has been reported, which employs Brønsted acid catalysts, such as acetic acid (AcOH),[202] and Lewis acid catalysts such as metal triflate.[105,203] These S_N1 reactions involved acid-catalyzed formation of ferrocenylmethyl cations, and nucleophilic substitution of alcohols, which only generates water as the main by-product and is environmentally friendly. Based on this work, a number of catalysts were employed to address the conjugation of FcMeOH and TEG (Table 5.4). When Brønsted acids (AcOH or TsOH) were used, the conversion of FcMeOH was rare as most of the returns were TEG complex even if 5 equivalents of alcohol was added and reacted for approximately two days (Table 5.4 entry 1-2). To improve the conversion, the reaction was heated at reflux, but the result was disappointing (Table 5.4 entry 3). The failure to observe FcMeOH and improve yield was attributed to decomposition and the colour change of reaction mixture provided direct evidence to support this, which was in agreement with previous research.[202] Metal triflates, widely used Lewis acids, were also investigated. It was found that in all cases metal triflates successfully catalysed the formation of the desired compound with similar conversion (Table 5.4 entry 4-7) and mass return (data not shown). It was worth noting that although ^{1}H NMR spectroscopy showed promising results, incomplete consumption of the starting material was observed and a variety of by-products were monitored by thin layer chromatography (TLC), resulting in difficulties in purification. A combined crude product from all triflates-catalysed reactions was purified by column chromatography on silica gel and gave an approximate 40% yield.

In an attempt to improve yield, TEG without hydroxyphthalimide was used for the etherification of FcMeOH. In previous work, it was found that TLC and ^{1}H NMR spectroscopy indicated less impurities when $Al(OTf)_3$ used to catalyse the etherification. As a result, $Al(OTf)_3$ was employed for the new investigation on the etherification of TEG without hydroxyphthalimide and FcMeOH. Surprisingly, this generated Fc-TEG-OH in an 80% yield. Subsequent Mitsunobu reaction with *N*-hydroxyphthalimide in the presence of PPh_3 and DIAD allowed straightforward access to the target Fc-TEG-ONPhth in a high yield of 93% (Scheme 5.4).

The next crucial step was to remove the hydroxyphthalimide protection from Fc-TEG conjugate giving the active hydroxylamine ($-ONH_2$) group for cell labelling (Table 5.5). Initially, ethanolamine was used due to its successful application previously described in this project. Following the same procedure, the reaction was performed in DCM at RT, but even after approximately two days, a trace of Fc-TEG-ONPhth was observed. To improve the conversion, the reaction was performed at a higher temperature (~40 ^{o}C) and an improved yield of 56% was achieved. However, the result was poor in contrast with previous ethanolamine-involved deprotection of N_3-TEG-ONPhth, therefore some modifications were performed. It was found when heated at a slightly higher temperature of 45-50 ^{o}C, the reaction give an acceptable yield of 77%. Recently, aminoxy-functionalized tetrathylene glycol has been successfully prepared at RT by deprotection of hydroxyphthalimide using a solution of MeOH and ammonia.[204] Applying this method by reacting Fc-TEG-ONPhth with ammonia at 45-50 ^{o}C gave a 69% yield (Table 5.5 entry 4).

5.2.1.5 The synthetic strategy for the preparation of Rc-TEG conjugates

Having obtained an Fc-TEG conjugate, ruthenocene (Rc) containing ruthenium, an element rarely appearing in cells, was thus selected to prepare another metallocene-TEG probe (Scheme 5.5). As a result of the expensive price of Rc (162.50 pounds per gram from Sigma-Aldrich), the synthetic route started with preparing Rc from ruthenium trichloride ($RuCl_3$). According to a literature procedure with minor modification, $RuCl_3$ reacted with freshly prepared cyclopentadiene (Cp) in the presence of zinc in ethanol, affording Rc as a yield of 95%.[106] Similar to Fc, monolithiation of Rc followed by reaction with DMF generated Rc monoaldehyde (RcCHO) at a yield of 82%. Ruthenocenylmethanol (RcMeOH) was obtained in quantitative yield by reduction with $NaBH_4$ and subsequent condensation with TEG using $Al(OTf)_3$ produced Rc-TEG at a yield of 81%. Mitsunobu coupling with *N*-hydroxyphthalimide resulted in formation of Rc-TEG-ONPhth (79% yield) and deprotection of the hydroxyphthalimide moiety using ethanolamine gave ruthenocenylmethyl-triethylene glycol hydroxylamine (Rc-TEG-ONH_2) in a yield of 74%.

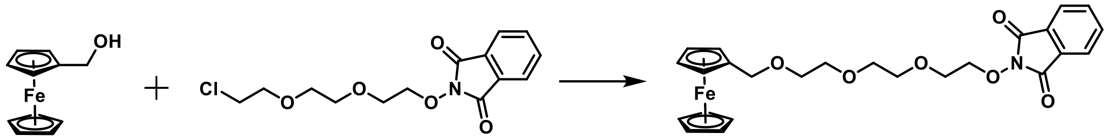

Entry	Base	Solvent	Catalyst	Conversion %[b]
1	Na_2CO_3	THF	NaI	<5
2	NaH	THF	NaI	<5
3	NaH	DMF	NaI	<5
4[a]	NaOH	PhMe/H_2O	TBAB	<5

Table 5.3 Attempted synthesis of the ferrocene-TEG conjugate from FcMeOH and Cl-TEG-ONPhth. Reaction conditions: 1 equivalent of FcMeOH and 2-6 equivalents of base in dry solvent was refluxed for 15 min followed by the addition of 10 mol% catalyst and Cl-TEG-ONPhth (1.4 equivalent) and refluxed for 2 days. a: The reaction was performed from 0 °C to RT; b: determined by analysis of the crude ^{1}H NMR spectrum.

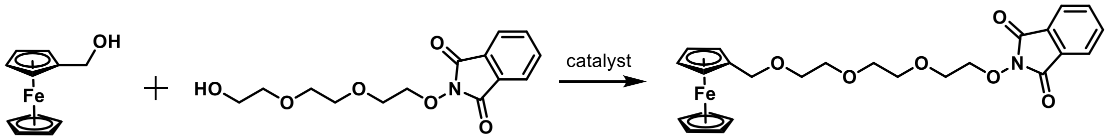

Entry	Temperature	Solvent	Catalyst	Conversion %[a]
1	RT	PhMe	AcOH	<5
2	RT	PhMe	TsOH	<5
3	Reflux	PhMe	TsOH	<5
4	RT	DCM	$Al(OTf)_3$	79
5	RT	DCM	$Y(OTf)_3$	65
6	RT	DCM	$In(OTf)_3$	81
7	RT	DCM	$Sm(OTf)_3$	72

Table 5.4 Acid catalysed condensation of FcMeOH and PhthNO-TEG. Reaction conditions: 5 mol% catalyst was added to the mixture of FcMeOH and HO-TEG-ONPhth in dry solvent, and the mixture was stirred for 1-2 days. a: determined by analysis of the crude ^{1}H NMR spectrum.

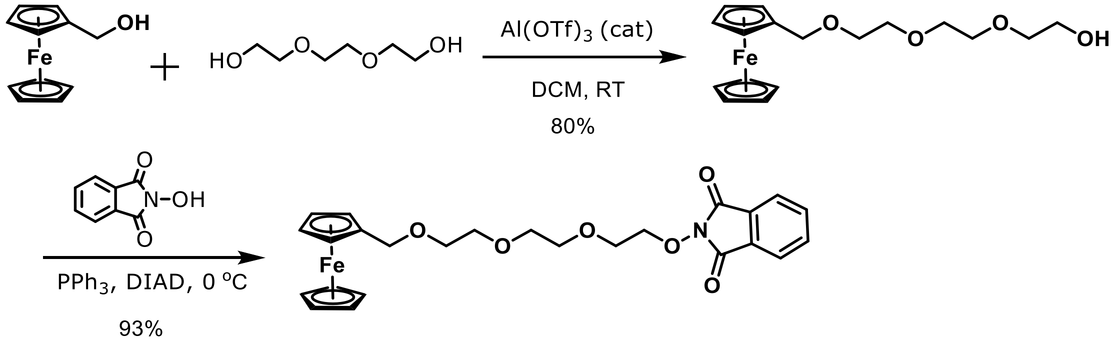

Scheme 5.4 Synthesis of Fc-TEG conjugates. Fc-TEG was prepared using a $Al(OTf)_3$ catalysed etherification. The target Fc-TEG-ONPhth was afforded via coupling of Fc-TEG with hydroxyphthalimide employing a Mitsunobu strategy.

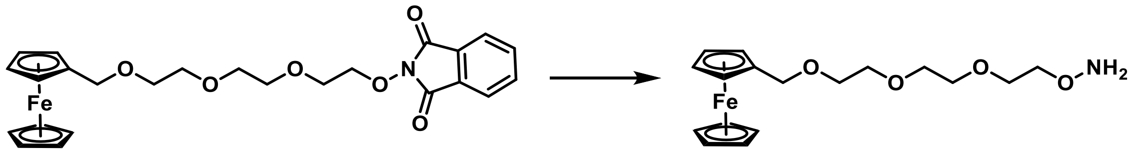

Entry	Temperature	Solvent	Reagent	Yield %[a]
1	RT	DCM	Ethanolamine	-[b]
2	40 °C	DCM	Ethanolamine	56
3	45-50 °C	THF	Ethanolamine	77
4	45-50 °C	MeOH	Ammonia	69

Table 5.5 Deprotection of Fc-TEG-ONPhth. Reaction conditions: Ethanolamine or ammonia was slowly added to the Fc-TEG-ONPhth solution, and the mixture was stirred for 1-2 days. a: referred to the isolated product; b: the crude product was directly used for further research without purification.

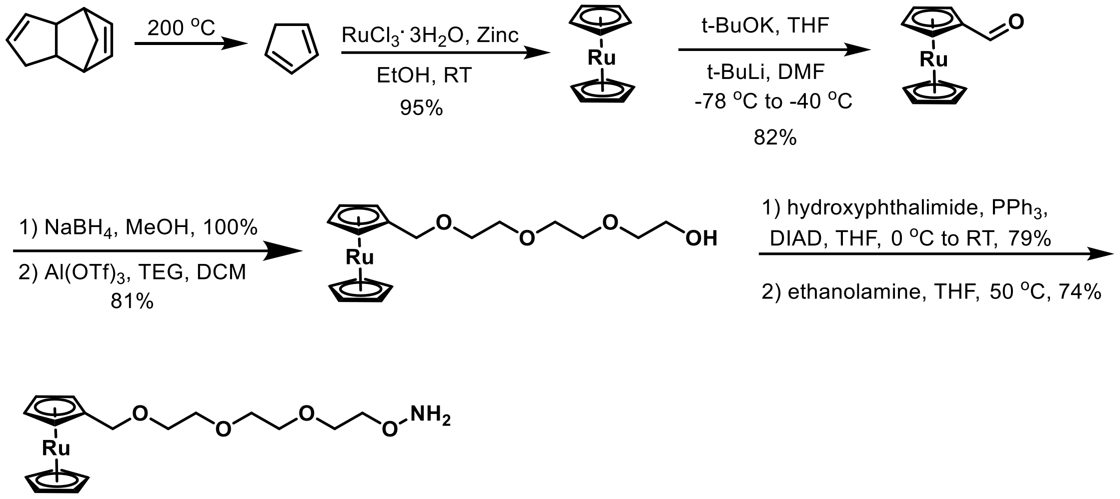

Scheme 5.5 Total synthesis of Rc-TEG conjugates. The target Rc-TEG-ONH_2 was efficiently synthesized in 7 linear steps with 37% overall yield. The key steps involved in the synthesis were monolithiation of Rc, $Al(OTf)_3$ catalysed conjugation between the TEG and the Rc moieties and deprotection of the hydroxyphthalimide moiety.

5.2.2 Optical properties and characterization of metallocene probes

Initially, the UV-vis absorption spectra of metallocene before and after functionalization was investigated. It has been reported that light causes noticeable decomposition of Fc when dissolved in halogenated solvents, therefore ethanol was used.[205] As shown in Figure 5.2 A, Fc displayed absorption peaks at about 340 and 440 nm, respectively, which was consistent with previous reports.[206] Essentially all of Fc analogues showed similar peaks at 340 nm, although the intensity was different, probably due to incorporation of TEG. As expected, for Fc conjugates the shift of the band around 440 nm was extremely slight compared to that of ferrocene. All indicated that conjugation with TEG had little effect on the natural optical properties of Fc. It was worth noting that for the condition using 10 mM solutions, the absorption of FcCHO was too strong for detailed analysis (data not shown). As a result, 1:10 diluted solutions were prepared to retest all compounds (Figure 5.2 B). It was clearly exhibited that although FcCHO still showed a distinctively strong absorption, most compounds have consistent absorption peaks according with the analysis in Figure 5.2 A.

When related to Rc containing complexes, it seemed to be more complicated. The peaks at 320 and 284 nm contributed to the Rc moiety, which was in agreement with a previous report,[207] but were suppressed by incorporation of aldehyde or hydroxyphthalimide groups (Figure 5.2 C). However, the inside figure in Figure 5.2 C clearly indicated that compared with the original Fc, no obvious shifts in the absorption profile of the Rc moiety occurred after the incorporation of TEG. All provided direct confirmation that functionalization of metallocenes in previous approaches allowed preservation of the optical properties of metallocenes and these probes have potential for application in cell labelling.

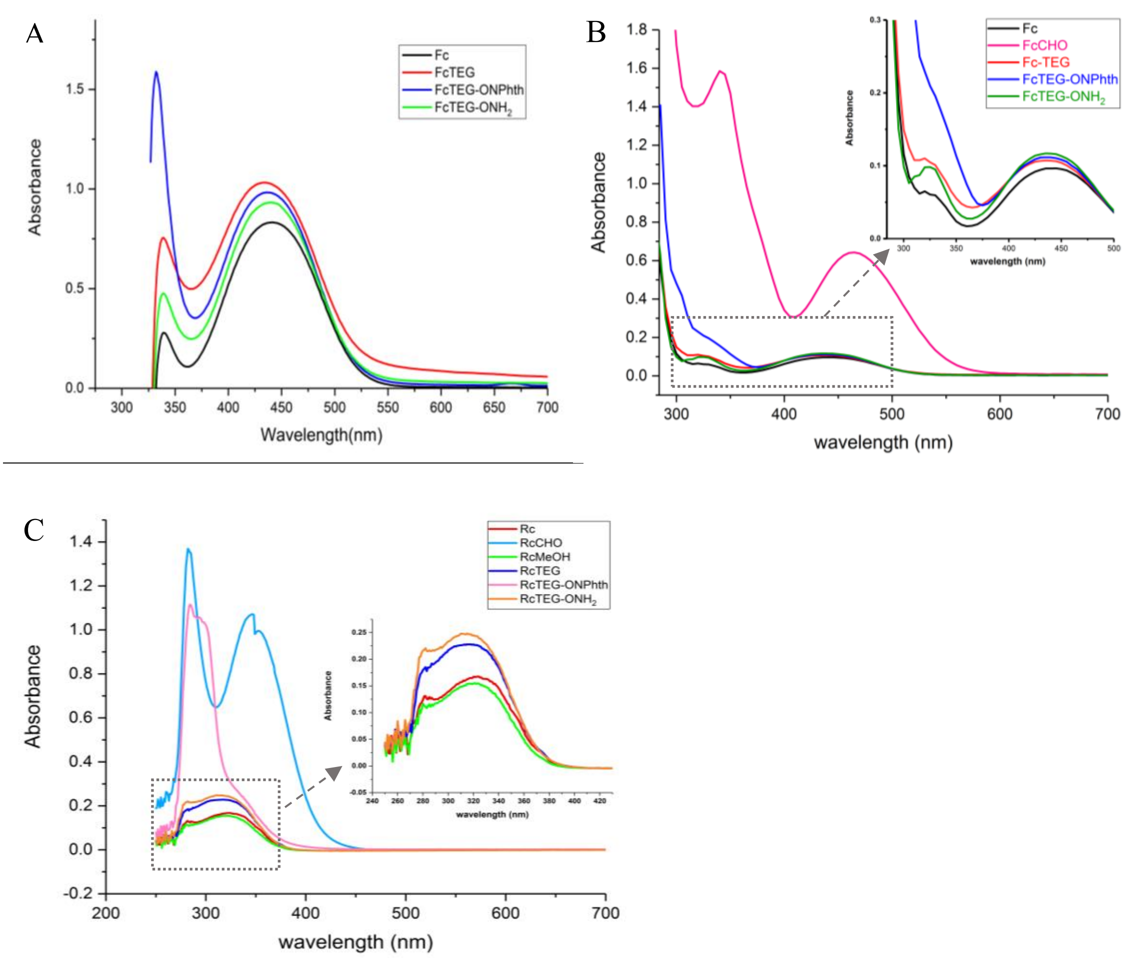

Figure 5.2 UV-Vis absorption spectra of metallocene probes. Complexes with an Fc moiety were dissolved in ethanol with a final concentration of 10 mM (**A**) or 1 mM (**B**) were tested for analysis of UV-Vis absorption. (**C**) Analysis of 1mM solution of Rc-containing complexes in ethanol.

The fluorescent properties of metallocene probes were next investigated. There are very few reports related to research on metallocene fluorescence.[208] As a result of a lack of references, full wavelength scanning of metallocene probes were performed to determine the optimal excitation wavelength. Considering the wavelength of maximum absorption normally show high relevance to intensity of fluorescence, fluorescence emission spectra was analysed with excitation of abovementioned peaks.

As shown in Figure 5.3 A, Fc-carrying complexes were tested using 330 nm of excitation light and it was found there were two characteristic peaks around 395 nm and 660 nm. The latter was characterized as the double frequency peak of excitation. The peaks around 395 nm were considered as effects of the Fc core, although the intensities of Fc, FcTEG and FcTEG-ONH$_2$ were extremely low. The insert picture in Figure 5.3 A clearly showed that Fc and its analogues exhibited similar fluorescence peak and the peak was derivative from the Fc moiety rather than functionalized components, which was consistent with the above analysis that functionalization has no significant influence on optical properties of Fc. The similar phenomenon was observed on the condition of 435 nm excitation. When excited at 435 nm, most of Fc complexes gave faint fluorescence and the exclusive sample with relatively high fluorescence was FcTEG-ONH$_2$. However it could be explained as the effect of modification rather than Fc itself.

Similar investigations with analysis of Fc-containing complexes were employed in the study of compounds with the Rc moiety (Figure 5.4). In the case of 284 nm excitation, a 568 nm peak characterized as the double frequency peak. A weak peak at 623 nm and broad multi peaks region ranging from 353 to 399 nm were observed in all compounds with the Rc moiety, in which RcTEG-ONH$_2$ showed the most strong fluorescence at approximately 375 nm (Figure 5.4 A). When excited at 315 nm, most compound exhibited triple adjacent peaks and merely RcTEG-ONH$_2$ showed a sharp peak that commonly appeared in fluorescence spectra of a certain fluorophore. Summarily, Rc-containing complexes displayed sophisticated optical features in contrast to Fc-carrying compounds and the probe RcTEG-ONH$_2$ exhibited peak around 375 nm when excited at 284 or 315 nm.

5.2.3 Fluorescence imaging live cells with metallocene probes

Having obtained the metallocene probes, fluorescent imaging of live cells was investigated using these probes. Initially, exponential-phase of *S. aureus* WT strains were incubated with FcTEG-ONH$_2$ or RcTEG-ONH$_2$ in PBS for 5 min at 37 ^{o}C, respectively. Based on optical properties tested above, the labelled cells were observed by wide field and three excitation channels of delta vision microscopy (Figure 5.5). It was found that when labelled with the Fc probe, excitation at 360, 492 and 555 all produced the discernible features such as “hot” spots on the cell surface (Red arrows in Figure 5.5 A) from the background, although the contrast was not comparable with that from common dye labelling. Compared with images from three channels, the FITC one displayed an informative pattern, in which the cell wall (Reds arrows) was labelled as well as the septum (Green arrows), while in other channels septal labelling was rarely found due to low contrast.

As for Rc labelling, some ‘hot-spot’ labelling seemed to occur (Yellow arrows in Figure 5.5 B), although the fluorescence in all channels were so faint that there were no features to be viewed. The direct observation of the discernible features in cells labelled with two probes confirmed that metallocene probes possess extremely weak fluorescence.

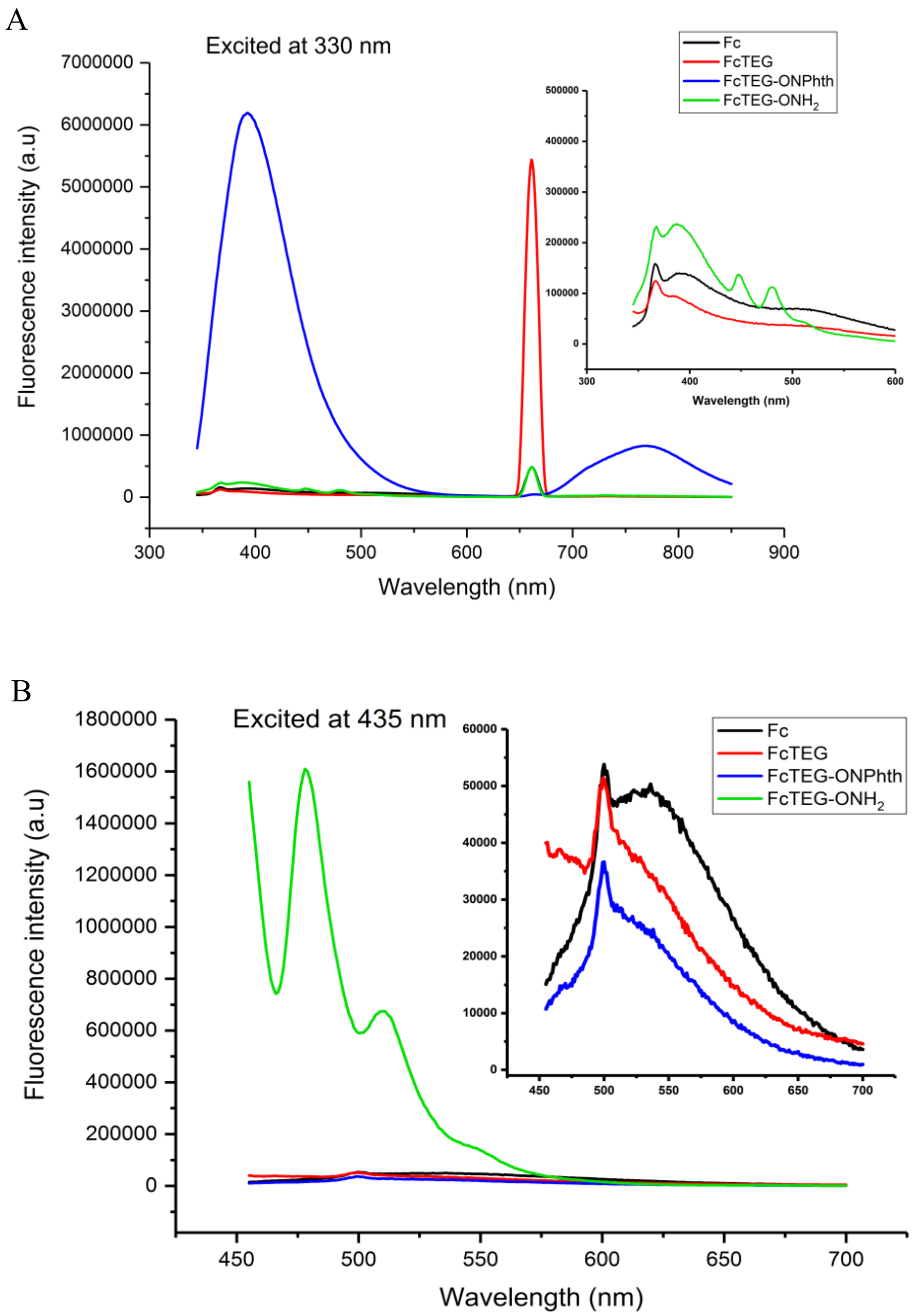

Figure 5.3 Fluorescence spectra of Fc probes. Fc-carrying complexes in ethanol with a final concentration of 1 mM were tested for analysis of fluorescence spectra. **(A-B)** Changes in fluorescence from variety of excitation wavelength.

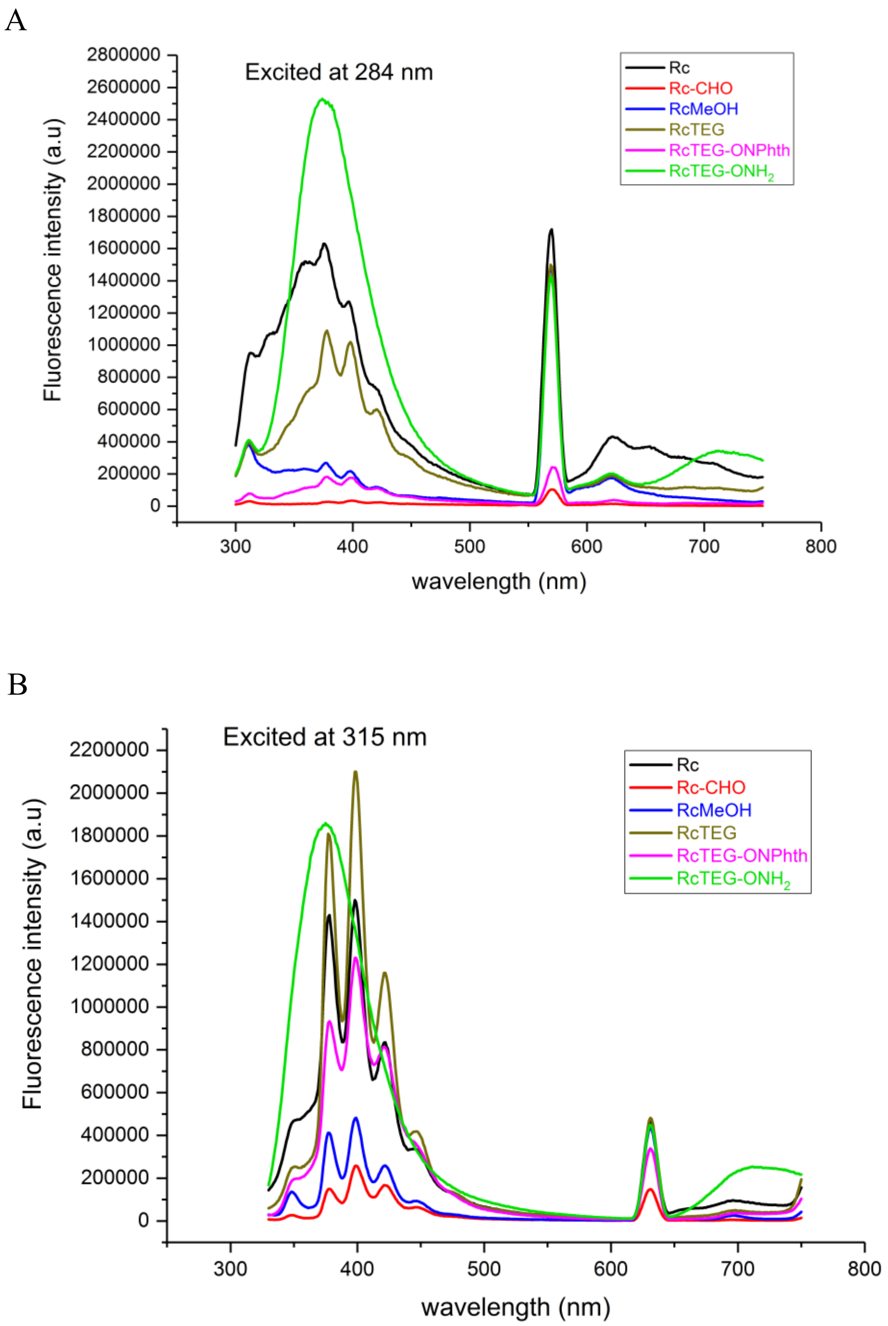

Figure 5.4 Fluorescence spectra of Rc probes. 1 mM of Rc-containing complexes in ethanol were tested for analysis of fluorescence spectra. **(A)** Fluorescence by full wavelength scanning. **(B-D)** Changes in fluorescence from variety of excitation wavelength.

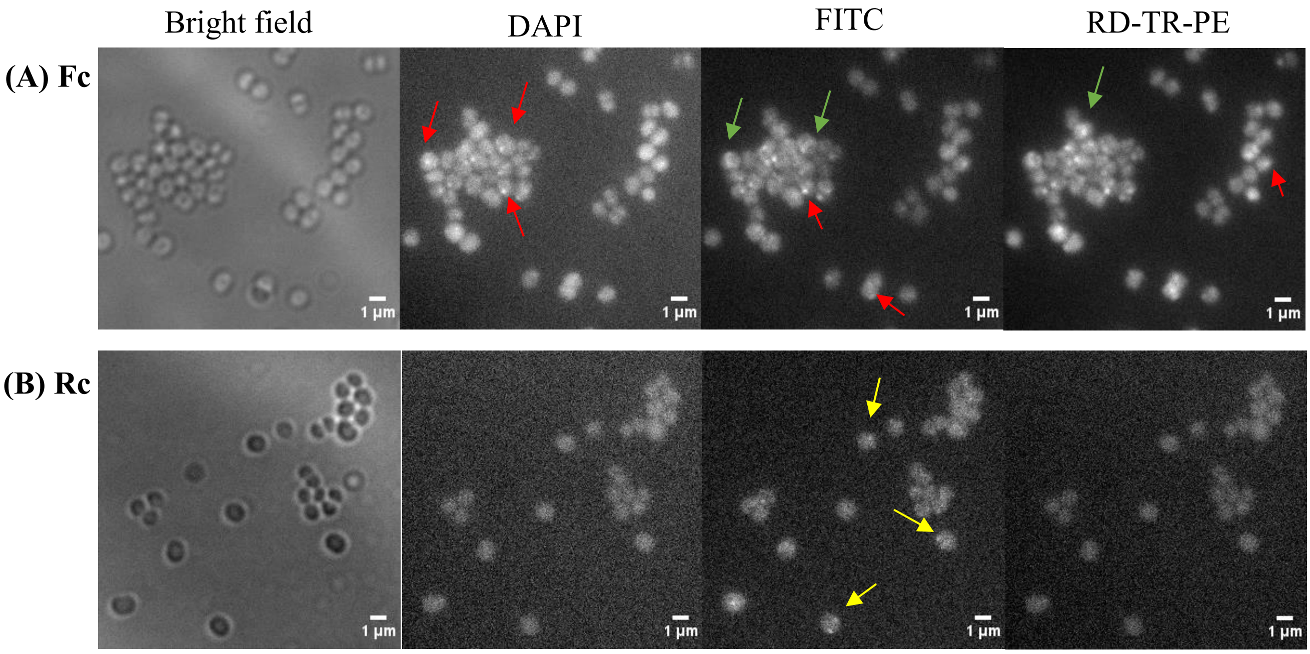

Figure 5.5 Fluorescence imaging of WT live cells. *S. aureus* WT strains were labelled with Fc **(A)** or Rc **(B)** probes, respectively, washed and fixed with ethanol before loading onto sides for imaging. The imaging was performed by bright field and three excitation channels, including DAPI (Ex: 360/40 nm and EM: 457/50 nm), FITC (Ex: 492/20 nm and EM: 528/38 nm) and RD-TR-PE (Ex: 555/28 nm and EM: 617/73 nm) filters. Arrows: labelled features.

5.2.4 TEM viewing cells with metallocene probes

Considering the poor signal-to-noise ratio, metallocene probes were unsuitable for fluorescent imaging of live cells. Therefore their application in EM was investigated. Initially, sacculi from exponential-phase of *S. aureus* WT strains were labelled with metallocene probes and stained with uranyl formate to enhance the contrast before viewing by EM. As shown in Figure 5.6, cells without metallocene probes labelling displayed a differentiated septa and relatively light-coloured off-septal structure with low density. When labelled with Fc probe, whole cell surface became dark in colour, which was conjectured as the effect of the high electron density of Fc core. Meanwhile, compared with the smooth surface of the unlabelled sample, the surface of samples labelled with Fc probes were not continuous and smooth any more, and there were flecks found on the off-septal region (Red dashed boxes in Figure 5.6). In Rc probe labelled samples, the similar phenomenon was observed that cells showed an enhanced contrast. Abundant flake-like structures (Green arrows in Figure 5.6) were clearly observed surrounding the septa, while infrequent structures were able to be found in Fc probe labelled samples and there was no observation at the septa in unlabelled cells. This suggested that the abundance of reducing termini tightly clustered at the septa of exponential-phase cells and subsequent labelling resulted in the aggregation of metallocene probes to form flake-like structures.

Although the hypothesis of flake-like structures was established, it was unable to rule out the possibility that post-staining with the metal complex affected probe labelling. Labels such as ferrocene and ruthenocene were extremely small (sub nanometre) and the high contrast from metal staining probably shielded the metallocene labelling, resulting in apparent nonspecific labelling. Therefore, samples without staining were also performed. As shown in Figure 5.7 A, in all cases septa and off-septal structures were clearly observed and distinguished from each other or base background in the absence of metal post-staining, although the contrast was weak compared with those samples with post-staining. Meanwhile, it was still found that Fc and Rc labels produced a relatively high contrast and fuscous flecks or stripes on cell surfaces (Yellow arrows in Figure 5.7 A).

To verify the specificity of the metallocene probes, $NaBH_4$ was used to reduce the aldehyde groups of cells, resulting in blocking of probe labelling. It was clearly shown that after $NaBH_4$ treatment, labelled cells exhibited the similar contrast and labelling states to unlabelled cells (Figure 5.7 B). This suggested that the structural features were attributed to metallocene probes labelling rather than background artefacts. Quantitative analysis of contrast changes before and after metallocene probe labelling were also investigated by measurement of a modified corrected total cell electronic density (CTCED). Corrected total cell fluorescence (CTCF) using the ImageJ measurement tool has been successfully applied for analysis of fluorescent images.[134,209] Inspired by this work, a similar concept was extended to CTCED, which was based on the equation that CTCED = Integrated density - (area of selected cell × mean electronic density of background readings). To reduce system errors, TEM images with the same magnification were chosen and no less than 50 cells were calculated for each sample (Figure 5.7 C). When labelled with metallocene probes, cells had significant low CTCED intensity, which suggested that the high electron density appeared, due to metallocene core of probes. This was consistent with the hypothetical statement identified above that metallocene probes labelled the reducing termini of the cell wall and led to an enhanced contrast.

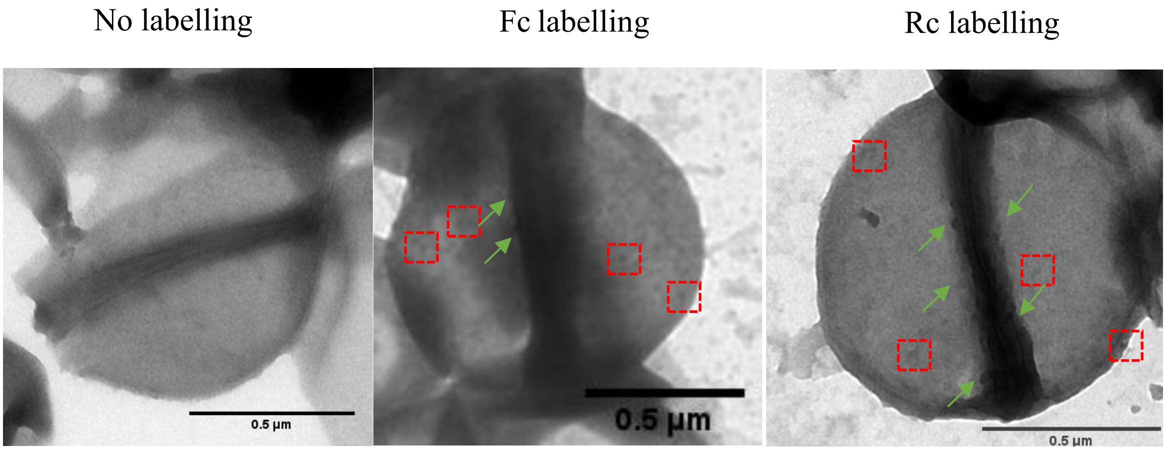
No labelling
Fc labelling
Rc labelling

Figure 5.6 TEM viewing of metallocene probes labelled cell sacculi. *S. aureus* WT strain was harvested and processed to prepare sacculi, which were resuspended in PBS at an appropriate concentration before labelling with metallocene probes and washing. These labelled sacculi were stained with uranyl formate, washed, dried and loaded on the grids for TEM viewing. Red dashed boxes: fleck features; Green arrows: flake-like structures.

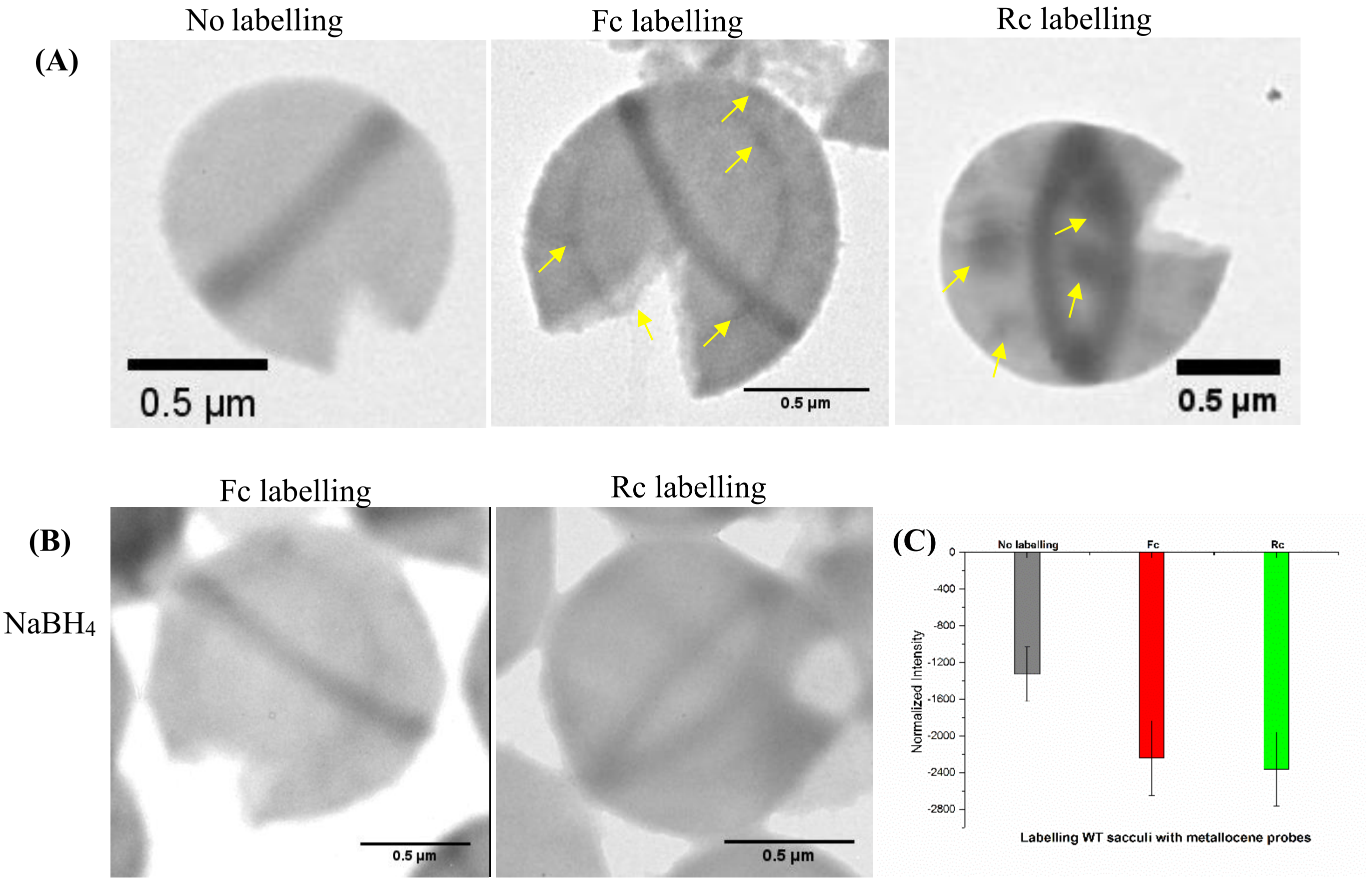

Figure 5.7. TEM viewing of metallocene probes labelled cell sacculi without uranyl formate post-staining. (A) *S. aureus* WT sacculi were labelled with metallocene probes as previously described, dried and directly loaded on the grids for TEM viewing. **(B)** Sacculi were pretreated with $NaBH_4$ in PBS before labelling with metallocene probes, which were then directly loaded on the grids without uranyl formate post-staining. **(C)** Quantitative analysis of labelled or unlabelled cells using CTCED. Arrows: labelled features.

5.3 Discussion

5.3.1 Synthesis and characterization of metallocene probes

Preparing suitable probes is a crucial task in cell imaging. In this regard, synthesis of metallocene-TEG conjugates were investigated. The key step was to incorporate a TEG linker into the metallocene moiety. Initial work was carried out employing S_N2 substitution. However, all attempts failed, no matter which leaving group was present at the end of the ferrocene or TEG moiety. Exploring an alternative route, the ferrocene-TEG conjugates were successfully synthesized, relying on $Al(OTf)_3$ catalysed condensation. As a result, the target Fc-TEG-ONH_2 probe was efficiently prepared from the inexpensive ferrocene in 5 linear steps with an overall yield of 41%. The promising results from the ferrocene probe inspired the development of another probe (Rc-TEG-ONH_2), which contains ruthenium and shows high specificity and low interference for cell imaging. The synthesis overall comprised 7 steps with 37% overall yield, following the similar synthetic procedure as for the ferrocene probe. Therefore, the synthetic strategy established here can be readily extended to prepare other metallocene probes, which will have widespread application across bioimaging techniques.

In addition, by UV-Vis and fluorescence characterization, no significant change in peaks was observed in most metallocene analogues and the stability of probes was confirmed. This indicated that characterized peaks are a direct consequence of the metallocene moieties and PEGylation has no influence on optical properties of metallocene.

5.3.2 Labelling cells with metallocene probes

As indicated above, metallocene probes were identified as fluorescent materials, although the intensity was not very high. This was confirmed by live cell labelling where the labelling pattern was consistent with the previous work using HAF488

(Chapter 3). Unexpectedly, Rc labelling was found to show poor contrast and differ significantly from Fc labelling. This may be explained by two possibilities. One was that by nature Rc has extremely faint fluorescence. Otherwise, the above optical analysis suggested that the main fluorescent bands of Rc were less than 400 nm, but the emission filters used here were approximately ranged from 457 to 617 nm, resulting in blocking of excitation light and inefficient imaging.

In an attempt to explore the potential benefits of metallocene probes, *S. aureus* sacculi were labelled and processed via different strategies for EM imaging. Compared with fluorescence imaging, EM imaging provided a higher quality observation with more detail. To better understand the dynamics of the cell wall, metallocene probe labelled sacculi from a variety of growth stage were characterised and correspondent diagrams were drawn for comparison and analysis (Figure 5.8). As depicted in Figure 5.8 A and E, the appearance of an intermittent band encircling the cell is assumed to be the incomplete septum or division plane. This feature is probably related to the “piecrust” structure observed from AFM imaging in previous work.[37] Compared with the complete septum in Figure 5.8 B, the imperfect band displayed a low contrast. New synthesis occurs primarily at the septum, which leads to labelling the reducing termini and a relatively high contrast in comparison with other cell zones. More importantly, in this complex process, abundant glycan chains with reducing termini appeared and subsequent labelling of metallocene probes extremely enhanced the contrast. These glycan chains from whether new synthesis or hydrolysis had different lengths and were crowded at the septum forming a hemp rope-like structure after multi sample treatments. In this feature, exposed reducing termini were recognized by metallocene probes, which formed flake-like structures. On the other hand, labelling of scattered reducing termini probably contributed to the formation of fleck features. In addition, prior to the cell splitting to two daughter cells, hydrolysis of cell wall of mother cells is needed and this may contribute to the production of reducing termini for labelling.

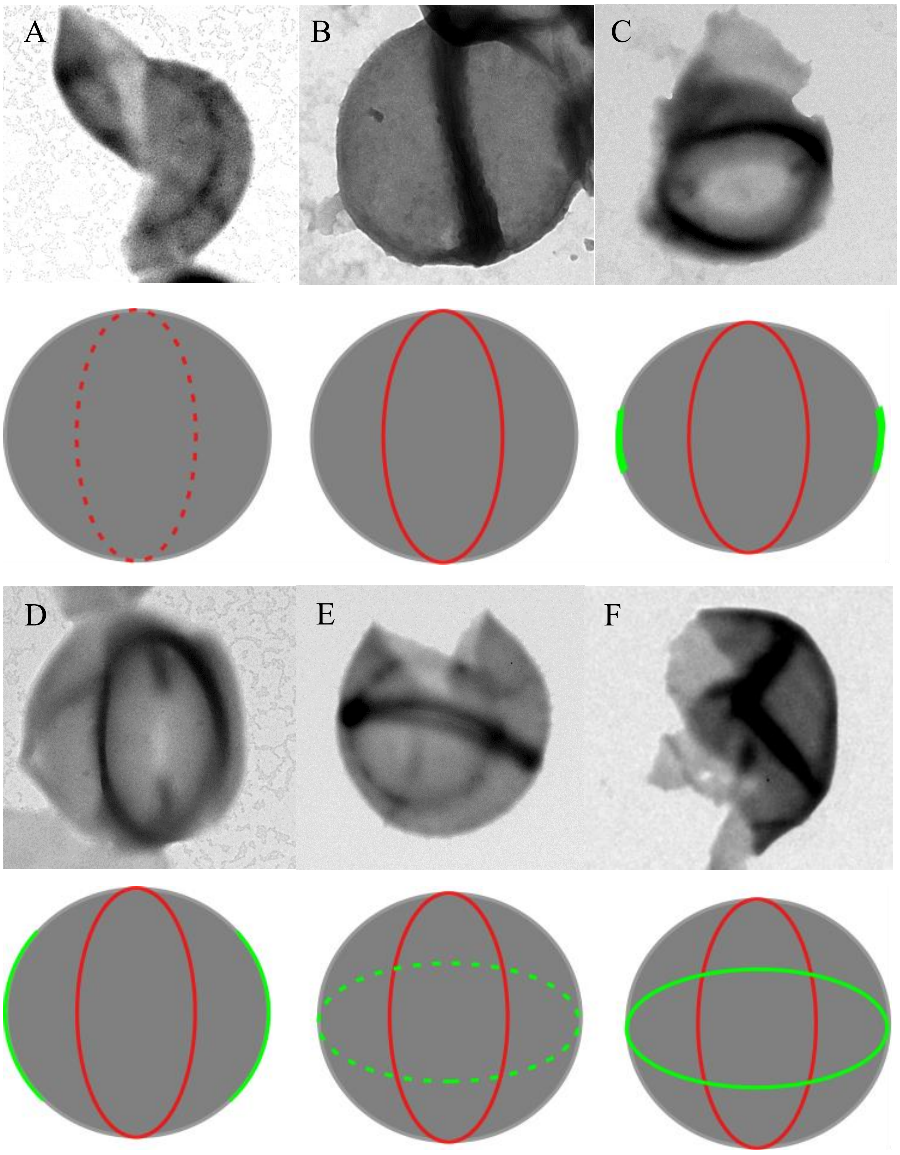

Figure 5.8. TEM viewing of characteristic labelled cells and corresponding schematics. TEM images were chosen from samples with different of staining pattern or magnification, and the contrast may be adjusted using ImageJ for observation. For ease of comparison partial schematics were rotated. Red curve: septum formation; green curve: formation of septum from next generation.

Chapter 6 General discussion

6.1 Status quo and current work

For decades, fluorescence imaging, as a non-invasive technique, has received a broad scope of attention in molecular and cellular biology due to its high molecular specificity, low cellular perturbation, and rapid response speed. It allows for a fruitful understanding of intricate physico-chemical biological processes, as well as localization of biomolecules of interest.[210,211] Whilst morphological observations and cell structural information have been achieved by fluorescence imaging, subcellular ultrastructures that are small in size are difficult to be observed due to the limited resolution of confocal and wide-field fluorescence microscopy (FM).[61] In principle, the shortest distance between two discriminated spots can be defined as the resolution of microscopy, which is diffraction limited to about 200-300 nm.[212] Unfortunately, cell mechanisms operate with precise control at the nanoscale, resulting in it being difficult to be deciphered by biologists. An exciting opportunity arose with the development of super-resolution microscopy, which was awarded the Nobel Prize in Chemistry 2014. Super-resolution imaging has great potential to track the dynamics of complex biological process and model subcellular ultrastructures with nano-level resolution, including SIM at 45-62 nm, STED at about 50 nm, and PALM/STORM at approximately 20 nm (Table 6.1).[213] Among these imaging techniques, SIM is one of the most widely used means because of its low laser power and imaging times, and high compatibility of dyes. In particular, STORM has capabilities of generating muticolour imaging and relatively higher resolution, and thus represents an interesting approach to decipherment and localization of biomolecules of interest.

Although super-resolution fluorescence imaging makes it possible to observe biomolecules with the resolution of dozens of nanometers, the resolution is barely satisfactory for ultrastructural morphology (0.1-10 nm).[214] The emergence of their inherent disadvantages, including lacking cellular context from achieved imaging results and requiring labelling with special fluorescent probes as well as time-consuming software development and data processing, tend to limit their biological applications, particularly in microbiology.[215,216] As a result, there is still a lack of high resolution generating approaches that are a prerequisite to provide a deep understanding of many biological processes. Diversely electron microscopy (EM) uses a beam of electrons rather than light photons used in FM and can therefore achieve sub-nano or sub-ångstrom resolution.[217,218] Up to now, EM, as an alternative to FM, has been an enticing research tool for extracting cellular structural information and the location of complex biological objects, but cannot be used for live-cell imaging, due to the requirements of a complex cell fixation and staining process, and lack of molecular specificity.[219,220] To overcome these problems, live correlative light-EM (CLEM), has been developed, which combines live-cell fluorescence imaging with EM observation and the help of data post-processing.[214,221,222]

Arguably, FM and EM imaging techniques have distinct advantages and disadvantages. As an extension of this concept, in this work, multifunctional probes were designed and prepared using organic synthesis methodology, which enabled functional analysis using both FM and EM imaging with maximum stability and integrity, and specifically targeting reducing termini of the bacterial cell wall (Scheme 6.1).

Compared with the lectin-based probe (WGA) and commercially available HAF488, the azide probe developed here showed comparable ability for PG glycan chains labelling (Figure 6.1A). The successful labelling in FM, super-resolution microscopy and EM imaging confirmed the broad feasibility of the synthetic probe, which provided information in order to understand the cell cycle. For instance, by STORM imaging, the azide probe clearly showed the process of cell division (Figure 6.1B). A combination of different FM and/or EM approaches were also carried out, which resulted in more useful measurement of cell dynamics. As shown in Figure 6.1D, the dark off-septal region in TEM using Fc probe was likely to be reducing termini labelling. This was confirmed by the visualization of fluorescence distribution in STORM. With respect to another feature in Figure 6.1D, STORM shows the cell was mainly labelled at the septum, which was confirmed by the dark septum and low-contrast off septum in TEM. The observation of flake-like structures surrounding the septa in TEM also provided corroborative evidence for the bright stripe-like septum by STORM.

6.2 Future work

Multifunctional probes have proven to be an extremely versatile small-molecule probes for FM and EM imaging for the investigation of the reducing termini. Via these approaches, cell dynamics are beginning to be elucidated. However, much effort is still needed. Combinations with other powerful approaches such as atomic force microscope (AFM) would be useful.

As for a scanning probe microscopy, AFM employs a sharp tip installed on a soft cantilever and the latter records the repulsive force between the tip and sample surface reflecting the topography of the molecule of interest.[223] In contrast to EM, complex sample treatments such as fixation and metal staining are unnecessary for AFM imaging. More importantly, AFM has the ability to image biological samples in relevant aqueous environments, which makes it possible to be used for real-time tracking of biophysiological processes and live organism imaging.[224] With great potential for nanoscale viewing of live cells, AFM, as an alternative to FM and EM, has emerged as a powerful tool in microbiology, due to the development of novel scanning tips and improvement of the apparatus.[225] This allows three-dimensional information to be gained on living cells with near the atomic-level detail in near physiological environments.[226,227] It should be stressed that despite wide application in biological research, AFM possesses several shortcomings that decrease the acceptance of biologists, including low scanning speed, failure to observe the entire cell and high cost.[228]

As a result, development of probes suitable for AFM on the basis of the above synthetic probes would integrate mutli-imaging techniques, provide corroborative information at the nanoscale and therefore open the door to decipher peptidoglycan architecture and the cell cycle.

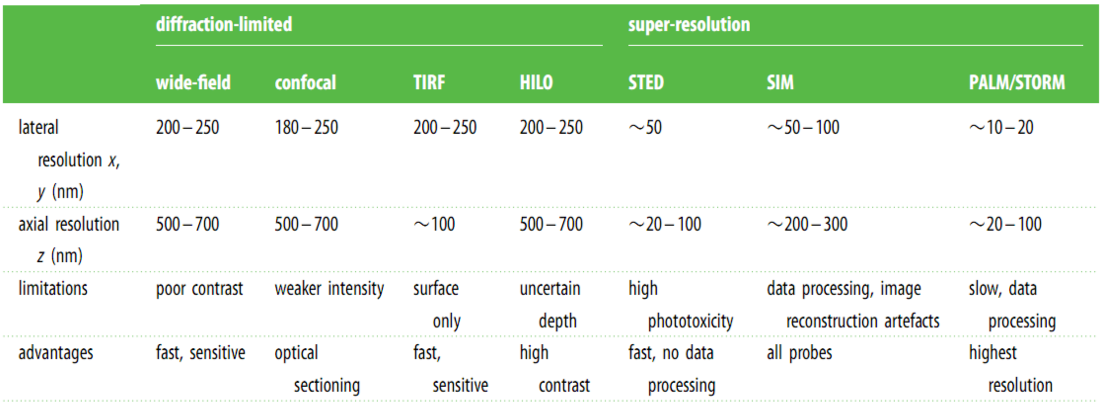

	diffraction-limited				super-resolution		
	wide-field	confocal	TIRF	HILO	STED	SIM	PALM/STORM
lateral resolution *x*, *y* (nm)	200–250	180–250	200–250	200–250	∼50	∼50–100	∼10–20
axial resolution *z* (nm)	500–700	500–700	∼100	500–700	∼20–100	∼200–300	∼20–100
limitations	poor contrast	weaker intensity	surface only	uncertain depth	high phototoxicity	data processing, image reconstruction artefacts	slow, data processing
advantages	fast, sensitive	optical sectioning	fast, sensitive	high contrast	fast, no data processing	all probes	highest resolution

Table 6.1 A comparison of fluorescence microscopy approaches. Ref. 213 with permission from *Phil. Trans. R. Soc. B.*[213]

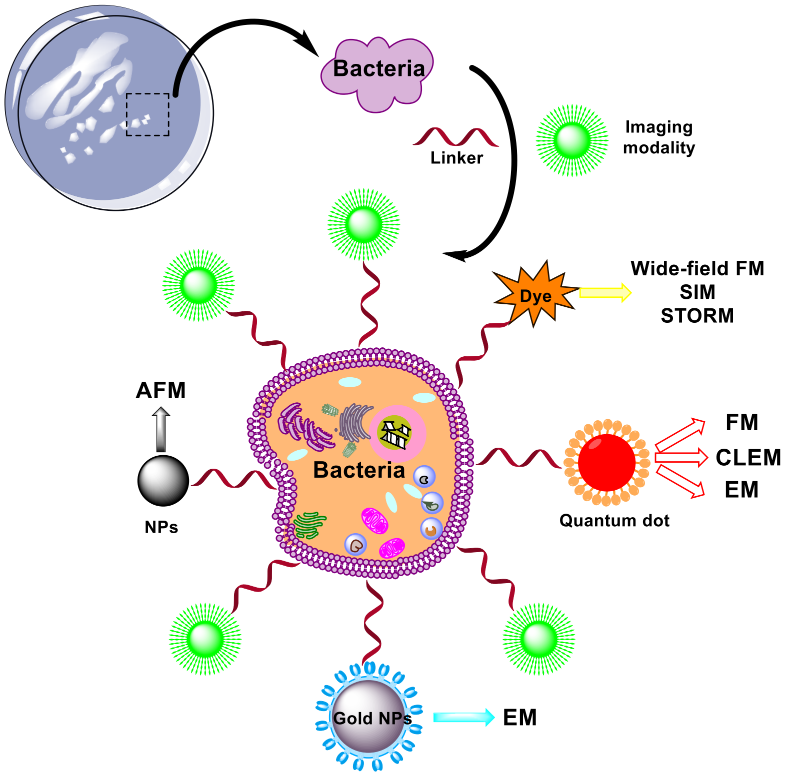

Scheme 6.1 Multi-modal labelling of the bacterial cell wall. Probes were prepared with recognition moiety and multi imaging modality such as dyes, quantum dots or gold nanoparticles by means of organic synthesis followed by cell labelling. Once attached to the cell wall, FM, EM or AFM was employed to provide high resolution of images to decipher cell dynamics.

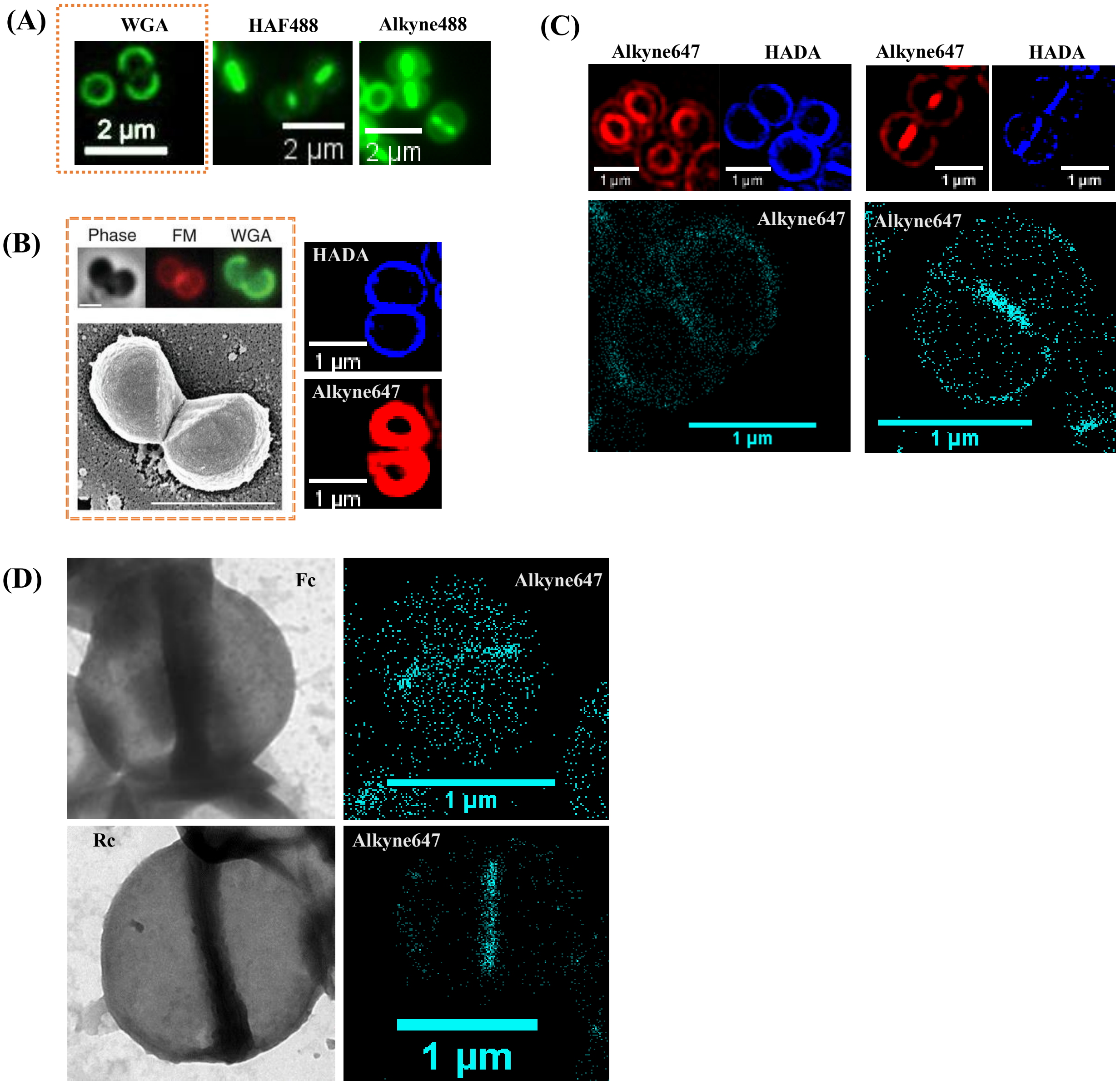

Figure 6.1 Multifunctional probes for imaging *S. aureus* with characteristic features using FM and EM. (A) Comparison of glycan related probes. Fluorescent WGA merely labelled the outer cell wall,[18] whilst HAF488 and the synthetic azide probe could mark both the septum and periphery. **(B)** Ultrafast cell separations. Cells were labelled with WGA and FM 4-64, membrane staining dye, (upper left). The corresponding SEM image was shown at the bottom (Ref 115 with permission from *Science*).[115] In my work, cells were labelled with HADA and the azide-probe/Alkyne647. Via SIM imaging, the latter showed the consistent observation of the ongoing daughter cells that merely connected within a thin cell wall layer. **(C)** Corroborative SIM and STORM imaging by the azide-probe/Alkyne647 labelling. **(D)** Corroborative TEM and STORM imaging by metallocene probes or the azide-probe/Alkyne647. Dashed boxes: published work.

Reference

(1) Van Reeth, E.; Tham, I. W.; Tan, C. H.; Poh, C. L. *Concept Magn Reson A* **2012**, *40*, 306.

(2) Fenster, A.; Downey, D. B.; Cardinal, H. N. *Phys Med Biol* **2001**, *46*, R67.

(3) Paulus, M. J.; Gleason, S. S.; Kennel, S. J.; Hunsicker, P. R.; Johnson, D. K. *Neoplasia* **2000**, *2*, 62.

(4) Juweid, M. E.; Cheson, B. D. *New Engl J Med* **2006**, *354*, 496.

(5) Giri, S.; Shaw, L. J.; Murthy, D. R.; Travin, M. I.; Miller, D. D.; Hachamovitch, R.; Borges-Neto, S.; Berman, D. S.; Waters, D. D.; Heller, G. V. *Circulation* **2002**, *105*, 32.

(6) Chan, J.; Dodani, S. C.; Chang, C. J. *Nat Chem* **2012**, *4*, 973.

(7) Kherlopian, A. R.; Song, T.; Duan, Q.; Neimark, M. A.; Po, M. J.; Gohagan, J. K.; Laine, A. F. *BMC Syst Biol* **2008**, *2*, 74.

(8) Brown, L.; Wolf, J. M.; Prados-Rosales, R.; Casadevall, A. *Nat Rev Micro* **2015**, *13*, 620.

(9) Vollmer, W.; Blanot, D.; De Pedro, M. A. *FEMS Microbiol Rev* **2008**, *32*, 149.

(10) Seltmann, G.; Holst, O. *The bacterial cell wall*; Springer Science & Business Media, 2013.

(11) Silhavy, T. J.; Kahne, D.; Walker, S. *CSH Perspect Biol* **2010**, *2*.

(12) Royet, J.; Dziarski, R. *Nat Rev Microbiol* **2007**, *5*, 264.

(13) Royet, J.; Dziarski, R. *Nat Rev Micro* **2007**, *5*, 264.

(14) Schleifer, K. H.; Kandler, O. *Bacteriol Rev* **1972**, *36*, 407.

(15) Heijenoort, J. V. *New Compr Biochem* **1994**, *27*, 39.

(16) Allocati, N.; Masulli, M.; Di Ilio, C.; De Laurenzi, V. *Cell Death Dis* **2015**, *6*, e1609.

(17) Alcorlo, M.; Martínez-Caballero, S.; Molina, R.; Hermoso, J. A. *Curr Opin Struc Biol* **2017**, *44*, 87.

(18) Wheeler, R.; Turner, R. D.; Bailey, R. G.; Salamaga, B.; Mesnage, S.; Mohamad, S. A. S.; Hayhurst, E. J.; Horsburgh, M.; Hobbs, J. K.; Foster, S. J. *Mbio* **2015**, *6*.

(19) Vollmer, W.; Joris, B.; Charlier, P.; Foster, S. *FEMS Microbiol Rev* **2008**, *32*, 259.

(20) Stapleton, M. R.; Horsburgh, M. J.; Hayhurst, E. J.; Wright, L.; Jonsson, I.-M.; Tarkowski, A.; Kokai-Kun, J. F.; Mond, J. J.; Foster, S. J. *J Bacteriol* **2007**, *189*, 7316.

(21) Herbert, S.; Bera, A.; Nerz, C.; Kraus, D.; Peschel, A.; Goerke, C.; Meehl, M.; Cheung, A.; Götz, F. *Plos Pathog* **2007**, *3*, e102.

(22) Ghuysen, J.-M.; Hakenbeck, R. *Bacterial cell wall*; Elsevier, 1994; Vol. 27.

(23) van Heijenoort, J. *Microbiol Mol Biol R* **2011**, *75*, 636.

(24) Suginaka, H.; Blumberg, P. M.; Strominger, J. L. *J Biol Chem* **1972**, *247*, 5279.

(25) Scheffers, D.-J.; Pinho, M. G. *Microbiol Mol Biol R* **2005**, *69*, 585.

(26) Sobhanifar, S.; King, D. T.; Strynadka, N. C. J. *Curr Opin Struc Biol* **2013**, *23*, 695.

(27) Sauvage, E.; Kerff, F.; Terrak, M.; Ayala, J. A.; Charlier, P. *FEMS Microbiol Rev* **2008**, *32*, 234.

(28) Pinho, M. G.; Kjos, M.; Veening, J.-W. *Nat Rev Micro* **2013**, *11*, 601.

(29) Nelson, D. E.; Young, K. D. *J Bacteriol* **2001**, *183*, 3055.

(30) Stapleton, P. D.; Taylor, P. W. *Sci Prog* **2002**, *85*, 57.

(31) Lovering, A. L.; Safadi, S. S.; Strynadka, N. C. J. *Annu Rev Biochem* **2012**, *81*, 451.

(32) Vollmer, W.; Höltje, J.-V. *J Bacteriol* **2004**, *186*, 5978.

(33) Koch, A. L. *Res Microbiol* **1998**, *149*, 689.

(34) Dmitriev, B. A.; Toukach, F. V.; Schaper, K.-J.; Holst, O.; Rietschel, E. T.; Ehlers, S. *J Bacteriol* **2003**, *185*, 3458.

(35) Dmitriev, B. A.; Toukach, F. V.; Holst, O.; Rietschel, E. T.; Ehlers, S. *J Bacteriol* **2004**, *186*, 7141.

(36) Turner, R. D.; Vollmer, W.; Foster, S. J. *Mol Microbiol* **2014**, *91*, 862.

(37) Turner, R. D.; Ratcliffe, E. C.; Wheeler, R.; Golestanian, R.; Hobbs, J. K.; Foster, S. J. *Nat Commun* **2010**, *1*, 26.

(38) Atilano, M. L.; Pereira, P. M.; Yates, J.; Reed, P.; Veiga, H.; Pinho, M. G.; Filipe, S. R. *PNAS* **2010**, *107*, 18991.

(39) Matias, V. R. F.; Beveridge, T. J. *Mol Microbiol* **2007**, *64*, 195.

(40) Tzagoloff, H.; Novick, R. *J Bacteriol* **1977**, *129*, 343.

(41) Margolin, W. *Curr Biol* **2009**, *19*, R812.

(42) Monahan, L.; Liew, A.; Bottomley, A.; Harry, E. *Front Microbiol* **2014**, *5*.

(43) Valeur, B.; Berberan-Santos, M. N. *J Chem Educ* **2011**, *88*, 731.

(44) Stokes, G. G. *Philos Trans R Soc Lond* **1852**, 463.

(45) Valeur, B.; Berberan-Santos, M. N. *Molecular fluorescence: principles and applications*; John Wiley & Sons, 2012.

(46) Allen, J. R.; Ross, S. T.; Davidson, M. W. *J OPTICS-UK* **2013**, *15*, 094001.

(47) Synge, E. *The London, Edinburgh, and Dublin Philosophical Magazine and Journal of Science* **1928**, *6*, 356.

(48) O'Keefe, J. A. *J Opt Soc Am* **1956**, *46*, 359.

(49) Ash, E.; Nicholls, G. *Nature* **1972**, 237, 510.

(50) Betzig, E.; Isaacson, M.; Barshatzky, H.; Lewis, A.; Lin, K. In *1988 Los Angeles Symposium--OE/LASE'88*; International Society for Optics and Photonics: 1988, p 91.

(51) Harootunian, A.; Betzig, E.; Isaacson, M.; Lewis, A. *Appl Phys Lett* **1986**, *49*, 674.

(52) Koopman, M.; Cambi, A.; de Bakker, B. I.; Joosten, B.; Figdor, C. G.; van Hulst, N. F.; Garcia-Parajo, M. F. *FEBS Lett* **2004**, *573*, 6.

(53) de Lange, F.; Cambi, A.; Huijbens, R.; de Bakker, B.; Rensen, W.; Garcia-Parajo, M.; van Hulst, N.; Figdor, C. G. *J Cell Sci* **2001**, *114*, 4153.

(54) Huang, B.; Bates, M.; Zhuang, X. *Annu Rev Biochem* **2009**, *78*, 993.

(55) Leung, B. O.; Chou, K. C. *Appl Spectrosc* **2011**, *65*, 967.

(56) Huang, B.; Babcock, H.; Zhuang, X. *Cell* **2010**, *143*, 1047.

(57) Gustafsson, M. G. L. *PNAS* **2005**, *102*, 13081.

(58) Kner, P.; Chhun, B. B.; Griffis, E. R.; Winoto, L.; Gustafsson, M. G. *Nat Meth* **2009**, *6*, 339.

(59) Gustafsson, M. G. *PNAS* **2005**, *102*, 13081.

(60) Rego, E. H.; Shao, L.; Macklin, J. J.; Winoto, L.; Johansson, G. A.; Kamps-Hughes, N.; Davidson, M. W.; Gustafsson, M. G. *PNAS* **2012**, *109*, E135.

(61) Schermelleh, L.; Heintzmann, R.; Leonhardt, H. *J cell Biol* **2010**, *190*, 165.

(62) Schmidt, R.; Wurm, C. A.; Jakobs, S.; Engelhardt, J.; Egner, A.; Hell, S. W. *Nat Meth* **2008**, *5*, 539.

(63) Harke, B.; Keller, J.; Ullal, C. K.; Westphal, V.; Hell, S. W. *Opt Express* **2008**, *16*, 4154.

(64) Donnert, G.; Keller, J.; Medda, R.; Andrei, M. A.; Rizzoli, S. O.; Lührmann, R.; Jahn, R.; Eggeling, C.; Hell, S. W. *PNAS* **2006**, *103*, 11440.

(65) Nägerl, U. V.; Bonhoeffer, T. *J. Neurosci* **2010**, *30*, 9341.

(66) Hess, S. T.; Girirajan, T. P.; Mason, M. D. *Biophys J* **2006**, *91*, 4258.

(67) Patterson, G. H.; Lippincott-Schwartz, J. *Science* **2002**, *297*, 1873.

(68) Subach, F. V.; Patterson, G. H.; Manley, S.; Gillette, J. M.; Lippincott-Schwartz, J.; Verkhusha, V. V. *Nat Meth* **2009**, *6*, 153.

(69) Sengupta, P.; Jovanovic-Talisman, T.; Lippincott-Schwartz, J. *Nat Protoc* **2013**, *8*, 345.

(70) Yildiz, A.; Forkey, J. N.; McKinney, S. A.; Ha, T.; Goldman, Y. E.; Selvin, P. R. *Science* **2003**, *300*, 2061.

(71) Holtzer, L.; Meckel, T.; Schmidt, T. *Appl Phys Lett* **2007**, *90*, 053902.

(72) Rust, M. J.; Bates, M.; Zhuang, X. *Nat Meth* **2006**, *3*, 793.

(73) Betzig, E.; Patterson, G. H.; Sougrat, R.; Lindwasser, O. W.; Olenych, S.; Bonifacino, J. S.; Davidson, M. W.; Lippincott-Schwartz, J.; Hess, H. F. *Science* **2006**, *313*, 1642.

(74) Bates, M.; Huang, B.; Dempsey, G. T.; Zhuang, X. *Science* **2007**, *317*, 1749.

(75) Wang, Y.; Shyy, J. Y.-J.; Chien, S. *Annu Rev Biomed Eng* **2008**, *10*, 1.

(76) Shimomura, O.; Johnson, F. H.; Saiga, Y. *J Cell Comp Physiol* **1962**, *59*, 223.

(77) Barondeau, D. P.; Kassmann, C. J.; Tainer, J. A.; Getzoff, E. D. *BIOCHEMISTRY-US* **2005**, *44*, 1960.

(78) Chudakov, D. M.; Matz, M. V.; Lukyanov, S.; Lukyanov, K. A. *Physiol Rev* **2010**, *90*, 1103.

(79) Lippincott-Schwartz, J.; Patterson, G. H. *Trends Cell Biol* **2009**, *19*, 555.

(80) Subach, F. V.; Malashkevich, V. N.; Zencheck, W. D.; Xiao, H.; Filonov, G. S.; Almo, S. C.; Verkhusha, V. V. *PNAS* **2009**, *106*, 21097.

(81) Fuchs, J.; Boehme, S.; Oswald, F.; Hedde, P. N.; Krause, M.; Wiedenmann, J.; Nienhaus, G. U. *Nat Meth* **2010**, *7*, 627.

(82) Mitronova, G. Y.; Belov, V. N.; Bossi, M. L.; Wurm, C. A.; Meyer, L.; Medda, R.; Moneron, G.; Bretschneider, S.; Eggeling, C.; Jakobs, S. *Chem-Eur J* **2010**, *16*, 4477.

(83) Lord, S. J.; Conley, N. R.; Lee, H. l. D.; Nishimura, S. Y.; Pomerantz, A. K.; Willets, K. A.; Lu, Z.; Wang, H.; Liu, N.; Samuel, R. *ChemPhysChem* **2009**, *10*, 55.

(84) Belov, V. N.; Wurm, C. A.; Boyarskiy, V. P.; Jakobs, S.; Hell, S. W. *Angew Chem Int Ed* **2010**, *49*, 3520.

(85) Kolmakov, K.; Wurm, C. A.; Meineke, D. N. H.; Göttfert, F.; Boyarskiy, V. P.; Belov, V. N.; Hell, S. W. *Chem-Eur J* **2014**, *20*, 146.

(86) Zrazhevskiy, P.; Sena, M.; Gao, X. *Chem Soc Rev* **2010**, *39*, 4326.

(87) Lidke, K.; Rieger, B.; Jovin, T.; Heintzmann, R. *Opt Express* **2005**, *13*, 7052.

(88) Hoyer, P.; Staudt, T.; Engelhardt, J.; Hell, S. W. *Nano Lett* **2010**, *11*, 245.

(89) Irvine, S. E.; Staudt, T.; Rittweger, E.; Engelhardt, J.; Hell, S. W. *Angew Chem Int Ed* **2008**, *120*, 2725.

(90) Zhang, Q.; Xie, J.; Yu, Y.; Lee, J. Y. *NANOSCALE* **2010**, *2*, 1962.

(91) Vosch, T.; Antoku, Y.; Hsiang, J.-C.; Richards, C. I.; Gonzalez, J. I.; Dickson, R. M. *PNAS* **2007**, *104*, 12616.

(92) Boons, G.-J. In *Carbohydrate Chemistry: Volume 36*; The Royal Society of Chemistry: 2010; Vol. 36, p 152.

(93) Horsburgh, G. J.; Atrih, A.; Foster, S. J. *J Bacteriol* **2003**, *185*, 3813.

(94) Huang, B.; Wang, W.; Bates, M.; Zhuang, X. *Science* **2008**, *319*, 810.

(95) Ovesný, M.; Křížek, P.; Borkovec, J.; Švindrych, Z.; Hagen, G. M. *Bioinformatics* **2014**, *30*, 2389.

(96) Liu, S.; Yu, Y.; Liebeskind, L. S. *Org Lett* **2007**, *9*, 1947.

(97) Hurley, C. A.; Wong, J. B.; Ho, J.; Writer, M.; Irvine, S. A.; Lawrence, M. J.; Hart, S. L.; Tabor, A. B.; Hailes, H. C. *Org Biomol Chem* **2008**, *6*, 2554.

(98) Billamboz, M.; Mangin, F.; Drillaud, N.; Chevrin-Villette, C.; Banaszak-Léonard, E.; Len, C. *J. Org. Chem* **2014**, *79*, 493.

(99) Gupta, S. S.; Raja, K. S.; Kaltgrad, E.; Strable, E.; Finn, M. G. *Chem Commun* **2005**, 4315.

(100) Styslinger, T. J.; Zhang, N.; Bhatt, V. S.; Pettit, N.; Palmer, A. F.; Wang, P. G. *J Am Chem Soc* **2012**, *134*, 7507.

(101) Arumugam, S.; Popik, V. V. *J Am Chem Soc* **2011**, *133*, 15730.

(102) Sanders, R.; Mueller-Westerhoff, U. T. *J Organomet Chem* **1996**, *512*, 219.

(103) Lousada, C. M.; Pinto, S. S.; Canongia Lopes, J. N.; Minas da Piedade, M. F.; Diogo, H. P.; Minas da Piedade, M. E. *J Phys Chem A* **2008**, *112*, 2977.

(104) Ikhile, M. I.; Bala, M. D.; Nyamori, V. O.; Ngila, J. C. *Appl Organomet*

Chem **2013**, *27*, 98.

(105) Allali, N.; Mamane, V. *Tetrahedron Lett* **2012**, *53*, 2604.

(106) Kündig, E. P.; Monnier, F. R. *Adv Synth Catal* **2004**, *346*, 901.

(107) Barlow, S.; Cowley, A.; Green, J. C.; Brunker, T. J.; Hascall, T. *Organometallics* **2001**, *20*, 5351.

(108) Bélanger, G.; Dupuis, M.; Larouche-Gauthier, R. *J. Org. Chem* **2012**, *77*, 3215.

(109) Erbas, S.; Gorgulu, A.; Kocakusakogullari, M.; Akkaya, E. U. *Chem Commun* **2009**, 4956.

(110) Cabeen, M. T.; Jacobs-Wagner, C. *Nat Rev Micro* **2005**, *3*, 601.

(111) Sletten, E. M.; Bertozzi, C. R. *Angew Chem Int Ed* **2009**, *48*, 6974.

(112) Kuru, E.; Tekkam, S.; Hall, E.; Brun, Y. V.; Van Nieuwenhze, M. S. *Nat. Protocols* **2015**, *10*, 33.

(113) Pilhofer, M.; Aistleitner, K.; Biboy, J.; Gray, J.; Kuru, E.; Hall, E.; Brun, Y. V.; VanNieuwenhze, M. S.; Vollmer, W.; Horn, M.; Jensen, G. J. *Nat Commun* **2013**, *4*.

(114) Lang, K.; Chin, J. W. *Chem Rev* **2014**, *114*, 4764.

(115) Zhou, X.; Halladin, D. K.; Rojas, E. R.; Koslover, E. F.; Lee, T. K.; Huang, K. C.; Theriot, J. A. *Science* **2015**, *348*, 574.

(116) Monteiro, J. M.; Fernandes, P. B.; Vaz, F.; Pereira, A. R.; Tavares, A. C.; Ferreira, M. T.; Pereira, P. M.; Veiga, H.; Kuru, E.; VanNieuwenhze, M. S.; Brun, Y. V.; Filipe, S. R.; Pinho, M. G. *Nat Commun* **2015**, *6*, 8055.

(117) Levine, D. P. *Clin Infect Dis* **2006**, *42*, S5.

(118) Hiramatsu, K. *Lancet Infect Dis* **2001**, *1*, 147.

(119) Reynolds, P. E. *Eur J Clin Microbiol Infect Dis* **1989**, *8*, 943.

(120) Loll, P. J.; Axelsen, P. H. *Annu Rev Biophys Biomol Struct* **2000**, *29*, 265.

(121) Kahne, D.; Leimkuhler, C.; Lu, W.; Walsh, C. *Chem Rev* **2005**, *105*, 425.

(122) Bruck, S.; Personnic, N.; Prevost, M.-C.; Cossart, P.; Bierne, H. *J Bacteriol* **2011**, *193*, 4425.

(123) Wheeler, R. *The University of Sheffield* **2012**.

(124) Gamblin, D. P.; Scanlan, E. M.; Davis, B. G. *Chem Rev* **2008**, *109*, 131.

(125) Lemieux, G. A.; Bertozzi, C. R. *Trends Biotechnol* **1998**, *16*, 506.

(126) Zeng, Y.; Ramya, T. N. C.; Dirksen, A.; Dawson, P. E.; Paulson, J. C. *Nat Meth* **2009**, *6*, 207.

(127) Bindman, N. A.; van der Donk, W. A. *J Am Chem Soc* **2013**, *135*, 10362.

(128) Tam, J. P.; Xu, J.; Eom, K. D. *Pept Sci* **2001**, *60*, 194.

(129) Kalia, J.; Raines, R. T. *Angew Chem* **2008**, *120*, 7633.

(130) Hackenberger, C. P. R.; Schwarzer, D. *Angew Chem Int Ed* **2008**, *47*, 10030.

(131) Dirksen, A.; Hackeng, T. M.; Dawson, P. E. *Angew Chem Int Ed* **2006**, *45*, 7581.

(132) Chan, Y. G. Y.; Frankel, M. B.; Missiakas, D.; Schneewind, O. *J Bacteriol* **2016**, *198*, 1123.

(133) Reed, P.; Veiga, H.; Jorge, A. M.; Terrak, M.; Pinho, M. G. *J Bacteriol*

2011, *193*, 2549.

(134) Burgess, A.; Vigneron, S.; Brioudes, E.; Labbé, J.-C.; Lorca, T.; Castro, A. *PNAS* **2010**, *107*, 12564.

(135) Perry, A. M.; Ton-That, H.; Mazmanian, S. K.; Schneewind, O. *J Biol Chem* **2002**, *277*, 16241.

(136) Yokogawa, K.; Kawata, S.; Nishimura, S.; Ikeda, Y.; Yoshimura, Y. *ANTIMICROB AGENTS CH* **1974**, *6*, 156.

(137) Ostash, B.; Saghatelian, A.; Walker, S. *Chem Biol* **2007**, *14*, 257.

(138) Derouaux, A.; Sauvage, E.; Terrak, M. *Front Immunol* **2013**, *4*, 78.

(139) Wyke, A. W.; Ward, J. B.; Hayes, M. V.; Curtis, N. A. *Eur J Biochem* **1981**, *119*, 389.

(140) Pinho, M. G.; Errington, J. *Mol Microbiol* **2003**, *50*, 871.

(141) Sizemore, R. K.; Caldwell, J. J.; Kendrick, A. S. *Appl Environ Microb* **1990**, *56*, 2245.

(142) Reed, P.; Atilano, M. L.; Alves, R.; Hoiczyk, E.; Sher, X.; Reichmann, N. T.; Pereira, P. M.; Roemer, T.; Filipe, S. R.; Pereira-Leal, J. B.; Ligoxygakis, P.; Pinho, M. G. *Plos Pathog* **2015**, *11*, e1004891.

(143) Gautam, S.; Kim, T.; Shoda, T.; Sen, S.; Deep, D.; Luthra, R.; Ferreira, M. T.; Pinho, M. G.; Spiegel, D. A. *Angew Chem Int Ed* **2015**, *54*, 10492.

(144) Lang, K.; Chin, J. W. *ACS Chem Biol* **2014**, *9*, 16.

(145) Sletten, E. M.; Bertozzi, C. R. *Angew Chem Int Ed* **2009**, *48*, 6974.

(146) Thirumurugan, P.; Matosiuk, D.; Jozwiak, K. *Chem Rev* **2013**, *113*, 4905.

(147) Moses, J. E.; Moorhouse, A. D. *Chem Soc Rev* **2007**, *36*, 1249.

(148) Kolb, H. C.; Finn, M. G.; Sharpless, K. B. *Angew Chem Int Ed* **2001**, *40*, 2004.

(149) Kolb, H. C.; Sharpless, K. B. *Drug Discov Today* **2003**, *8*, 1128.

(150) Jewett, J. C.; Bertozzi, C. R. *Chem Soc Rev* **2010**, *39*, 1272.

(151) Harris, J. M. In *Poly(Ethylene Glycol) Chemistry: Biotechnical and Biomedical Applications*; Harris, J. M., Ed.; Springer US: Boston, MA, 1992, p 1.

(152) Inada, Y.; Furukawa, M.; Sasaki, H.; Kodera, Y.; Hiroto, M.; Nishimura, H.; Matsushima, A. *Trends Biotechnol*, *13*, 86.

(153) Zheng, M.; Davidson, F.; Huang, X. *J Am Chem Soc* **2003**, *125*, 7790.

(154) Pasut, G.; Veronese, F. M. In *Polymer Therapeutics I*; Satchi-Fainaro, R., Duncan, R., Eds.; Springer Berlin Heidelberg: Berlin, Heidelberg, 2006, p 95.

(155) Abedi, S.; Karimi, B.; Kazemi, F.; Bostina, M.; Vali, H. *Org Biomol Chem* **2013**, *11*, 416.

(156) Rad, M. N. S.; Behrouz, S.; Karimitabar, F.; Khalafi-Nezhad, A. *Helv Chim Acta* **2012**, *95*, 491.

(157) Abdel-Rahman, M. A.; Al-Abd, A. M. *Eur J Med Chem* **2013**, *69*, 848.

(158) Bouzide, A.; Sauvé, G. *Org Lett* **2002**, *4*, 2329.

(159) Mbongo, A.; Fréchou, C.; Beaupére, D.; Uzan, R.; Demailly, G. *Carbohyd Res* **1993**, *246*, 361.

(160) Stein, T. *Mol Microbiol* **2005**, *56*, 845.

(161) Zweers, J. C.; Barák, I.; Becher, D.; Driessen, A. J.; Hecker, M.;

Kontinen, V. P.; Saller, M. J.; Vavrová, L. u.; van Dijl, J. M. *Microb Cell Fact* **2008**, *7*, 10.

(162) Hayhurst, E. J.; Kailas, L.; Hobbs, J. K.; Foster, S. J. *PNAS* **2008**, *105*, 14603.

(163) Coltharp, C.; Xiao, J. *Cell Microbiol* **2012**, *14*, 1808.

(164) Bates, M.; Dempsey, G. T.; Chen, K. H.; Zhuang, X. *ChemPhysChem* **2012**, *13*, 99.

(165) Fleurie, A.; Lesterlin, C.; Manuse, S.; Zhao, C.; Cluzel, C.; Lavergne, J.-P.; Franz-Wachtel, M.; Macek, B.; Combet, C.; Kuru, E.; VanNieuwenhze, M. S.; Brun, Y. V.; Sherratt, D.; Grangeasse, C. *Nature* **2014**, *516*, 259.

(166) Kamiyama, D.; Huang, B. *Dev Cell*, *23*, 1103.

(167) Wang, W.; Li, G.-W.; Chen, C.; Xie, X. S.; Zhuang, X. *Science* **2011**, *333*, 1445.

(168) Fernandez-Suarez, M.; Ting, A. Y. *Nat Rev Mol Cell Bio* **2008**, *9*, 929.

(169) Risco, C.; Sanmartín-Conesa, E.; Tzeng, W.-P.; Frey, Teryl K.; Seybold, V.; de Groot, Raoul J. *Structure* **2012**, *20*, 759.

(170) van Elsland, D. M.; van Kasteren, S. I. *Angew Chem Int Ed* **2016**, *55*, 9472.

(171) Lim, R. K. V.; Lin, Q. *Chem Commun* **2010**, *46*, 1589.

(172) Wolbers, F.; ter Braak, P.; Le Gac, S.; Luttge, R.; Andersson, H.; Vermes, I.; van den Berg, A. *Electrophoresis* **2006**, *27*, 5073.

(173) Beatty, K. E.; Xie, F.; Wang, Q.; Tirrell, D. A. *J Am Chem Soc* **2005**, *127*, 14150.

(174) Ramil, C. P.; Lin, Q. *Chem Commun* **2013**, *49*, 11007.

(175) Yang, M.; Jalloh, A. S.; Wei, W.; Zhao, J.; Wu, P.; Chen, P. R. *Nat Commun* **2014**, *5*, 4981.

(176) Tiyanont, K.; Doan, T.; Lazarus, M. B.; Fang, X.; Rudner, D. Z.; Walker, S. *PNAS* **2006**, *103*, 11033.

(177) Stephens, D. J.; Allan, V. J. *Science* **2003**, *300*, 82.

(178) Yao, Z.; Carballido-López, R. *Annu Rev Microbiol* **2014**, *68*, 459.

(179) Kealy, T. J.; Pauson, P. L. *Nature* **1951**, *168*, 1039.

(180) Wilkinson, G.; Rosenblum, M.; Whiting, M. C.; Woodward, R. B. *J Am Chem Soc* **1952**, *74*, 2125.

(181) Pfab, W.; Fischer, E. O. *Z Anorg Allg Chem* **1953**, *274*, 316.

(182) Dunitz, J. D.; Orgel, L. E.; Rich, A. *Acta Crystallogr* **1956**, *9*, 373.

(183) Dunitz, J. D.; Orgel, L. E. *Nature* **1953**, *171*, 121.

(184) Laszlo, P.; Hoffmann, R. *Angew Chem Int Ed* **2000**, *39*, 123.

(185) Alt, H. G.; Köppl, A. *Chem Rev* **2000**, *100*, 1205.

(186) Golovin, M. N.; Wilkinson, D. P.; Dudley, J. T.; Holonko, D.; Woo, S. *J Electrochem Soc* **1992**, *139*, 5.

(187) Tucker, J. H.; Collinson, S. R. *Chem Soc Rev* **2002**, *31*, 147.

(188) Astruc, D.; Ornelas, C.; Ruiz, J. *Acc Chem Res* **2008**, *41*, 841.

(189) Fiorina, V. J.; Dubois, R. J.; Brynes, S. *J Med Chem* **1978**, *21*, 393.

(190) Hoyer, J.; Hunold, A.; Schmalz, H.-G.; Neundorf, I. *Dalton T* **2012**, *41*,

6396.

(191) Vorotyntsev, M. A.; Vasilyeva, S. V. *Adv Colloid Interface Sci* **2008**, *139*, 97.

(192) Chantson, J. T.; Vittoria Verga Falzacappa, M.; Crovella, S.; Metzler-Nolte, N. *ChemMedChem* **2006**, *1*, 1268.

(193) Long, N.; Blackwell Science: Malden, MA, USA, 1998.

(194) Roberts, J. D.; Caserio, M. C. *Basic Principles of Organic Chemistry*; W. A. Benjamin, 1977.

(195) Lee, H. Z. S.; Buriez, O.; Labbé, E.; Top, S.; Pigeon, P.; Jaouen, G.; Amatore, C.; Leong, W. K. *Organometallics* **2014**, *33*, 4940.

(196) Gasser, G.; Ott, I.; Metzler-Nolte, N. *J Med Chem* **2011**, *54*, 3.

(197) Tarasova, O. g. A.; Tatarinova, I. V.; Vakul'skaya, T. I.; Khutsishvili, S. S.; Smirnov, V. I.; Klyba, L. V.; Prozorova, G. F.; Mikhaleva, A. b. I.; Trofimov, B. A. *J Organomet Chem* **2013**, *745–746*, 1.

(198) Suzaki, Y.; Endo, H.; Kojima, T.; Osakada, K. *Dalton T* **2013**, *42*, 16222.

(199) Gelinas, B.; Forgie, J.; Rochefort, D. *J Electrochem Soc* **2014**, *161*, H161.

(200) Tonhauser, C.; Alkan, A.; Schömer, M.; Dingels, C.; Ritz, S.; Mailänder, V.; Frey, H.; Wurm, F. R. *Macromolecules* **2013**, *46*, 647.

(201) Adam, M. J.; Hall, L. D. *Can J Chem* **1980**, *58*, 1188.

(202) Gharib, B.; Hirsch, A. *Eur J Org Chem* **2014**, *2014*, 4123.

(203) Shisodia, S. U.; Auricchio, S.; Citterio, A.; Grassi, M.; Sebastiano, R. *Tetrahedron Lett* **2014**, *55*, 869.

(204) Taraballi, F.; Russo, L.; Battocchio, C.; Polzonetti, G.; Nicotra, F.; Cipolla, L. *Org Biomol Chem* **2014**, *12*, 4089.

(205) Bozak, R. E. In *Adv Photochem*; John Wiley & Sons, Inc.: 2007, p 227.

(206) Tarr, A. M.; Wiles, D. M. *Can J Chem* **1968**, *46*, 2725.

(207) Gray, H. B.; Sohn, Y. S.; Hendrickson, N. *J Am Chem Soc* **1971**, *93*, 3603.

(208) Fery-Forgues, S.; Delavaux-Nicot, B. *J Photochem Photobiol, A* **2000**, *132*, 137.

(209) Ansari, N.; Müller, S.; Stelzer, E. H. K.; Pampaloni, F. In *METHOD CELL BIOL*; Conn, P. M., Ed.; Academic Press: 2013; Vol. Volume 113, p 295.

(210) Ntziachristos, V. *Appl Catal, A* **2006**, *8*, 1.

(211) Terai, T.; Nagano, T. *Curr Opin Chem Biol* **2008**, *12*, 515.

(212) Huang, B.; Jones, S. A.; Brandenburg, B.; Zhuang, X. *Nat Meth* **2008**, *5*, 1047.

(213) Schneider, J. P.; Basler, M. *Philos T Roy Soc B* **2016**, *371*.

(214) de Boer, P.; Hoogenboom, J. P.; Giepmans, B. N. G. *Nat Meth* **2015**, *12*, 503.

(215) Tuson, H. H.; Biteen, J. S. *Anal Chem* **2015**, *87*, 42.

(216) de Souza, N. *Nat Meth* **2015**, *12*, 37.

(217) Williams, D. B.; Carter, C. B. In *Transmission Electron Microscopy: A Textbook for Materials Science*; Springer US: Boston, MA, 1996, p 3.

(218) Batson, P. E.; Dellby, N.; Krivanek, O. L. *Nature* **2002**, *418*, 617.

(219) Sueters - Di Meo, J.; Liv, N.; Hoogenboom, J. P. In *Encyclopedia of Analytical Chemistry*; John Wiley & Sons, Ltd: 2006.

(220) Kobayashi, S.; Iwamoto, M.; Haraguchi, T. *Microscopy* **2016**, *65*, 296.

(221) Wolff, G.; Hagen, C.; Grünewald, K.; Kaufmann, R. *Biol Cell* **2016**, *108*, 245.

(222) Karreman, M. A.; Hyenne, V.; Schwab, Y.; Goetz, J. G. *Trends Cell Biol* **2016**, *26*, 848.

(223) Hoh, J. H.; Hansma, P. K. *Trends Cell Biol* **1992**, *2*, 208.

(224) Engel, A.; Muller, D. J. *Nat Struct Mol Biol* **2000**, *7*, 715.

(225) Dufrêne, Y. F. *ACS Nano* **2017**, *11*, 19.

(226) Dufrêne, Y. F. *Curr Opin Microbiol* **2003**, *6*, 317.

(227) Santos, N. C.; Castanho, M. A. R. B. *Biophys Chem* **2004**, *107*, 133.

(228) Lehenkari, P. P.; Charras, G. T.; Nykänen, A.; Horton, M. A. *Ultramicroscopy* **2000**, *82*, 289.